Quaternary Ventilation of the Indian Ocean Deep Basins, Foraminiferal Isotopic and Abundance Approach

A thesis submitted in partial fulfilment of

the requirements for the degree

of

Doctor of Philosophy

to

Discipline of Earth Science

Indian Institute of Technology Gandhinagar, India

by

Nisha Bharti

(Roll No. 16330005)

Under the guidance of

Prof. Ravi Bhushan

Geosciences Division

Physical Research Laboratory, Navrangpura

Ahmedabad-380009

To,

The wonderful Earth

Declaration

I declare here that this thesis report represents my own ideas in my own words and I have included others ideas with appropriate citations from original sources. I also declare that I have followed all principles of academic honesty and integrity and have not misrepresented or fabricated or falsified any idea/fact/source/data in my submission. I understand that any violation of the above can cause disciplinary action by the Institute and can also evoke penal action from the sources which have thus not been properly cited or from whom proper permission has not been taken when needed.

Nisha

Bharti

Date: May 24, 2022

(Roll No.: 16330005)

Department of Earth Science

Indian Institute of Technology Gandhinagar

Gandhinagar, Gujarat-382355

CERTIFICATE

It is certified that the work contained in the thesis titled **"Quaternary Ventilation of the Indian Ocean Deep Basins, Foraminiferal Isotopic and Abundance Approach"** by **Ms. Nisha Bharti** (Roll no: 16330005), has been carried out under my supervision and that this work has not been submitted elsewhere for a degree.

Prof. Ravi Bhushan

(Thesis Supervisor)

Professor,

Geosciences Division,

Physical Research Laboratory,

Ahmedabad, India

Date: May 24, 2022

Acknowledgment

It has been five years since I joined PRL for my research journey. It was a memorable time, with deep learning about the earth, the ocean as well as life. I feel privileged to thank all the people who helped me throughout the downwelling and upwelling of the Ph.D. life and helped to enlighten me through the research journey. The experience during the oceanographic expedition was great. Learning about the magnificent and vast ocean while onboard was enlightening. I could experience the greatness of the huge, energetic ocean.

I wish to express deep gratitude to my mentor Prof. Ravi Bhushan for supporting me throughout the research journey. I would specially thank him to provide such an interesting research topic, which I could enjoy working on during the tough days as well. Working with him was a great learning experience. I feel gratitude for the enormous amount of time and effort put by him to establish the world-class AMS lab for radiocarbon dating, without which this work would not be possible. I would also like to thank him for giving me the freedom to explore my field. He taught me to research with a positive attitude even in adverse scenarios. His guidance and supervision have helped me to develop as a researcher.

I would also like to express my sincere regard to my DSC members, Dr. Arvind Singh, Dr. Neeraj Rastogi, and Dr. Dibyendu Chakraborty, for their helpful discussions, evaluation, and crucial comments. I would like to thank Dr. Anil D. Shukla and Dr. Deepak Panda for their help with Scanning Electron Microscope. I am thankful to Prof. R. D. Deshpande, Prof. M. M. Sarin, Prof. Sunil K. Singh, Prof. M. G. Yadava, Prof. J. S. Ray, Dr. A. D. Shukla, Dr. Sanjeev Kumar, Dr, A. K. Sudheer, Dr. Vineet Goswami, Dr. A. H. Laskar and Mr. R. A. Jani for their valuable inputs and comments during area seminar. I am thankful to the director, dean, and the academic committee for their support during my Ph.D. tenure for critically evaluating my research work and providing fruitful inputs. I am also thankful to all the professors for their informative lectures during the course work. I would like to express my sincere gratitude to Dr. Luke Skinner to help me in the data visualisation, enlightening discussions, which greatly enhanced my thesis. I also wish to thank Dr. Maria D. Fuente and Dr. Julia Gottschalk for their insightful discussions.

I am extremely thankful to the Ministry of Earth Sciences (MoES) to provide the research vessel for sediment core collection. I specially thank the scientific team and crew members of expedition SS172, SS152, SK312, and SK304. I would also like to acknowledge the support of the staff members of the PRL library, computer center, administration, account section, workshop, CMG, purchase, and stores during this period.

Life during this thesis work would have been boring without my PRL colleagues. I would like to express my gratitude to Muruganantham, Chandana, Chinmay, Kiran, Anil and Romi for their support, help, and motivation during the initial Ph.D. days. I would like to convey my warm appreciation to my cubicle mate Ankur for being a great company and helping hand. I am also thankful to Partha for his enormous help during lab measurements as well as in discussions during paper and thesis writing and for being a great company. I would also like to thank Shivam, Sanjit, and Harsh for their help during lab measurements and the great company. These people have been a great support during the tough Ph.D. days. I will always cherish the time spent with them. I also thank all the Chemistry lab members, Upasana, Satish, Venky, Subha, Atinder, Damu, Mahesh, Priyanka, Abhishek, Rahul, Jaldhi, Ramsha, Payal, Ishita, Deep, Akshay, Riya, Devaprasad, Chandrima, Puneet, Suresh and Rohit for their kind support, cooperation and encouragement during my Ph.D. tenure. Their friendliness and cooperative attitude made me feel at home. I am thankful to Pravin bhai and Rashmik bhai for their kind support during the laboratory work. I am grateful to Deepika, Susree and Surendra to be a kind friends, Abdur, Sandeep, Priyank, Harish, Ayan and Prabir for all the fun times and memorable and happy stay at PRL. I thoroughly enjoyed their company. I also want to thank Akanksha and Shivangi for the interesting discussions, fun, care and for being great companions. Words will be less to thank my childhood friend Simpi, School friend Nikki, and grad friends Shalini, Jyoti, and Hemlata. I also wish to thank my masters' friends Vivek and Feba for being motivation and support.

I want to thank my family for their immense love, care, and sacrifice, without which this work was not possible. It's my pleasure to acknowledge my late grandmother to inculcate my interest in the soil. I also wish to thank mummy, papa, Pintu bhaiya and Tinku bhaiya as well as my sister-in-law for the love and great support. I would also like to thank my nephew "Buggu" for being a source of entertainment during the thesis writing. I am grateful to my cousins Dinesh bhaiya, Rajesh bhaiya, and Mukesh bhaiya for being the inspiration, motivation, and support throughout my Ph.D. period. It,s fortune to thank my fiancee Ankesh Ji for the love and care, my mother in law and my in laws family for the inspiration and support during my research journey.

I feel gratitude to Puchu, langurs, peacocks, squirrels, birds, rabbits, trees, flowers and the entire wildlife of the PRL campus, which kept me entertained, healthy and happy.

Although I tried, it is almost impossible to mention everyone who has contributed to this journey of research in some or other way. I am thankful to everyone of them who helped complete this thesis work.

~Nisha Bharti

Abstract

The ocean covers ~71% surface area of the earth with a maximum depth of ~11,034 m. Ocean stores huge amount of heat and balances Earth's heat budget, and contributes to ~96.5% water available on the earth, which has high heat-storing capacity. It stores almost 50 times more CO_2 than the atmosphere. Thus, the ocean plays a key role in regulating the earth's climate by regulating heat and atmospheric CO_2. Earth has witnessed several warm and cold phases since its formation, primarily due to the astronomical and orbital forcing of the sun, known as glacial and interglacial events. Numerous studies around the globe have suggested that the earth was ~5ºC colder during the last glacial maxima (LGM: 18,000-25,000 cal yrs BP) compared to the pre-industrial time. Deglaciation commenced ~15000 yrs ago and sustained up to present. These global climatic excursions accompanied by changes in the global ice sheet extension led to the modification in the ice-melt freshwater flux. Changes in the atmospheric condition along with freshwater flux modified the convective process in the deep water formation regions, mainly the Northern Atlantic and the Southern Ocean. Various paleoclimatic data suggested that global deep ocean circulation or thermohaline circulation was either slowed down or was shut down during the LGM. The thermohaline circulation acts as a cardiovascular system of the ocean by distributing nutrients, dissolved gases, heat, and CO_2 in the global ocean. In response to the modification of the deep water or thermohaline circulation, the biological, physical as well chemical process of the global ocean got altered.

Foraminifera, a marine microorganism dwelling in the ocean since early Cambrian, precipitate calcium carbonate shell in equilibrium with the seawater having planktic as well as benthic mode of life, records the paleoclimatic as well as paleo deep water signature. Isotopic, elemental, and species abundance analysis in the well-preserved foraminifera have been used globally to reconstruct the past climate as well as deep-sea conditions. The disequilibria between surface and deep-sea radiocarbon concentration recorded in calcite shells of planktic and benthic foraminifera have been measured in various marine sediment cores from the Pacific, the Atlantic, as well as the Southern Ocean. Most records suggest that the deep ocean was poorly ventilated during the glacial time. However, few records suggest no change in the glacial ocean ventilation. Paleo-ventilation records along with other supporting proxies compared

with the past atmospheric CO_2 and $\Delta^{14}C$ records from the Pacific, Atlantic, and the Southern Ocean suggest that the ocean probably played a key role in glacial depletion and deglacial increase of the atmospheric CO_2. The decrease and increase in the air-sea gas exchange during the glacial and deglacial period respectively were probably the reason for this atmospheric CO_2 changes. However, it remains to be resolved in view of some studies which differ from this understanding. Additionally, the role of the various ocean in global average poor deep-sea ventilation remains to be explored, with some ocean basins sparsely studied for their role in glacial-interglacial climatic changes. The Indian Ocean, which contributes ~20% to the global oceanic volume, remains one of the most understudied ocean basins. There is no ventilation age record from the deep Indian Ocean so far, except one from the Southern Ocean sector.

In view of this, three major basins of the Indian Ocean i.e. Western, Central, and Eastern basin have been investigated in this study based on Accelerator Mass Spectrometry (AMS) radiocarbon dating of the coexisting planktic and benthic foraminifera in four marine sediment cores. Along with this, stable carbon isotope was measured in planktic and benthic foraminifera to decipher the past changes in the contribution of different water masses, and oxygen isotope for the past temperature variations. Additionally, benthic foraminifera species abundance was analysed to understand the changes in the past deep-sea environment in terms of food supply and dissolved oxygen.

Replicated radiocarbon ventilation age record from two sediment cores of the Central Indian Ocean (CIO) and other supporting parameters along with published Neodymium isotope data suggest isolation of the CIO during the last glaciation. The peak of the ventilation age during Heinrich Stadial-1 and Heinrich Stadial-2 suggested the response of the CIO to the hydrographic changes in the Northern Atlantic. Much higher glacial radiocarbon ventilation age record from the CIO compared to the global paleo ventilation age record proposes the contribution of hydrographic changes originating in the Indian Ocean as well. Paleo ventilation age records from the CIO, the South West Indian Ocean (SWIO), and the Eastern Indian Ocean (EIO) show a remarkable difference in the evolution of paleo-deep circulation in the western, central, and eastern basin of the Indian Ocean. However, during a certain period, contribution of mantle-derived dead CO_2 was also evident in the SWIO as well as in the EIO.

Summarising the whole thesis work, the present study was able to reconstruct the first paleo-ventilation age record for the deep water from major deep basins of the Indian Ocean. It highlights the under-estimated and under-appreciated role of the glacial Indian Ocean in the global average poor ventilation of the deep ocean during the last glaciation and the subsequent changes in the carbon cycle.

Thesis content

List of Figures

List of Tables

Acronyms

AABW: Antarctic Bottom Water

ACC: Antarctic Circumpolar Current

ACR: Antarctic Cold Reversal

AGE: Automated Graphitisation Equipment

AMOC: Atlantic Meridional Overturning Circulation

AMS: Accelerator Mass Spectrometer

AS: Arabian Sea

AURIS: PRL-Accelerator Unit for Radioisotope Studies

B-A: Bølling-Allerød warming

BoB: Bay of Bengal

BFAR: Benthic Foraminifera Accumulation Rate

CDW: Circumpolar Deep Water

CEIO: Central Equatorial Indian Ocean

CHS: Carbonate Handling System

CIO: Central Indian Ocean

DBD: Dry Bulk Density

DIC: Dissolved Inorganic Carbon

DWBC: Deep Western Boundary Current

D-O: Dansgaard-Oeschger oscillations

EA: Elemental Analyser

EIO: Eastern Indian Ocean

ESA: Electrostatic analyser

FIRI: Fourth International Radiocarbon Intercomparison

HE: Heinrich Event

HOSS: High Organic Sediment Sample

HS: Heinrich Stadial

HS-1: Heinrich Stadial-1

HS-2: Heinrich Stadial-2

HS-3:Heinrich Stadial-3

IAEA: International Atomic Energy Agency

IC: Inorganic Carbon

IDW: Indian Deep Water

IEW: Indian Ocean Equatorial Westerlies

IRD: Ice-Rafted Debris

IRMS: Isotope Ratio Mass Spectrometer

ITF: Indonesian Throughflow

ITW: Indonesian Throughflow Water

IO-MOC: Indian Ocean Meridional Overturning Circulation

ka BP: Kilo years before present

kyr: Kilo years

LCDW: Lower Circumpolar Deep Water

LGM: Last Glacial Maxima

LGP: Last Glacial Perioda

LIS: Laurentide Ice Sheet

LOSS: Low Organic Sediment Sample

LSR: Linear Sedimentation Rate

MIS: Marine Isotopic Stages

MOC: Meridional Overturning Circulation

NADW: North Atlantic Deep Water

NBS: National Beauro of Standards

NEM: North East Monsoon

NGRIP: North Greenland Ice Core Project

NH: Northern Hemisphere

NIDW: North Indian Deep Water

OC: Organic Carbon

PDB: Pee Dee Belemnite

PDW: Pacific Deep Water

PGW: Persian Gulf Water

PMOC: Pacific Meridional Overturning Circulation

PSU: Practical Salinity Unit

PVC: Poly Vinyl Chloride

RA: Relative Abundance

RI: Rare isptope

RSW: Red Sea Water

SAMW: Subantarctic Mode Water

SBoB: Southern Bay of Bengal

SEC: South Equaotorial current

SST: Sea surface Temperature

SWIO: South West Indian Ocean

SWM: South West Monsoon

THC: Thermohaline Circulation

UCDW: Upper Circumpolar Deep Water

VIRI: Fifth International Radiocarbon Intercomparison

VPDB: Vienna Pee Dee Belemnite

WIO: Western Indian Ocean

WOCE: World Ocean Circulation Experiment

YD: Younger Dryas

Chapter 1.

Introduction

The ocean is a huge reservoir of CO_2, containing at least 50 times more CO_2 than the atmosphere (Raven and Falkowski, 1999). Hence it plays a crucial role in the global carbon cycle and glacial-interglacial climatic events. Numerous paleo-oceanographic and paleoclimatic studies from all over the globe suggest that the earth has been at least 5ºC cooler during the last glaciation compared to the preindustrial period, and deglaciation commenced ~15 ka BP (Gornitz, 2009). Additionally, CO_2 trapped in the Antarctic and Greenland ice core suggest that atmospheric CO_2 during the last glacial period was ~90 ppm lower than the preindustrial period (Monnin et al., 2001). While numerous studies proposed that the ocean played a key role in changing the atmospheric CO_2 during the late Quaternary (Sigman and Boyle, 2001; Galbraith et al., 2007; Marchitto et al., 2007; Anderson et al., 2009; Skinner et al., 2010; 2017; Burke and Robinson, 2012; Hain et al., 2014; Menviel et al., 2014; Freeman et al., 2016; Gray et al., 2018; Galbraith and Skinner, 2020), some regions of the ocean remained understudied and underappreciated in the global paleoclimatic perspective, mainly the Indian Ocean (Skinner et al., 2017; Zhao et al., 2018). Specially, the evolution of deep water circulation in the Indian Ocean since the last glacial period remains poorly understood. Only a handful of radiocarbon records of benthic foraminifera are available from the deep Indian Ocean (e.g., Gottschalk et al., 2020; Ronge et al., 2020), despite its geographic and hydrographic importance and 20% volumetric contribution to the global ocean. Also, great deal of spatial heterogeneity has been observed in the paleo-oceanographic studies in the Pacific, Atlantic, and the Indian Ocean. However, the role of the Indian Ocean basin in changing atmospheric

CO_2 during quaternary glaciation and interglaciation remains poorly addressed and underappreciated in the global perspective (Skinner et al., 2017).

The Indian Ocean is landlocked in the north and facilitates the upward limb or upwelling limb of the thermohaline circulation. Hence, it acts as an ideal location to study the changes in the paleo deep ocean circulation and paleo deep water ventilation. Therefore, the present study attempts to address the changes in the paleo-deep water condition of the Indian Ocean, for the late Quaternary period using radiocarbon dating of co-exiting planktic and benthic foraminifers, stable carbon and oxygen isotopic study, benthic foraminifera assemblage study, and geochemical investigation of marine sediments. The present study also endeavours to decipher the productivity variation in the Central Indian Ocean. The study has been performed in five marine sediment cores from the three deep basins of the Indian Ocean (Western Indian Ocean basin, Central Indian Ocean basin, and Eastern Indian Ocean basin). The large disequilibrium between planktic and benthic foraminifera radiocarbon ages from the two sediment cores of the Central Indian Ocean basin suggest increased isolation of the deep Central Indian basin during the last glaciation compared to the global ocean. This evidence was also verified with low abundance of benthic foraminifera species susceptible to high dissolved oxygen. Hence, this study deciphers the underappreciated role of the Indian Ocean in glacial-interglacial carbon cycle (Skinner et al., 2017; Zhao et al., 2018). However, radiocarbon evidence from the south- west Indian Ocean suggests input of mantle-derived dead CO_2, during the Holocene. The Eastern Indian Ocean basin also suggested an anomalous radiocarbon peak at 19.7 ka BP, possibly due to mantle-derived dead CO_2.

1.1 Global Thermohaline Circulation (THC)

Thermohaline circulation or Great Ocean Conveyer belt refers to the conceptual mechanism of water movement in the global ocean driven by fluxes of heat and freshwater across the sea surface and interior mixing of heat and salt (Rahmstorf, 2006). It comprises vertical transport as down-welling in the subpolar ocean, upwelling in the equatorial ocean, and horizontal transport in the deep ocean as deep flow along mid-oceanic ridges. Another widely used term for deep water circulation “Meridional Overturning Circulation (MOC)” is the north-south flow of the water masses, which also includes wind-driven horizontal transport of warm and saline water as surface current (Rahmstorf, 2006). Independent overturning circulation exists in the

Atlantic, Indian and Pacific Ocean, known as Atlantic Meridional Overturning Circulation (AMOC), Indian Ocean Meridional Overturning Circulation (IO-MOC; Jayasankar et al., 2019), and Pacific Meridional Overturning Circulation (PMOC) respectively. Surface currents are fast of the order of ~50 $cm.s^{-1}$, whereas deep horizontal currents are slower of the order of a few $cm.s^{-1}$ (Talley, 2011). THC facilitating the transport of heat, nutrients,

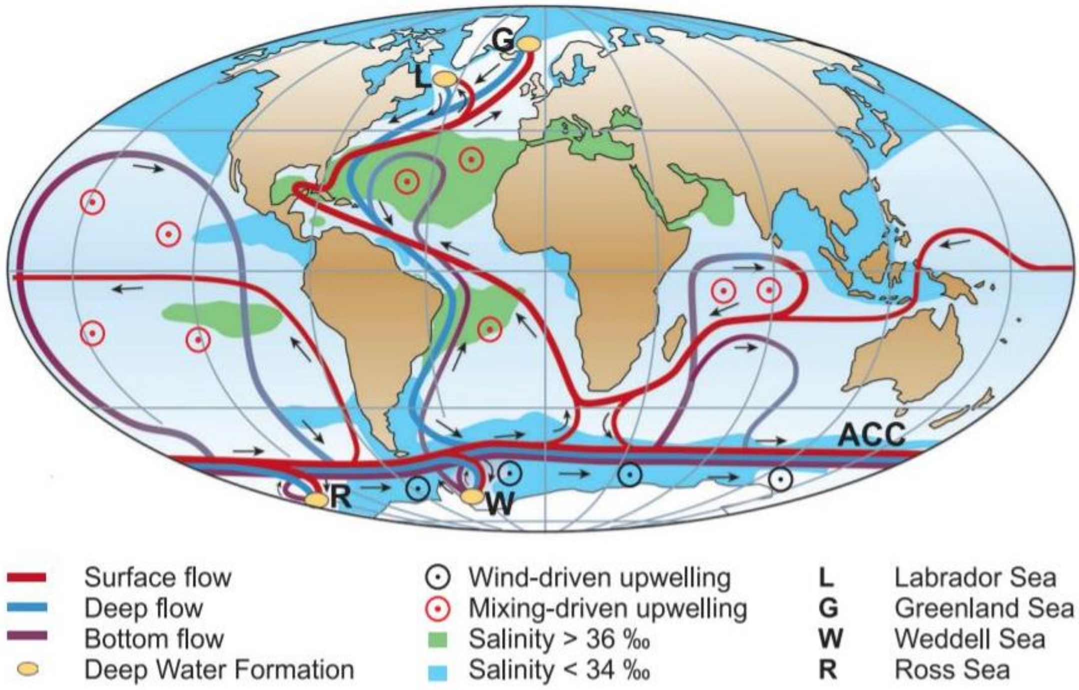

Figure 1.1. Schematic representation of the global thermohaline circulation. Surface currents are shown in red, deep waters in light blue, and bottom waters in dark blue. The main deep water formation sites are shown in orange. Source: (Rahmstorf, 2002).

CO_2, dissolved oxygen from the deep water formation regions to the global ocean, act as a cardio-vascular system of the ocean and helps in balancing the earth's heat budget. Owing to these properties of the THC, which affect the biology of the ocean as well as the climate of the earth, it becomes important to address the rate of the THC in changing climate scenarios, especially changing CO_2 (Rahmstorf, 2002). Deep water ventilating the global ocean mainly forms as North Atlantic Deep Water (NADW)) in the Northern Atlantic (N. Atlantic) and Antarctic Bottom Water (AABW) in the Southern Ocean (Figure 1.1). The NADW is sourced mainly from the Norwegian Sea, the Greenland Sea, the Labrador Sea, and from the Mediterranean Sea in the N. Atlantic. Whereas, AABW is sourced from the Ross Sea, Weddell Sea, Adélie coast, and Prydz Bay in the Southern Ocean (Rahmstorf et al., 2005; Orsi, 2010). Gulf stream and its northern extension N. Atlantic current carry the warm, saline surface water via Iceland -Scotland Ridge towards the Nordic Seas (the Greenland Sea, Norwegian Sea, and Iceland Sea) and the Labrador Sea (Marshall and Schott, 1999), which contributes nearly two-third of the NADW. Another fraction is contributed by the upwelled AABW in the Atlantic (Talley, 2013). In the N. Atlantic, winter cooling along with the local circulation patterns facilitate the deep mixing and convection (Marshall and Schott, 1999; Handmann et al., 2018), which leads to the formation of NADW, characterized by young age, high salinity (>34.9 in the N. Atlantic), high dissolved oxygen (>5.5 ml/l in N. Atlantic) and low nutrient (Tomczak and Godfrey, 2003; Talley, 2013).

Table 1.1. Physical properties of the deep water mass ventilating the global ocean

Major Deep water masses	Potential temperature (°C)	Salinity (PSU)	Dissolved oxygen (ml/l)	Water Depth (m)	References
IDW (low oxygen; fraction of UCDW and NADW)	0.6-3.5	34.5-34.7	<4.03	~1500-3800 m	(Talley, 2013; Lee et al., 2015)
PDW (low oxygen)	1,1-2.2	34.65-34.75	<4.03	~1500-3800 m	(Pickard, 1979; Talley, 2013)
NIDW (high silicate, low oxygen/ aged NADW/CDW)	1.6-3.2	34.74-34.86	2.05-3.14	2000-2500 m	(You, 2000; Goswami et al., 2014)
UCDW (mixture of NADW, AABW and Pacific intermediate water)	1.6-1.9	34.6-34.7	-	-	(Orsi et al., 1999; Amakawa et al., 2019)
LCDW (salinity maxima of CDW)	0.3-1.5	~34.06-34.72	> 4.48	<~4000 m in Indian Ocean	(Orsi et al., 1999; 2002; Amakawa et al., 2019)
CDW (deep salinity maxima)	1.0-2.3	34.62-34.77	4.29-4.59		(You, 2000; Kim et al., 2020)
NADW (high salinity, oxygen, low nutrient)	1.9-2.7	~34.78-34.85	>4.76-5.50	1500-3500 m	(Toole and Warren, 1993; Stichel et al., 2012)
AABW (fresher, Colder)	-1.0-0.2	~34.66-34.71	-	>3800 m	(Haine et al., 1998; Orsi et al., 1999; Orsi, 2010)

NADW sinks and occupies the depth of ~1000-4000 m in the Atlantic Ocean and moves southward as Deep Western Boundary Current (DWBC). Because of the Mid-Atlantic Ridge, deep flow in the Atlantic is divided along two pathways, i.e. on the eastern and western basin of the Mid Atlantic Ridge. A fraction of the NADW travels towards the Indian Ocean, which is unmixed, and the remaining part upwells in the Antarctic Circumpolar Current (ACC) region up to 200 m depth in the Weddell sea (Talley, 2013), aided by the Ekman divergence caused by the wind (Rahmstorf, 2006). In the Southern Ocean, the upwelled water feeds to the formation of Antarctic Bottom Water (AABW), aided by increased salinity of surface water due to brine rejection and heat loss during winter. By mixing of NADW, Ross Sea, and Weddell Sea Deep Waters (a subset water mass of AABW), diffusively formed Indian Deep Water (IDW) and Pacific Deep Water (PDW), Circumpolar Deep Water (CDW; Talley, 2013) forms in the Southern Ocean (mainly in the Weddell Sea, Ross Sea and along Adélie Coast (Sloyan, 2006)). CDW moves northward towards the Pacific Ocean and the Indian Ocean between depths of ~2000-3800 m as Upper Circumpolar Deep Water (UCDW) (Piotrowski et al., 2009; Talley, 2011), possibly mixing with overlying southward moving IDW (in the Indian Ocean) and PDW (in the Pacific Ocean) in the same depth range. Below UCDW, northward moving Lower Circumpolar Deep Water (LCDW; cold, more saline compared to IDW/PDW) having a major contribution of AABW ventilates the deep Indian Ocean and the Pacific Ocean. Diapycnal mixing in the Indian Ocean and the Pacific Ocean leads to southward return flow of NADW and AABW to the upper ocean, which finally upwells in the Southern Ocean sea surface as aged IDW and PDW (Talley, 2013). Further, the upwelled IDW and PDW flows in the Indian Ocean and Pacific Ocean thermocline as high nutrient Subantarctic Mode Water (SAMW) and follows their path towards the N. Atlantic and eventualy goes on to form NADW (Talley, 2013).

1.2 Indian Ocean Oceanographic Setting

Indian Ocean overturning circulation is a vital unit of the global THC, facilitating the diffusive upwelling of the deep water and upward limb of the THC via the Indonesian Throughflow (ITF) and Agulhas flow. Due to its northern land limits, Indian Ocean circulation is unique compared to the Atlantic and the Pacific Ocean. Based on the World Ocean Circulation Experiment (WOCE) and GEOSECS hydrographic study, a detailed study was conducted to understand the process of deep circulation in the Indian Ocean (Mantyla and Reid, 1995; Kumar and Li, 1996; van Aken et al., 2004; McCave et al., 2005; Goswami et al., 2014). During the last few decades, it was realised that the deep water in the Indian Ocean was ventilated by the waters sourced not only from the Atlantic and Southern Ocean, but also from the Pacific Ocean, and regional diffusive formation of deep water takes place well within the deep Indian Ocean basin. Mid Oceanic Ridges and Fracture Zones play an important role in modifying the deep circulation pathways in the Indian Ocean (Mantyla and Reid, 1995), which creates separate deep circulation in three basins of the Indian Ocean e.g., in the Western Indian Ocean (WIO) basin, Central Indian Ocean (CIO) basin and the Eastern Indian Ocean (EIO) basin (Toole and Warren, 1993). Additionally, there are many volcanic hotspots in the Indian Ocean basin (Morgan, 1978; Mahoney et al., 1989; Gamo et al., 2001; Tao et al., 2012), which has potential to affect the chemical properties of the deep waters (Nishioka et al., 2013).

The water below 3800 m depth in the Indian Ocean is sourced from the AABW or subset water mass of the AABW. However, in the depth between 2000-3800 m, diffusively formed water mass circulates in the Indian Ocean basin (Tomczak and Godfrey, 2003), which has major contribution from the NADW. This water mass has been termed as southward moving North Indian Deep Water (NIDW; Mantyla and Reid, (1995), Johnson et al., (1998), McCave et al., (2005), and Wilson et al., (2012)), northward moving IDW by some authors (Tomczak and Godfrey, 2003; Lee et al., 2015; Amakawa et al., 2019), southward moving IDW by Talley, (2013), as well as UCDW by Piotrowski et al., (2009). These diffusively formed water can be identified by low oxygen and high nutrient (Table 1.1), and they are old compared to the AABW and NADW. High saline NIDW is formed possibly due to mixing of CDW with sinking high salinity Persian Gulf Water (PGW) and the Red Sea Water (RSW) in the north-west Indian Ocean, which mostly influences the western basin, central basin, and the eastern Perth basin (Kumar and Li, 1996; McCave et al., 2005). Contrary to NIDW, IDW forms in the Indian Ocean due to diapycnal diffusion and mixing of the water masses due to warming, while moving northward towards the Indian Ocean (Talley, 2013) and it consists of NADW and UCDW (Amakawa et al., 2019). UCDW is formed by mixing of NADW, AABW as well as intermediate water mass from the Pacific Ocean. However, ambiguity remains regarding the flow direction and identification of these water masses in different regions of the Indian Ocean, due to only minute differences in the physical properties of these water masses (Table 1.1).

Deep water in the western Indian Ocean traverses through various fracture zones of southwest Indian Ridge (with the deepest sill depth of 3900 m). From the Madagascar basin, the deep water flows as northward deep western boundary current towards the Mascarene basin, and finally reaches the Somali basin via Amirante Passage (Donohue and Toole, 2003; MacKinnon et al., 2008). LCDW flows below 4000 m in the SWIO, though there is a partial flow of LCDW in Madagascar and Mascarene basin via some fractures lying above 3900 m along the South-West Indian Ridge (Amakawa et al., 2019). At the depth of 2000-4000 m, high nutrient subset water mass of the CDW i.e. UCDW, NIDW, and IDW ventilate the WIO. The AABW and LCDW originating from the Ross and Adélie coast enters the Australian-Antarctic and South Australian basin and then fill the South Australian basin. Further, it enters the CIO basin via the south-east Indian Ridge. The AABW and LCDW fill the Perth basin and EIO basin and further spill into the CIO basin through gaps of Broken Plateau (Sloyan, 2006; Talley, 2011).

1.3 Quaternary Glacial and Interglacial Events

Polar Earth receives a very small fraction of direct heat from the sun. Hence it remains the coolest place on Earth, and the presence of moisture in these regions causes glaciation. Glaciers cover ~10% surface area of the Earth at present, and it has experienced dramatic changes in terms of its volume, extent, and rate of flow throughout the geological history of the Earth (Benn and Evans, 2014). Paleoclimatic data suggests that throughout the Earth's history, it faced several glacial and deglaciation cycles (Sarnthein et al., 2003) due to changes in the Earth’s orbit around the sun, along with plate tectonics and atmospheric CO_2 changes (Broecker et al., 1968; Berger, 1988). Milankovitch cycle with cyclicity periods of 23,000, 41,000, and 100,000 yrs have been observed in the paleoclimatic records corresponding to the changes in the Earth’s precession, tilt and eccentricity (Imbrie et al., 1992). These cyclicities have been responsible for the periodic change in the incoming solar radiation on the Earth and hence various feedback mechanisms controlling the global climate. Glacier and ice sheets exert a cooling effect by increasing their topographic elevation and reflecting incoming solar radiation i.e. ice-albedo feedback. Hence, cooling will expand ice sheets which may lead to further cooling and conversely warming can accelerate the ice sheet retreat (Gornitz, 2009). This mechanism is critical for glacial-interglacial termination. Further, ice sheets also played an important role in changing the freshwater budget of the ocean, mainly in the N. Atlantic and the Southern Ocean. Increased freshwater flux probably led to a complete shutdown or slowdown of the THC, which decreased the poleward heat transfer and led to cooling in mid-latitude and the subpolar Atlantic (Gornitz, 2009). The rapid advancement of ice sheets (mainly Laurentide ice-sheet, which covered most of the Canada and northern United States) during climatic reversal led to the deposition of ice-rafted debris (IRD layers) in the N. Atlantic (Bond et al., 1992). These events are known as Heinrich events (HE) and have cyclicity of ~10,000 yrs (Bond et al., 1992). Along with changes in the extension of ice sheets in Greenland during these glacial events, Earth witnessed changes in both global temperature as well as sea level. The late Quaternary, the period of interest in perspective of radiocarbon witnessed various climatic events and different terms have been used to define these climatic intervals by the paleo-climatologist e.g., Marine Isotope Stage (MIS), Dansgaard-Oeschger (D-O) cycles, Last Glacial Maxima (LGM), Heinrich Events (HEs), Antarctic Cold Reversal (ACR), Bølling-Allerød Warming (B-A), Last Glacial Termination, Younger Dryas (YD), 8.2 ka cold event and Holocene.

Marine Isotopic Stages (MIS) are oxygen isotope stages representing warm and cold climate oscillations, first recorded in foraminiferal oxygen isotope records by Emiliani (1955). The MIS are numbered in such a manner that the odd numbers correspond to minimum δ^{18}O or warm period, and even number corresponds to maximum δ^{18}O or cold period. Nearly 100 MIS have been reported for the last 2.6 million years, among them the last 3 MIS fall under the radiocarbon age limit (Groeneveld et al., 2014). D-O cycles are rapid fluctuations of temperature from cold glacial climate to warm glacial climate during the Wisconsinan Glaciation (~115-19 ka BP: (Gornitz, 2009), which is observed in the δ^{18}O record in sediment cores from the N. Atlantic. Though this cycle has been noticed globally, Antarctica exhibited warming during the cold phase of the D-O event, which was probably the effect of bipolar Seesaw (Gornitz, 2009). Moreover, LGM is defined as the interval of the Last Glacial Period (LGP), when the global ice sheet was at its maximum volume (Mix et al., 2001). Based on various paleoclimatic studies, it is believed that LGM commenced between 18,000-25,000 cal yrs BP, however, timing, as well as extent and nature of the LGM, remains a debatable topic (Clark et al., 2009; Gornitz, 2009). Many mountainous and continental glaciers record predated LGM (Hughes et al., 2013), and it showed that the ice sheets during 26.5-10 ka BP were at the same position during LGM (Clark et al., 2009). LGM also corroborates with cool tropics (by ~5°C), higher surface wind due to increased meridional temperature gradient, increased dustiness due to enhanced arid conditions, exposed continental shelf (Gornitz, 2009) as well as lowering of greenhouse gases (water vapor). Meanwhile, due to massive discharge of Laurentide Ice Sheet (LIS) from Hudson Strait ice stream, Heinrich layers of Ice Rafted Debris (IRD) were found in the N. Atlantic (Heinrich, 1988; Bond et al., 1992) from the Labrador Sea to 40°N during several glacial events (Hodell et al., 2017). These events known as Heinrich Events have occurred 6 times during the Wisconsinan Glaciation. The commonly used term "Heinrich Stadial (HS)" was the cold period, which included the Heinrich event. The last prominent HS i.e. HS-1 is analogous to Mystery Interval (17.5-14.5 ka BP) (Hodell et al., 2017). B-A interstadial (15-12.7 ka BP) was the warm phase of the Weichselian late glacial or last glacial-interglacial termination, which led to increased summer temperature (Gornitz, 2009). It was followed by a cold event known as Younger Dryas (YD; 12.7-11.5 ka BP). YD has been hypothesized to have occurred due to reduced AMOC, possibly caused by increased meltwater contribution form the northern hemisphere ice sheet. Holocene served as the end of the Pleistocene climate and hence went through rapid climatic reversals. Based on tree ring dating and annual ice layers, it is believed that Holocene initiated by 11.5 ka BP (Gornitz, 2009).

1.4 Marine carbon cycle, Thermohaline Circulation and atmospheric CO_2

The marine carbon cycle is an integral part of the "global carbon cycle", which deals with the transfer of the carbon to the surface, intermediate and deep ocean. The surface ocean takes the atmospheric CO_2 and distributes it to the different parts of the ocean via (1) the solubility pump, (2) the carbonate pump, and (3) the biological pump. Various authors have used these terms differently, especially the biological pump (Galbraith and Skinner, 2020). The solubility pump is responsible for the transport of carbon from the surface to the deep ocean in the form of dissolved inorganic carbon (DIC), through physical (deep water circulation) and chemical processes. The solubility of CO_2 is inversely proportional to the temperature. This results in cold deep water formation regions having higher concentrations of DIC, and warm equatorial ocean experiences degassing of the marine CO_2. Carbonate pump is sometimes described as a part of the biological pump. Marine organisms like foraminifers, coccolithophores, and mollusks precipitate hard calcium carbonate shell, fix marine DIC (Equation 1.1) and hence act as carbonate pump.

$$Ca^{+2} + 2HCO_3^{-1} \rightarrow CaCO_3 + CO_2 + H_2O$$

Moreover, biological pump involves fixing of CO_2 into particulate organic carbon as well as respiration of organic carbon, converting it back into DIC. By drawing the atmospheric CO_2 from the surface and storing it in the deep ocean, it acts in sequestration of the atmospheric CO_2. However, degassing of marine CO_2 during upwelling counteracts this process. The role of the biological pump in regulating atmospheric CO_2 depends on the rate of ocean circulation, air-sea gas exchange, ocean pH, and total oceanic carbon inventory (Galbraith and Skinner, 2020). The ocean can store 50 times more CO_2 than the atmosphere, which makes it a key player in the decrease of atmospheric CO_2 during LGM and increase during the last deglaciation.

1.5 Radiocarbon dating and marine reservoir age

Radiocarbon dating technique is an absolute dating method which can be employed for determining the chronology of events in sediment samples. Carbon has three naturally occurring isotope ^{12}C (~98.89%), ^{13}C (~1.11%), ^{14}C (trace). Among these isotopes, ^{14}C is known as "radiocarbon", which can be used as potential chronometer for the late Quaternary, and dating is based on the principle of measurement of residual ^{14}C in a sample. ^{14}C is produced in the atmosphere due to the interaction of cosmic rays produced slow thermal neutron with atmospheric ^{14}N (see equation below). The production rate of radiocarbon in the atmosphere is ~1.6 to 2 atoms.cm^{-2}.s^{-1} (Key, 2001). Radiocarbon thus produced in the atmosphere readily gets oxidized to $^{14}CO_2$, further diffuses in the atmosphere and ocean, and becomes part of the food chain. As long as the organism is alive, it keeps exchanging CO_2 from the atmosphere and hence has radiocarbon concentration similar to that in the atmosphere. Once the organism dies, atmospheric $^{14}CO_2$ exchange stops, and ^{14}C starts decreasing due to its loss via radioactive β^- decay to ^{14}N (Figure 1.2 and equation below). Half-life of ^{14}C i.e. 5730±40 yrs makes it an appropriate tracer to determine the age of any fossil that existed during the last ~55,000 yrs. However, the radiocarbon production rate varied with time (Köhler et al., 2006), which requires calibration of radiocarbon age to know the true age. In the last few decades, radiocarbon community (INTCAL group) has refined the radiocarbon age calibration curve using tree rings, corals, varved sediments and speleothems using a method other than radiocarbon (Reimer et al., 2013; 2020).

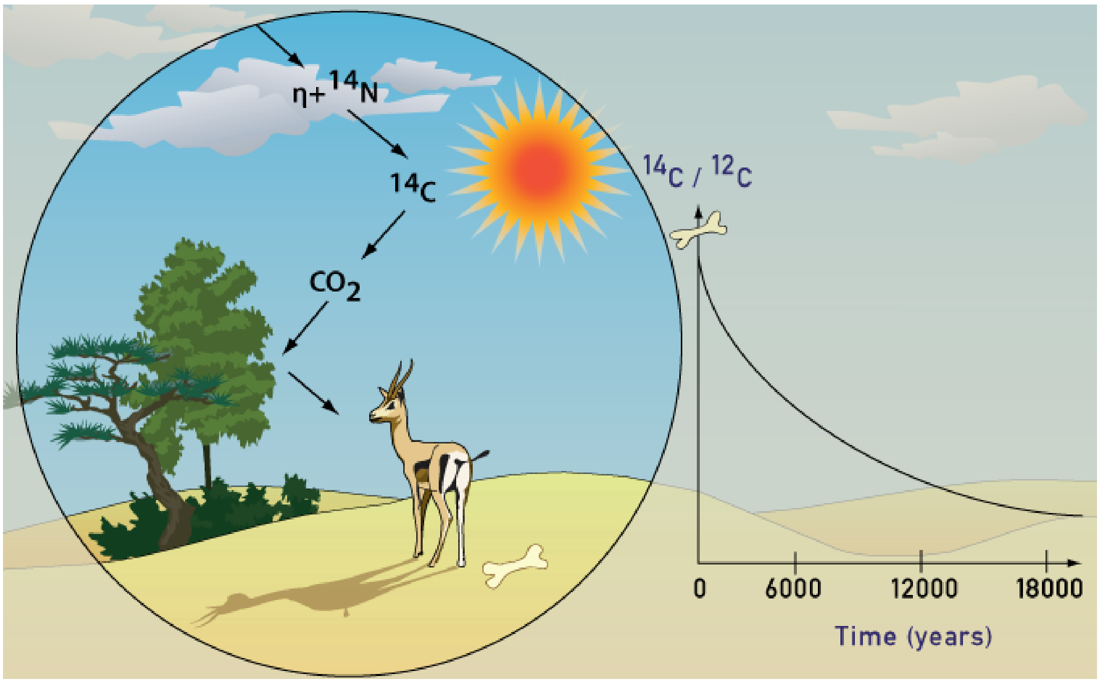

Figure 1.2. Schematic showing basis of radiocarbon dating technique. Source: www.naturphilosophie.co.uk

$$^{14}N + n \longrightarrow {}^{14}C + p$$

$$^{14}C \longrightarrow {}^{14}N + \nu_e^- + Q + \beta^-$$

Large overturning circulation time of the ocean (~1000 yrs) compare to atmospheric equilibration time (in order of decades), makes ocean undersaturated with respect to atmospheric radiocarbon concentration. The deep and intermediate water in the global ocean is always depleted in the ^{14}C with respect to the atmosphere**,** as it is not in contact with the atmosphere. This aged deep and intermediate water upwells in various part of the global ocean and contribute older CO_2 to the mixed layer, causing reservoir effect. Further, it results in older age of marine sourced samples contemporary to the terrestrial samples. Moreover, the reservoir age of the mixed layer varies spatially in the ocean due to upwelling and surface/subsurface currents, causing need for localized reservoir age correction known as ΔR. ΔR is the deviation of the marine sample radiocarbon age from the global mean reservoir age (550 yrs) (Heaton et al., 2020). The degree of disequilibrium of radiocarbon age between mixed layer and atmosphere also varied spatially, with higher amplitude in the Southern Ocean (de la Fuente et al., 2015; Galbraith et al., 2015; Skinner et al., 2019).

1.6 Foraminifera- a Magnificent Narrator of Paleo-ocean

The word foraminifera is derived from the Latin word "Foramen" which means "hole bearing". They are single-celled organisms (protists) with reticulated pseudopods, characterized by the net kind of structure made of cytoplasm, which helps to catch food. Foraminifera makes a $CaCO_3$ shell (test) which has one or more chambers, while some organisms also produce the shell or agglutinated sediment particles. The hard calcium carbonate shell of this tiny well-preserved organism, which lived since early Cambrian (Boersma, 1986; Culver, 1991), preserve the story of the past ocean water it inhabited during its life-cycle. The conversion of CO_2 to calcium carbonate during foraminiferal shell formation and dominance of foraminiferal ooze in the global ocean makes it an important component of the carbon cycle, a closely related factor of the earth's climate. In the foraminiferal database, so far 54,600 species have been listed and among them ~9,600 species are extant (in existence) and ~45,000 species have been recorded as fossilised (Hayward et al., 2020). Most of the foraminifera are marine, however, some are also known to dwell in freshwater conditions and fewer are non-aquatic too (Lejzerowicz et al., 2010). Its abundance in the ocean from poles to the equator, surface ocean to ocean-floor, deep ocean to coastal ocean, mangrove areas to tidal flats, and present to Cambrian period makes it scientifically important in biostratigraphy, paleoecology, paleobiogeography, paleo-oceanography, and paleoclimate (Gooday et al., 1992; Gooday, 1994; Saraswat and Nigam, 2013). In the marine environment, foraminifera is either planktic (surface-ocean dwellers) or benthic (sea-floor dwellers). 99% of the extant species are benthic foraminifera and only the remaining 1% (40 species) are planktic (Dowsett, 2007). Dominant environmental factors for planktic foraminifera are well understood compared to the benthic foraminifera, because of its dependency on temperature, salinity and surface productivity. However, for benthic foraminifera, it depends on the pore-water chemistry of sea-floor sediment (Gupta, 1999), and hence its ecological aspects are still a debatable part of the research.

1.6.1 Planktic and Benthic Foraminifera

Planktic foraminifera mostly dwell in the photic zone of the ocean and is characterized by their floating lifestyle. Their size usually ranges from 100 μm to 1 mm in length. Foraminifera are adapted to the planktic mode of life for the past ~200 Ma and its rapid evolution thereafter makes it an ideal proxy for biostratigraphy. Also, their sensitivity to the physical, biological, and chemical properties of seawater makes it a classic index for paleo-oceanographic, paleo-ecological and paleoclimatic studies (Table 1.2). Some planktic foraminifera species prefer mixed layer of the ocean (e.g., *Globigerinoides ruber, Trilobatus sacculifer*) and some species are found in the thermocline (e.g., *Globorotalia scitula, Globorotalia crassaformis, Globorotalia menardii, N. pachyderma;* (Kemle-von Mücke and Oberhänsli, 1999; Ravelo and Hillaire-Marcel, 2007)).

Table 1.2. Use of planktic foraminifera to reconstruct climatic parameters.

Climatic parameters	Tracer	Planktic Species	References
Chronology of marine sediment core	$\Delta^{14}C$	Mainly mixed layer species e.g., *G. bulloides., T. sacculifer, G. ruber, O. universa*	(Stuiver et al., 1998b; Broecker et al., 1999; Hughen, 2007)
Biostratigraphy	Absence/presence of species	e.g., occurance of *pink ruber* at ~125 ka BP	(Berggren and Miller, 1988)
Paleo sea surface temperature	$\delta^{18}O$, $\delta^{13}C$ and Mg/Ca	*T. sacculifer, G. bulloides, G.ruber, O. universa*	(Bemis et al., 1998; Ravelo and Hillaire-Marcel, 2007)
Upwelling intensity	$\delta^{18}O$, $\delta^{13}C$ and faunal study	*N. pachyderma, N. dutertrei, G. bulloides*	(Steens et al., 1992; Thunell and Sautter, 1992; Naidu and Malmgren, 1996)
Seasonality in sea-ice distribution	Presence of Subpolar species in polar region	*T. quinqueloba, G. bulloides, G. glutinata*	(Sarnthein et al., 2003; Berben et al., 2014; 2017)
Paleo productivity	$\delta^{13}C$	Mixed layer dwelling species	(Sun et al., 2006)
Paleo-monsoon reconstruction	$\delta^{18}O$	*G. ruber, T. sacculifer*	(Tiwari et al., 2006)
Paleo pH of surface ocean	$\delta^{11}B$	Subsurface species	(Raitzsch et al., 2018)

Benthic foraminifera have evolved since Cambrian time and is a major part of the benthic faunal community. They dwell in various conditions of the ocean floor from the intertidal zone to brackish water environment and from deep seafloor and trenches to continental margin. However, they are dominant fauna in tropical and subtropical shallow marine environments. Benthic foraminifera are generally less than 1mm, however, some species have bigger sizes up to 20 cm (Gooday et al., 2011). They are sensitive to temperature, salinity, quantity of food or organic matter, quality of food, seasonality of food supply, bottom water dissolved oxygen, ocean current velocity, and ocean water pH (Gooday, 1994; 1996; Jorissen et al., 1995; 2007; Saraswat and Nigam, 2013). The export productivity and dissolved oxygen remain the main controlling factors for the benthic foraminifera assemblage (Kaiho, 1994; Gupta, 1999; Loubere and Fariduddin, 2003; Jorissen et al., 2007). In oligotrophic regions with well-oxygenated conditions, benthic foraminifera assemblage are mainly governed by food supply. However, in eutrophic and poorly oxygenated bottom water conditions, bottom water dissolved oxygen remains the limiting factor (Jorissen et al., 1995). Based on the microhabitat they dwell (Figure 1.3), benthic foraminifera have been categorized as epifaunal (dwelling in the sediment-water interface) and infaunal benthic foraminifera (dwelling in sediment) (Figure 1.3).

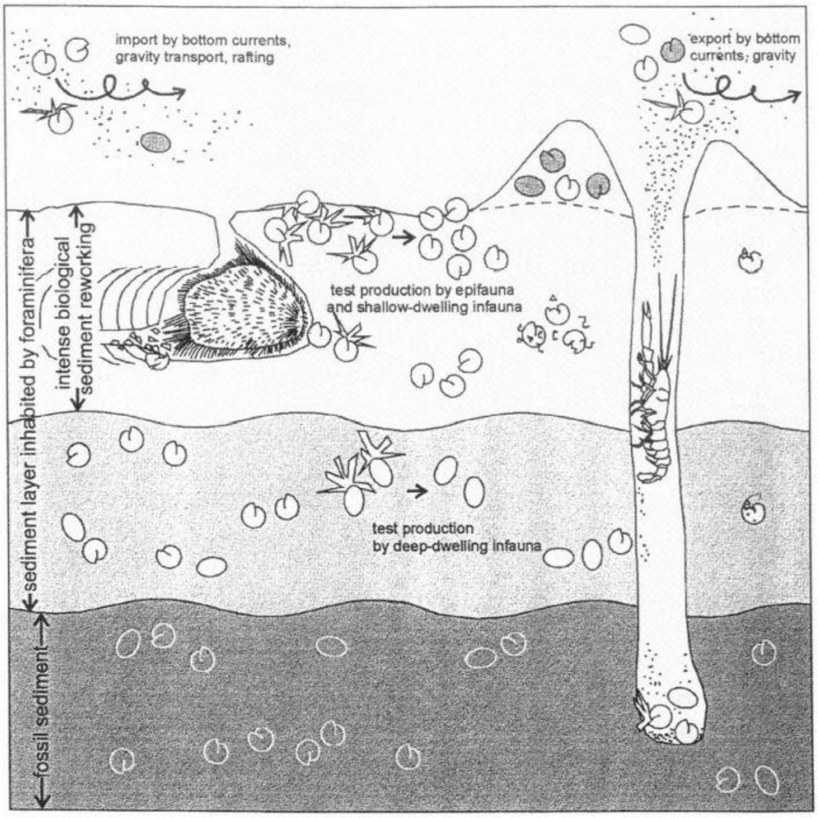

Figure 1.3. Conceptual sketch showing the various microhabitat of benthic foraminifera (Jorissen, 2003).

Most of the epifaunal foraminifera dwell in the upper 2 cm, which is the oxic layer of the sediment. Infaunal benthic foraminifera dwell mostly between 1-4 cm, however, few penetrate up to 10 cm in the sediment (e.g., *Melonis* spp., known as microaerophiles (Jorissen, 2003)). Epifaunal benthic foraminifera calcify in the bottom water, hence it is sensitive to the chemical, physical and biological properties of the bottom water. However, infaunal benthic foraminifera depend on the pore water chemistry of the sediment as well (Gupta, 1999). Hence, epibenthic foraminifera are preferred to reconstruct paleo deep water properties. Benthic foraminifera can be used to trace numerous other properties of the ancient deep ocean, past climate, etc (Table 1.3).

Table 1. 3. Use of benthic foraminifera to reconstruct paleoclimatic parameters.

Climatic parameters	Tracer	Species	References
Paleo deep water temperature	$\delta^{18}O$, Mg/Ca	*C. wuellerstorfi, P. wuellerstorfi, Epibenthic foraminifera*	(Rosenthal et al., 1997; Ravelo and Hillaire-Marcel, 2007)
Nutrient proxy	Cd, Ba	*Cibicidoides* spp., *Uvigerina* spp.	(Lea and Boyle, 1989; Rosenthal et al., 1997; Gupta, 1999)
Paleo ocean circulation	$\delta^{18}O$, $\delta^{13}C$, $\Delta^{14}C$, and $^{143}Nd/^{144}Nd$	*P. wuellerstorfi, Cibicidoides* spp., *Mixed Epifaunal benthic foraminifera*	(Duplessy et al., 1980; Broecker et al., 1984; Gupta, 1999; Mackensen and Bickert, 1999)
Paleo-productivity	Species assemblage and abundance	*U. peregrina U. proboscidea, Uvigerina* spp., *M. barleeanum*	(Loubere, 1991; Fariduddin and Loubere, 1997; Jorissen et al., 2007)
Paleo-seasonality of productivity	Species assemblage and abundance	*E exigua, A. weddellensis, M. barleeanum*	(Sun et al., 2006)
Deep-sea oxygenation	Species assemblage and abundance, I/Ca	*C. wuellerstorfi, G. subglobosa, O. umbonatus* and *many anoxic indicator*	(Kaiho, 1994; Bernhard et al., 1997; Jorissen et al., 2007)
Coastal pollution	Deformation in foraminifera shells and concentration of heavier elements e.g., Pb, Zn, Cu, Cr, and Cd	*Elphidium, quinqueloculina, Nonion*	(Yanko et al., 1994; Frontalini and Coccioni, 2008)
Biostratigraphy	Species assemblage and abundance	Benthic foraminifera species	(Bolli et al., 1994)
Paleobathymetry	Assemblage composition	Benthic foraminifera species	(Sliter and Baker, 1972)
Current velocity	Occurrence on the elevated substrate, above sediment water-formation or in shallow infaunal microhabitat	*Angulogerina angulosa, Cibicidoides* spp., *Planulina ariminensis, Discanomalina* spp., and *E. exigua*	(Lutze and Thiel, 1989; Linke and Lutze, 1993; Schönfeld, 1997; Schönfeld et al., 2012)
Paleo pH of deep ocean	$\delta^{11}B$ and $\delta^{7}Li$	*Amphistegina lessonii, C. mundulus* and *C. wuellerstorfi*	(Spivack et al., 1993; Roberts et al., 2018)

1.6.2 Stable Oxygen Isotope in Planktic and Benthic Foraminifera

The oxygen isotope ratio of well-preserved foraminifera has been used for decades to understand the evolution and history of the earth, because of its near equilibrium calcification with the seawater oxygen isotope ratio (Shackleton, 1967; Ravelo and Hillaire-Marcel, 2007). Naturally occurring oxygen has three stable isotopes i.e., ^{16}O, ^{17}O, ^{18}O, which comprise 99.759%, 0.037%, and 0.204% of the total oxygen on earth (Faure, 1986). These isotopes undergo isotopic fractionation during physical, chemical, and biological processes occurring in the ocean, atmosphere, and land. Isotopic fractionation is the relative partitioning of heavier and lighter isotopes between two co-existing phases, and fractionation is of two kinds i.e., equilibrium fractionation and kinetic fractionation. In equilibrium fractionation, there is no net reaction but isotopic fractionation takes place. However, kinetic fractionation happens during unidirectional or incomplete processes e.g., diffusion, evaporation, biological reactions. Since foraminifera calcifies under isotopic equilibrium with seawater and the fractionation factor is temperature dependent, the $^{18}O/^{16}O$ ratio in well-preserved foraminifera can be used to reconstruct past temperature. $^{18}O/^{16}O$ ratio is reported as δ notation, normalized with respect to an international standard "Vienna Pee Dee Belemnite (VPDB)".

$$\delta^{18}O = \left[\frac{\left(\frac{^{18}O}{^{16}O}\right)_{CaCO_3}}{\left(\frac{^{18}O}{^{16}O}\right)_{VPDB}} - 1\right] * 1000 ‰$$

Surface dwelling foraminifera can be used to reconstruct paleo SST, evaporation-precipitation balance, and salinity changes. Oxygen isotopic ratio in the deep ocean is primarily a function of water mass mixing, circulation, and ice volume. The $\delta^{18}O$ value measured in benthic foraminifera records the signature of temperature as well, due to its temperature-dependent isotopic fractionation during calcification. For species calcifying in equilibrium with seawater, $\delta^{18}O$ value of calcite increases by 0.21-0.23 ‰ per 1°C decrease in temperature (Shackleton, 1967; Ravelo and Hillaire-Marcel, 2007). Due to the effect of changing ice volume, the average $\delta^{18}O$ value of the global ocean was ~1.1‰ higher during LGM than today (Adkins et al., 2002). From earlier studies, it is known that deep water originating from the Southern Ocean has relatively low $\delta^{18}O$ value (-0.3‰), whereas, deep water originating in the N. Atlantic has high $\delta^{18}O$ value (+0.3‰) (Adkins et al., 2002). Hence, $\delta^{18}O$ value recorded in epifaunal benthic foraminifera can provide information about the changes in the contribution of deep water masses originating from the N. Atlantic and the Southern Ocean (Skinner et al., 2003; Skinner and Shackleton, 2005), as well as changes in the temperature, and ice volume (Ravelo and Hillaire-Marcel, 2007).

1.6.3 Stable Carbon Isotope Systematics in Planktic and Benthic Foraminifera

Carbon isotope is utilized preferentially during photosynthesis, causing organic matter to be depleted in heavier carbon isotope and surrounding water to be enriched in the heavier carbon isotope. Since foraminifera calcifies in equilibrium with seawater, it records the carbon isotopic ratio of the seawater. Hence carbon isotope of surface-dwelling foraminifera can be used as a paleo-productivity proxy. $\delta^{13}C$ value is represented by the following equation, similar to $\delta^{18}O$ value.

$$\delta^{13}\mathrm{C} = \left[\frac{\left(\frac{^{13}C}{^{12}C}\right)_{CaCO_3}}{\left(\frac{^{13}C}{^{12}C}\right)_{VPDB}} - 1\right] * 1000\ ‰$$

The distribution of $\delta^{13}C$ value in deep water is controlled by deep water mixing, nutrient regeneration, nutrient utilization balance and surface CO_2 exchange (Curry et al., 1988; Lynch-Stieglitz et al., 1995; Mackensen and Bickert, 1999; Ravelo and Hillaire-Marcel, 2007; Piotrowski et al., 2009). Nutrient-depleted NADW has characteristic enriched $\delta^{13}C$ value compared to AABW. Hence, $\delta^{13}C$ value of benthic foraminifera calcifying in near equilibrium with seawater (e.g., *C. wuellerstorfi, Cibicidoides kullenbergi, Uvigerina* spp.(Gottschalk et al., 2016)) can be used to decipher the contribution of NADW and AABW, given minimal changes in the global ocean nutrient utilization-regeneration balance (Ravelo and Hillaire-Marcel, 2007).

1.6.4 Radiocarbon Dating of Foraminifera, as a Proxy of Paleo-ocean Ventilation Age

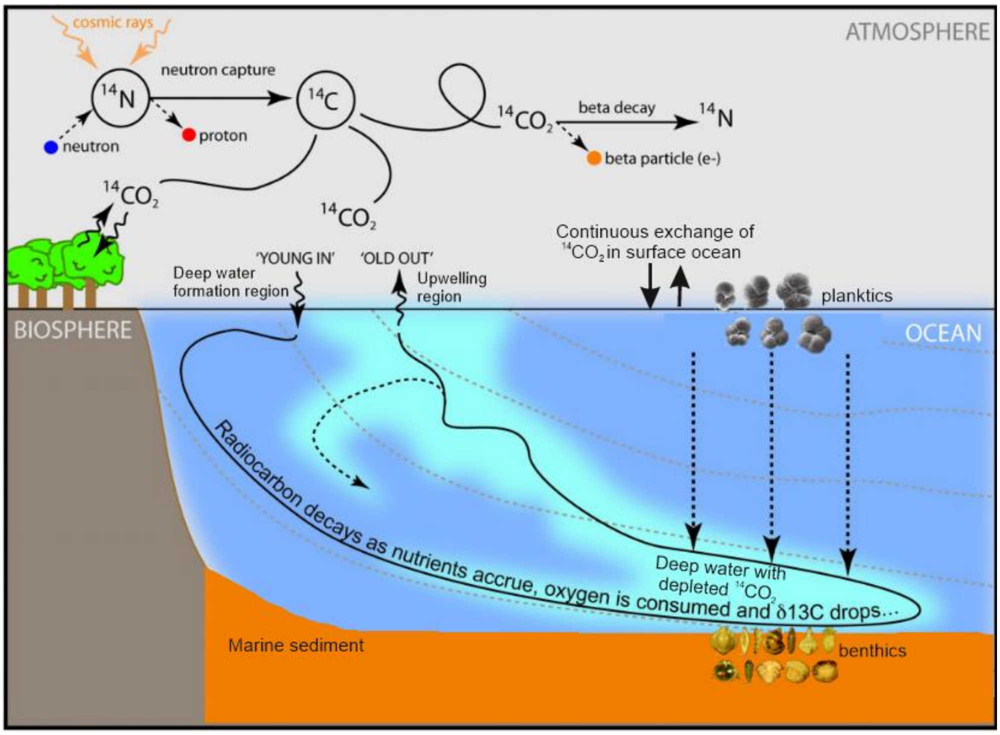

Figure 1.4. Schematic of radiocarbon cycle in the ocean and paleo-ventilation age estimation (modified from wserv4.esc.cam.ac.uk).

Planktic foraminifera calcify in the surface ocean, recording radiocarbon signatures similar to that in the surface ocean, and hence can be used to estimate the deposition time of the sediment. However, benthic foraminifera calcify in the deep ocean with depleted radiocarbon concentration, primarily due to decay of $^{14}CO_2$ while its journey from the deep water formation region to the different ocean basins (Figure 1.4). Since the deep water looses contact with the atmosphere while its journey in the deep ocean, it remains poorly ventilated compared to the surface ocean. Hence, the "ventilation" word for the water masses has been coined to represent the transition of the water during its journey in the global ocean deep basin. Time taken for a parcel of water to be transported from its source region (deep water formation region) at the ocean surface to its current core location in the deep ocean is defined as "Ventilation age' or 'transit time'. The radiocarbon ventilation ages have varied in the past and have mainly been estimated using three metrics: (1) benthic versus planktonic (B-P) age offsets (Broecker et al., 1984); (2) benthic/bottom-water versus atmosphere (B-Atm) age offsets (Soulet et al., 2016); and (3) projection ages (Adkins and Boyle, 1997). Each of these metrics (Appendix A) has its advantages and limitations (Adkins and Boyle, 1997; Skinner and Shackleton, 2004a; DeVries and Primeau, 2010), for example, with respect to the need for accurate estimates of calendar age, source-region contributions, source-region 'preformed age' (i.e. reservoir age), or local surface reservoir age. These limitations can be sorted out using other proxies. The oxygen isotope ratio of surface-dwelling species can be used for chronostratigraphic alignment with the ice core $\delta^{18}O$ value, to correct for temporal changes in the reservoir ages. Along with $\Delta^{14}C$, $\delta^{13}C$ value, and abundance, as well as trace element analysis (I/Ca) in benthic foraminifera can be used as a secondary proxy to know the deep water ventilation in terms of the deep water oxygenation. Further, $\delta^{13}C$, $\delta^{18}O$ value of benthic foraminifera, deep water paleo-temperature estimation using Mg/Ca, as well as the relative abundance of benthic foraminifera can be used to understand the changes in the relative contribution of different water masses.

1.7 Review of the Paleo-deepwater Circulation Studies

Since the first pioneering study on radiocarbon ventilation age estimation by Broecker et al., (1984), numerous records of paleo radiocarbon ventilation age from the Pacific Ocean (Sikes et al., 2000; Broecker et al., 2004a; Galbraith et al., 2007; Broecker et al., 2008; Okazaki et al., 2010; de la Fuente et al., 2015; Skinner et al., 2015; Sikes et al., 2016; Skinner et al., 2017; Umling and Thunell, 2017), the Atlantic Ocean (Keigwin and Schlegel, 2002; Skinner and Shackleton, 2004a; Robinson, 2005; Barker et al., 2010; Skinner et al., 2013; Hain et al., 2014; Skinner et al., 2014; Freeman et al., 2016; Skinner et al., 2021), the Southern Ocean (Goldstein et al., 2001; Skinner et al., 2010; 2013; 2019; Burke and Robinson, 2012; Hain et al., 2014; Hines et al., 2015; Sikes et al., 2016; Ronge et al., 2020) and the Indian Ocean (Bryan et al., 2010; Gottschalk et al., 2020; Naik and Nisha, 2020), has been made. These studies were helpful in understanding the ventilation property of the intermediate and deep/bottom water masses, changes in the relative contribution of NADW and AABW, as well as the role of the ocean in changing glacial-interglacial atmospheric CO_2. Most of the radiocarbon ventilation age records suggest increased glacial (B-Atm) ^{14}C age offset (Skinner et al., 2017; Zhao et al., 2018). However, several investigations show no change compared to the pre-industrial radiocarbon ventilation age estimates (e.g., (Broecker et al., 2008; Okazaki et al., 2010)) and large regional heterogeneity has been found in different ocean basins (de la Fuente et al., 2015; Skinner et al., 2017; Zhao et al., 2018). Limitations in three methods to estimate paleo ventilation ages (Appendix A) has also been debated in the last decade, and now attempts are being made to rectify the changes in the paleo mixed layer reservoir age using tephrochronology, alignment of $\delta^{18}O$ value of ice core, and surface dwelling foraminifera (e.g., de la Fuente et al., 2015; Skinner et al., 2019, 2010). Secondary deep water oxygenation proxies such as trace element study (I/Ca, Mn/Ca in benthic foraminifera) and benthic foraminifera relative abundances are being used (e.g., Bernhard et al., 1997; Murgese and De Deckker, 2007; Smart et al., 2010). Source of different deep water mass has been traced using ε_{Nd} in sediment or foraminifera, benthic foraminiferal $\delta^{13}C$ value (e.g., Piotrowski et al., 2008; 2009; Wilson et al., 2012) as well as Pa/Th and/or $^{231}Pa/^{230}Th$ in the sediment (McManus et al., 2004; Gherardi et al., 2005; Henry et al., 2016).

Various studies concur that changes in the atmospheric CO_2 during glacial-interglacial events were significantly influenced by changes in the deep ocean circulation (Sigman and Boyle, 2001), with the ocean being a sink of CO_2 during the LGM (Brovkin et al., 2007; Freeman et al., 2016; Menviel et al., 2017; Skinner et al., 2017), and a source of CO_2 to the atmosphere during deglaciation (Galbraith et al., 2007; Marchitto et al., 2007; Anderson et al., 2009; Skinner et al., 2010; Burke and Robinson, 2012; Hain et al., 2014; Gray et al., 2018). However, regional heterogeneity in the paleo-deep water ventilation changes remains and evidence is not enough to conclude. Hence, quaternary changes in the THC remain debatable and interesting topic to solve the mystery behind the glacial atmospheric CO_2 depletion and deglacial atmospheric CO_2 rise.

Focusing on the Indian Ocean, some paleo-deep oceanographic studies for the quaternary period have been done using $\delta^{13}C$ value, trace element analysis, and benthic foraminifera relative abundances (McCave et al., 2005; Thomas et al., 2006; Waelbroeck et al., 2006; Murgese and De Deckker, 2007; Ahmad et al., 2008; 2012; Piotrowski et al., 2008; Smart et al., 2010; Raza and Ahmad, 2013; Chandana et al., 2017; Lathika et al., 2021). However, most of these studies focused on the northern Indian Ocean. Moreover, due to the control of various mechanisms on most of the paleoclimatic proxies, quaternary deep circulation and its role in the carbon cycle remains to be resolved.

1.8 Research gap in the prescribed field and aim of the present study

The Indian Ocean acts as an excellent location to study changes in the deep water ventilation induced by the ocean-atmosphere gas exchange and transport changes originating in the N. Atlantic, the Southern Ocean, and/or the N. Pacific, because there in no competing deep water formation in the Indian Ocean. While, the majority of available radiocarbon evidence from the global ocean shows increased (B-Atm) age offsets during the Last Glacial Maximum (Skinner et al., 2017) (LGM), a great deal of spatial heterogeneity has been observed, and many regions of the ocean remain distinctly under-studied. One of the most significant gaps in data coverage is in the Indian basin (Skinner et al., 2017; Zhao et al., 2018). There are only a handful of continuous radiocarbon ventilation age time-series from the deep Indian Ocean available at present (e.g., Gottschalk et al., 2020; Ronge et al., 2020). Various recent studies concurred that ocean played an important role in glacial-interglacial changes in the atmospheric CO_2 (Sigman and Boyle, 2001; Brovkin et al., 2007; Galbraith et al., 2007; Marchitto et al., 2007; Anderson et al., 2009; Skinner et al., 2010; 2017; Burke and Robinson, 2012; Hain et al., 2014; Freeman et al., 2016; Gray et al., 2018). However, the role of the Indian Ocean basin in changing atmospheric CO_2 during quaternary glaciation and interglaciation remains poorly addressed and underappreciated in global prospective (Skinner et al., 2017), despite its 20% volumetric contribution to the global ocean. Hence this study attempts to address the following scientific objectives:

(1) To reconstruct paleo quaternary ventilation age of the deep water in the CIO basin, using paired radiocarbon dating of planktic and benthic foraminifera in two marine sediment cores, one from the CEIO and another from the SBoB.
(2) To decipher paleo-deep water oxygenation condition of the CEIO using relative abundances of benthic foraminifera species.
(3) To estimate paleo ventilation age of the deep water in the SWIO basin using paired radiocarbon dating of planktic and benthic foraminifera.
(4) To reconstruct paleo ventilation age of the deep water in the EIO basin using paired radiocarbon dating of planktic and benthic foraminifera.
(5) To reconstruct paleo-productivity in the CEIO using OC, IC, $\delta^{13}C$, $\delta^{18}O$ value of planktic and benthic foraminifera.
(6) To decipher the qualitative relative changes in the contribution of the NADW and AABW in different basins of the Indian Ocean, using collated carbon and oxygen isotope analysis.

Chapter 2.

Methodology

2.1 Introduction

The ocean plays an important role in regulating the global carbon cycle (Skinner et al., 2010; 2017; Freeman et al., 2016; Galbraith and Skinner, 2020). Numerous radiocarbon ventilation age reconstruction from the Pacific (Galbraith et al., 2007; Lund et al., 2011b; de la Fuente et al., 2015; Umling and Thunell, 2017), the Atlantic (Robinson, 2005; Skinner et al., 2013; Chen et al., 2015), and the Southern Ocean (Skinner et al., 2010; Burke and Robinson, 2012; Hines et al., 2015) provides evidence of change in the ventilation of the deep ocean during the last glaciation. However, the role of the Indian Ocean in the past carbon cycle, in terms of its deep water ventilation remains unaddressed. In this study, an attempt is made to address changes in the ventilation property of the deep Indian Ocean basins using stable and radioactive carbon isotopes in well-preserved foraminifera, chronologically preserved in marine sediments. Towards this, analyses of both planktonic and benthic foraminifera species for their stable isotope and radiocarbon composition, their abundance, and trace element analysis in foraminifers have been conducted.

The Indian Ocean being landlocked from the north, does not facilitate any local source of deep water formation. Additionally, the Indian Ocean facilitates the upwelling limb of the global overturning circulation (Wyrtki, 1973), which ultimately feeds warm and salty water to the NADW formation (Talley, 2013). Hence, it is an ideal location to study changes in the deep water ventilation, induced by the ocean-atmosphere exchange process happening in the N. Atlantic and the Southern Ocean. Marine sediment cores from the three major deep Indian Ocean basins lying above the lysocline depth (Kolla et al., 1976) have been selected for ventilation study. Two cores are located in the Central Indian Ocean basin, one is in the Central Equatorial Indian

Ocean region (SS152/3828) and another one is in the Southern Bay of Bengal (SS172/4040). Both these cores, along with a core in the South West Indian Ocean (SK312/09) are ventilated by the same water mass i.e. Upper Circumpolar Deep Water/Indian Deep Water. However, the core from the eastern Equatorial Indian Ocean (SK304/12) is ventilated by the Lower Circumpolar Deep Water. Basin-wise core locations have been selected to get a clear understanding of the changes in the ventilation property of water mass coming from different pathways to fill the Indian Ocean basins (Wyrtki, 1973).

2.2 Sampling Location and Sample Processing

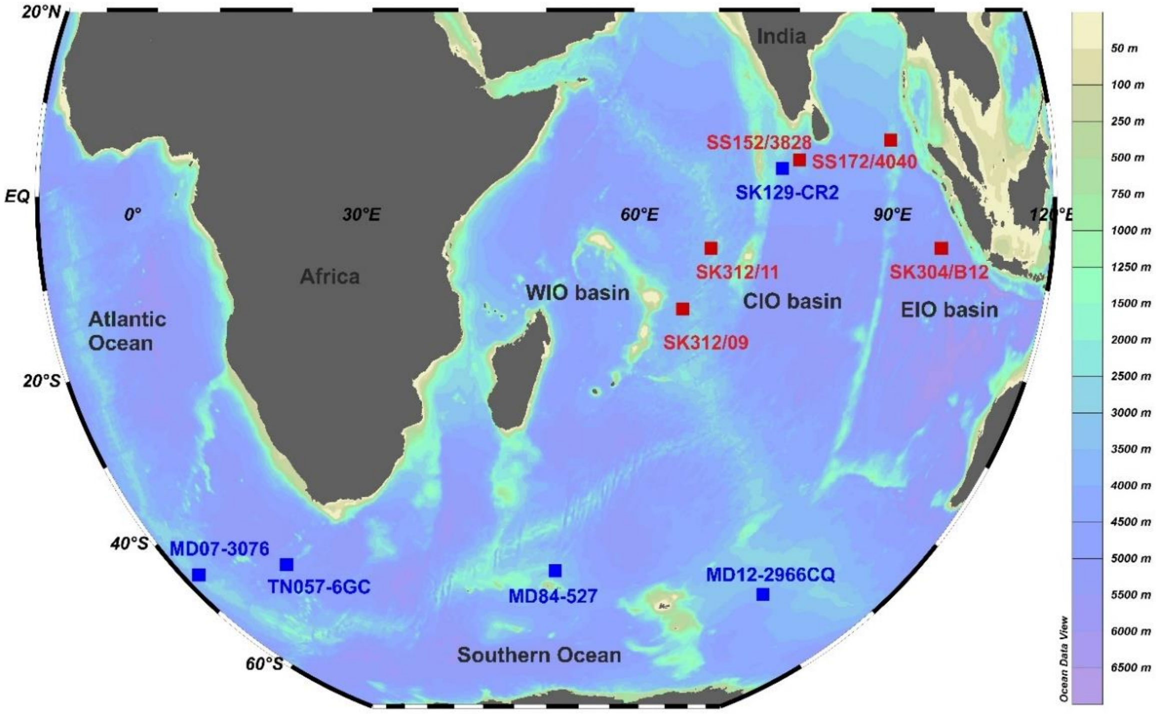

Figure 2.1: Sediment core locations: Sediment cores from this study (red color): SS152/3828 (3.89° N, 78.06° E, water depth-3166m, core length-40 cm), SS172/4040 (6.03° N, 89.94° E, water depth-2788m, core length-130 cm), SK312/11 (4.73° S, 67.90° E, water depth-3100m, core length-564); SK312/09: (11.99° S, 64.99° E, water depth-3449m, core length-565); SK304/12: (5.46° S, 97.37° E, water depth-4206m, core length-1.5m); Sediment cores from other studies (blue color): SK129–CR2 (3°N, 76°E, water depth-3800 m; Piotrowski et al., 2009), MD12-2296CQ (47.43S; 86.41°E, water depth-3615 m (Gottschalk et al., 2020), MD84-527 (43.82°S, 51.32° E, water depth-3262m; Curry et al., 1988), TN057-6GC (42.89°S, 8.96° E, water depth-3750m; Gottschalk et al., 2016), MD07-3076 (44.46°S; -14.47°E, water depth-3,770m; Skinner et al., 2010).

Five marine sediment cores (Figure 2.1) were analysed representing the Western Indian Ocean basin (WIO basin), the Central Indian Ocean basin (CIO basin), and the Eastern Indian Ocean basin (EIO basin). Two sediment cores from the CIO basin, core SS152/3828 from the southern boundary of the Laccadive Sea and core SS172/4040 from the Ninety-east ridge of SBoB were recovered during FORV Sagar Sampada oceanographic cruise 1997 and 1999 respectively. Two sediment cores from the Southwest Indian Ocean basin, core SK312/11 and the core SK312/09 were collected during the ORV Sagar Kanya oceanographic cruise in April-May 2014 using a gravity corer. However, the sediment core SK304/B12 was collected during the cruise 304 of ORV Sagar Kanya in 2013. Details of all the sediment cores analysed in this study have been summarised in Table 2.1, along with the details of earlier studied sediment cores used for data comparison in the present study. All these gravity cores were collected using contamination-free PVC pipe, stored at low temperature, and sub-sampled at 1-2 cm intervals for better resolution. The sediment core was brought to the laboratory and stored at low temperatures. While an aliquot (5-10g) for geochemical parameters was oven-dried at 85°C and crushed, an aliquot for the foraminifera assemblage study was oven-dried at 55°C.

Table 2.1: Details of the marine sediment cores analysed and compared in this study.

Sediment cores ID	Location	Core length (cm)	Water depth (m)	Details
SS152/3828	3.89° N, 78.06° E	40	3166	This study
SS172/4040	6.03° N, 89.94° E	130	2788	This study
SK312/11	4.73° S, 67.90° E	564	3100	This study
SK312/09	11.99° S, 64.99° E	565	3449	This study
SK304/12	5.46° S, 97.37° E	150	4206	This study
SK129–CR2	3°N, 76°E	-	3800	(Piotrowski et al., 2009)
MD12-2296CQ	47.43S, 86.41°E	-	3615	(Gottschalk et al., 2020)
MD84-527	43.82°S, 51.32° E	-	3262	(Curry et al., 1988)
TN057-6GC	42.89°S, 8.96° E	-	3750	(Gottschalk et al., 2016)
MD07-3076	44.46°S, -14.47°E	-	3770	(Skinner et al., 2010)

2.3 Foraminifera Extraction, Identification, and Processing Protocol

Nearly 15-20 g of sediment was taken for radiocarbon dating as well as assemblage study. However, for abundance and assemblage study, only 5-10 g of sediment was taken. Dried sediment was soaked overnight in a solution of sodium hexametaphosphate and hydrogen peroxide (Figure 2.2). It was further wet sieved repeatedly (number of repetitions depends on the type of sediment) in distilled water using a 63-µm sieve after ultra-sonication for 2 to 5 minutes. When the clay fraction was high in the sample, the sample was soaked again and the whole step was repeated. Wet sieved foraminifera was oven-dried at 55°C and dry sieved using 150 µm, 250 µm, 425-µm sieves and a collection bin in a sieve shaker for easier picking of foraminifera (Figure 2.3). Picking of µm size specimen from bulk microfossils was done under stereo-microscope (Micros Hornet 1280 with zoom ratio 8:3) using 000 size nylon brush dipped in deionized water (Figure 2.2). Only clean and unbroken specimens of benthic and planktic foraminifera were picked. Picked specimens of planktic and benthic foraminifera, weighing 5 to 11 mg were crushed between cleaned glass plates and kept in 2 ml cleaned centrifuge tubes. Crushed specimens were cleaned to remove any foreign carbonate in the foraminiferal shell by following the similar method developed for Mg/Ca analysis by Barker et al., ((2003): Figure 2.4). Since radiocarbon analyses require more sample weight than the samples for Mg/Ca, the volume of the cleaning agent was doubled in volume than described (Barker et al., 2003). Samples were rinsed repeatedly (4-5 times) in an ultra-sonicator for 1-2 minutes to remove particulate matter and clay, followed by final clay removal by a repeated ultra-sonification in a 250 µl methanol bath (Aristar grade). Organic matter was also removed by oxidizing the sample in Suprapure Hydrogen peroxide (1% H_2O_2) buffer solution (buffered by Aristar grade Sodium hydroxide) at 90°C. Samples in buffer solution were heated for 5 minutes, removed from the oven, tapped, and kept again for heating up to 5 minutes. This step was repeated and finally rinsed twice in ultrapure water. Samples were leached in 0.001M HNO_3, ultrasonicated for ~30 seconds to remove any secondary calcification and quickly rinsed in ultrapure water 2-3 times to prevent excess dissolution. The remaining liquid was drained using a micro-pipette. The cleaned specimen was further oven-dried at 50°C and graphitised for radiocarbon dating.

In view of the same aliquot of benthic foraminifera species being used for radiocarbon as well abundance study, methodology for counting benthic foraminifera was set accordingly. Abundance and assemblage study of benthic foraminifera (>150 µm) was done only in the core SS152/3828, at 14 depth intervals (Table 2.2 and Table 2.3). Samples, which were sieved especially for abundance study were counted in a single size fraction (>150 µm). The counting done for each species was normalized to 10 g of sediment and then converted into percentage abundance or relative abundance. Benthic foraminifera samples which were sieved for radiocarbon dating as well were counted separately in three size fractions (150-250 and 250-425 and >425-µm fraction) and added to get abundance for >150-µm fraction. Size fraction 150-250 µm weighing 0.1-0.2 g aliquot, corresponding to 4-6 g sediment weight (split made using

Otto Microsplitter) was scanned, which yielded 90-250 specimen per sample. Abundances of both size fractions (>250 µm and 150-250 µm) were normalized to 10 g of sediment for each size fraction and added together to get abundance of >150 µm fraction per 10 g of sediment at each depth (Appendix Table C.1). Later it was converted to the relative abundance or percentage abundance for further comparison (Appendix Table C.2). All the available well-preserved specimens were separated and identified up to species level following the foraminifera key book (Loeblich and Tappan, 1987) and World Register for Marine Species (Hayward et al., 2020). Species absolute abundance at each depth was converted into percentage abundance, mentioned as relative abundance (RA). Benthic foraminifera density was estimated based on the number of specimens per gram of sediment. Benthic Foraminifera Accumulation Rate (BFAR) was calculated using the following equation (Herguera and Berger, 1991):

$$BFAR\ (number\ of\ specimens/cm^2\ kyr^{-1}) = BF \times LSR \times DBD.$$

Where BF is the number of benthic foraminifera per gram of dry sediment, LSR is the linear sedimentation rate (cm/kyr), and DBD is the dry bulk density (g/cm^3) of the sediment. DBD was calculated by using organic carbon (OC) and $CaCO_3$% data of the present study in the equation developed by (Clemens et al., 1987).

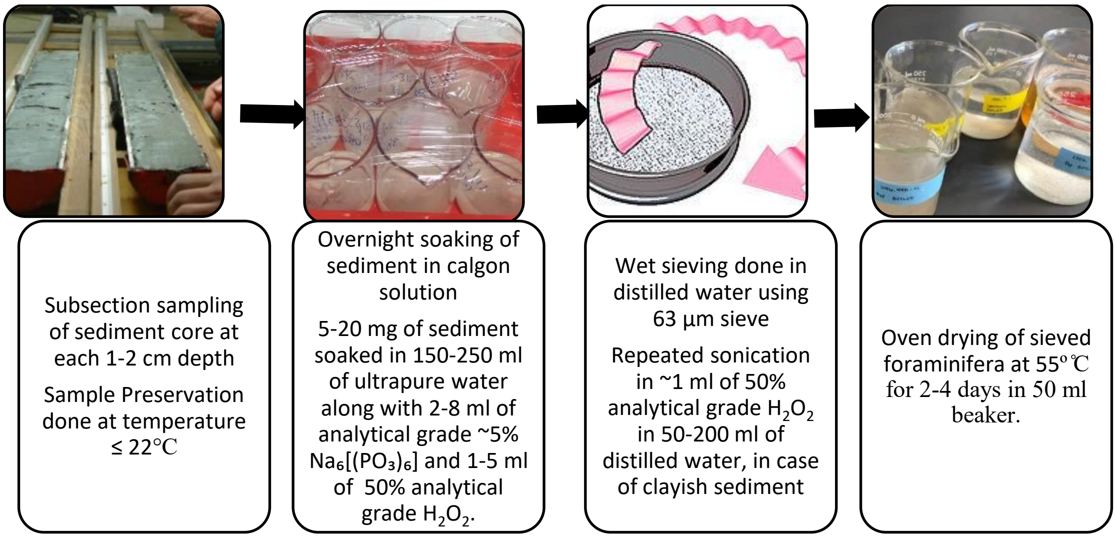

Figure 2.2: Schematic for bulk foraminifera extraction from marine sediment

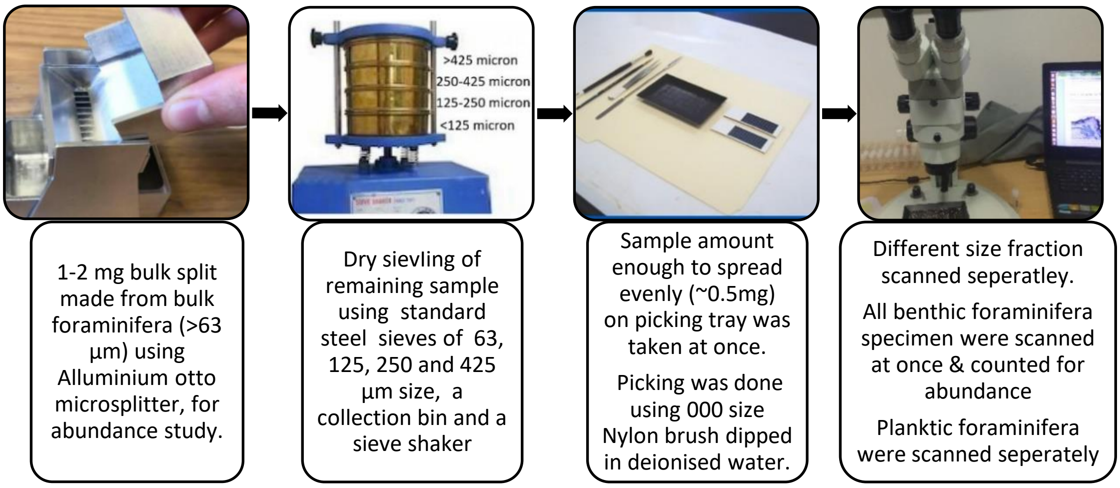

Figure 2.3: Schematic of foraminifera species, separation, identification, and scanning

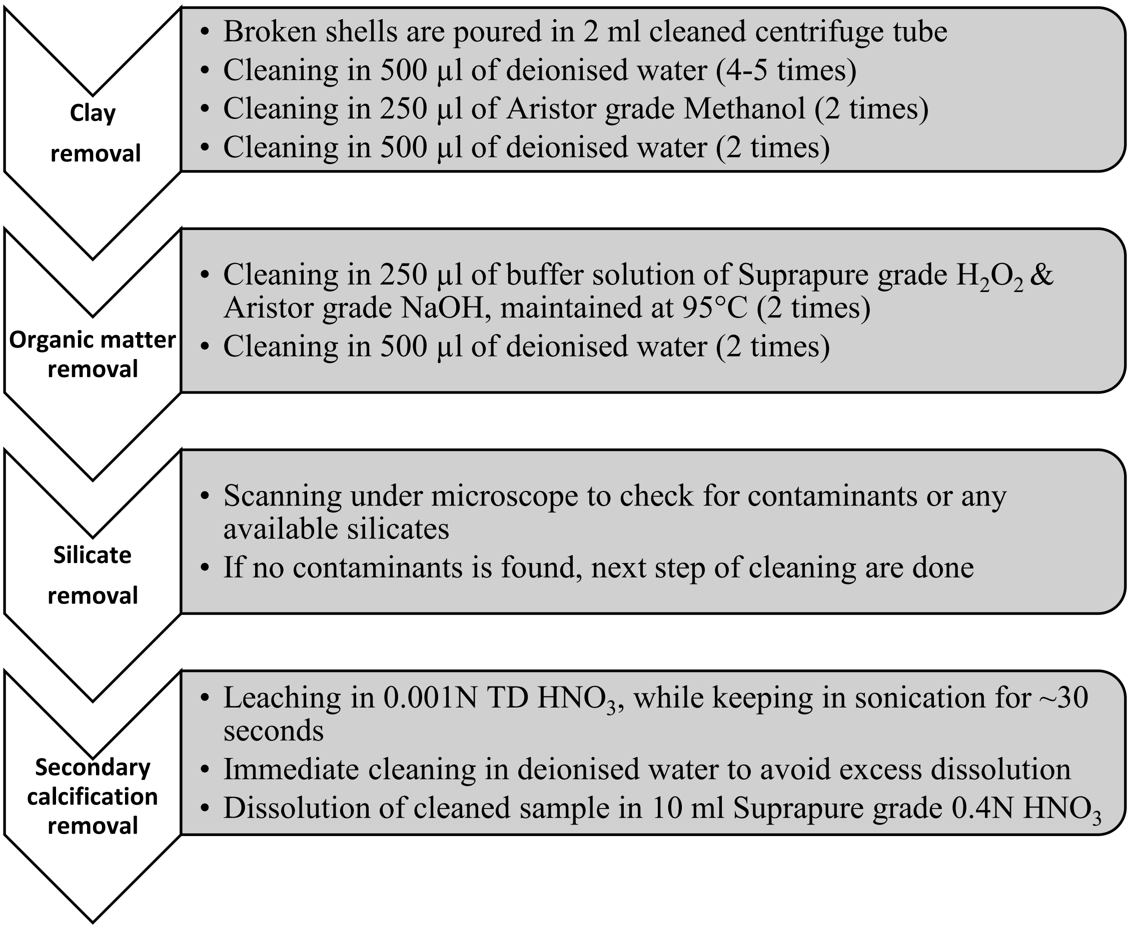

Figure 2.4: Schematic showing cleaning procedure of foraminifera species for trace element analysis

Table 2.2: Details of the sediment weight taken to analyse two size fractions and the corresponding number of specimens identified at six depths.

Depth (cm)	Sediment weight scanned for 150-250 µm fraction (g)	Number of specimens scanned in 150-250 µm fraction	Sediment weight scanned for >250 µm fraction (g)	Number of specimens scanned in >250 µm fraction
3-4	4.9	144	13.8	269
16-17	4.6	100	18	143
22-24	5.2	91	19	300
28-29	4.0	121	20.9	156
33-35	5.4	225	20	320
38-39	5.7	245	5.4	572

Table 2.3: Sample weight and counts for the samples, specially sieved for abundance study.

Depth (cm)	Sediment weight (g)	Number of specimens (>150 µm)
6-7	5.4	128
11-12	8.3	268
17-18	6.2	120
26-27	9.4	390
29-30	8.7	340
31-33	6.9	359
35-36	5.2	418
36-37	5.6	369

2.4 Calcium Carbonate Measurements

The calcium carbonate content in sediments of the core SS15/3828 (Appendix Table C.3) was measured using the Coulometer (UIC Coulometer, Model 5012). CO_2 was liberated by reacting the carbonate present in the sediment with 40% orthophosphoric acid at 70°C. CO_2 produced from the sample was passed through the silica gel moisture trap before passing it to the coulometric cell to form titratable acid. Calcium carbonate concentration in the sediment was calculated using titration current which is directly proportional to the percentage transmittance of the titratable acid (Bhushan et al., 2001). Na_2CO_3 was used as carbonate standard which was measured once every 8-10 samples. The $CaCO_3$ concentration was further converted into percentage $CaCO_3$ by dividing it by the weight of the sediment. The precision of the $CaCO_3$ measurement was less than 3%.

2.5 Organic Carbon and Total Nitrogen Measurement

For Organic Carbon (OC) measurements, sediment was decarbonated to remove inorganic carbon (IC) by heating the sample at 85°C in 1.2 N HCl. The step was repeated until the whole IC present in the sample got hydrolyzed. The decarbonated sample was further oven-dried at 80°C and crushed. OC and total nitrogen were measured using an Elemental Analyser (Flash 2000). Crushed decarbonated sample weighing ~20-25 mg was packed in a tin foil and inserted into the combustion column maintained at 950°C with an adequate flow of high purity helium and oxygen for a definite time. Evolved CO_2 from the combustion column along with nitrogen oxides was passed through a reduction column maintained at 650°C, containing metallic copper. Further, these gases were passed through the chromatographic column after passing through a moisture adsorbent. The gases enter a highly sensitive thermal conductivity detector, which produces electric signals proportional to the concentrations of the gases. For calibration, standards High Organic Sediment Sample (HOSS) and Low Organic Sediment Sample (LOSS) were used (Bhushan et al., 2001)). OC was converted into a percentage (OC%; Appendix Table C.3), which was further used to decipher the paleo-productivity of the CEIO, and OC/N (Table A4) to decipher terrestrial flux. The precision of measurement for OC and Nitrogen was 4% and 6% respectively.

2.6 Stable Carbon and Oxygen Isotope Measurements

Stable carbon and oxygen isotope measurements in planktic and epifaunal benthic foraminifera were done using Continuous flow Isotope Ratio Mass Spectrometer (IRMS) (Thermoscientific make Dellta V Plus), coupled with Gasbench-II. IRMS measurements on planktic foraminifera for the core SS152/3828 (Appendix Table C.7, C.9 and core SS172/4040 (Appendix Table C.8, C.10) were done on intact species in the size range of 250-425 µm, whereas for benthic foraminifera stable isotope measurements, > 250-µm size was taken to get enough amount of sample (200-500 µg). For planktic foraminifera, cleaned and unbroken shells were picked for measurements without further cleaning. However, benthic foraminiferal shells were crushed in 12 ml septum glass vials and cleaned using Suprapure Methanol. Samples were further cleaned by ultrapure water, decanted using rolled lint-free tissue paper. Cleaned benthic foraminiferal carbonate samples were further dried at 90°C for 2-3 days.

The cleaned benthic foraminifera samples/intact planktic foraminifera samples were taken in 12 ml glass vials, closed tightly by Butyl septum caps, and placed in CHS autosampler attached with IRMS. International standard (NBS-18) was run in between each 15-20 samples along with lab standard (MMB (Makrana Marble)) which was run after every 4-6 samples. Coral lab standard (PRL-C) was also analysed intermittently for precision. Sample vials were flushed with Helium to remove any atmospheric gases in the vial. Further, carbonate was hydrolysed to CO_2 gas using 100% ortho-phosphoric acid, while heating the sample at 85°C for more than 60 minutes. CO_2 gas evolved from the samples was passed through the Naflon trap to remove moisture for further ionization. The isotopic ions were detected by the Faraday cup detector based on their mass/charge ratio and stable isotope concentration in the sample.

For stable carbon and oxygen isotope measurement in carbonate samples, Vienna Pee Dee Belemnite (VPDB) was used as an international standard. $\delta^{18}O$ and $\delta^{13}C$ value of lab standards (MMB; Appendix Table C.4 and PRL-C; Appendix Table C.5) and international standard (NBS-18; Appendix Table C.6) can be found in the data section. $\delta^{18}O$ value of planktic foraminifera from the CEIO (SS152/3828; Appendix Table C.7) and SBoB and $\delta^{13}C$ (SS172/4040; Appendix Table C.8) are also available in the same section, along with $\delta^{18}O$ and $\delta^{13}C$ value of benthic foraminifers from the CEIO (SS152/3828; Appendix Table C.9 and SBoB (SS172/4040; Appendix Table C.10). The measured precision for both carbon and oxygen isotope measurements, based on repeat measurements for ~2 years were always better than 0.1‰.

Table 2.4: Details of the measured stable carbon and oxygen isotope standards

Standards	n	$\delta^{13}C$ (‰) measured	$\delta^{18}O$ (‰) measured	Recommended $\delta^{13}C$ value	Recommended $\delta^{18}O$ value
MMB	78	4.0±0.1	10.7±0.1	3.9	-10.7
PRL-C	35	2.8±0.1	-5.6±0.1	-	-
NBS-18	14	4.9±0.1	22.9±0.1	-5.01	-23.01

2.6.1 Stable Carbon Isotope Ratio in Different Species of Foraminifera

Stable carbon isotope was measured in different species of benthic and planktic foraminifera to judge the right species which represent the precise changes in the $\delta^{13}C$ value of the paleo Indian Ocean ambient water in where the shell calcified. Large variations were observed in the $\delta^{13}C$ value of different species of planktic and benthic foraminifera (Figure 2.5, Figure 2.6). The average $\delta^{13}C$ value of *G. ruber* and *G. sacculifer* were found to be 1.5‰ and 1.9‰ respectively in both the CEIO as well as the SBoB. However, average $\delta^{13}C$ value of *G. menardii* was 1.5‰ and 1.3‰ in the

CEIO and SBoB respectively. δ^{13}C value of *G. ruber*, *G. sacculifer,* and *G. menardii* varied between 1.1-1.5‰, 1.5-1.9‰ and 1.2-1.5‰ respectively in the CEIO and between 1.1-1.5‰, 1.6-1.9‰ and 1.0-1.3‰ respectively in the SBoB. δ^{13}C value of *G. sacculifer* always remained higher in both the CEIO as well as the SBoB. However, δ^{13}C value of *G. ruber* and *G. menardii* showed huge variation and overlap each other in the CEIO. While, *G. menardii* had lower δ^{13}C value in SBoB throughout the last 37 kyrs.

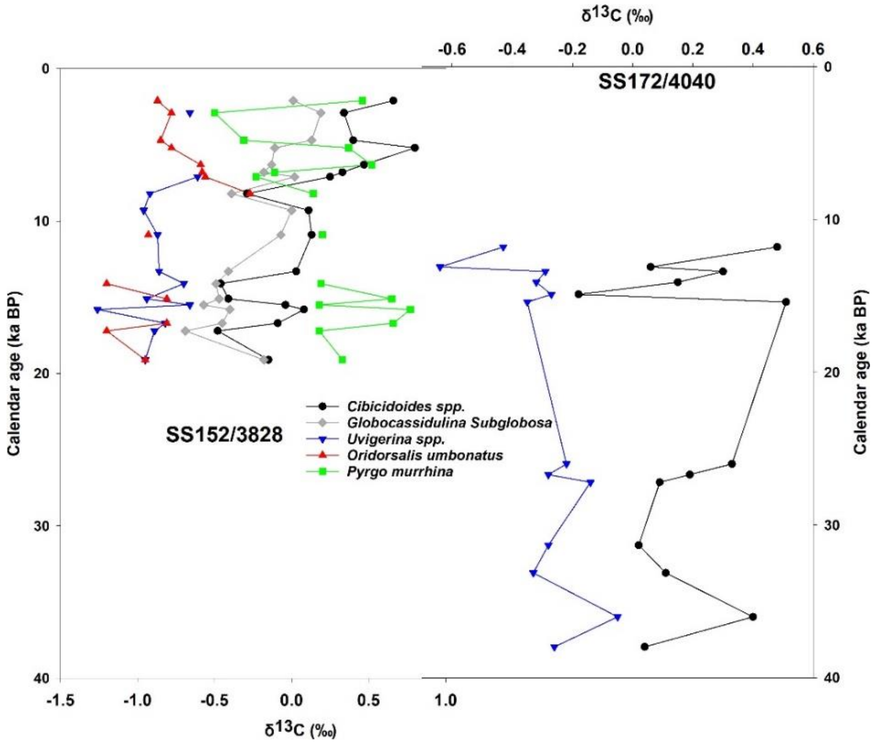

Figure 2.5: δ^{13}C of different species of benthic foraminifera in the CEIO (SS152/3828; water depth-3166m) and SBoB (SS172/4040; water depth-2788m).

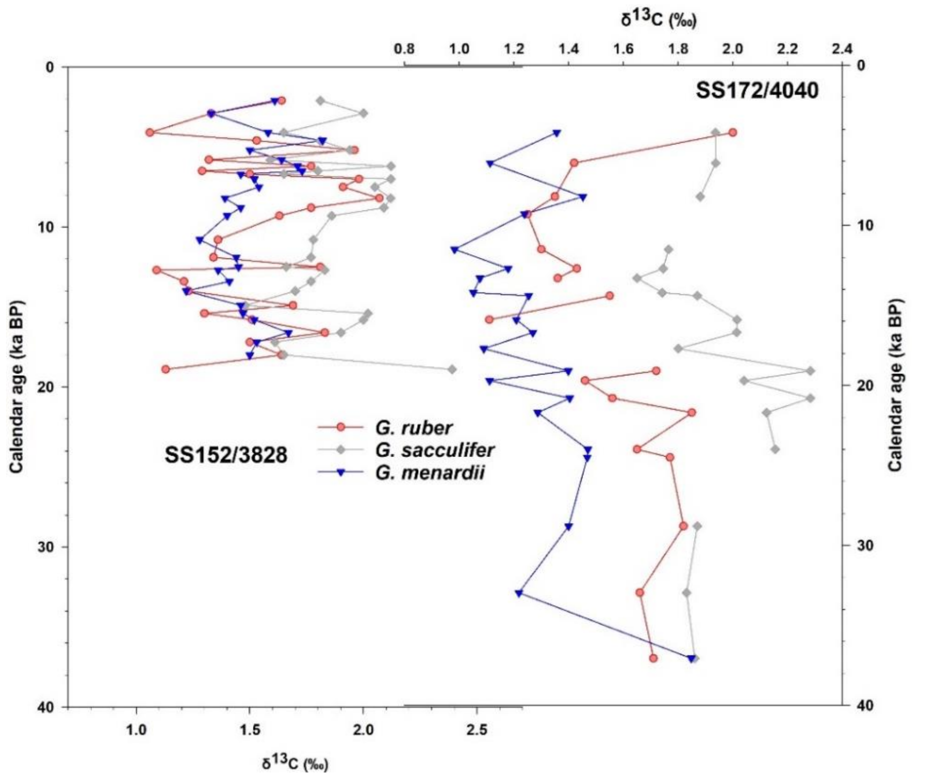

Figure 2.6: $\delta^{13}C$ of different species of planktic foraminifera in the CEIO (SS152/3828; water depth-3166m) and SBoB (SS172/4040; water depth-2788m).

2.6.2 Stable Oxygen Isotope Ratio of Different Foraminifera Species

Stable oxygen isotope was also measured in different species of benthic and planktic foraminifera to know which species represent the precise $\delta^{18}O$ record of ambient water, where the shell calcified. Large variations were found in $\delta^{18}O$ value of different species of planktic and benthic foraminifera (Figure 2.7, Figure 2.8). The average $\delta^{18}O$ value of *G. ruber*, *G. sacculifer,* and *G. menardii* were -1.8‰, -1.6‰ and -0.5‰ respectively in the CEIO and -1.5‰, -0.9‰ and -0.1‰ respectively in the SBoB. The $\delta^{18}O$ value of *G. ruber*, *G. sacculifer,* and *G. menardii* varied between -2.8 to -0.6‰, -2.4 to -0.4‰ and -1.2 to 0.8‰ respectively in the CEIO and -2.5 to -0.8‰, -2.1 to -0.3‰ and -0.9 to 0.4‰ respectively in the SBoB. Both, in the CEIO as well as SBoB, the $\delta^{18}O$ value of *G. menardii* was enriched throughout. While $\delta^{18}O$ of *G. ruber*, *G.*

sacculifer overlapped each other in the CEIO, δ18O value of *G. ruber* remained depleted compared to *G. sacculifer* in the SBoB.

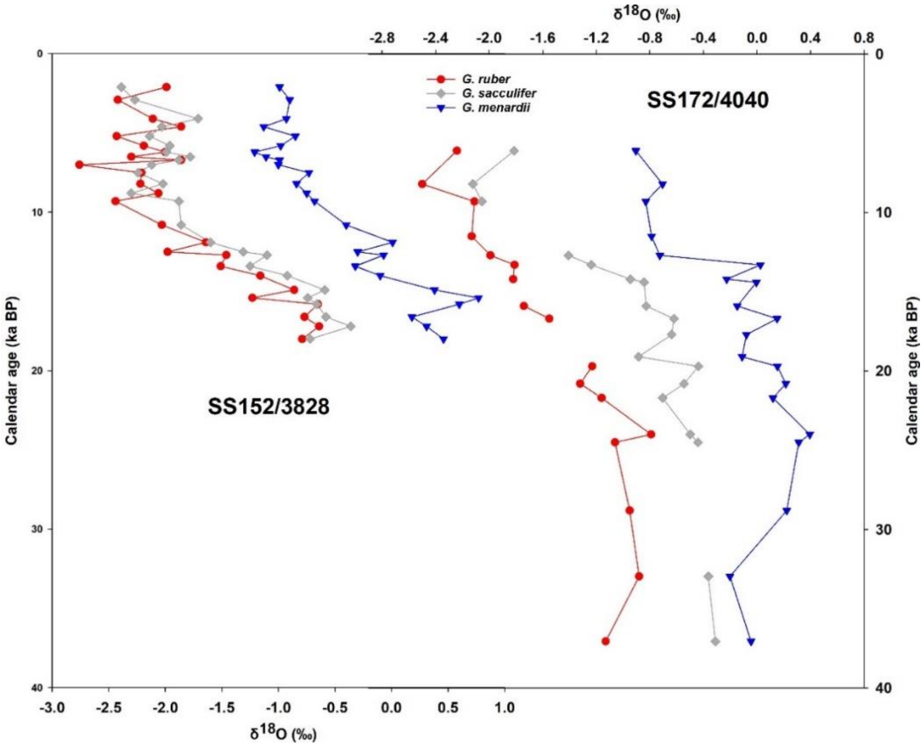

Figure 2.7: Downcore variation in oxygen isotope of different species of planktic foraminifera in the CEIO (SS152/3828) and SBoB (SS172/4040).

The δ18O value of *Cibicidoides* spp., *Globocassidulina subglobosa*, *Uvigerina* spp., *Oridorsalis umbonatus* and *Pyrgo murrhina (*Figure 2.8) averaged to 3.0‰, 3.2‰, 4.3‰, 3.2‰ and 3.4‰ respectively and varied between 2.2 to 4.2‰, 2.1 to 4.3‰, 4.0 to 4.6‰, 1.9 to 4.6‰, 2.3 to 4.8‰ respectively in the CEIO. The δ18O value of *Cibicidoides* spp. and *Uvigerina* spp. averaged to 3.3‰ and 4.0‰ in the SBoB and varied between 2.7 to 4.0‰ and 3.6 to 4.5‰ in the SBoB respectively. δ18O value of *Uvigerina* spp. was found highest. While, δ18O value of *Cibicidoides* spp, *Globocassidulina subglobosa* and *Oridorsalis umbonatus* and *Pyrgo murrhina* followed the same trend.

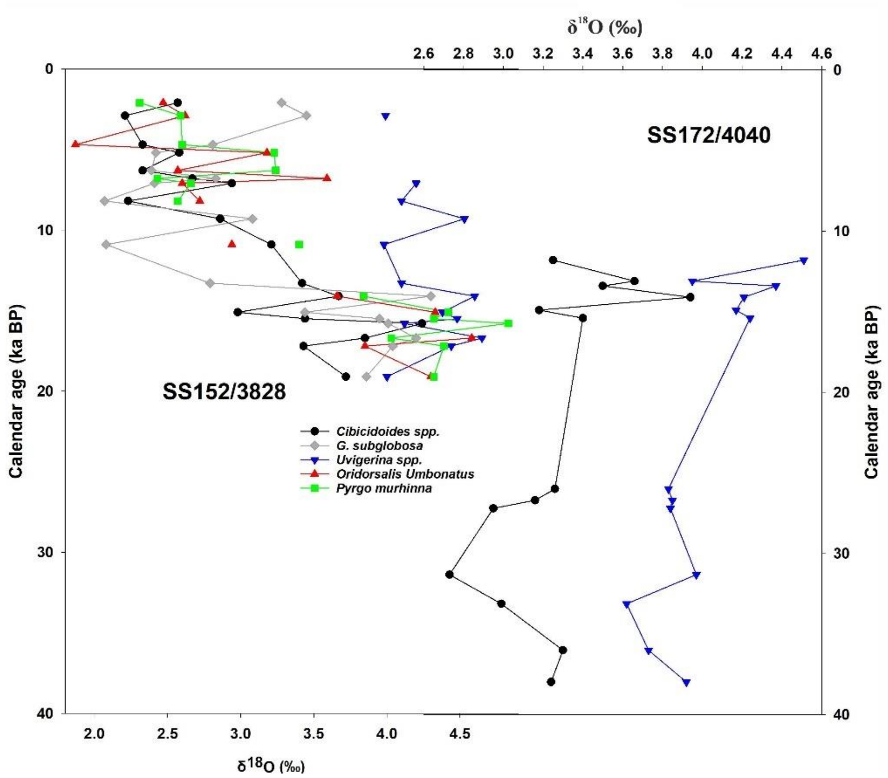

Figure 2.8: Downcore variation in the oxygen isotope of different species of benthic foraminifera in the CEIO and SBoB.

2.7 Sample Graphitisation for AMS Measurement

For radiocarbon measurements using AMS, sample carbon needs to be converted to graphite for its measurement. Towards this, cleaned foraminifers (weighing 4-10 mg) were placed in 12 ml clean glass vials with butyl septum caps and kept in CHS (Carbonate Handling System; Figure 2.9a) sample holder. The vials containing the samples were flushed with Helium (He) gas at the rate of ~75 ml/min rate. The calcite present in the foraminifera was treated with 0.3 ml of ortho-Phosphoric acid (H_3PO_4) in CHS sample holder, with temperature set at 85°C for complete hydrolysis of carbonate to CO_2. The CO_2 gas evolved was further passed through phosphorus pentoxide for moisture removal and transferred to Automated Graphitisation Equipment (AGE-3: Figure 2.8b). In AGE-3, CO_2 gas is trapped in a microporous aluminosilicate zeolite trap, which was further heated to release CO_2 in the sample reactor tube. Pre-cleaned and pre-heated reactor tubes containing ~5 mg of Fe powder was conditioned before sample CO_2 gas reached the reactor. The Hydrogen and CO_2 in the reactor tube were taken in the ratio of 2.3:1 (Wacker et al., 2010). Further, CO_2 was reduced to C as graphite using the standard Hydrogen - Iron catalyst method, in the presence of hydrogen (H_2) at a temperature of 580°C in the following reaction (Wacker et al., 2010)

$$CO_2 + 2H_2 \rightarrow C + 2H_2O$$

Conversion of organic carbon to CO_2 was done using Elemental Analyser (EA: Figure 2.9c) connected with AGE-3. The weight of the sample was taken so that it contained ~1000 µg C and packed in tin foil using packing tools before inserting it into EA auto-sampler. The complete process was done in a cleaned environment to avoid any contamination. The EA allowed complete combustion of organic carbon into CO_2 gas in the combustion column before passing to the reduction column. It underwent moisture removal and CO_2 gas was separated from Nitrogen oxides using a gas separation column. The CO_2 gas was further passed through the zeolite trap to AGE-3 and conversion of organic carbon sourced CO_2 gas to C took place similarly, as in the case of conversion of carbonate sourced CO_2 gas to carbon.

.

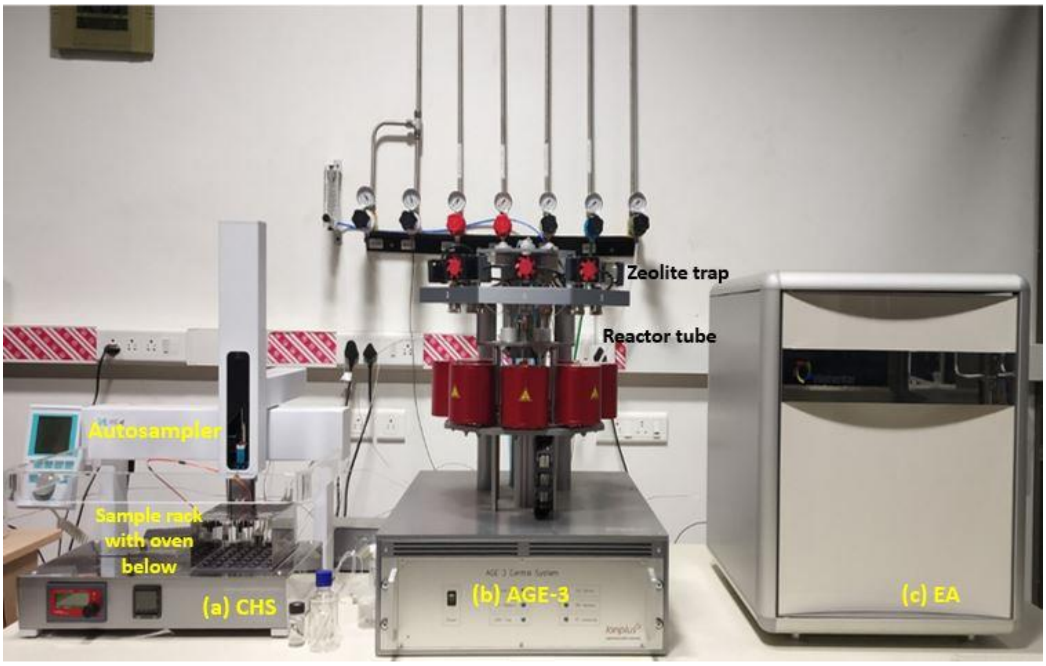

Figure 2.9: Image of Coupled CHS and AGE-3, along with EA unit at PRL. (a) Carbonate Handling System with 12 ml vial stand for carbonate sample along with autosampler, with an attached needle with Helium flow for evacuation and sample transfer from CHS to AGE-3. (b) Automated Graphitisation Unit attached with zeolite trap for inlet of CO_2, with seven ovens in maroon color to heat seven reactor tubes which facilitate the reduction of CO_2 to C. (c) Elemental Analyser facilitates the combustion of organic carbon to CO_2 for transfer of CO_2 from organic radiocarbon standards.

Benthic and planktic foraminifera for each depth were graphitised in pairs along with reference and primary standards. Carbonate reference standards (FIRI-C, IAEA C-2, VIRI-R), organic carbon reference standard (VIRI-U, FIRI-E), carbonate blank (IAEA-C1), and organic carbon blank (Anthracite) were also graphitised along with the samples. Primary standards (NBS Oxalic Acid-I (OX-I), NBS Oxalic Acid-II (OX-II)) along with organic carbon reference standards and blank were combusted in the Elemental Analyser (EA) and the liberated CO_2 was graphitised in AGE-3. The foraminifera, carbonate standards, and carbonate blank were oxidized to CO_2 using CHS and AGE-3. Graphitised samples were further pressed in a target holder made of aluminum oxide and sealed by a copper pin using metallic pressing tools and graphitisation pressing equipment. Cleaned planktic shells of foraminifers were radiocarbon dated both prior and post-cleaning to check the foraminifera cleaning protocol for radiocarbon dating. An insignificant difference observed in the Libby age of samples before and after cleaning attests to negligible processing contamination (Table 2.5).

Table 2.5: *Libby age of G. ruber before and after cleaning.*

Sample details	Libby age before cleaning (yrs.)	Libby age after cleaning (yrs.)
G. ruber - 1	12274±109	12576±95
G. ruber -2	12746±110	12852±85
G. ruber -3	8576±89	8509±98

2.8 Radiocarbon (^{14}C) Measurement with Accelerator Mass Spectrometer

Aluminum targets containing sample graphite, standards, and blank were counted using 1 MV accelerator mass spectrometer (AMS: Figure 2.10) PRL-AURiS (PRL-Accelerator Unit for Radioisotope Studies). Negative ion source (Cs+) at 110°C were being used to convert graphite into 35 KeV negative ion beam, which prevents molecular interference caused by $^{14}N_2$. Negative ions produced were passed through the bouncer-injector (BI) magnet, where by applying suitable voltage, different isotopes of carbon were selected and introduced sequentially into the tandem accelerator. Within the tandem accelerator, stripper gas (Argon) breaks the molecules into elemental ions and converts the ion beam into various states of positively charged ions ($^{14}C^{2+}$), which is fed to a 90° high energy magnet and directs the stable isotopes (^{12}C and ^{13}C) towards faraday cups for stable isotope ratio measurement. Rare isotope

(^{14}C) is directed towards rare isotope (RI) magnet via electrostatic analyser (ESA). The energy loss and the residual energy of rare isotope is being measured in a gas ionization.

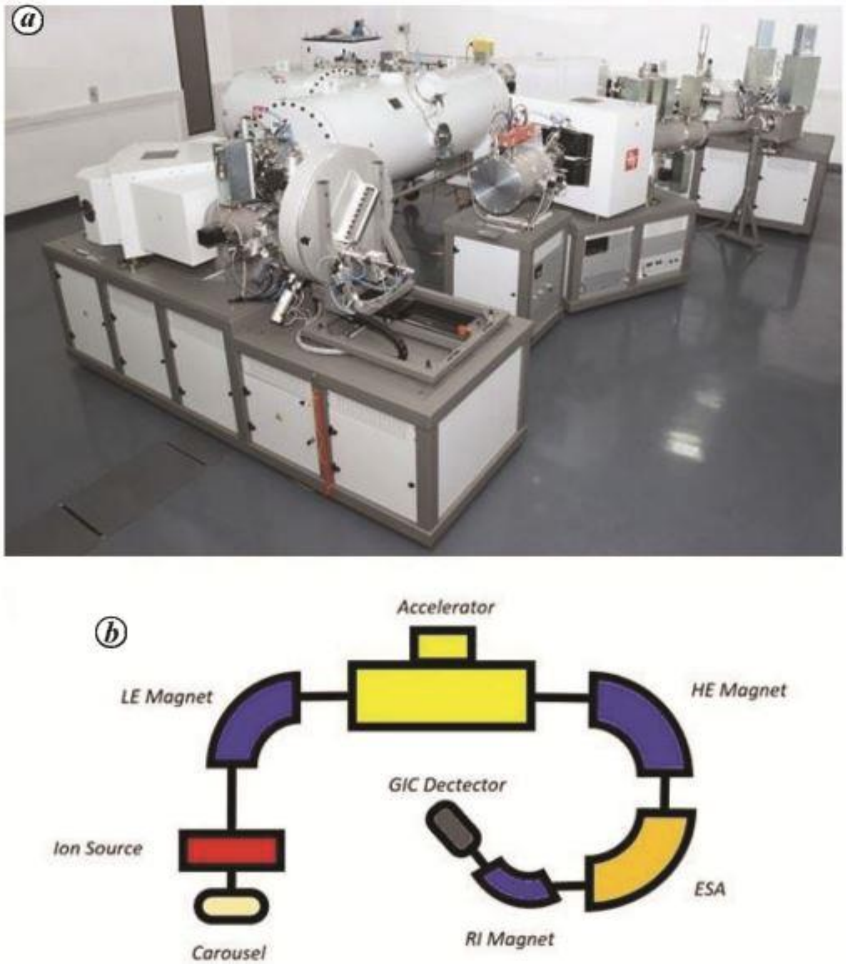

Figure 2.10: a) Photograph of 1 MV AMS installed at AURiS, PRL (b) Schematic of AMS at AURiS (Bhushan et al., 2019b)

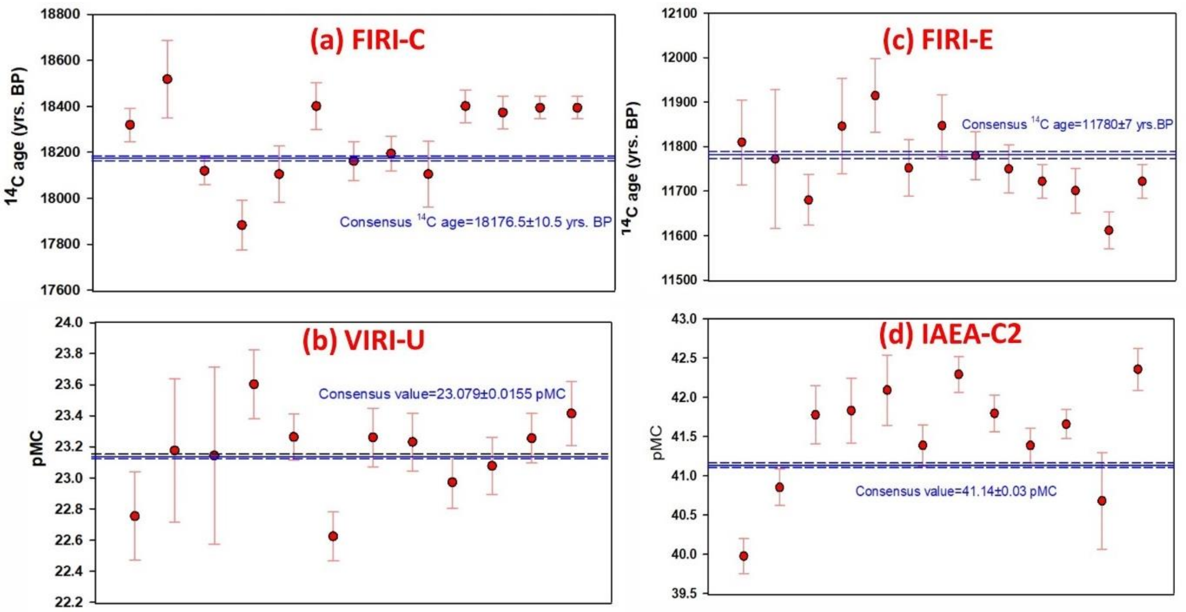

Figure 2.11: Comparison of measured radiocarbon reference standards with consensus value. (a) ^{14}C age of FIRI-C (b) pMC of FIRI-E (c) ^{14}C age of VIRI-U (d) pMC of IAEA-C2.

detector, which gives ^{14}C counts (Bhushan et al., 2019a). Sample carousel containing 50 targets can be loaded at a time and ~20-25 targets are run in one batch. Targets were sputtered cleaned for 1-2 minutes to remove any surficial contamination while storage of samples. Counting was done in several blocks of 10 cycles to get the precise result of $^{14}C/^{12}C$. A cycle of primary standards (NBS Oxalic acid-1, NBS Oxalic acid-2) along with organic carbon reference standard (VIRI-U, FIRI-E), carbonate blank (IAEA-C1), and organic carbon blank (Anthracite) were also run in each set of samples for quality control. The measured precision (relative standard deviation) for FIRI-C, FIRI-E, VIRI-U, and IAEA-C2 was 1.0%, 0.7%, 1.1%, and 1.7% respectively. While, the measured accuracy for FIRI-C, FIRI-E, VIRI-U, and IAEA-C2 was 0.4%, 0.1%, 0.3 %, and 0.9% respectively. The Libby age or pMC can be found in Figure 2.11. HVEE graphite was run during every change of sample to minimize background.

2.8.1 Radiocarbon Age for Different Species of Foraminifera

Foraminifera species are found in ocean environments from well ventilated surface oceans to poorly ventilated deep oceans. Radiocarbon concentration in their shell depends upon the radiocarbon concentration of the dissolved inorganic carbon (DIC) of the water body where it calcifies. Since the atmosphere is the primary source of radiocarbon, the deep ocean which is not in contact with the atmosphere always remains depleted in radiocarbon. Hence, $\Delta^{14}C$ of the DIC varies in surface, subsurface, intermediate water, and the deep-sea. Thus, the radiocarbon dates vary for different species of foraminifera calcifying at various depths at the same time (Broecker et al., 1999).

AMS radiocarbon dating was done in different species of foraminifera to select the right species for ventilation age studies. Subsurface species, *G. ruber* and *G. sacculifer* calcify with the signature of DIC of the subsurface water (Dowsett, 2007), and hence it is closely related to radiocarbon concentration of the atmosphere compared to the species calcifying in the intermediate water i.e., *G. menardii* and deep dwelling benthic foraminifera species. In principle, *G. ruber* and *G. sacculifer* should have lower radiocarbon age compared to the *G. menardii* and benthic foraminifera species. However, during the mid-Holocene, Libby age of *G. menardii* was found to be lower compared to the subsurface species, both in the CEIO as well as SBoB. Large variation in the radiocarbon age of *G. ruber* and *G. menardii* up to 2736 yrs during 15.8 ka BP (Figure 2.12) suggests that the species selection can significantly obscure the chronology of the marine sediment cores. It further signifies the importance of species selection in building chronology and in the ventilation studies, and further suggests that surface-subsurface dwelling species should be used for radiocarbon dating of sediment cores. To avoid misinterpretation, monospecific species calcifying in the sub-surface ocean (*G. ruber*) was selected for both ventilation age estimation as well as for the chronology, in the three cores SS152/3828, SS172/4040, SK312/09 as well as SK304/B12.

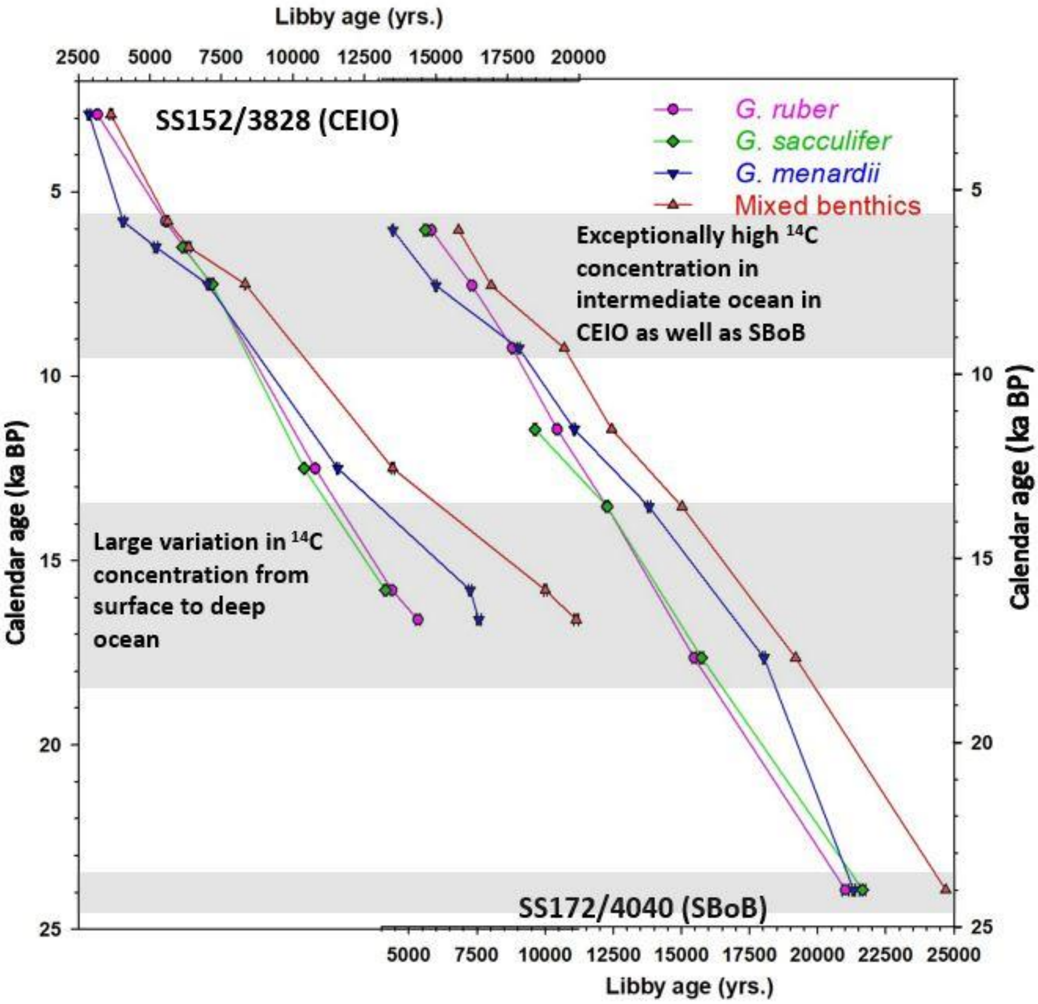

Figure 2.12: Radiocarbon ages of different species of foraminifera in the Central Equatorial Indian Ocean and the Southern Bay of Bengal.

2.8.2 AMS radiocarbon dating and Age-Depth Model of selected sediment cores

A total of five marine sediment cores from three different Indian Ocean basins were radiocarbon dated using sub-surface species (*G. ruber* and *G. sacculifer*). The sedimentation rate in the CIO basin (including two cores; Figure 2.13a and 2.13b) varied between 0.9-8.5 cm.kyr^{-1} and averages to 2.5 cm.kyr^{-1}. While, sedimentation rate in the SWIO (Figure 2.13c) and the EIO (Figure 2.13d) was 2.1 cm.kyr^{-1} and 6.0 cm.kyr^{-1} respectively. A sudden increase in sedimentation rate (from 0.8 cm.kyr^{-1} during 13.5 ka BP to 12.3 cm.kyr^{-1} at 13.8 ka BP) was found in the

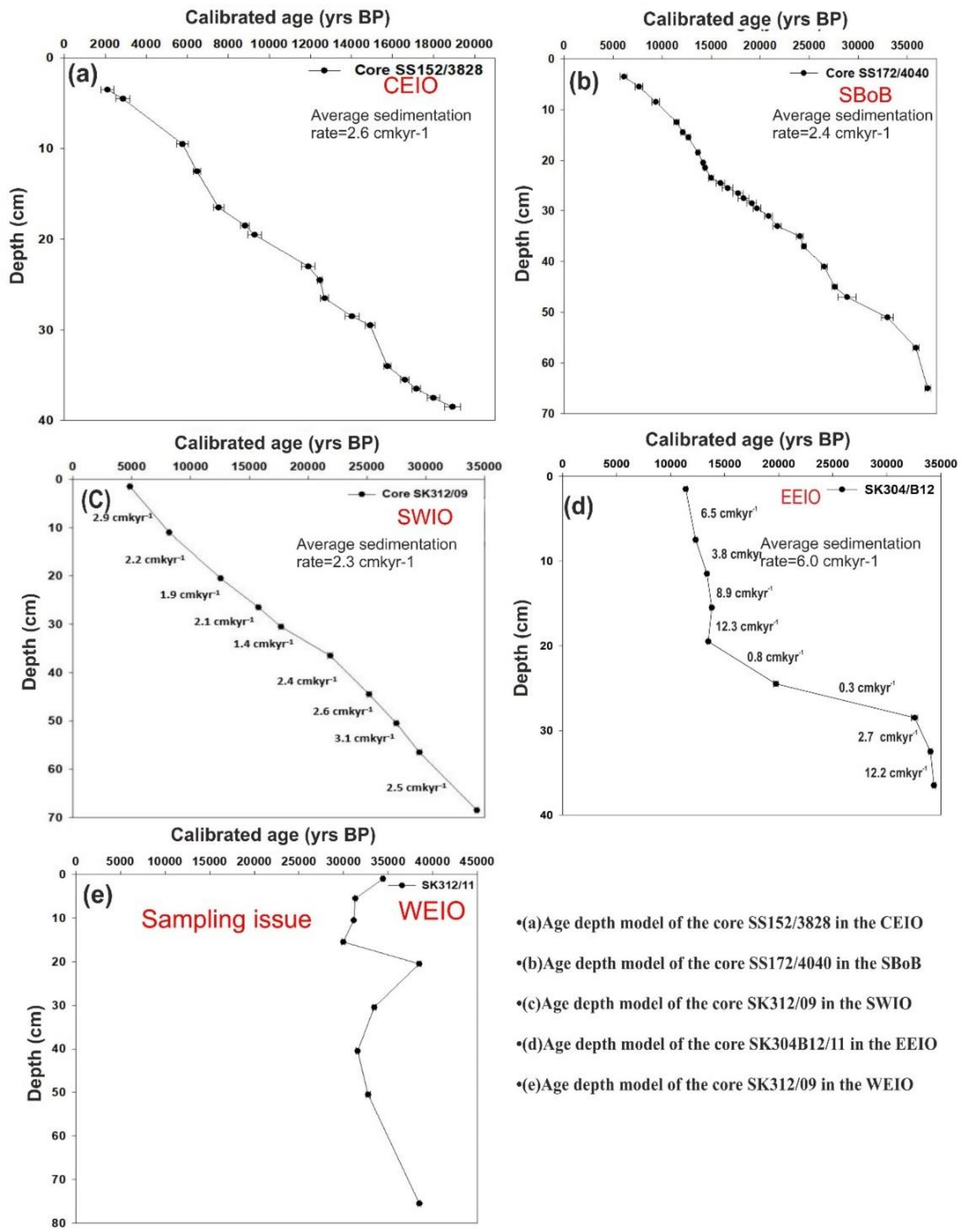

Figure 2.13: Age-depth model of the studied marine sediment core from basin of the Indian Ocean and the sedimentation rates.

core SK304/B12. This core lies near to Sunda trench, which is a geologically active region (Teh et al., 2018). Hence, the large variation in the sedimentation rate in this region gives the possibility of volcanic input to the core location. Moreover, volcanic material was also found in the bulk sieved sample of the foraminifera from this core. The calendar age of the top layer of the core SK312/11 from the WIO (Figure 2.13e) was 34.4 ka BP, which is rather impossible. Further, the calendar age didn’t change significantly up to 75 cm of the core length. It gives the possibility of double bounce of the core while drilling and hence core wasn’t studied further.

Chapter 3.

Benthic Foraminifera Assemblage and Abundance Variation in the Central Equatorial Indian Ocean; Response to Paleo Deepwater Environment

3.1 Introduction

Benthic foraminifera, is a single-celled marine microorganism found widespread with high diversity in the ocean, plays a crucial part in the deep-sea food web and marine carbon cycle (Gooday et al., 1992; Moodley et al., 1997; Bernhard, 2000; Bernhard et al., 2008). Due to the potential preservation capacity of their shells, benthic foraminifera act as an useful proxy for paleoclimatic and paleo-ocean circulation studies (Kaiho, 1991; Moodley et al., 1998; Mackensen et al., 2000). Their life, distribution, and diversity in the deep-sea environment are mainly controlled by two components, they are deep water dissolved oxygen concentration and input of organic carbon input to the deep-sea (Kaiho, 1994; Gupta et al., 2006; De and Gupta, 2010; Sarkar and Gupta, 2014). Other controlling factors such as quality of food supply, carbonate saturation depth, and chemistry of seafloor also depend on these two components (Jorissen et al., 2007). The benthic foraminiferal assemblages thus can vary both as a function of space and time, as it is dependent both on local as well as global processes i.e., export productivity and deep water oxygenation respectively.

Based on the microhabitat preference of benthic foraminifers, they have been categorized as epifaunal (those dwelling at the sediment-water interface) and infaunal communities (those dwelling within the sediment; (Corliss, 1985). Epifaunal community is rounded and symmetrical and infaunal community is generally angular, asymmetrical, and elongated. The dominance of the infaunal benthic foraminifera represents high productivity and low oxygen environment, whereas the dominance of the epifaunal benthic foraminifera represents low productivity and high oxygen environment (Corliss and Emerson, 1990; Rathburn and Corliss, 1994; Jorissen et al., 1995; Bharti et al., 2017). Further, the composition of assemblages also varies based on the bottom water dissolved oxygen and export productivity. Assemblage dominated by *Cibicidoides wuellerstorfi, Globocassidulina subglobosa, Oridorsalis umbonatus,* and *Pyrgo murrhina* represents high bottom water dissolved oxygen (dissolved oxygen >1.5ml/l) (Corliss, 1979; Kaiho, 1994; Fariduddin and Loubere, 1997; Gupta and Thomas, 1999; Jorissen et al., 2007; De and Gupta, 2010). Whereas, assemblage dominated by *Uvigerina peregrina*, *Uvigerina proboscidea*, *Bolivina robusta*, *Bolivina spp*., *Pullenia bulloides,* and *Melonis barleeanum* suggest high and continuous organic flux to the deep-sea sediments (Gooday, 1993; Loubere et al., 1993; Rathburn and Corliss, 1994; Jorissen et al., 1995; Carson et al., 2008; Raj et al., 2009; De and Gupta, 2010). Additionally, assemblage dominated by *C. wuellerstorfi*, *G. crassa*, *G. subglobosa*, and *O. umbonatus* represents low export productivity (Gooday, 1994; Fariduddin and Loubere, 1997; Gupta and Thomas, 1999; Carson et al., 2008; De and Gupta, 2010; Singh and Gupta, 2010; de Almeida et al., 2015). Moreover, in oligotrophic and well oxygenated bottom water environment, an episodic flux of phytodetrital organic matter leads to colonization of certain opportunistic species, which are indicators of the past seasonality of export productivity e.g. *Epistominella exigua*, *Laticarinina pauperata*, *M. barleeanum*, and *P. murrhina* (Lohrenz et al., 1992; Fariduddin and Loubere, 1997; Loubere, 2003; Sun et al., 2006; Smart et al., 2007). Based on the understanding of ecological sensitive benthic foraminifera species, relative abundances of the dominant species have been placed in three different groups. These groups represent past variation in the deep water dissolved oxygen, past variation in the productivity, and past seasonality changes in the export productivity. Deep water oxygenation variations have also been analysed in the benthic foraminifera $\delta^{13}C$ value, as a supporting proxy for deep water ventilation (Duplessy, 1988; Mackensen and Bickert, 1999; Skinner and Shackleton, 2004b). Here the paleo productivity variation has been compared with OC, (Bhushan et al., 2001; Punyu et al., 2014) and the seasonality changes have been verified with the linear sedimentation rate, as well as planktic foraminifera $\delta^{13}C$ value.

The nutrients and oxygen are chiefly brought by the overturning circulation in the deep ocean and is mainly governed by the overturning rate and contribution of the deep water masses i.e., North Atlantic Deep Water (NADW) and Antarctic Bottom Water (AABW). Palaeoceanographic studies provide numerous evidence of modification in the NADW formation and ventilation of deep water in the global ocean during Heinrich Stadials and LGM (Duplessy et al., 1980; Sarnthein et al., 2003; Skinner et al., 2010). The stable carbon isotopic ratio of epibenthic foraminifera, which is dependent on the rate of the overturning circulation and ratio of contributing water masses, records such changes notably and has been widely employed to understand palaeoceanographic changes (Duplessy et al., 1980; Curry and Oppo, 2005; Murgese and De Deckker, 2007). Numerous paleo-benthic foraminifera assemblage studies in the Indian Ocean on million-year time scale have revealed changes in the deep-sea environment led by deep ocean circulation (Gupta and Thomas, 1999; Gupta et al., 2006). However, only a few studies focused on millennium timescale changes (Murgese and De Deckker, 2007; Smart et al., 2010; Singh et al., 2015; Devendra et al., 2019), although major global climatic events are known to have occurred during the last 19 millennium. Thus, the present study attempts to understand past changes in the ecological condition of the deep Central Equatorial Indian Ocean (CEIO) using benthic foraminifera assemblage and abundance, along with stable carbon isotopic ratio of *Cibicidoides* species and geochemical analysis of the sediment. The present study primarily focuses on the following part of the climatic intervals: Last Glacial Maxima (LGM: ~17.5-18.9 ka BP), Heinrich Stadial-1 (HS-1: ~15.4-17.5 ka BP), BØlling- AllerØd warming (B-A warming: ~14.0-15.0 ka BP), Younger Dryas (YD:11.6-12.8 ka BP), Early Holocene (8-11 ka BP), Mid Holocene (6-8 ka BP), and Late Holocene (2-6 ka BP).

3.2 Regional setting of the Central Equatorial Indian Ocean

A sediment core from the Central Equatorial Indian Ocean (SS152/3828, water depth-3166 m, 3.8°N, 78.1°E) collected from an open ocean location towards the southern boundary of Laccadive Sea has been investigated (Figure 3.1A). The CEIO is unique as it acts as a transition zone between the Arabian Sea (AS) and the Bay of Bengal (BoB) and is influenced by both monsoon systems i.e., South West Monsoon (SWM) during summer (June-Sept) and North East Monsoon (NEM) during winter (Nov-Feb) (Tomczak and Godfrey, 2003; Tiwari et al., 2006). However, maximum productivity in the CEIO takes place during the SWM (Yadav et al., 2021). Strong Indian Ocean Equatorial Westerlies (IEW) prevails almost throughout the year, which strengthens during the inter-monsoon season in the Equatorial (Eq.) Indian Ocean and helps in regulating the productivity of the CEIO (Beaufort, 1997; Punyu et al., 2014; Sarkar and Gupta, 2014). Productivity in the Eq. Indian Ocean is low compared to the Northern Indian Ocean (Kumar et al., 2016). Eq. Indian Ocean productivity is also low compared to Eq. Atlantic and Eq. Pacific due to lack of equatorial upwelling in the Eq. Indian Ocean (Schott and McCreary, 2001). The Eq. Indian Ocean is influenced by seasonal reversal of wind, which changes its monsoonal strength during glacial and interglacial intervals (Tiwari et al., 2006; Chandana et al., 2018) and hence the productivity.

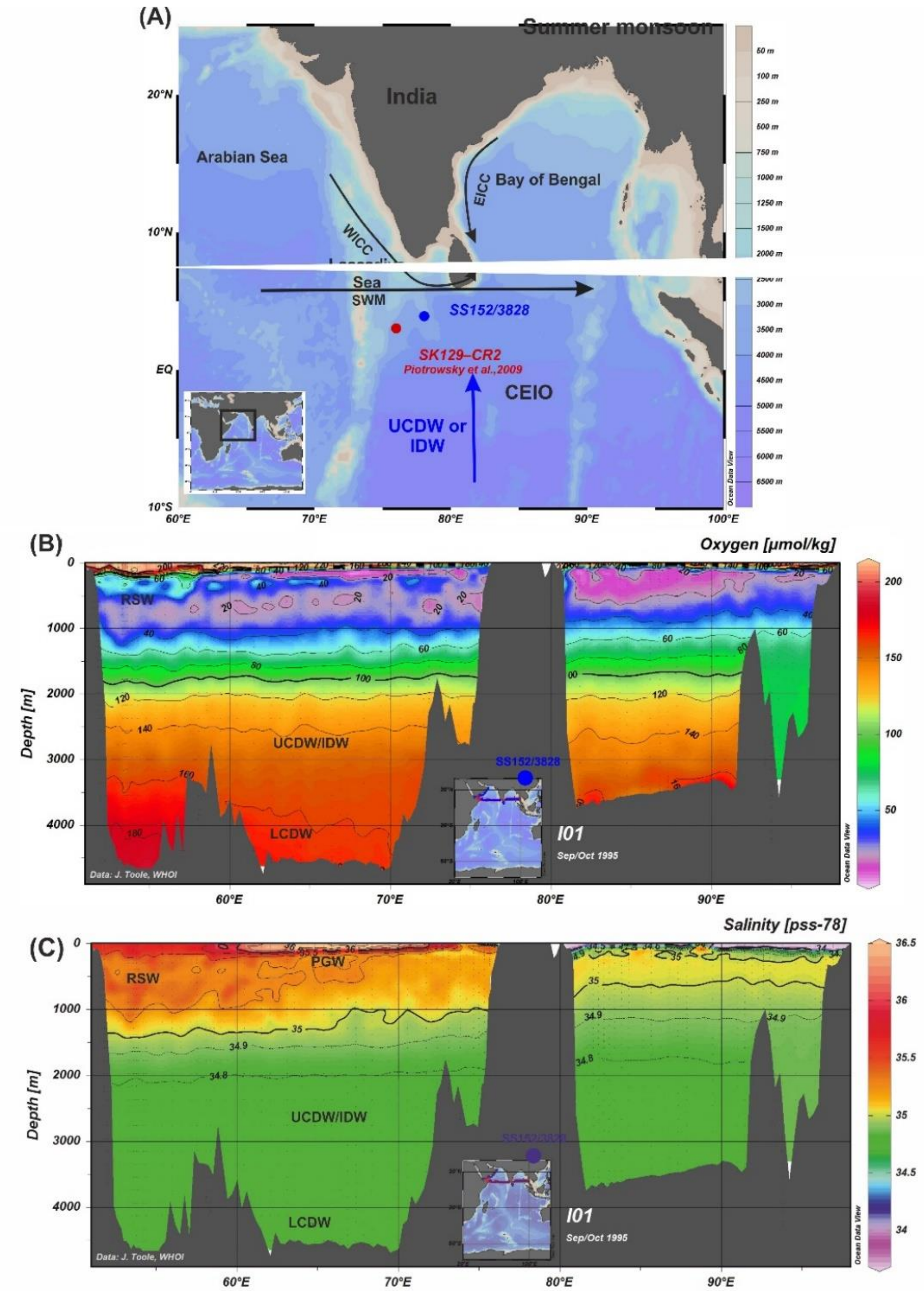

Figure 3.1: Location of the sediment core in the Central Equatorial Indian Ocean. SS152/3828 in dark blue dot (3.8°N, 78.1°E; Core length~39 cm, 3166 m) and SK129-CR2 in dark red dot (3°N, 76°E, 3800 m (Piotrowski et al., 2009). The black marrow marks the surface current during summer monsoon and blue arrow marks the flow of Upper Circumpolar Deep Water (UCDW)/Indian Deep Water (IDW) at the core location Vertical profile of (B) dissolved oxygen and (C) dissolved salinity in the CEIO based on eWOCE data.

The deep waters at the core location (SS152/3828) are ventilated by deep water masses sourced mainly from Upper Circumpolar Deep Water (UCDW) and/or Indian Deep Water (IDW), which forms by mixing of majorly high salinity, higher oxygen

NADW and marginally well oxygenated AABW in the Antarctic Circumpolar Current (ACC) region (Talley, 2011; 2013) and can be traced above lysocline of the Equatorial Indian Ocean (Kolla et al., 1976; Piotrowski et al., 2009). Based on GEOSECS dissolved oxygen data (Weiss, 1983) from the Eq. Indian Ocean (Figure 3.1B), it was found that deep water in the core location is well oxygenated at present.

3.3 Benthic foraminifera assemblages and their abundances

The sediment core SS152/3828 (3.89° N, 78.06° E; water depth 3166 m; core length 39 cm) was sub-sampled at 1-2 cm intervals. The subsamples were taken in two aliquots, one for the geochemical analysis and another for the study of benthic foraminiferal assemblages and isotopic analysis. While, aliquot for geochemical parameters was oven-dried at 85°C, crushed, and stored, another aliquot for the foraminifera assemblage study was oven-dried at 55°C. Wet sieved and dried bulk foraminifera (>63 µm) were sieved using 425, 250, and 150 µm standard sieves, and benthic foraminifera in the size fraction >150 µm were counted. Since samples from similar depths were used for both, radiocarbon dating and abundance study of benthic foraminifera, the protocol for benthic foraminifera assemblage study was modified accordingly. Counting of foraminifera was done separately in two size fractions (>250 µm and 150-250 µm) for six depths. Due to the large amount of 6 samples taken for ventilation study, an aliquot (split using Otto Microsplitter) of bulk foraminifera sample of 150-250 µm size, weighing only 0.1-0.2 g, were scanned for benthic foraminifera abundance. In >250 µm size fraction, whole size fraction was scanned. While for 8 depths sieved specifically for abundance study, all available benthic foraminifera in >150 µm fraction were counted. The weight of the sediment along with the number of specimens scanned in different size fractions can be found in Tables 2.1 and 2.2 (Chapter 2). Abundances of both size fractions were normalized to 10 g of sediment for each size fraction and added together to get abundance of >150 µm fraction per 10 g of sediment at each depth (Appendix Table C.1). All the available well-preserved specimens were separated and identified up to species level following the key book of Loeblich & Tappan (1987) and the World Register for Marine Species (Hayward et al., 2020). Further all species were classified into two groups (epifauna and infauna) based on their morphology and existing literature about the species microhabitat (Appendix Table B.1 and Table B.2). Though some species have been reported to dwell both as infauna as well as epifauna in certain conditions, infauna-epifauna separation in this study has been done based on major understanding of the species, to compare the downcore faunal distribution. Species absolute abundance at each depth was converted into percentage abundance, mentioned as relative abundance (RA). Benthic foraminifera density was estimated based on the number of specimens per gram of sediment. Benthic Foraminifera Accumulation Rate (BFAR) was calculated using the following equation (Herguera and Berger, 1991):

$$BFAR\ (number\ of\ specimens/cm^2\ kyr^{-1}) = BF \times LSR \times DBD$$

Where BF is the number of benthic foraminifera per gram of dry sediment, LSR is the linear sedimentation rate (cm/kyr), and DBD is the dry bulk density (g/cm^3) of the sediment. DBD was calculated based on the following equation by Clemens et al., (1987).

$$DBD=3.104 \times 10^{-5}(\%CaCO_3)^2 + 2.176 \times 10^{-3}(\%\ CaCO_3) + 0.430$$

3.4 Radiocarbon Dating and Age depth model

Radiocarbon dating was carried out using 1MV Accelerator Mass Spectrometry (AMS at PRL-AURiS facility (PRL-Accelerator Unit for Radioisotope Studies (Bhushan et al., 2019b; 2019a). Towards this, monospecific surface-dwelling planktic foraminifera *Globigerinoides ruber* weighing 10-12 mg was picked (except for two depths where *Globigerinoides sacculifer* was mixed for getting ample amount of sample). Foraminifer shells and cleaned, graphitised and measured for radiocarbon concentration using AMS. Radiocarbon age was calculated using the standard method (Stuiver et al., 1998a). AMS ^{14}C age was further calibrated using R package “Bchron” (Parnell et al., 2008) and MARINE20 Calibration curve (Stuiver et al., 1998a; Heaton et al., 2020; Reimer et al., 2020), using localized reservoir age correction (ΔR) of 98 ± 22 yrs (Dutta et al., 2001; Southon et al., 2002). The localized reservoir age correction was done to correct for deviation of local mixed layer reservoir age from the global mean reservoir age.

The chronology of the core SS152/3828 was established based on radiocarbon dating of planktic foraminifer (250-425 µm size *G. ruber*) from 17 depths interval using Accelerator Mass Spectrometry (AMS). The 39 cm core span 18900 yrs. The chronology for the intermediate depths of the core (SS152/3828) where AMS radiocarbon measurements were not done was calculated using linear interpolation of established calibrated ages (Table 3.1), which spans 18900 cal BP. The sedimentation rate was estimated using linear interpolation of calibrated age at 17 depths.

The core SS152/3828 yielded an average sedimentation rate of 2.6 cm.kyr^{-1} with a minimum sedimentation rate of 1.1 cm.kyr^{-1} during 18.9-18.0 ka BP and a maximum of 8.5 cm kyr^{-1} during 12.7-12.5 ka BP (Figure 3.2). In the present study, period 2.1-10.0 ka BP has been marked as Holocene, 10.0-16.9 ka BP has been marked as deglaciation, which also covers Younger Dryas (~11.6-12.9 ka BP) and Heinrich Stadial-1 (~15.6-17.8 ka BP). Whereas, 17.8-18.9 ka BP has been marked as LGM.

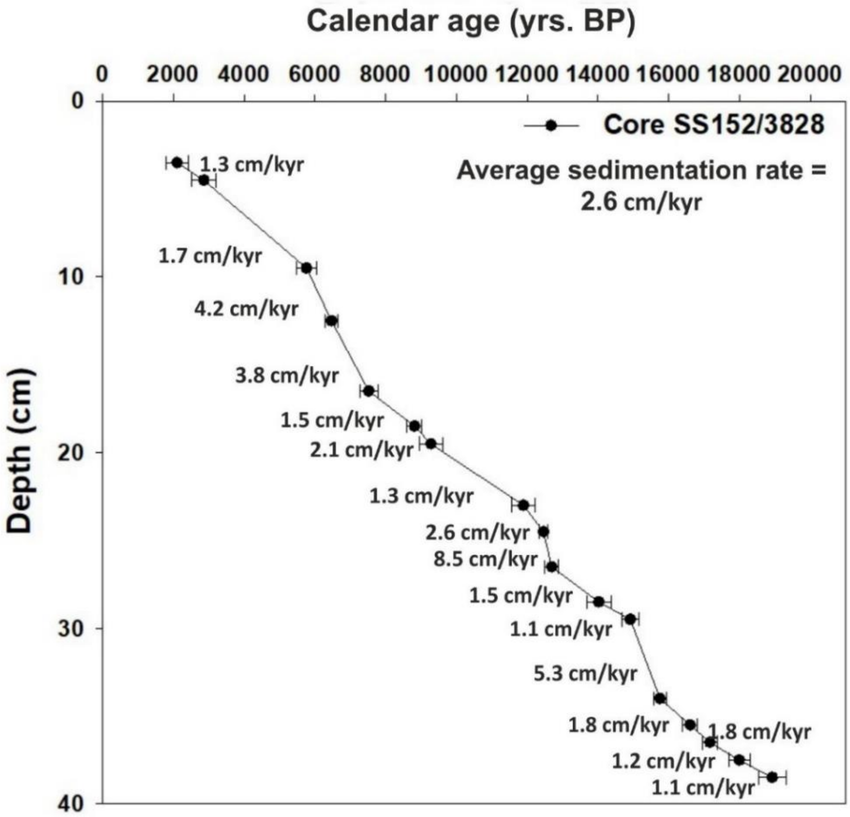

Figure 3.2: Age-depth plot of the core SS152/3828 based on AMS radiocarbon calibrated age with sedimentation rates. The filled circles mark the calendar age for the core SS152/3828. The topmost section of the core (3.5 cm) corresponds to 2.1 ka BP, whereas the bottommost section corresponds to 18.9 ka BP. Assuming linear sedimentation between two radiocarbon-dated intervals, sedimentation rates have been calculated.

3.5 Measurements of stable carbon and oxygen isotope composition and other geochemical parameters

Oxygen and Carbon isotope was measured in *G. ruber* of size fraction 250-425 µm and cleaned C. *wuellerstorfi* from >250 µm size fraction. All isotopic values are reported relative to Vienna-Pee Dee Belemnite (V-PDB) value. The external precision

for $\delta^{18}O$ value was always better than ±0.1‰ (1σ standard deviation), estimated based on measurement of calcite standard Makrana Marble (MMB). For organic carbon (OC) and total nitrogen (N_{Tot}) measurement, ~20-24 mg of decarbonated sediment was taken. Precision for N_{Tot} and OC was always better than 6% and 4% respectively (Bhushan et al., 2001). Whereas inorganic carbon (IC) measurement was done in 5-10 mg of homogenized sediment. Measurement for both OC as well as IC was
done in 27 depth intervals of the 39 cm long core. The precision of IC was always better than 3%.

S. N.	Sample ID	Lab ID	Depth (cm)	Species	Radiocarbon age ± 1σ error (yrs)	Calibrated age ± 1σ error (yrs BP)
1	SS3828/3-4	AURIS-00878	3.5	*G.ruber, G. sac*	2523±108	2103±322
2	SS3828/4-5	AURIS-02258	4.5	*G. ruber*	3164±45	2860±336
3	SS3828/9-10	AURIS-01621	9.5	*G. ruber*	5547±35	5761±275
4	SS3828/12-13	AURIS-02301	12.5	*G. ruber*	6190±75	6468±170
5	SS3828/16-17	AURIS-01623	16.5	*G. ruber*	7158±42	7522±250
6	SS3828/18-19	AURIS-02299	18.5	*G. ruber*	8405±45	8813±213
7	SS3828/19-20	AURIS-01619	19.5	*G. ruber*	8715±47	9278±323
8	SS3828/22-24	AURIS-02296	23	*G. ruber*	10708±87	11897±326
9	SS3828/24-25	AURIS-01605	24.5	*G. ruber*	11081±34	12462±112
10	SS3828/26-27	AURIS-01618	26.7	*G. ruber*	11176±94	12697±194
11	SS3828/28-29	AURIS-02292	28.5	*G. ruber*	12551±60	14025±345
12	SS3828/29-30	AURIS-01603	29.5	*G. ruber*	13119±49	14917±228
13	SS3828/33-35	AURIS-01599	34	*G. ruber*	13678±37	15757±191
14	SS3828/35-36	AURIS-02290	35.5	*G. ruber*	14369±76	16610±209
15	SS3828/36-37	AURIS-01597	36.5	*G. ruber*	14812±42	17165±209
16	SS3828/37-38	AURIS-01595	37.5	*G. ruber*	15495±38	18000±297
17	SS3828/38-39	AURIS-00880	38.5	*G. ruber, G. sac*	16453±199	18928±385

Table 3.1: Radiocarbon dates of the core SS152/3828

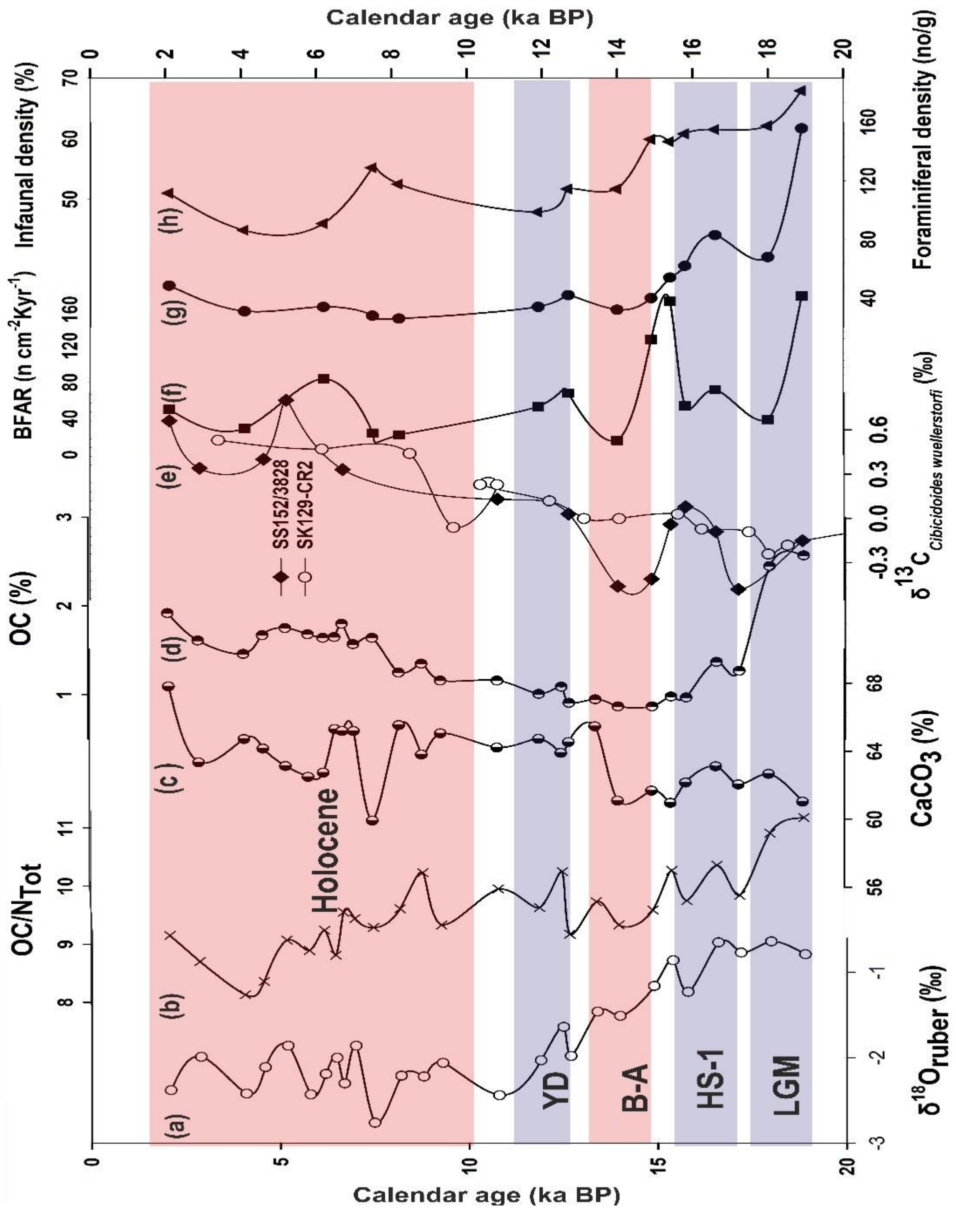

Figure 3.3: Variation in geochemical, isotopic, and benthic foraminifera assemblage parameters: From left to right, a) downcore variation in $\delta^{18}O$ value Globigerinoides ruber ($\delta^{18}O_{ruber}$), b) C/N, c) $CaCO_3$, d) OC%, e) $\delta^{13}C$ of Cibicidoides wuellerstorfi respectively. f) Benthic Foraminifera Accumulation Rate (BFAR), g) Benthic Foraminifera density, and h) Infaunal density in the core SS152/3828. Grey curve marks $\delta^{13}C$ of the core SK129-CR2 (Piotrowski et al., 2009). The light blue band represents cold period and the light red band represents warm period.

Geochemical parameters such as organic carbon (OC%), calcium carbonate ($CaCO_3$%) and C_{org}/N_{Tot} were measured in surface sediments to understand the productivity and sediment provenance at the core location. OC ranged between 0.9% during 14.0-14.9 ka BP as well as at 12.7 ka BP to 2.6% at 18.9 ka BP. While OC/N_{Tot} varied from 8.1 at 4.1 ka BP to 11.2 at 18.9 ka BP (Figure 3.3), indicating primarily the marine source of sediment. The calcium carbonate ranged between 59.9% to 67.8%

at 7.5 ka BP and 2.1 ka BP respectively, indicating calcareous ooze as a major fraction of the sediment (Figure 3.3). Overall, early deglaciation and LGM witnessed decreased $CaCO_3$%. The average $\delta^{18}O$ value of *G. ruber* for the last 18.9 kyrs was -1.9‰ varying between -0.6 to -2.8‰ (Figure 3.3). In the CEIO, LGM has been marked clearly by enriched $\delta^{18}O$ value (-0.7‰) and Holocene with depleted $\delta^{18}O$ value (-2.2‰). While, $\delta^{13}C$ value of *G. ruber* varied between 1.1-2.1‰, attaining maximum value during 7.0-8.2 ka BP. $\delta^{13}C$ value of epifaunal benthic foraminifera (*C. wuellerstorfi*) varied between -0.5‰ at 17.5 ka BP to 0.8‰ at 5.3 ka BP.

3.6 Benthic foraminiferal assemblage and abundances variation for the last 18.9 kyrs

Benthic foraminifera assemblage scanned at 14 depths comprised 65 benthic foraminiferal species with significant variation in their relative abundances (Appendix Table C.2). Most of the 65 identified species were calcareous and only few were agglutinated. The infaunal and the epifaunal group contained 43 and 22 species respectively. The diversity in the benthic foraminifera ranged from 28 species at 12.7 ka BP to 39 species at 2.1 ka BP (Figure 3.3). Infaunal diversity also reached minima (15) and maxima (24) at the same time as benthic foraminiferal diversity. While epifaunal diversity reached its maxima (15) at the same time, but minima (8) at 7.5 ka BP. The foraminifera density varied between 26-156 individuals per gram of sediment, with the lowest at 8.2 ka BP and the highest at 18.9 ka BP (Figure 3.3). While, BFAR varied between 16 $n.cm^{-2}\,kyr^{-1}$ at 14 ka BP to 175 $n.cm^{-2}\,kyr^{-1}$ at 18.9 ka BP. Infaunal density was minimum (45%) at 4.1 ka BP and maximum (68%) at 18.9 ka BP. A total of 9 species has been identified as dominant members in the CEIO, based on their abundance of more than 10% in at least one depth. These species are: *C. wuellerstorfi*, *E. exigua*, *G. subglobosa*, *M. barleeanum*, *O. umbonatus*, *Uvigerina hispida*, *U. peregrina*, *U. proboscidea* and *Uvigerina* sp.1. While there were 19 species, which had minimum of 5% abundance in at least one scanned depth and 30 species had minimum of 3% abundance in at atleast one scanned depth.

3.6.1 Dominant benthic foraminifera assemblage and its preferred environment

Substantial variation is observed in the benthic foraminiferal assemblages for the last 18.9 kyrs. The Central Indian Ocean witnessed the dominance of *Uvigerina* spp., *E. exigua*, and *C. wuellerstorfi* during the LGM, with *Uvigerina* spp. being the most dominant species. During HS-1, the benthic foraminiferal assemblage was dominated by *Uvigerina* spp., *O. umbonatus*, *E. exigua*, *C. wuellerstorfi* as well as *M. barleeanum,* with a predominance of *U. hispida*. The Holocene assemblages were dominated by *G. subglobosa*, *O. umbonatus, M. barleeanum*, *C. wuellerstorfi* and *E. exigua,* with a predominance of *G. subglobosa,* in general. Among the dominant species, *C. wuellerstorfi* is known to dwell in all conditions of deep basins but is often found in high oxygen and low OC environments (Corliss, 1985; Jorissen et al., 2007; Murgese & De Deckker, 2007). *Epistominella exigua* is a marker species of seasonal flux or pulsed organic carbon (Gooday & Rathburn, 1999; Ernst & Zwaan, 2004; Hayward et al., 2013). *Globocassidulina subglobosa* dwells in low organic carbon flux environments with well oxygenated bottom water conditions and may also indicate pulsed organic matter (Gooday, 1993; Schmiedl et al., 1997; Loubere, 1998; Gupta & Thomas, 1999; Loubere & Fariduddin, 2003). *Melonis barleeanum* is known to be a deep infaunal species, an indicator of refractory organic matter, mesotrophic condition, and intermediate organic flux, and it is also linked to intermediate to high seasonality in the Indian Ocean (Fontanier et al., 2002; Drinia & Anastasakis, 2012). *Oridorsalis umbonatus* is an indicator of well oxygenated water with oligotrophic conditions (Miao & Thunell, 1993; Gupta & Thomas, 2003; Singh & Gupta, 2010). *Uvigerina* spp. mostly indicate high amounts of food availability or increased export productivity (Hayward et al., 2013). *Uvigerina proboscidea* dwells mostly in intermediate to high levels of productivity and can survive in variable oxygenation (Lutze & Coulbourn, 1984; Smart et al., 1994; Gupta et al., 2006a; Raj et al., 2009). *Uvigerina peregrina* is also an indicator of the oxygen minimum zone and dominates in high productivity environments (De & Gupta, 2010). This species has also been suggested to be tolerant to low quality food supply, and hence it can also act as an indicator of increased seasonal food supply (e.g., Fontanier et al., 2003; Koho et al., 2008 and Theodor et al., 2016). The dominant faunal composition in the CEIO for the last 18.9 kyrs shows remarkable change in the deep-sea environment.

In addition to identifying the dominant assemblage group, we grouped benthic foraminifera species to understand the changes in deep water oxygenation, export productivity, and phytodetrital input. Based on the understanding of preferred microhabitat of the benthic foraminiferal species (with the relative abundance of ≥ 5%), three groups were defined: a high dissolved oxygen group to study the variability in bottom water oxygenation, a high organic carbon group to study the variability in paleoproductivity, and a phytodetrital sensitive group to study the seasonality of export productivity.

3.6.2 Paleo bottom water oxygenation variability

Based on the preferred environments of the dominant benthic foraminifera species, we compared the relative abundance of *C. wuellerstorfi*, *Cibicidoides* spp., *G. subglobosa*, *O. umbonatus*, and *L. pauperata* over the last 18.9 kyrs to reconstruct deep-sea oxygenation

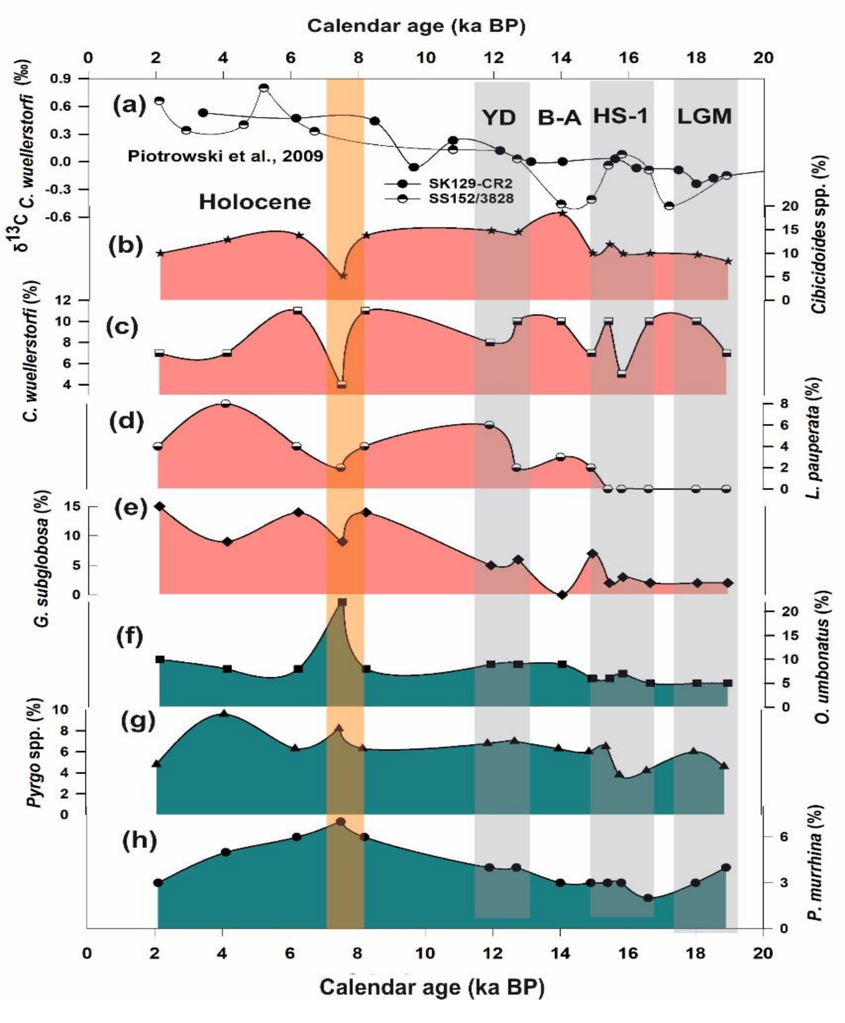

Figure 3.4: Relative abundance of foraminifera species dwelling in high dissolved oxygen conditions and $\delta^{13}C$ of C. wuellerstorfi. X-axis is calendar age in terms of kilo years before present (ka BP). Along Y-Axis, (a) $\delta^{13}C$ of C. wuellerstorfi in SS152/3828 and SK129-CR2 (3°N, 76°E, 3800m, (Piotrowski et al., 2009)), (b), (c),

(d), (e), (f), (g) and (h) are relative abundances of species known to be sensitive to bottom water dissolved oxygen.

(Figure 3.4). *P. murrhina* and *L. pauperata* are well known oxic indicators (Kaiho, 1994; Gupta & Thomas, 2003; Murgese & De Deckker, 2005) and have been compared along with other dominant dissolved oxygen sensitive species in Figure 3.4. Relative abundances of *P. murrhina, Pyrgo* spp.*, O. umbonatus* were very low, with almost zero abundances of *G. subglobosa* and *L. pauperata* during the LGM as well as the HS-1, compared to the Holocene. All these species are known to dwell in well oxygenated conditions (refer section 3.4.1). However, *C. wuellerstorfi* shows a minor increase in abundance during the LGM compared to the Holocene. During the YD, the abundance of all the dissolved oxygen sensitive species was comparatively medium to high. The Holocene had considerably high abundances of all the dissolved oxygen sensitive species throughout (Figure 3.4). The most striking peak of the benthic foraminifera abundance was found at 7.5 ka, with the highest abundances during the last 18.9 kyrs of *Pyrgo* spp., *P. murrhina, O. umbonatus* with a sudden decrease in the abundance of *G. subglobosa, L. pauperata, Cibicidoides* spp. as well as minimum abundance of *C. wuellerstorfi*. Interestingly, 7.5 ka coincides with a sudden decrease in the BFAR, as well as foraminiferal and infaunal density (Figure 3.3). This indicates major and sudden changes in the oxygenation of the deep water ventilating the core location during this period. Exceptionally low ventilation age was also found at 7.5 ka in the CEIO and SB0B paleo-ventilation age record of Bharti et al. (2022), which suggests the intrusion of a comparatively well-ventilated water mass at 7.5 ka and hence a well oxygenated deep-sea environment.

3.6.3 Paleo-productivity variation in the Central Equatorial Indian Ocean

Based on the dominant benthic foraminiferal species responses to high organic carbon discussed in section 3.4.1, we compared *M. barleeanum, Melonis* spp.*, U. hispida, U. peregrina, U. proboscidea,* and *Uvigerina* spp. in order to reconstruct past productivity and food supply in the CEIO (Figure 3.5). Among these species, *Uvigerina* spp. is the dominant shallow infaunal species in Indian Deep Water (Corliss, 1978) and a predominantly high productivity taxa (Smart et al., 2010). It has shown high density in areas with high organic carbon (Lutze, 1980; Lutze &

Coulbourn, 1984), and its abundance shows large variability for the last 18.9 kyrs in the CEIO, ranging from 44% during the LGM to 0% during 2.1-7.5 ka. *U. hispida* and *U. peregrina* showed high abundance during the LGM with the highest abundance peak of *U. proboscidea*, during HS-1. *M. barleeanum* was slightly depleted during the LGM compared to the Holocene. The abundance of *Uvigerina* spp. suddenly decreased during the B-A event and again increased during the YD. During the Early to mid-Holocene, a minimal abundance of the *Uvigerina* spp. was observed, which decreased to 0% during the late Holocene. However, the abundance of *Melonis* spp. only changed from slightly low during the glaciation to intermediate during the Holocene. Similar to the dissolved oxygen sensitive species in Figure 3.4, all the productivity sensitive species (Figure 3.5) also witnessed a peak at 7.5 ka. All the high productivity species showed a dip in abundance at the same time. Though a slightly decreased abundance of high productivity species may suggest decreased food supply at 7.5 ka, the organic carbon data show a minor increase in the productivity compared to the trend. Near zero abundance of *Uvigerina* spp. during the late Holocene with moderately high food supply at 7.5 ka suggests control by other factors as well. *M. barleeanum*, a deep infaunal species that is related to high food supply (De & Gupta, 2010) and feeds on laterally advected refractory organic matter is sensitive to the quality of the food as well. Hence, it cannot be directly used as a productivity indicator (Goldstein & Corliss, 1994).

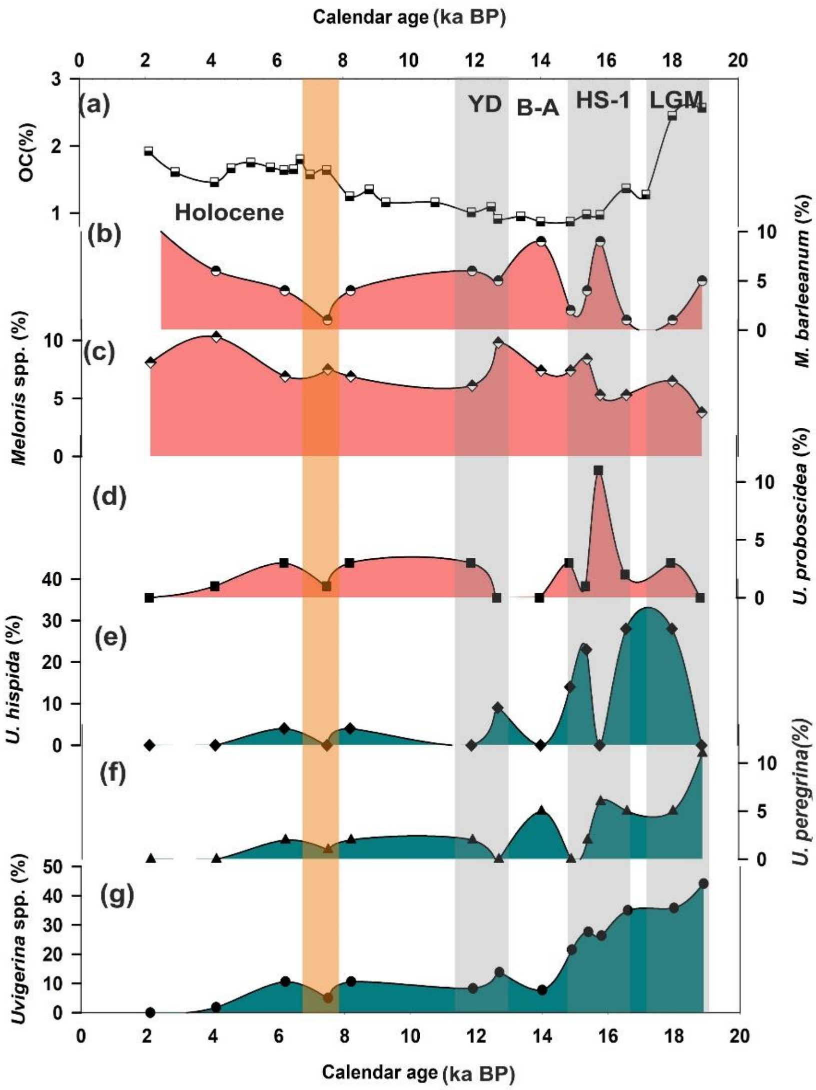

Figure 3.5: Plot of paleo-productivity parameters: X-axis is calendar age in kilo years before present. Y-axis represents (a) Organic Carbon (%) and (b), (c), (d), (e), (f) and (g) are relative abundances of M. barleeanum, Melonis spp.*, U. proboscidea, U. hispida, U. peregrina and Uvigerina* spp. *respectively.*

3.6.4 Past seasonality of the export productivity variation

Certain species have been identified as suspension feeders. They are not very specific to food type and colonize during episodic flux of organic matter. They have been grouped under phytodetrital sensitive species to observe the variability in seasonality (Figure 3.6). *E. exigua* showed substantial variation in its density from minima (3%) at 8.2 ka and 6.2 ka to maxima (10.9%) at 15.8 ka. This species was abundant during the LGM and HS-1 and least abundant

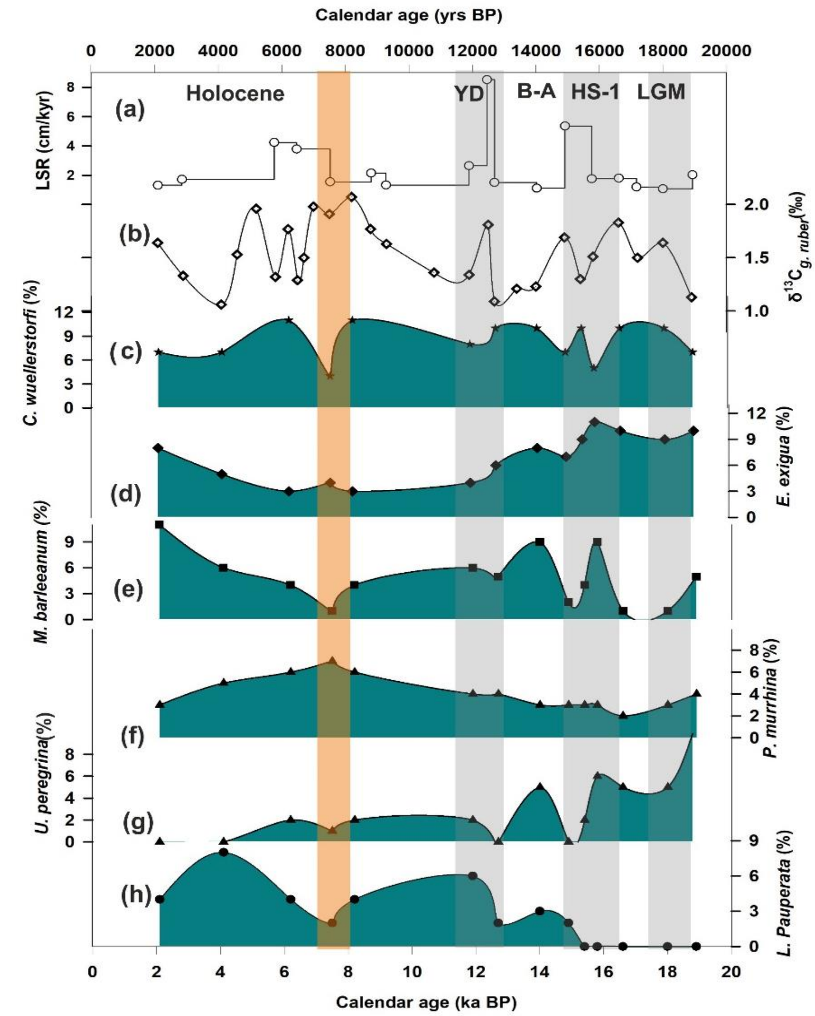

Figure 3.6: Downcore variation in seasonality parameters: (a) Linear sedimentation rate (LSR), (b) $\delta^{13}C$ of Globigerinoides ruber and (c), (d), (e), (f) and (g) are relative abundance of phytodetrital sensitive benthic foraminifera species, C. wuellerstorfi, E. exigua, M. barleeanum, P. murrhine, U. peregrina and L. pauperata. respectively.

during the early to the mid-Holocene. *M. barleeanum* varied similarly as *E. exigua* for the last 14 kyrs. It was very low during the Glaciation-interglaciation termination (16-18 ka), in contrast to *E. exigua*, suggesting unavailability of refractory organic matter during that time (Gupta, 1999). *P. murrhina* varied inversely to *E. exigua*, in general, having minimum density among other seasonality sensitive species with its abundance at a minimum during HS-1. *U. peregrina* also showed increased abundance during the LGM and HS-1 similar to *E. exigua*, indicating increased seasonality of food supply. Considering that *E. exigua* is well studied for sensitivity to episodic organic flux (Gupta & Srinivasan, 1992; Smart et al., 1994; Raj et al., 2009), it is inferred that phytodetrital input was enhanced during ~14-18.9 ka as well as during the late Holocene. Enhanced seasonality was also observed in the Southern Indian Ocean, during the same time interval by Smart et al. (2010). Considering *E. exigua* as the base indicator of seasonality, it could be inferred that *M. barleeanum* and *U. peregrina* abundance in some way are positively related to seasonality, whereas *P. murrhina* abundance varied opposite to the seasonality trend. Additionally, the abundance trends of *C. wuellerstorfi* and *L. pauperata* do not seem to be related to seasonality in the CIO basin.

Similar to the species of the dissolved oxygen sensitive group (Figure 3.4) and productivity sensitive species (Figure 3.5), the phytodetrital sensitive species also showed a peak at 7.5 ka (Figure 3.6). While *P. murrhina* showed maximum at that time, *E. exigua* had a minor local maximum at that time, corroborating the minimum value of other species in the seasonality sensitive group. The interval 7.5 ka also had enriched $\delta^{13}C$ value of *G. ruber*, which suggests enhanced overhead productivity (Penaud et al., 2010; Devendra et al., 2019) as well as a minor and sudden increase in the linear sedimentation rate.

3.7 Paleo Environment of the Central Equatorial Indian Ocean for the last 18.9 ka BP

Deep sea ecosystem had been quite different during the glciation in the central basin of the EIO. Inferences based on the benthic foraminiferal assemblage, stable carbon isotopic records, and productivity parameters suggest remarkable variability in the deep water environment for the last 18.9 kyrs. During the late LGM, the relatively higher abundance of *Uvigerina* spp. along with high OC suggests increased export productivity. The deep waters were poorly oxygenated, as suggested by the comparatively low abundance of all the high dissolved oxygen requiring taxa, except *Cibicidoides* spp. However, $CaCO_3$ variability does not suggest increased overhead productivity during the LGM (Figure 3.3). Hence, the high export productivity in the CEIO during the LGM was due to the high preservation of the sediment, supported by poorly oxygenated bottom water, as is also evident in the depleted $\delta^{13}C$ value of *C. wuellerstorfi* (Figure 3.4). The increased productivity in the EIO during the LGM has also been observed by Punyu et al. (2014) and Devendra et al. (2019).

HS-1 showed low benthic $\delta^{13}C$ value and a maxima of two dominant and important species, *U. proboscidea* (Figure 3.5), which can survive in variable oxygenation conditions (Lutze & Coulbourn, 1984) and *E. exigua*, an opportunistic species (Loubere, 1998). The sustained low abundance of high dissolved oxygen sensitive species suggests poor ventilation. Despite a good preservation environment led by poor ventilation, the food supply to the bottom was minimal, which further suggests low overhead productivity as well as poor bottom water ventilation, supporting the dominance of opportunistic species such as *E. exigua* as well as *U. proboscidea* surviving in variable oxygen. The poor ventilation in the Central Indian Ocean basin during HS-1 was also found in the ventilation age reconstruction of the Indian Ocean by Bharti et al. (2022). Poor ventilation probably resulted from the decreased formation of NADW (Adkins et al., 1998; Sarnthein et al., 2003; Sikes et al., 2016). Furthermore, low BFAR, as well as low foraminiferal density during HS-1, suggest stressed conditions for the benthic fauna.

The B-A warming period coincided with the lowest BFAR, low planktic $\delta^{13}C$ value, low sedimentation rate, minimal OC as well as $CaCO_3$, accompanied with decreased abundance of *Uvigerina* spp. This suggests low overhead productivity and a stressed condition during the B-A warming period. Low benthic $\delta^{13}C$ value and slightly increased abundance of dissolved oxygen sensitive species compared to the LGM suggests moderate deep water oxygenation compared to the LGM and HS-1.

The YD was the period of the highest sedimentation rate, increased calcareous production with low export productivity, and low benthic foraminifera density. *Uvigerina* spp. were also less abundant, while the abundance of dissolved oxygen sensitive species was moderate. This suggests a moderate oxygenation environment during the YD.

The infaunal density in the CEIO during the Holocene remained always low compared to the LGM and HS-1. The early period of the Holocene witnessed low BFAR, low foraminiferal density, increased benthic $\delta^{13}C$ value, increasing OC, high $CaCO_3$, increased planktic $\delta^{13}C$ value as well as moderate abundance of *Uvigerina* spp. This suggests moderate and increasing productivity towards the mid-Holocene. High abundance of dissolved oxygen sensitive species suggests a well oxygenated environment. The peak observed in all species during the mid-Holocene indicates a sudden change in the deep-water condition focused at 7.5 ka. The abundance of the dissolved oxygen sensitive species (i.e., *L. pauperata*, *Pyrgo* spp., and *O. umbonatus*) was high at 7.5 ka except for *G. subglobosa* and *L. pauperata*, which show opportunistic behavior in the Indian Ocean (Gooday, 1994; Gupta & Thomas, 1999; Jorissen et al., 2007). This suggests a well oxygenation condition of the deep CEIO at 7.5 ka along with moderate productivity.

The late Holocene was led by increased calcareous as well as organic productivity with slightly increased BFAR and foraminiferal density. This suggests increased export productivity as well as overhead productivity during the late Holocene. On the contrary, a negligible abundance of *Uvigerina* spp. at that time suggest low food supply. While sedimentation rate was low during this time, it is indicative of a low burial rate. The abundance of dissolved oxygen sensitive species was moderate to high during the late Holocene along with enriched $\delta^{13}C$ value, suggesting well oxygenated deep water in the CEIO.

3.8 Conclusion

This study based on foraminiferal assemblage, stable isotopic composition, and geochemical parameters attests to the widely accepted consensus that the assemblage of benthic foraminifera is governed by bottom water oxygenation as well as productivity. The negligible abundance of *Uvigerina* spp. during Holocene despite moderate food supply, suggests the possibility of its sensitivity to the upper limit of dissolved oxygen and/or interspecies competence. The present study also confirms poor ventilation of bottom water in the CEIO during LGM as well as HS-1. Earlier studies in the deep CIO basin e.g., trace element study in the sediment by Chandana et al., (2017) along with stable carbon isotopic record of the benthic foraminifera (Ahmad et al., 2008; 2012) and benthic foraminifera assemblage study from the deep Indian Ocean basin (Murgese and De Deckker, 2007) also suggested poorly ventilated glacial deep Indian Ocean. However, this study contradicts the hypothesis of increased overhead productivity in the CEIO during LGM by Piotrowski et al., (2009) and Punyu et al., (2014) and suggests increased export productivity caused by better preservation of OC and indicates less likelihood of increased overhead productivity.

Chapter 4.

Late Quaternary Ventilation of the Central Indian Ocean basin

4.1 Introduction

The deep ocean circulation, as a means of transporting nutrients, heat, carbon, and oxygen, acts as a physical, chemical and biological regulator for the ocean and helps to govern the global climate. Variations in the deep ocean circulation during the last glacial and deglacial periods have been traced in the stable and radioactive carbon isotopic composition of benthic foraminifera (e.g. (Chen et al., 2015; de la Fuente et al., 2015; Duplessy et al., 1980; Gottschalk et al., 2020; Okazaki et al., 2010; Peterson and Lisiecki, 2018; Robinson, 2005; Sikes et al., 2016; Skinner et al., 2021, 2010). Several studies have attributed a considerable proportion of the ~90 ppm decrease in atmospheric CO_2 during the last glacial period, compared to the pre-industrial period (Monnin et al., 2001), to changes in the efficiency of the biological pump (e.g. (Sigman et al., 2010)). The efficiency of the biological pump is influenced by changes in ocean 'ventilation' (which here denotes the effects of both ocean overturning rates, and air-sea gas exchange efficiency), via its influence on the relative magnitudes of the equilibrium, disequilibrium, and respired carbon inventories of the ocean (Eggleston and Galbraith, 2018). Thus, investigation of past ocean ventilation has potential to provide insights into the causes of past atmospheric CO_2 and global climatic change.

Here we distinguish (radiocarbon) 'ventilation age' from 'transit time', or 'ideal age' (i.e., the time taken for a parcel of water to be transported from its source region at the ocean surface to its current location in the deep ocean). This is because tracers such as radiocarbon are also influenced by spatially and temporally variable air-sea gas/isotope exchange rates, such that the radiocarbon ventilation age at a given deep ocean location is influenced by the relative contribution from different surface ocean source regions, combined with the gas-exchange efficiency in each source region, and the transit times from each source region. Past radiocarbon ventilation ages have mainly been estimated using three metrics: (1) benthic versus planktonic (B-P) age offsets (Broecker et al., 1984); (2) benthic/bottom-water versus atmosphere Benthic-Atmosphere (B-Atm) age offsets (Soulet et al., 2016); and (3) projection ages (Adkins & Boyle, 1997). Each of these metrics has its advantages and limitations (Adkins & Boyle, 1997; DeVries & Primeau, 2010; Skinner & Shackleton, 2004), for example with respect to the need for accurate estimates of calendar age, source-region contributions, source-region 'preformed age' (i.e. reservoir age), or local surface reservoir age. While, the majority of available radiocarbon evidence from the global ocean shows increased B-Atm age offsets during the Last Glacial Maximum (Skinner et al., 2017) (LGM), a great deal of spatial heterogeneity has been observed, and many regions of the ocean remain distinctly under-studied. One of the most significant gaps in data coverage is in the Indian basin (Skinner et al., 2017).

The Indian Ocean is landlocked in the north and does not have any local source of deep-water formation, and hence is an ideal location to study changes in the deep-water ventilation induced by the ocean-atmosphere gas exchange and transport changes originating in the North Atlantic (N. Atlantic), the Southern Ocean, or the North Pacific. Additionally, the Indian Ocean facilitates the upwelling limb of the global overturning circulation, which ultimately feeds warm and salty water to the regions of North Atlantic Deep Water (NADW) formation (Talley, 2013). The evolution of deep water circulation in the Indian Ocean since the last glacial period remains poorly understood, and only a handful of continuous radiocarbon ventilation age time-series from the deep Indian Ocean are available at present (e.g. (Gottschalk et al., 2020; Ronge et al., 2020). Here we present radiocarbon records of monospecific planktic and epifaunal benthic foraminifera from two sediment cores: SS-152/3828 (3166 m, 3.89° N, 78.06° E) and SS-172/4040 (2788 m, 6.03° N, 89.94° E 3.89° N, 78.06° E), collected from the Central Equatorial Indian Ocean (CEIO) and the Southern Bay of Bengal (SBoB) respectively. Both core locations are far from deep water formation regions and hence they are suitable to study the large-scale integrated effects of past deep ocean ventilation changes (Primeau, 2005). Existing stable carbon and oxygen isotopic ratios of *Cibicidoides wuellerstorfi* from Piotrowski et al., (2009) have also been used as auxiliary proxies to understand the changes in the contributing water masses. Since the dissolved oxygen concentration of deep waters is mainly dependent on the accumulation of respired carbon with increased residence time in the ocean interior and is less sensitive to ocean-atmosphere gas exchange efficiency, relative abundances of dissolved oxygen sensitive benthic foraminifer species have been used tentatively to constrain the effects of water mass residence time.

Hence the present study tries to resolve the gap in understanding the role of the least explored Indian Ocean Deep basin in the deglacial carbon cycle and the deep ocean ventilation change. Our results, replicated at two separate sediment core sites in the deep Central Indian Ocean (CIO) Basin, demonstrate the hitherto under-appreciated role of the Indian Ocean in deglacial marine carbon cycling and glacial-interglacial atmospheric CO_2 change.

4.2 Hydrographic setting of the Central Equatorial Indian Ocean and the Southern Bay of Bengal

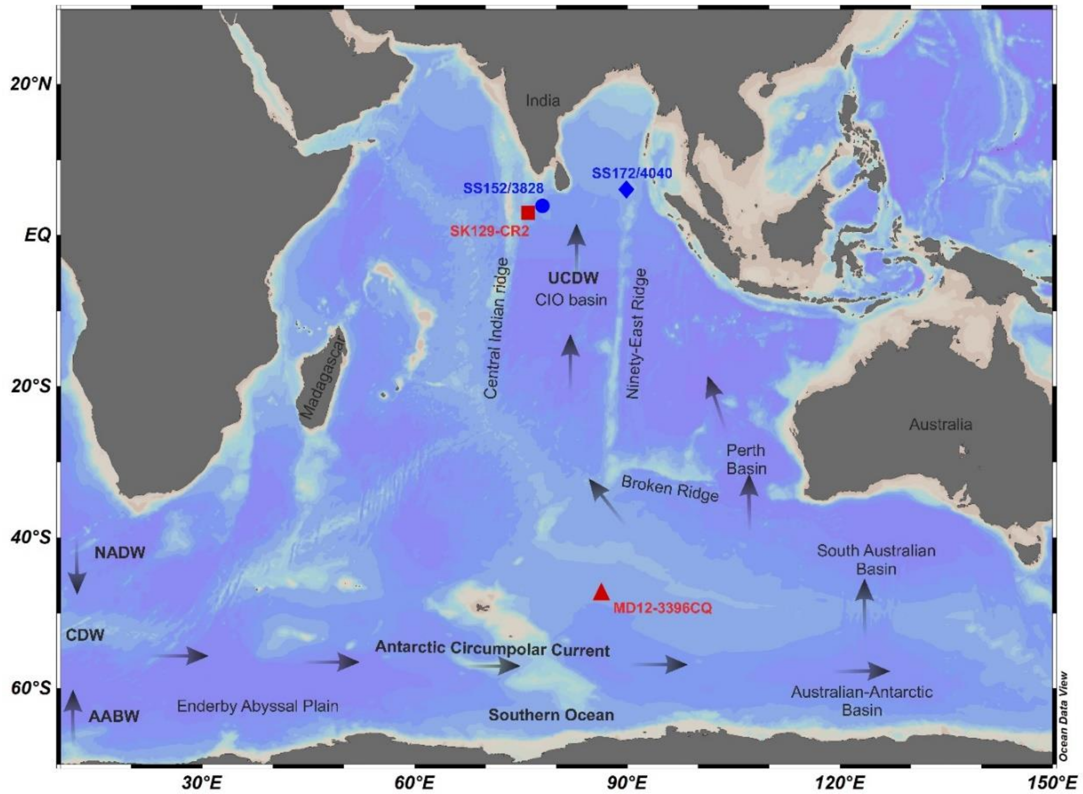

Figure 4.1: Sediment core locations and deep flow at the core locations: Sediment core SS152/3828 (core length-40 cm, water depth-3166m, 3.89° N, 78.06° E) is located in the CEIO and SS172/4040 (core length-130 cm, water depth-2788m, 6.03° N, 89.94° E) in the SBoB. Sediment core SK129–CR2 (water depth-3800 m, 3°N, 76°E; Piotrowski et al., 2009) is located in the CEIO and Core MD12-3396CQ (water depth-3,615 m, 47.43S; 86.41°E;Gottschalk et al., 2020) in the Southern Indian Ocean; Upper Circumpolar Deep Water ventilates the three cores in the CIO basin (Piotrowski et al., 2009) and Lower Circumpolar Deep Water ventilates the core in the Southern Indian Ocean (Gottschalk et al., 2020).

A sediment core from the southern boundary of Laccadive Sea (SS152/3828, core length-40 cm, water depth-3166m, 3.89° N, 78.06° E) and another from the ninety-east ridge of SBoB (SS172/4040, core length-130 cm, water depth-2788m, 6.03° N, 89.94° E), were collected (Figure 4.1) during the oceanographic cruise onboard *FORV Sagar Sampada* in 1997 and 1999 respectively. These gravity cores were collected using contamination-free PVC pipe, stored at low temperature and sub-sampled at 1-2 cm intervals. The core location SS152/3828 in the CEIO receives sediment from the overhead productivity which is mainly regulated by the Indian monsoon (Tomczak and Godfrey, 2003; Tiwari et al., 2006). Whereas, core SS172/4040 in the SBoB receives sediment both from overhead productivity and lithogenic sediment derived from the Himalayan, Tibetan, and Peninsular rivers (Banerjee et al., 2019). The ventilation of the deep water at both the core locations is predominantly by northward moving UCDW (Talley, 2013), which originates from the ACC region. UCDW can be observed in the depth range of ~2.0 -3.8 km (Piotrowski et al., 2009) at ~700-800 m above lysocline in the Indian Ocean (Kolla et al., 1976). The UCDW has a major contribution from saline NADW along with a minor contribution of relatively fresh Antarctic Bottom Water (AABW) (Talley, 2011). UCDW enters the CIO basin via the Southeast Indian Ridge in the South Australian basin and gaps of Broken Plateau via the DWBC (Talley, 2011). This is similar to the DWBC flowing in the WIO basin (Mantyla and Reid, 1995; Piotrowski et al., 2009)). While the effect of diapycnal mixing on UCDW in the deep Indian Ocean basin remains poorly understood or ambiguous, hydrographic data substantiate the increased diffusion of deep waters while moving northward with increased nutrient and decreased oxygen content (Wyrtki, 1973; Talley, 2013). Since tropical northern land limits of the Indian Ocean prevent the localized formation of deep water, the main source of deep water remains solely from the N. Atlantic and the Southern Ocean. Meanwhile, bottom topography also plays a significant role in constraining the deep circulation in the CIO basin below 2000 m (Talley, 2011).

4.3 Chronology and ^{14}C age of planktic and benthic foraminifera

Clean specimens of *G. ruber* from the 250-425 μm fraction and mixed epifaunal benthic foraminifera (>250 μm fraction) were picked under a stereo microscope. The benthic foraminifera from the core SS152/3828 was also counted for abundance study at 14 depths (see method in chapter 2.2). Picked specimens of *G. ruber* and benthic foraminifera, weighing 6 to 12 mg cleaned glass plates and cleaned following the method of (Barker et al., 2003) developed for Mg/Ca analysis. Cleaned foraminifera (4-10 mg) were graphitized using CHS coupled with AGE-3. Benthic and planktic foraminifera at each depth were graphitized in pairs, along with standards and blank. Graphitized samples were measured for radiocarbon at PRL AURiS using a compact 1 MeV Accelerator Mass Spectrometer (Bhushan et al., 2019a; Bhushan et al., 2019b) and results have been reported as conventional radiocarbon dates (Stuiver and Polach, 1977).

Radiocarbon ages of planktic and benthic foraminifera from core SS152/3828 and core SS172/4040 (Figure 4.2, Table 4.1) were normalized and corrected for isotopic fractionation, as per standard methods (Stuiver and Polach, 1977; Stuiver et al., 1998a). Radiocarbon ages of planktic foraminifera were further calibrated using the R package "Bchron" (Parnell et al., 2008) and MARINE20 Calibration curve (Heaton et al., 2020) using a reservoir age correction versus the global mean (ΔR) of -98± 22 yrs for the core SS152/3828 and -126± 70 yrs for the core SS172/4040 (Dutta et al., 2001; Southon et al., 2002). Sediment depth-age models, including uncertainties, were generated for the cores SS152/3828 (Table 3.1) and SS172/4040 (Table 4.1) using the R package Bchron, using the calibrated planktonic foraminifer radiocarbon ages. The sedimentation rate of the cores SS152/3828 and SS172/4040 varied between 1.1-8.5 $cm.ka^{-1}$ (average sedimentation rate - ~2.6 $cm.ka^{-1}$) and 0.9-6.7 cm ka^{-1} (~2.4 $cm.ka^{-1}$) respectively.

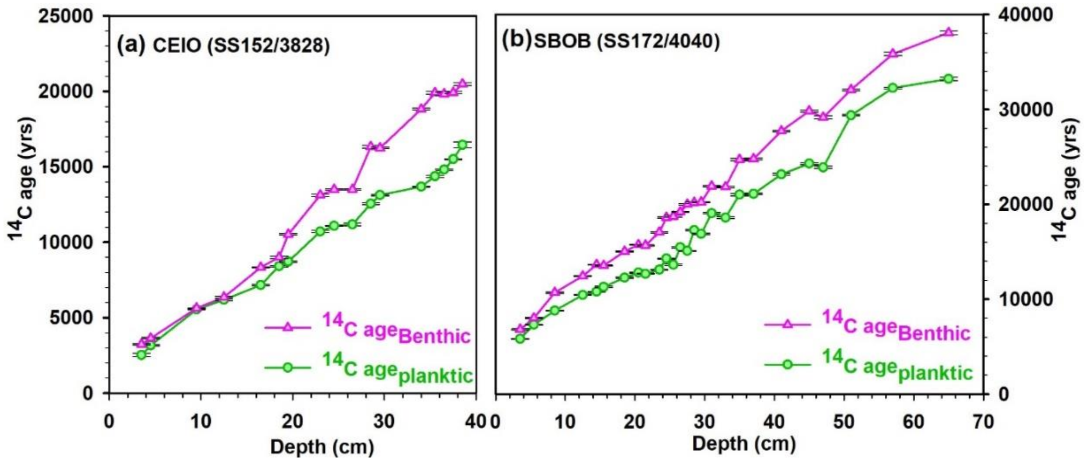

Figure 4.2: Measured Radiocarbon ages of paired benthic and planktic foraminifera in the CEIO (SS152/3828) and the SBoB (SS172/4040): ^{14}C age of Benthic foraminifera (Pink dots), ^{14}C age of planktic foraminifera (green dots), (a) radiocarbon results from the CEIO and (b) radiocarbon results from the SBoB. Vertical error bars represent 1-sigma uncertainty in ^{14}C age.

Table 4.1: Radiocarbon and calendar ages of planktic foraminifera from the Southern Bay of Bengal.

S. N	LAB ID	Sample ID	Depth (cm)	Libby age ±1σ error (yrs)	Calendar age ±1σ error (yrs. BP)
1	AURIS-01652	(SS4040/3-4/GR)	3-4	5823±40	6091±372
2	AURIS-02256	(SS4040/5-6.GR)	5-6	7317±59	7633±382
3	AURIS-02254	(SS4040/8-9GR)	8-9	8797±33	9347±369
4	AURIS-02252	(SS4040/12-13/GR)	12-13	10438±52	11474±269
5	AURIS-02250	(SS4040/14-15/GR)	14-15	10789±46	12093±167
6	AURIS-01650	(SS4040/15-16/GR)	15-16	11296±74	12667±200
7	AURIS-01647	(SS4040/18-19/GR)	18-19	12271±61	13642±177

8	AURIS-02247	(SS4040/20-21/GR)	20-21	12804±65	14174±127
9	AURIS-02245	(SS4040/21-22/GR)	21-22	12672±48	14370±139
10	AURIS-01646	(SS4040/23-24/GR)	23-24	13110±51	14985±252
11	AURIS-02228	(SS4040/24-25/GR)	24-25	14283±57	15946±437
12	AURIS-02226	(SS4040/25-26/GR)	25-26	13628±59	16680±548
13	AURIS-01644	(SS4040/26-27/GR)	26-27	15469±66	17724±542
14	AURIS-02224	(SS4040/27-28/GR)	27-28	15093±57	18290±541
15	AURIS-02221	(SS4040/28-29/GR)	28-29	17263±75	19139±497
16	AURIS-01631	(SS4040/29-30/GR)	29-30	16890±67	19658±401
17	AURIS-01629	(SS4040/30-32/GR)	30-32	19050±78	20849±426
18	AURIS-02199	(SS4040/32-34/GR)	32-34	18587±80	21745±412
19	AURIS-00875	(SS4040/34-36/GR)	34-36	21020±135	24039±359
20	AURIS-01627	(SS4040/36-38/GR)	36-38	21088±76	24465±230
21	AURIS-02197	(SS4040/40-42/GR)	40-42	23147±87	26517±286
22	AURIS-01625	(SS4040/44-46/GR)	44-46	24289±87	27599±290
23	AURIS-02194	(SS4040/46-48/GR)	46-48	23883±120	28849±909
24	AURIS-02192	(SS4040/50-52/GR)	50-52	29376±79	32962±592
25	AURIS-02190	(SS4040/56-58/GR)	56-58	32247±91	35867±295
26	AURIS-02188	(SS4040/64-66/GR)	64-66	33215±166	37062±299

4.4 Projection Age Estimation in the Central Equatorial Indian Ocean and the Southern Bay of Bengal.

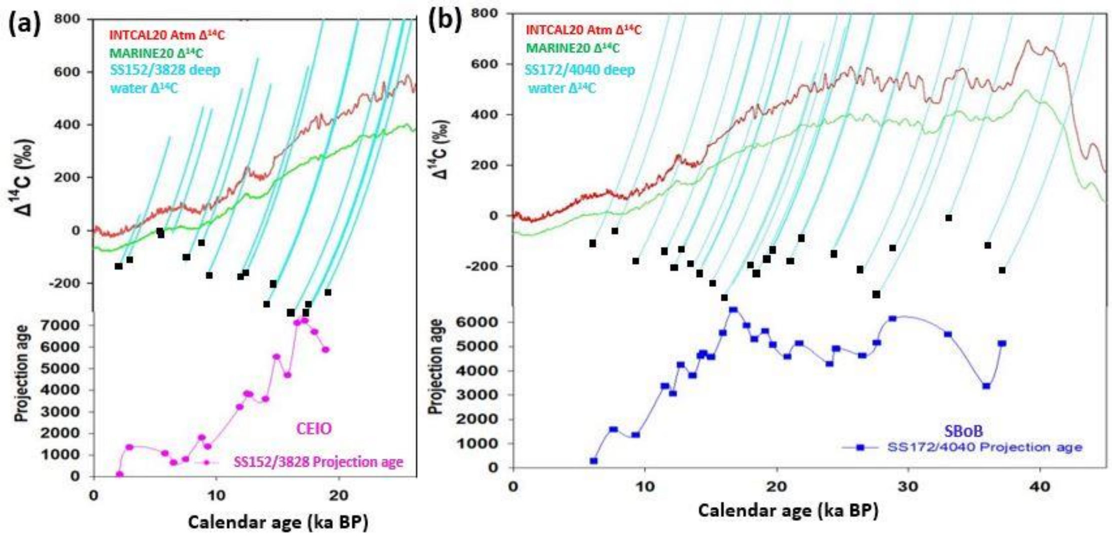

*Figure 4.3: Projection age estimates for the deep CEIO and the SBoB: In both (a) and (b) INTCAL20 atmospheric $\Delta^{14}C$ is in per mil (red curve), MARINE20 $\Delta^{14}C$ is in per mil (green curve), Benthic $\Delta^{14}C$ is in per mil (black square), radioactivity decay trajectory is cyan curve, calendar age is Bchron age of planktic foraminifera **(a)** projection age (in yrs) estimation in the core SS152/3828 (pink curve) **(b)** projection age (in yrs) estimation in the core SS172/4040 (blue curve)*

Projection ages for deep water in the CEIO (Figure 4.3a) and the SBoB (Figure 4.3b) were calculated using the method of Adkins and Boyle (1997). Initial $\Delta^{14}C$ of the deep water or benthic $\Delta^{14}C$ was corrected for decay back by following the radioactivity decay trajectory to intersect the INTCAL20 atmospheric $\Delta^{14}C$ (Reimer et al., 2020), or the MARINE20 $\Delta^{14}C$ curve (Heaton et al., 2020). However, both of these reference curves are imperfect, as the MARINE20 curve represents only tropical and subtropical water sources (Heaton et al., 2020), while the INTCAL20 curve doesn't consider ocean-atmosphere $\Delta^{14}C$ disequilibrium at all. While one might attempt to correct the INTCAL20 atmospheric $\Delta^{14}C$ for an assumed deep water source region $\Delta^{14}C$ offset (Lund et al., 2011b; Skinner and Shackleton, 2004), deep water in the study area is ventilated by at least two sources, and their contribution to the deep ocean likely changed over time (Böhm et al., 2015; Piotrowski et al., 2009; Rahmstorf, 2002). Therefore, to avoid making unwarranted assumptions regarding sourcing and source region disequilibrium, projection ages have been calculated as the difference between the calendar age corresponding to the INTCAL20 $\Delta^{14}C$ intersection point and the calendar age of the deep water $\Delta^{14}C$ (Benthic $\Delta^{14}C$). This approach unambiguously yields maximum and inherently over-estimated values for projection ages.

4.5 Result and Discussion

4.5.1 Estimates of paleo- radiocarbon ventilation ages in the Indian Ocean

The ventilation age of deep water has been estimated in several regions of the global ocean using contemporaneous benthic and planktonic ^{14}C ages. However, there are conflicts in the radiocarbon ventilation age estimates in many regions (de la Fuente et al., 2015; Gottschalk et al., 2020; Ronge et al., 2020; Umling and Thunell, 2017), primarily because of complexities in obtaining calendar age chronologies and estimating paleo-surface reservoir ages. In this context, it may be advantageous to compare different radiocarbon ventilation age metrics, each with its own advantages and drawbacks. Thus B-P age offsets do not require accurate knowledge of calendar age but neglect the possibility of variable surface reservoir ages, both at the core location and in deep-water source regions.

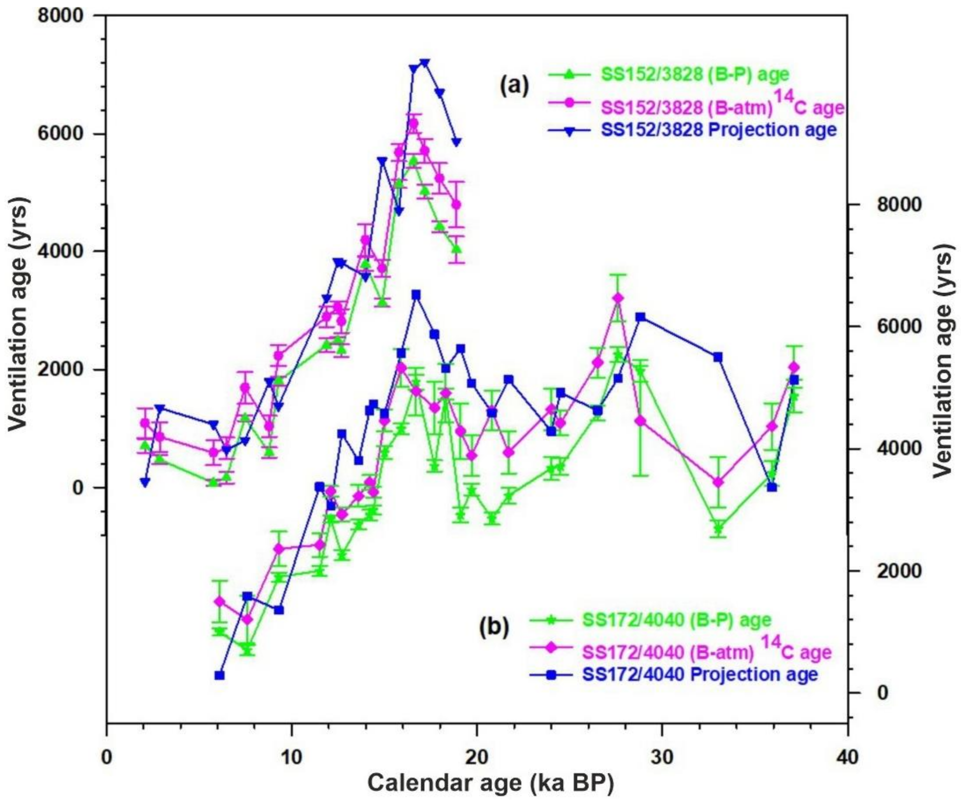

*Figure 4.4: Paleo-radiocarbon ventilation age estimates in the CEIO and the SBoB using different methods: (B-P) age (green curve), (B-Atm) age (pink curve), Projection age (blue curve). **(a)**ventilation age estimates in the CEIO, **(b)** Ventilation age estimates in the SBoB. Calendar age is Bchron age of Planktic foraminifera in ka BP. Vertical error bars represent combined uncertainties of ^{14}C ages.*

In contrast, B-Atm radiocarbon age offsets require accurate knowledge of calendar age, or local surface reservoir age offsets, but not necessarily both. They are also referenced to a single near-homogeneous reference (here the INTCAL20 curve; (Reimer et al., 2020)), unlike B-P. Finally, the 'projection age' method (Figure 4.4) requires both an independent calendar chronology for benthic foraminifer dates and knowledge of the $\Delta^{14}C$ of a presumed deep-water source. While this method takes into consideration the effect of changing atmospheric $\Delta^{14}C$ and is independent of the changes in the surface reservoir age at the core location (Adkins et al., 1998; Lund et al., 2011b), it comes with the significant drawback of requiring the assumption of a single known deep-water source region, with known $\Delta^{14}C$ (Skinner & Shackleton, 2004).

Here, all three radiocarbon ventilation metrics (B-P, B-Atm, and projection age) exhibit a similar trend for the last 37 ka (Figure 4.4). B-P age offsets varied between 78 and 5535 yrs in the CEIO, and between 706 and 5543 yrs in the SBoB. B-Atm age offsets varied between 591 and 6174 yrs in the CEIO, and between 1204 and

6468 yrs in the SBoB. Both B-P and B-Atm age offsets were lowest at ~5.8 ka BP and highest at ~16.6 ka BP (i.e., within HS1) in the CEIO, over the last 19 ka. Meanwhile, they were lowest ~7.6 ka BP and highest ~27.6 ka BP in the SBoB, over the last 37 ka. Projection ages varied between 641 and 7215 yrs (at 5.8 ka BP and 16.6 ka BP respectively) in the CEIO (Figure 4.4a), and between 1358 and 5888 yrs (at 7.6 ka BP and 15.9 ka BP respectively) in the SBoB (Figure 4.4b). As might be expected, B-Atm age offsets remained intermediate relative to the other two radiocarbon ventilation metrics (Figure 4.4). Differences between B-P and B-Atm age offsets remained low, likely due to minimal temporal changes in surface reservoir ages at the tropical core location. This is likely due to an absence of upwelling or deep mixing at either of the two studied locations of the CIO (Schott and McCreary, 2001) and the prevalence of pCO_2-effects alone on radiocarbon disequilibrium in the tropical surface ocean (Galbraith et al., 2015). Glacial B-Atm age offsets estimates in the EIO are significantly higher compared to the Northern and the Equatorial Pacific (de la Fuente et al., 2015; Galbraith et al., 2007; Lund et al., 2011a; Okazaki et al., 2010). This contrasts with the modern situation, where the (bomb-corrected) ^{14}C age difference between the surface and 3 km water depth in the CEIO as well as SBoB is low (~1200 yr) compared to the Eq. Pacific and the N. Pacific (~1400-2200 yrs) (Broecker et al., 2004; Key, 2004). This may suggest enhanced ventilation via the North or South Pacific during the last glaciation, though compiled radiocarbon data suggest that this was likely restricted to Heinrich Stadial 1 and the Younger Dryas (Okazaki et al., 2010; Skinner et al., 2013, 2019). Indeed, given that the CEIO and SBoB records also show glacial B-Atm age offsets significantly higher than observed in both the shallow and the deep Southern Ocean (Burke and Robinson, 2012; Gottschalk et al., 2020; Ronge et al., 2020; Skinner et al., 2010, 2019), it would appear that at least some part of the observed signal is attributable to a change in the hydrography and circulation of the deep Indian Ocean.

4.5.2 Relative abundance, stable carbon and oxygen isotope ratio of Benthic Foraminifera and Neodymium isotopic variation in the Central Indian Ocean Basin.

Along with the radiocarbon concentration, stable carbon and oxygen isotopic ratios of benthic foraminifera can provide valuable insight into the paleo-oceanographic condition of the region (Lund et al., 2011a; Peterson and Lisiecki, 2018). Global average seawater $\delta^{18}O$ value varies as a function of ice volume, with local deviations from the global average resulting from evaporation, precipitation and sea-ice formation at the sea surface, as well as water transports and mixing, that convey surface properties into the ocean interior. Due to temperature-dependent isotopic fractionation of foraminifer species calcifying in equilibrium with seawater, $\delta^{18}O$ value of calcite increases by 0.21-0.23‰ for a 1°C decrease in temperature (Shackleton, 1967). Due to the ice volume effect, the average $\delta^{18}O$ value of the global ocean was enhanced by ~1.1‰ during LGM as compared to today (Adkins et al., 2002). Moreover, in the modern ocean, deep water originating from the Southern Ocean has relatively low $\delta^{18}O$ (-0.3‰), and deep water originating from N. Atlantic has high $\delta^{18}O$ value (+0.3‰) (Adkins et al., 2002). Hence, $\delta^{18}O$ value of epifaunal benthic foraminifera can provide information about the changes in the contribution of deep water masses originating from the N. Atlantic and the Southern Ocean (Lund et al., 2011a; Skinner et al., 2003; Skinner & Shackleton, 2005), and changes in the temperature and ice volume (Ravelo and Hillaire-Marcel, 2007). Stable oxygen and carbon isotope of *C. wuellerstorfi* from a previously studied core (SK129-CR2) in the CIO Basin (Piotrowski et al., 2009) has been used here to assess changes in the contributing water masses (Figure 4.5b, 4.5c). In the CIO basin, $\delta^{18}O$ value varied between 2.6-4.5‰ and averaged to 3.0‰ during Holocene, 3.9‰ during younger Dryas, 4.2‰ at B-A warming (14.0 ka BP), 4.1‰ at HS-1 (15.6 ka BP), 4.2‰ during LGM and again 4.1‰ during HS-2. This suggests 1.1-1.2‰ increase in $\delta^{18}O$ value during HS-2, HS-1 as well as B-A warming, compare to Holocene, out of which, ~0.1‰ can be attributed to cooling of the deep water (Shackleton, 1967). However, the enriched $\delta^{18}O$ value during B-A warming equalling the LGM value suggests cold water, which can't be explained by intensified contribution from warm NADW alone, and could suggest the contribution of Southern sourced cold AABW, or a cooling of this water mass instead. This might be consistent with the inference of enhanced air-sea exchange of southern sourced deep water during the B-A, based on combined radiocarbon and Nd isotopes (Skinner et al., 2013). Alternatively, and perhaps more likely, it may reflect the delayed arrival of the deglacial melt signal in the deep, as yet poorly ventilated, CIO (Gebbie, 2012).

The $\delta^{13}C$ value in deep water is mainly controlled by deep water mixing and surface CO_2 exchange, with some contribution from gradual respired organic carbon accumulation in the ocean interior (Lynch-Stieglitz et al., 1995; Ravelo and Hillaire-

Marcel, 2007). Nutrient depleted NADW has characteristically enriched $\delta^{13}C$ value compared to AABW, and hence $\delta^{13}C$ value of epibenthic foraminifer can provide information about changes in the contribution of NADW & AABW, given minimal changes in global ocean nutrient utilization-regeneration balance (Ravelo and Hillaire-Marcel, 2007). The $\delta^{13}C$ value of *C. wuellerstrofi* ranged between -0.2‰ to 0.5‰ in the CEIO, for the last 40 kyrs. The Holocene average value was 0.3‰, whereas LGM and HS-1 average value was low (-0.1‰). It was also low during HS-1 (0.0‰). Overall depleted $\delta^{13}C$ values compared to the Holocene, can be observed throughout the last 15-40 ka (Figure 4.5b). Depletion of $\delta^{13}C$ value during LGM and HS-1 has also been reported from other studies from the Indian Ocean (Ahmad et al., 2012; Murgese and De Deckker, 2007), which corroborates with global $\delta^{13}C$ value depletion in the Pacific Ocean and the Atlantic Ocean (Duplessy et al., 1980; Peterson et al., 2014) and reduced contribution of NADW.

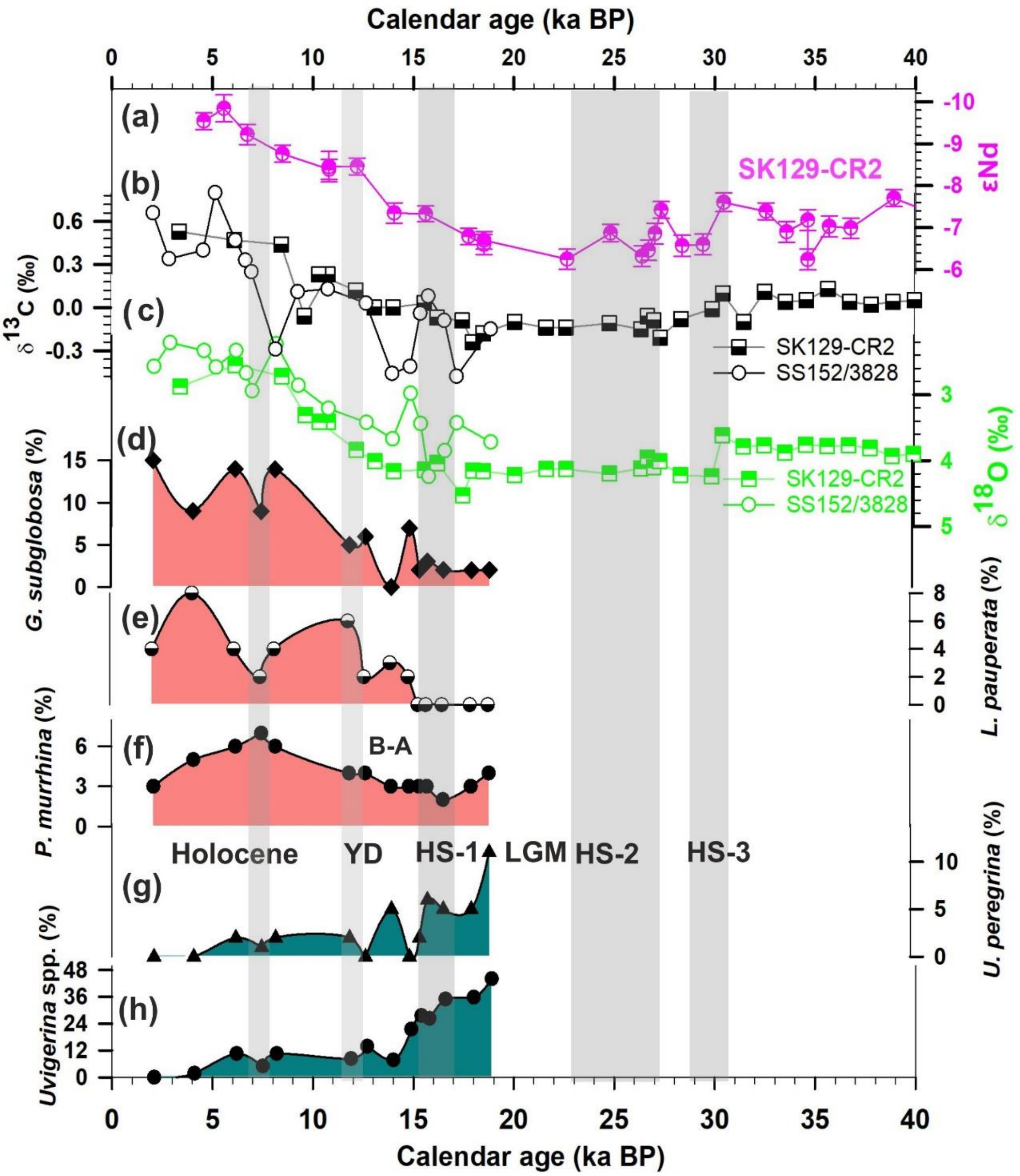

Figure 4.5: Neodymium isotope and benthic foraminifera stable isotopic ratios, compared with the relative abundances of dissolved oxygen sensitive species: ***(a)*** *εNd (pink curve; Piotrowski et al., 2009),* ***(b)*** *$\delta^{13}C$ of C. wuellerstorfi in the core SK129-CR2 (black curve; Piotrowski et al., 2009)* ***(c)*** *$\delta^{18}O$ value of C. wuellerstorfi in the core SK129-CR2 (green curve; Piotrowski et al., 2009),* ***(d), (e), (f), (g)*** *and* ***(h)*** *are relative abundances of G. subglobosa, L. pauperata, P. murrhina, U. peregrina and Uvigerina* spp. *respectively. Grey bars represent different climatic intervals.*

To observe the changes in the bottom water oxygenation, relative abundances (RA) of benthic foraminifera species have been used (Figure 4.5d, 4.5e, 4.5f, 4.5g, 4.5h), which is related to the rate of the thermohaline circulation but independent of the changes in the ocean-atmosphere equilibration of radiocarbon. The changes during the major climatic intervals of the past 19 ka BP, can be inferred with relative abundances of bottom water dissolved oxygen sensitive species. Significantly low RA of *G. subglobosa*, *L. pauperata* and *P. murrhina* (Figure 4.5d, 4.5e, 4.5f) was found during LGM as well as HS-1, compare to Holocene. Moreover, an enormously high RA of *Uvigerina* spp. and *U. peregrina* (Figure 4.5g, 4.5h) was found during LGM and HS-1. This indicates poor oxygenation of the bottom water during HS-1 as well as LGM (Chapter 3.6.2, Chapter 3.6.3), potentially associated with enhanced respired carbon accumulation due to a more sluggish deep ocean circulation. Neodymium isotopes represent another proxy for tracing changes in the contributing water masses (Rutberg et al., 2000; Piotrowski et al., 2009). The εNd of top sediment layer in the Fe–Mn leachate from SK129–CR2 representing the modern deep EIO bottom waters (Bertram and Elderfield, 1993) records the εNd of CEIO deep waters. It is notable that εNd in the CEIO was enriched during glaciation compared to the Holocene and follows a similar trend to the $\delta^{13}C$ record of SK129–CR2 (Figure 4.5a). Piotrowski et al (2009) argue for a minimal effect of terrestrially derived Nd at the core location, and therefore for εNd primarily capturing the signature of contributing water masses. Enriched εNd and depleted $\delta^{13}C$ value during glaciation (~17-40 ka BP) in SK129–CR2 has been attributed to the decreased N. Atlantic derived water mass contribution in the Indian Ocean. This is consistent with the combined stable isotope data, foraminiferal abundances, and radiocarbon age offsets.

4.5.3 Paleo- radiocarbon ventilation age estimates in the Indian Ocean and its linkage with atmospheric CO_2 and atmospheric $\Delta^{14}C$.

Various studies concur that glacial-interglacial changes in the atmospheric CO_2 (Figure 4.6b) were significantly influenced by changes in deep ocean circulation (Galbraith and Skinner, 2020; Sigman and Boyle, 2001), with the ocean being a sink of CO_2 during the LGM (Brovkin et al., 2007; Freeman et al., 2016; Menviel et al., 2017; Skinner et al., 2017) and a source of CO_2 to the atmosphere during deglaciation (Anderson et al., 2009; Burke and Robinson, 2012; Galbraith et al., 2007; Gray et al., 2018; Hain et al., 2014; Marchitto et al., 2007; Skinner et al., 2010). As marine origin CO_2 has depleted radiocarbon concentration compared to the atmosphere, it may have contributed to changes in the atmospheric $\Delta^{14}C$ across the deglaciation (Figure 4.6a), along with changes in the cosmogenic radiocarbon production rate (Marchitto et al., 2007; Muscheler et al., 2004). LGM atmospheric $\Delta^{14}C$ was almost >400‰ higher than the preindustrial value (Reimer et al., 2020), and only ~200‰ of this change can be explained by changes in radiocarbon production rates at most (Dinauer et al., 2020). Accordingly, a significant portion of the deglacial atmospheric $\Delta^{14}C$ change likely arose from carbon cycle change, including in particular a change in the marine radiocarbon inventory (Bard, 1998; Dinauer et al., 2020; Hain et al., 2014; Köhler et al., 2006). Model based studies have attributed ~20-37‰ to the glacial changes in the partial pressure of CO_2 (Bard, 1998; Galbraith et al., 2015), leaving anything from ~100 to over 400‰ attributable to other carbon cycle effects. A large volume of radiocarbon-depleted water in the deep CIO basin during the last glacial, evident from our reconstructed B-Atm age offsets, which reach up to ~6500 ^{14}C yrs (Figure 4.6f), likely contributed to increased atmospheric $\Delta^{14}C$ at the LGM, particularly if radiocarbon production rates also increased at the LGM (Köhler et al., 2006).

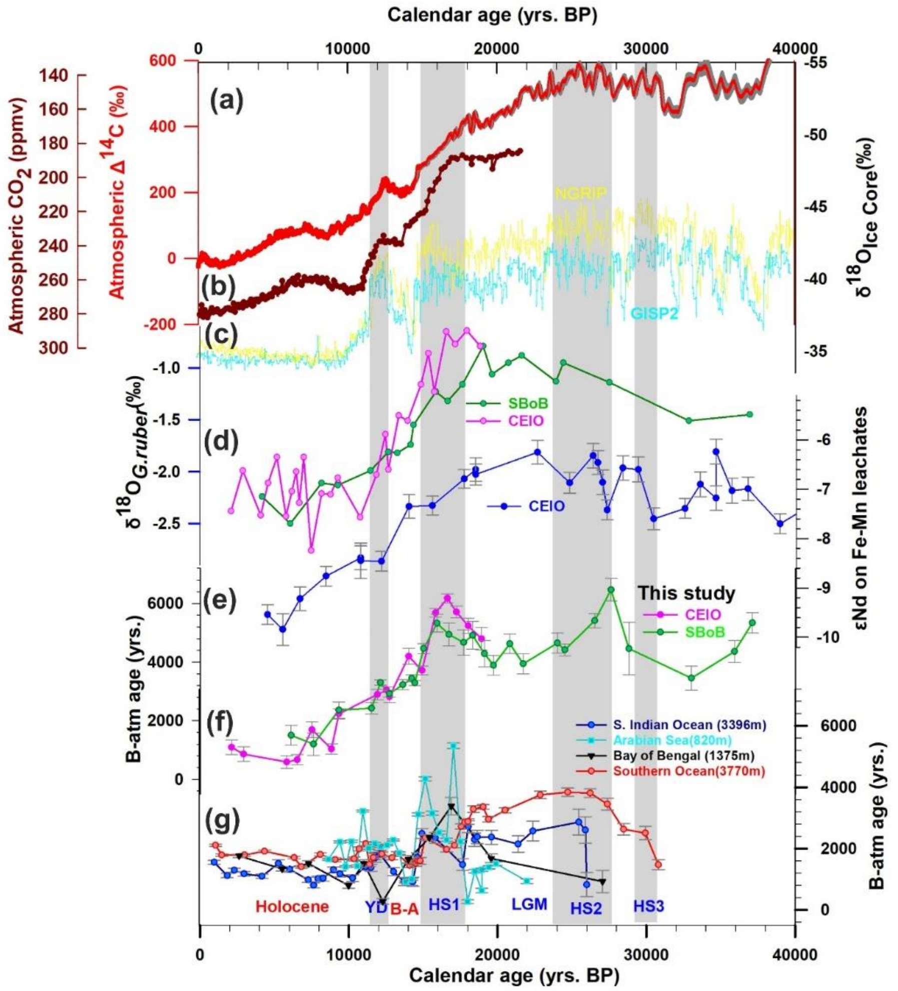

Figure 4.6: Paleo radiocarbon ventilation age estimates in the Indian Ocean & the Southern Ocean and its possible linkage with the atmospheric CO_2, atmospheric $\Delta^{14}C$, ε_{Nd} and $\delta^{18}O$ (colored): ***(a)*** *INTCAL20 atmospheric $\Delta^{14}C$ in per mil (red) with $\Delta^{14}C$ uncertainty in shaded grey (Reimer et al., 2020)* ***(b)*** *EPICA Dome C Ice core CO2 data in ppmv (Brown) (Monnin et al., 2004)****(c)*** *NGRIP ice core 50 yr mean $\delta^{18}O$*

record (yellow) and GISP2 ice core 50 yr mean $\delta^{18}O$ record (sky blue), placed on GICC05 timescale (Rasmussen et al., 2014; Seierstad et al., 2014). ***(d)*** *$\delta^{18}O$ of G. ruber in CEIO (pink circle) & $\delta^{18}O$ of G. ruber in SBoB (green square)* ***(e)*** *ε_{Nd} in CEIO (SK129-CR2; blue circle; (Piotrowski et al., 2009))* ***(f)*** *Paleo- radiocarbon ventilation age or B-Atm age in CEIO (Pink triangle; this study), SBoB (green square; this study)* ***(g)*** *Paleo- radiocarbon ventilation age or B-Atm age (water depth shown in the legend details) in the Southern Indian Ocean (Blue diamond;(Gottschalk et al., 2020)) Southern Ocean (Red circle; (Skinner et al., 2010)), Arabian Sea (Cyan circle; Bryan et al., 2010) and Bay of Bengal (black circle; (Ma et al., 2019)). Light grey bands represent the major climatic event for the last 40 ka, with events mentioned in the middle of the plot, red color represents the warm event and blue color represents the cold event. Calendar age in the x-axis is Bchron age of planktic foraminifera.*

In addition to the poor ventilation prevailing from 40 to 10 ka BP in the Indian Ocean, radiocarbon ventilation age peaked during HS-1 and HS-2, as evident from Figure 4.6f. This may be explained by the decreased production or complete shutdown of the NADW during these periods (Elliot et al., 2002; Gherardi et al., 2005; Henry et al., 2016; Howe et al., 2016). Weak AMOC during Heinrich events was potentially associated with, and reinforced by, the decreased transport of Agulhas salty water towards the N. Atlantic (Ma et al., 2021). Interestingly, B-Atm age peaked during HS-1 in the intermediate Arabian Sea (Bryan et al., 2010) and the intermediate Bay of Bengal (Ma et al., 2019) as well. This may reflect the upwelling of old carbon from the deep to the intermediate layer of the Indian Ocean, as suggested by Bryan et al., (2010). Conversely, strengthening of AMOC during the Bølling-Allerød (B-A) warming (McManus et al., 2004) is associated with a decrease in the radiocarbon ventilation age in the CIO Basin post HS-1. Notably, peak radiocarbon ventilation ages are not observed during HS-1 & HS-2 in the southern Indian Ocean and the Southern Ocean (Figure 4.6g), most likely due to the predominance of AABW sourced water, and therefore a lack of NADW influence, in the subpolar ocean (Rahmstorf, 2002). It is to be particularly noted that radiocarbon ventilation ages further decreased between the B-A and the late Holocene, in contrast to most other available radiocarbon ventilation records (Figure 4.6g) from the Atlantic Ocean (Chen et al., 2015; Robinson, 2005), the Southern Ocean (Burke & Robinson, 2012; Hines et al., 2015; Skinner et al., 2015; Skinner et al., 2010), the Pacific Ocean (de la Fuente et al., 2015; Galbraith et al., 2007; Lund et al., 2011a; Umling and Thunell, 2017; Zhao et al., 2018), southern Indian Ocean (Gottschalk et al., 2020; Ronge et al., 2020) and intermediate Indian Ocean as well (Bryan et al., 2010; Ma et al., 2019). Therefore, whereas previously it seemed that deep ocean radiocarbon ventilation hardly changed after the B-A, in stark contrast to atmospheric CO_2 for example, our new records indicate that this was not the case. The further tentative suggestion of minimum radiocarbon ventilation ages in both the CEIO and the SBoB (Figure 4.6f) during the mid-Holocene (being as low as 591 yrs in CEIO) might be explained by northern high latitude salinification leading to an intensified AMOC (Shi and Lohmann, 2016). Overall, the large amplitude of the radiocarbon ventilation age changes reconstructed from the CIO Basin, compared to compiled estimates from the global ocean (Zhao et al., 2018), likely arises from its geographical location and its complete dependency on distal subpolar ocean sources for deep water renewal and gas-exchange.

4.6 Conclusion

Our new radiocarbon data demonstrate coherent ventilation changes across the last deglaciation in the CEIO and the SBoB, which appear to have been ventilated by the same water mass for the last 37 ka. Multiple lines of proxy evidence suggest that the CIO Basin contributed significantly to low global ocean ventilation/oxygenation, and therefore also to atmospheric CO_2 sequestration, during the last glacial period. Positive millennial-scale radiocarbon ventilation age anomalies that broadly coincide with HS-1 and HS-2 suggest the influence of hydrographic/circulation changes originating in the N. Atlantic, in addition to the effects of gas-exchange and transports in the Southern Ocean. Of particular note is the observation of a large radiocarbon ventilation change, equivalent to >2500 ^{14}C yrs, that occurred subsequent to the B-A. The latter demonstrates that the deep ocean was not completely 'rejuvenated' half-way through the last deglaciation, as previously suggested by data from outside of the CIO. This further underlines the potentially crucial, and previously under-appreciated role of the deep Indian Ocean in deglacial radiocarbon and carbon cycle change.

Chapter 5.

Paleo Radiocarbon Ventilation Ages of Deep water in the South Western Indian Ocean Basin

5.1 Introduction

Deep water circulation in the Indian Ocean is divided along three basins of the Indian Ocean i.e., Western Indian Ocean (WIO) basin, Central Indian Ocean (CIO) basin, and Eastern Indian Ocean (EIO) basin. The deep water circulation in the CIO basin and EIO basin is mostly meridional due to less fractured topographic boundaries created by the Ninety East Ridge and the Central Indian Ridge, whereas the deep flow in the WIO is divided into several small basins due to numerous small and large ridges (Tomczak and Godfrey, 2003). Because of the presence of various ridges in the basin, difference in circulation pattern can be found which substantiates the need to study the evolution of deep water circulation in different basins of WIO. The Southwest Indian Ocean (SWIO) plays a major role in the thermohaline circulation by facilitating the formation of poleward moving Agulhas current and northward moving deep water formed in the Southern Ocean as well as diapycnal mixing of water masses. There are numerous present-day deep circulation studies in the SWIO, based on temperature, salinity profile, and volumetric transport (Pichon, 1960; Warren, 1971; Toole and Warren, 1993; Donohue and Toole, 2003; van Aken et al., 2004; MacKinnon et al., 2008), as well as trace element isotopic analysis (e.g., McCave et al., 2005; Thomas et al., 2006; Amakawa et al., 2019). These hydrographic studies have validated that deep circulation is divided into various basins due to numerous ridges and fracture zones in the SWIO i.e., Madagascar basin, Mascarene basin, Mozambique basin, and Crozet basin. The evolution of the overturning circulation during glacial and interglacial events remains sparsely studied in the SWIO (e.g., Curry et al., 1988; McCave et al., 2005), despite its significant role in the thermohaline circulation.

The majority of studies on coexisting planktic and benthic foraminifera suggest that the global ocean witnessed increased ventilation ages or poorly ventilated deep water during the Last Glacial Maximum (Skinner, 2017; LGM). However, a large spatial heterogeneity has been observed with some regions experiencing little change or even reduced radiocarbon ventilation age during LGM (Broecker et al., 2004b; 2008; Okazaki et al., 2010; Lund et al., 2011b). Few oceanic basins remained distinctly under-studied, which includes the Indian Ocean basin (Skinner et al., 2017) with only a few paleo-ventilation age records of the deep water (Ronge et al., 2016; 2020; Gottschalk et al., 2020). mainly in the Southern Ocean sector of the Indian Ocean, where surface and deep circulation is controlled mainly by the Southern Ocean. Moreover, there is no radiocarbon ventilation record from the Western Indian Ocean basin available so far. Thus, this study attempts to unravel the effect of decreased formation of NADW and/or AABW on the rate of deep water circulation in the WIO basin. Along with the paleo ventilation age record in the Central Indian Ocean basin, a comparative study of the paleo deep ocean circulation in different basins of the Indian Ocean would be attempted.

5.2 Surface and Deep Oceanographic setting

The core SK312/09 (Figure 5.1) lies in between the central part of the Mascarene Plateau (always shallower than 1000m) and the Central Indian Ridge, south to Vema Trench (Heezen and Nafe, 1964; Fisher et al., 1967). The mean surface current in this location is mainly dominated by westward-moving South Equatorial Current (SEC) along 15°S, which brings Indonesian Throughflow Water (ITW) towards the WIO basin (da Silva et al., 2011). SEC bifurcates at eastern Madagascar into East Madagascar current and Mozambique current, which finally feeds one of the fast moving ocean current i.e., Agulhas current (Tomczak and Godfrey, 2003; McCave et al., 2005). The upper ocean water in the southwest Indian Ocean mainly comprises upwelled deep water within the Indian Ocean and the Pacific Ocean as well as subducted water from the southeastern Pacific and southeastern Indian Ocean (Talley, 2013).

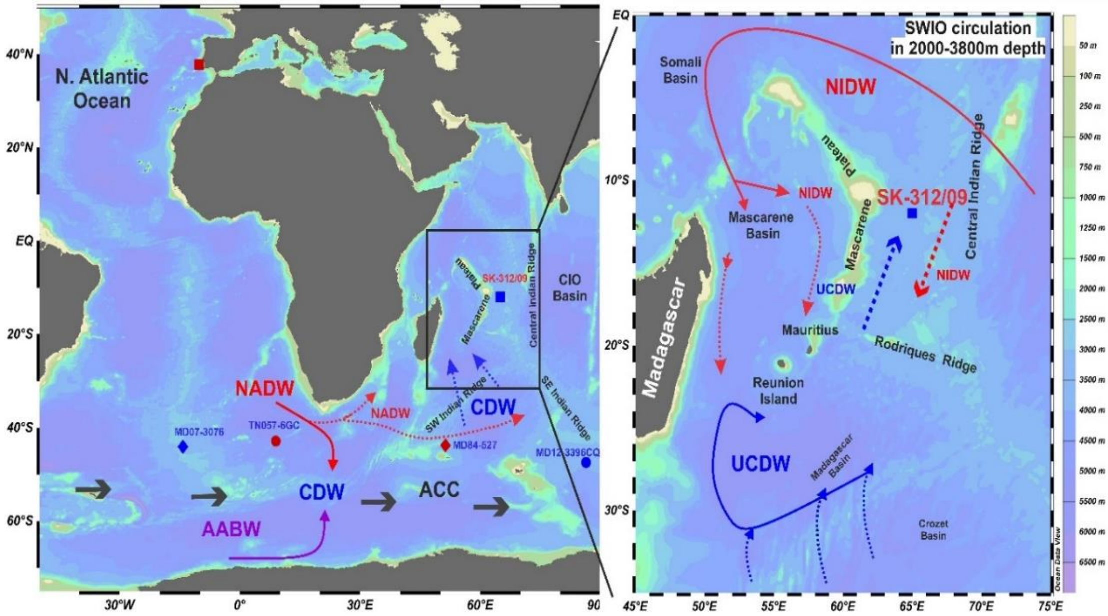

Figure 5.1: Study area: Schematic of deep flow in the Southwest Indian Ocean (SWIO) basin (modified from (Amakawa et al., 2019)) and sediment core location discussed in the study. Core SK312/09 (11.99°S, 64.99° E, water depth-3449m, core length-565; this study) and MD84-527 (43.82°S, 51.32° E, water depth-3262m; (Curry et al., 1988)) lies in the SWIO. The core MD07-3076 (44.15°S, -14.15° E, water depth-3770m; (Skinner et al., 2010)) and TN057-6GC (42.89°S, 8.96° E, water depth-3750m; (Gottschalk et al., 2016)) lies in the Southern Atlantic Ocean. The core MD12-3396Q (47.43S; 86.41°E; water depth-3,615 m; (Gottschalk et al., 2020)) lies in the Southern Indian Ocean.

Deepwater in the Southwest Indian Ocean is mainly sourced from the AABW, which flows to the study area via the Madagascar basin (Figure 5.1). Deepwater in the western side of the Madagascar basin comes by crossing various fracture zones (with deepest sill depth of 3900m) of Southwest Indian Ridge, however, the water current in the eastern side of the Madagascar basin is mainly characterised by low nutrient and high oxygen CDW coming from the Crozet basin (Toole and Warren, 1993; Donohue and Toole, 2003). From the Madagascar basin, the deep water flows as Northward deep western boundary current, towards the Mascarene basin, and finally reaches the Somali basin via Amirante Passage (Donohue and Toole, 2003; MacKinnon et al., 2008). The deep water in the WIO has been referred as northward moving IDW, a mixture of CDW and N. Atlantic derived NADW and characterized by high salinity (Tomczak and Godfrey, 2003; Lee et al., 2015; Amakawa et al., 2019), southward moving North Indian Deep Water (NIDW), which is chemically similar to CDW but contains high nutrient (You, 2000); Mantyla and Reid, 1995; Johnson et al., 1998; McCave et al., 2005; Wilson et al., 2012), as well as CDW (Pahnke et al., (2008). The recirculation takes place in the SWIO between 12°S-18°S due to the mixing of UCDW with low oxygen water originating from the Southeast Pacific and NIDW (McCave et al., 2005). LCDW flows below 4000 m in the SWIO, though there is partial flow of LCDW in the Madagascar and Mascarene basin via some fractures lying above 3900 m along the South West Indian Ridge (Amakawa et al., 2019). The major understanding towards this deep water ventilation in the SWIO is that the water which ventilates the study area is a modified CDW. However, there are uncertainties regarding the characterization and flow direction of the deep water, especially in the northern part of the SWIO. The alternating source of deep water during stadials (Skinner et al., 2014) adds further complexity in reconstructing paleo-deep water circulation.

The studied core lies in the proximity to mantle derived eruptions due to the occurrence of Reunion and Rodrigues Hotspot in the south (Morgan, 1978) and active spreading zone i.e. Central Indian ridge in the east (Mahoney et al., 1989). On the way to Mascarene basin and Somali basin, deep water flow crosses through various volcanic hotspots such as hotspot on South Western Indian ridge (Tao et al., 2012), Rodrigues triple junction (Gamo et al., 2001), and the Central Indian ridge as well as Reunion Hotspot (Morgan, 1978). These hotspots can contribute dead CO_2 and CH_4 to the bottom water, further depleting the radiocarbon concentration of the bottom water (Ishibashi et al., 2015). Moreover in the SWIO, the deep-sea hydrothermal vent and volcanic activity possibly have played an important role in affecting the deep-sea paleo-ventilation age reconstruction (e.g., Ronge et al., 2020, 2016). Additonally, the deep water pathways in the Indian Ocean, particularly in the SWIO basin are constrained by bottom topography due to the presence of various ridges and fracture zones (Mantyla and Reid, 1995). Various faults on the Rodrigues ridge and uneven ocean floor can lead to mixing of the deep water masses while flowing from the Madagascar basin (if it is northward moving CDW) to the study area (Mantyla and Reid, 1995). However, due to the lack of sediment core analysis in the region between the Mascarene Plateau and the Central Indian Ridge, the effect of mantle activity, bathymetry and vertical mixing on the deep water in the study area remains elusive.

5.3 Radiocarbon Dating and Sedimentation Rates

The chronology of the core SK312/09 was established using AMS radiocarbon dating of *G. ruber* at 10 depths intervals (Table 5.1). The radiocarbon age of paired *G.*

ruber and mixed benthic foraminifera (Figure 5.2) at 10 depths were used for ventilation age reconstruction. Further, radiocarbon age of planktic foraminifera was calibrated using the INTCAL20 curve in CALIB 8.2 software. The SWIO core has average sedimentation

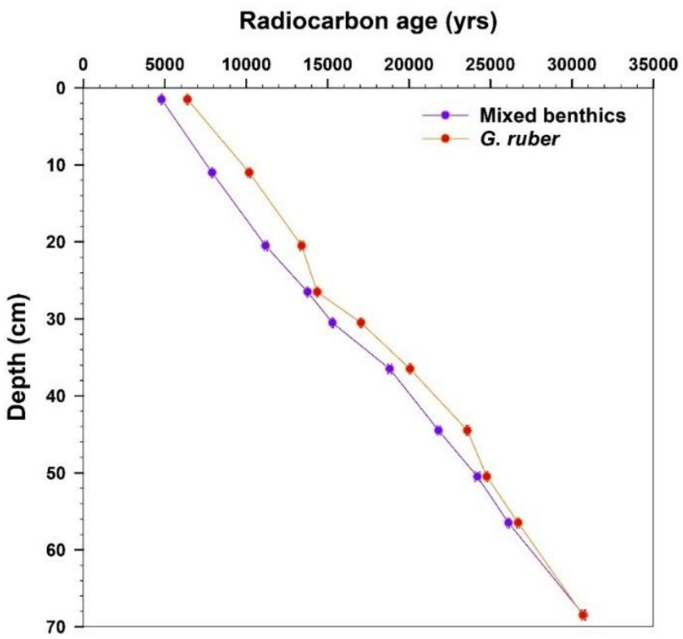

Figure 5.2: Radiocarbon age of paired planktic (purple color) and benthic (orange color) foraminifera from the South West Indian Ocean.

Table 5.1. Chronology of the core SK312/09.

LAB ID	Sample ID*	Depth (cm)	Libby age ±1σ error (yrs)	Calendar age ±1σ error (yrs. BP)
AURIS-03383	SK312-09/0-3/GR	1.5	4796±35	4853±120
AURIS-03381	SK312-09/10-12/GR	11	7899±36	8183±105
AURIS-00884	SK312/09/20-21/GR	20.5	11183±107	12553±141
AURIS-03376	SK312-09/26-27/GR	26.5	13764±40	15767±143
AURIS-03374	SK312-09/30-31/GR	30.5	15293±43	17687±164
AURIS-00883	SK312/09/36-37/GR	36.5	18812±109	21875±190
AURIS-03371	SK312-09/44-45/GR	44.5	21810±82	25183±166
AURIS-00882	SK 312/09/50-51/GR	50.5	24194±147	27501±160
AURIS-03368	SK312-09/56-57/GR	56.5	26104±74	29464±179
AURIS-03366	SK312-09/68-69/GR	68.5	30734±98	34351±125

- **GR: Globigerinoides ruber*

rate of 2.3 cm.kyr^{-1} for the last 35 kyrs ranging between 1.4 -3.1 cm.kyr^{1} (Figure 5.3), which is similar to the sedimentation rate estimates from the SWIO i.e. 1-4 cm.kyr^{-1} in Madagascar and Mascarene basin (McCave et al., 2005). Comparatively high sedimentation rate (2.9 cm.kyr^{-1}) observed during Mid to Late Holocene as well as during HS-2 (2.5-3.1 cm.kyr^{-1}) signifies either high productivity or better preservation of the sediment during these periods. However, early YD and late LGM witnessed a low sedimentation rate (1.9 cm.kyr^{-1} for 11.1-13.8 ka BP and 1.4 cm.kyr^{-1} for ~17.7-21.9 ka BP), indicating decreased export productivity or poor preservation of sediment. This is caused mainly due to well-oxygenated/well-ventilated deep environment or decreased overhead productivity.

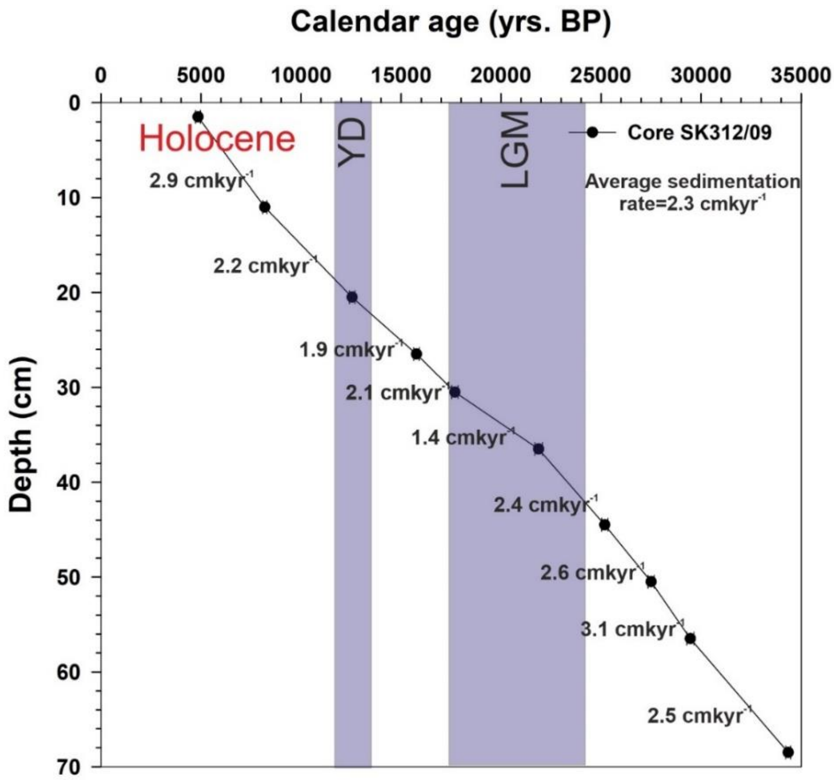

Figure 5.3: Age-depth model of the core SK312/09 from the Southwest Indian Ocean along with sedimentation rates based on radiocarbon-dated time intervals. Error in sedimentation rate ranged between 0.1-0.3 cm.kyr^{-}.

5.4 Projection Age Estimates in the SWIO Basin

Projection ages for the deep water in the SWIO were calculated using the method of Adkins and Boyle (1997) as shown in Figure 5.4. Initial $\Delta^{14}C$ of the deep water or benthic $\Delta^{14}C$ (Table C.17) was traced back by following the radioactivity decay trajectory to intersect the INTCAL20 atmospheric $\Delta^{14}C$ (Reimer et al., 2020).

However, the INTCAL20 curve doesn't consider ocean-atmosphere $\Delta^{14}C$ disequilibrium, and it can lead to over or underestimation of ventilation age. While, it is possible to correct the INTCAL20 atmospheric $\Delta^{14}C$ for an assumed deep water source region $\Delta^{14}C$ offset (Skinner and Shackleton, 2004a; Lund et al., 2011b), the deep water in the study area is ventilated by at least two sources i.e., NADW and CDW, and their contribution to the deep ocean probably changed over time (Rahmstorf, 2002; Tomczak and Godfrey, 2003; Piotrowski et al., 2009; Böhm et al., 2015). Thus, to avoid making

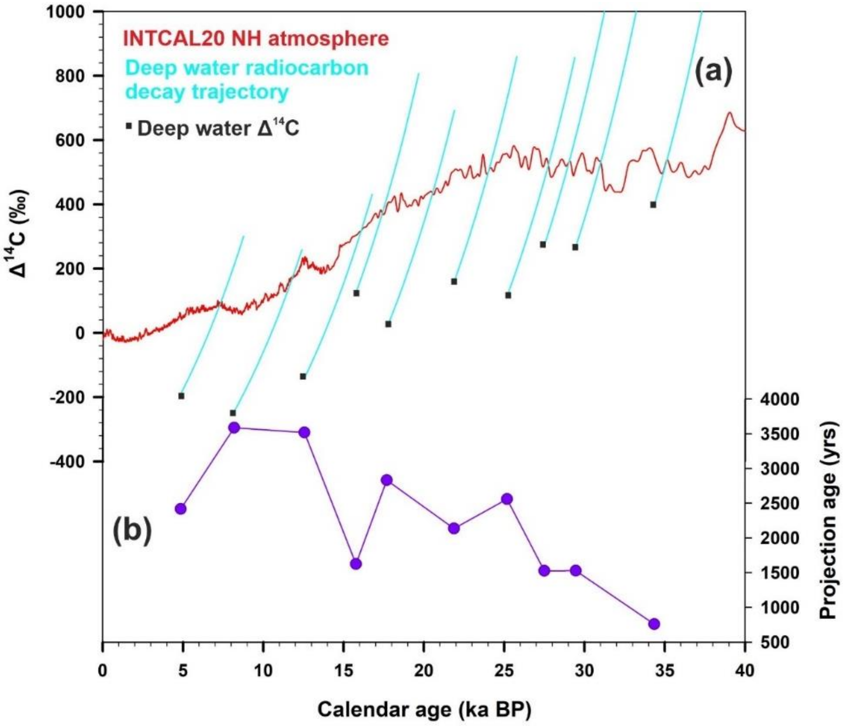

Figure 5.4: Projection age estimation of deep water in the South West Indian Ocean basin: (a) red curve is INTCAL20 NH atmospheric $\Delta^{14}C$, the cyan curve is radioactivity decay trajectory, black dots are initial deep water $\Delta^{14}C$ based on benthic radiocarbon age (b) Purple curve is projection age estimates.

unwarranted assumptions regarding sourcing and source region disequilibrium, projection ages have been calculated as the difference between the calendar age corresponding to the INTCAL20 $\Delta^{14}C$ intersection point and the calendar age of the deep water $\Delta^{14}C$ (Benthic $\Delta^{14}C$). This approach unambiguously yields maximum projection ages. Using this method, projection age in the SWIO ranged from 758 yrs at 34.3 ka BP to 3586 yrs at 8.2 ka BP for the last 35 kyrs. These estimates of projection ages are nearly a quarter of the glacial projection age estimates in the CIO basin (Figure 4.4) and also showed a contrasting evolution of ventilation age estimates.

5.5 Paleo Ventilation Age Estimates in the Southwest Indian Ocean Basin

The ventilation age estimates were calculated using three different methods i.e., (B-P) age offsets (Broecker et al., 1984); benthic/bottom-water versus atmosphere (B-Atm) age offsets (Soulet et al., 2016); and projection age method (Adkins & Boyle, 1997). The ventilation ages derived from these three different methods showed similar variation for the studied core. (Figure 5.5). B-P age offset remained lowest during the last 35 kyrs, while (B-Atm) radiocarbon age offsets were in between the other two ventilation age metrics, which was similar to the trend of ventilation age matrices in the CIO basin (Figure 4.4). B-P age offset varied between -64 yrs at 34.3 ka BP to 2285 yrs at 8.2 ka BP; (B-Atm) offset varied between 788 yrs at 34.3 ka BP to 2883 yrs at 12.5 ka BP, and projection age varied between 758 yrs to 3586 yrs. When compared to the earlier ventilation age estimates for the CIO basin (Figure 4.4), the Southern Ocean, and the Atlantic Ocean, (B-Atm) age offset in the SWIO was low and peaked during Holocene. However, the low resolution of the paleo-ventilation age reconstruction possibly led to obscured paleo-ventilation age evolution in the SWIO.

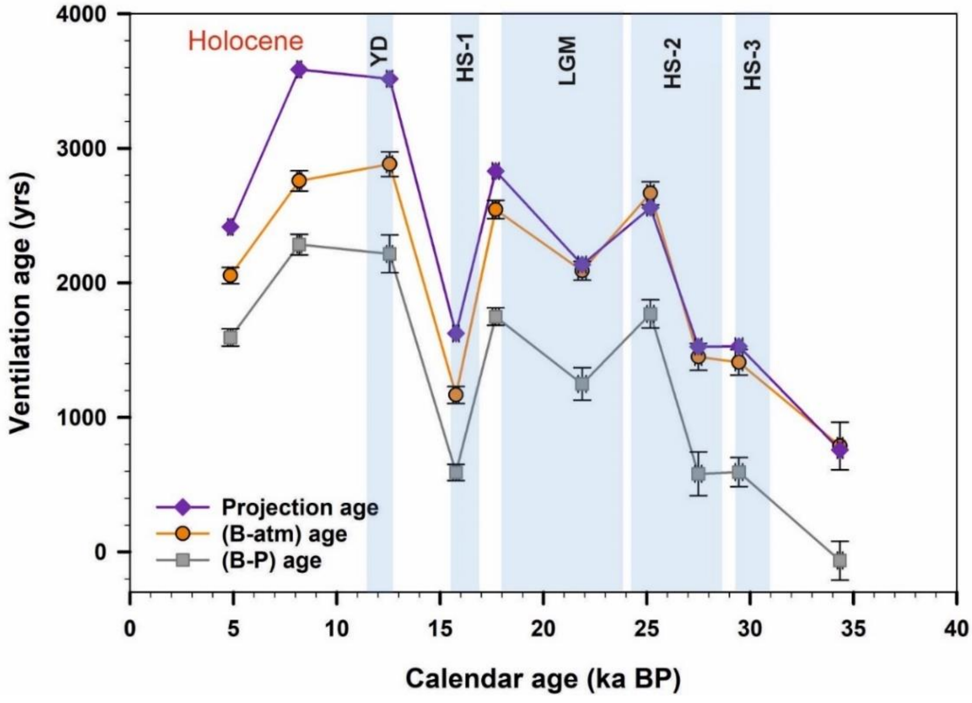

Figure 5.5: Paleo-ventilation age record in the South West Indian Ocean basin. Purple color marks the projection ages, orange color marks the radiocarbon ventilation age or (B-Atm) age and grey color mark the (B-P) age.

5.6 Global Comparison of Deepwater Circulation in the Southwest Indian Ocean for the Last 35 kyrs

The term ventilation age represents the time taken by the deep water mass to reach from the formation region to the core location i.e. transit time. The ventilation age reconstruction based on radiocarbon dating of foraminifera referred as "radiocarbon ventilation age" is also affected by radiocarbon disequilibria in the mixed layer and changes in the contribution of the water masses (Volk and Hoffert, 1985). Thus, both the factors, the radiocarbon disequilibria and change in the contribution of the water masses need to be understood using other paleo-oceanographic proxies. Towards this, the present studied core was compared with the stable isotopic composition of carbon and oxygen isotope of monospecific epibenthic foraminifera species from earlier studies (Figure 5.6; Curry et al., 1988; Skinner and Shackleton, 2004b; Gottschalk et al., 2016). Along with studies from earlier radiocarbon ventilation age reconstructions from the Southern part of the Atlantic (Skinner et al., 2010) and the southern boundary of the Indian Ocean was compared (Gottschalk et al., 2020).

In Figure 5.6a, it can be observed that glacial $\delta^{18}O$ value was ~1.3-1.6‰ higher than the Holocene $\delta^{18}O$ value in the southern sector of the Indian Ocean and the Atlantic Ocean. Subtracting the ice-volume effect, which led to 1.1‰ increase in the global $\delta^{18}O$ value (Adkins et al., 2002), ~0.2-0.4‰ increase signifies ~0.8-1.6°C cooling (Shackleton, 1967) of deep water during the glacial period, which further has implications to either colder CDW and/or increased or total contribution from the AABW during the glacial period (Skinner et al., 2014). Whereas, in the case of $\delta^{13}C$, the $\delta^{13}C$ value of N-E Atlantic was always higher compared to $\delta^{13}C$ value in the SWIO and the Southern Atlantic (S. Atlantic) Ocean owing to its ventilation from N. Atlantic derived NADW with enriched $\delta^{13}C$ value (Ravelo and Hillaire-Marcel, 2007). Consistently depleted glacial $\delta^{13}C$ value compared to the Holocene can be observed in the N-E Atlantic, SWIO, as well as S.Atlantic (Figure 5.6b). This probably confirms the reduced or curtailed formation of NADW during glaciation (Rutberg et al., 2000; Elliot et al., 2002; Gherardi et al., 2005; Henry et al., 2016; Howe et al., 2016). During HS-1, $\delta^{13}C$ value decreased further in the N-E Atlantic Ocean as well as S. Atlantic Ocean, indicating further decrease or shutdown of the NADW (Ravelo and Hillaire-

Marcel, 2007). However, $\delta^{13}C$ value in the SWIO doesn't vary in sync with N-E Atlantic and indicates additional control from the southern sourced water.

The most outstanding finding of the present study was the matching peak of (B-Atm) ^{14}C age offset, the $\delta^{13}C$ value of the N-E Atlantic and S. Atlantic during HS-2, LGM, HS-1 and YD (Figure 5.6). It suggests the control of N. Atlantic in the SWIO deep circulation, in a direct way (by ventilating the SWIO) or indirect way (by alternating the NADW or AABW source). The reduced NADW transport to the SWIO should have led to an increased (B-Atm) ^{14}C age offset, however, in contrast, SWIO shows significantly low (B-Atm) ^{14}C age offset during HS-3, early HS-2 as well as HS-1. This could be the result of complete reversal of deep water source during these events from the N. Atlantic to the Southern Ocean (Skinner et al., 2014), and/or the deep water formation region had been through an enhanced air-sea gas exchange in the Southern Ocean (Skinner et al., 2010; Galbraith and Skinner, 2020). The ^{14}C age offset (B-Atm) in the southern boundary of the Indian Ocean also varies, rather in a similar way as in the SWIO (Gottschalk et al., 2020) up to HS-1 since 35 ka BP. The significantly high S. Atlantic ^{14}C age offset (B-Atm) during HS-1 suggests its ventilation from the sluggish and aged CDW or AABW (Rahmstorf, 2002; Skinner et al., 2010). Whereas, the Holocene (B-Atm) ^{14}C age was low in the Southern Indian Ocean, as well as in the S. Atlantic Ocean. However, in the SWIO,

(B-Atm) ^{14}C age offset was high during the Holocene compared to glaciation, despite enhanced formation of the NADW at that time (McManus et al., 2004). This could have resulted due to (1) the increased contribution from aged deep water compared to glaciation, (2) input of mantle-derived CO_2 to the study area (Ronge et al., 2016; 2020) and, (3) decreased air-sea gas exchange in the Southern Ocean deep water formation region (Galbraith and Skinner, 2020). However, numerous paleo-ventilation age record from the Southern Ocean suggests strengthened overturning circulation during the Holocene when compared to last glaciation (Skinner et al., 2010; 2015; Burke and Robinson, 2012; Hines et al., 2015), and thus the first explanation seems unacceptable. The latter two explanations could be the plausible mechanism for the deep water ventilation of the SWIO.

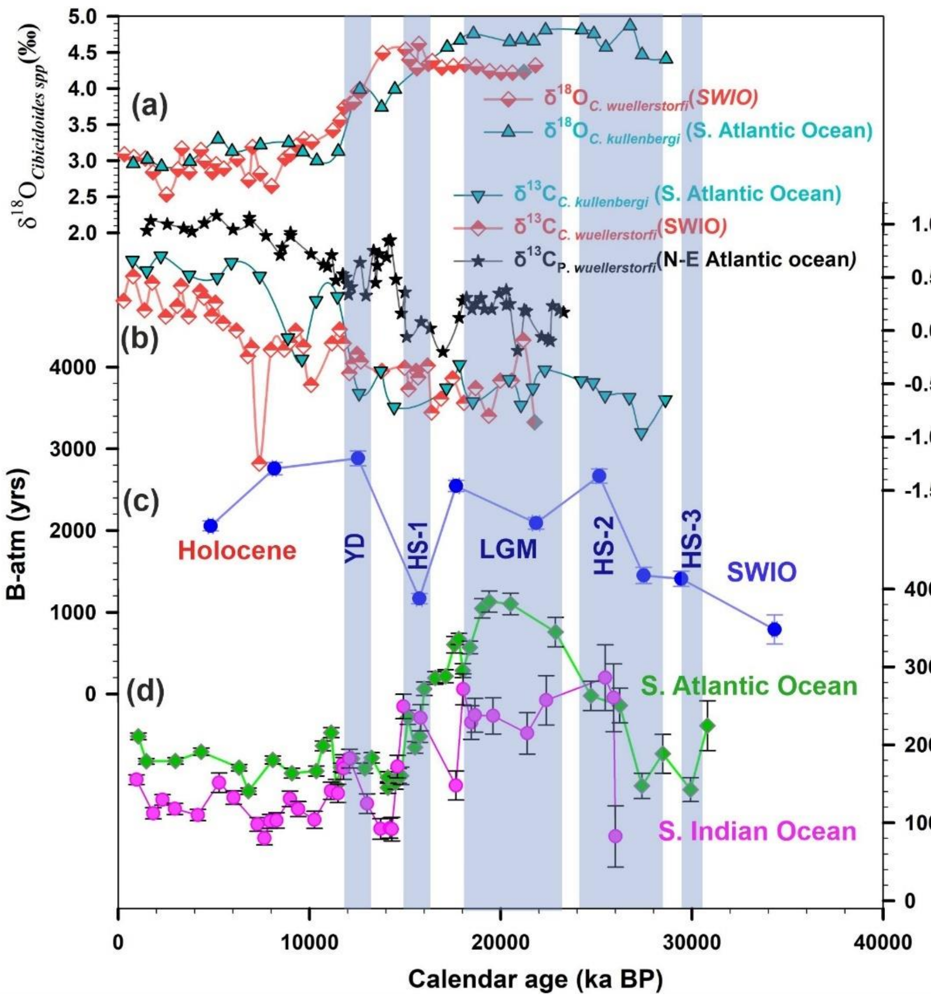

Figure 5.6: Paleo-circulation of the Southwest Indian Ocean in global perspective: (a) stable oxygen isotope of monospecific benthic foraminifera species from the South West Indian Ocean (red diamond; (δ^{18}O of Cibicidoides spp.*; water depth:1800m; Curry et al., 1988)) and the Southern Atlantic Ocean (dark cyan triangle; (δ^{18}O of Cibicidoides kullenbergi;water depth:3750m; Gottschalk et al., 2016)). (b) δ^{13}C of monospecific benthic foraminifera from the South West Indian Ocean (δ^{13}C of Cibicidoides* spp. *in red diamond; Curry et al., 1988)), Southern Atlantic Ocean ((δ^{13}C of Cibicidoides kullenbergi in the dark cyan triangle; (Gottschalk et al., 2016)) and North Atlantic Ocean (δ^{13}C of Cibicidoides wuellerstorfi in black star; (water depth: 3146m; Skinner and Shackleton, 2004)). (c) (B-Atm) ^{14}C offset from the South West Indian Ocean. (d) (B-Atm) ^{14}C offset from the Southern Atlantic Ocean (Skinner et al., 2010) and Southern Indian Ocean(Gottschalk et al., 2020).*

The rough topography of the SWIO along with the recirculation of northward moving CDW and southward moving NIDW can facilitate the prominent diapycnal mixing of the water masses (McCave et al., 2005). In addition, the changes in the contribution and/or extent of the southward moving and northward moving deep water masses in the northern boundary of the SWIO can have an additional contribution to the changes in the ventilation property of the deep water. Given the low resolution of the (B-Atm) ^{14}C age, it becomes difficult to ascertain the cause related to the evolution of the deep circulation in the SWIO during glacial and interglacial periods. A more resolved (B-Atm) ^{14}C age record can constrain these findings.

Chapter 6.

Anomalous Paleo Ventilation Record of Deep Waters from the Eastern Indian Ocean Basin

6.1 Introduction

The scientific expedition in the Indian Ocean started just ~ 62 yrs ago. Since then several hydrographic and paleo-climatic studies have been carried out in the Indian Ocean. However, the Indian Ocean paleo-oceanography for the deep waters remains poorly understood, compared to the Pacific and the Atlantic Ocean (Skinner et al., 2017). Despite being the largest deep basin, the Eastern Indian Ocean basin **(**EIO) remains to be explored. There are only a few studies on deep paleo-oceanography, focusing on the Quaternary ocean circulation changes from the EIO, mainly in the southern part of the EIO (Gupta and Thomas, 2003; Liu et al., 2015; Muller, 2002; Murgese et al., 2008; Murgese and De Deckker, 2007).

The decrease in the atmospheric CO_2 during the glacial period and the subsequent increase has largely been attributed to the perturbations in the deep ocean circulation (Franois et al., 1997; Galbraith et al., 2015; Skinner et al., 2017; Ronge et al., 2020; Lathika et al., 2021). However, this is debatable topic due to the regional heterogeneity of the paleo-ventilation (de la Fuente et al., 2015; Skinner et al., 2017; Zhao et al., 2018). Since there are no radiocarbon ventilation age records from the EIO, the role of the EIO in the glacial atmospheric CO_2 changes remained ambiguous. This study from the EIO tries to unravel the paleo-oceanography history of the EIO based on radiocarbon dating of paired planktic and benthic foraminifera. This chapter will present some results of paleo-oceanographic changes of the EIO.

6.2 Oceanographic Setting of the EIO Basin

The sediment core SK304-B12 (5.46° S, 97.37° E, water depth-4206 m, core length-1.5 m; Figure 6.1) under investigation is from the lysocline depth of the EIO (Kolla et al., 1976). The core location has proximity to eolian dust transport from the dry Australian region as well as volcanic material from the Sunda-Banda arc system (Liu et al., 2015). The core is located ~500 km away from the Sunda-Banda arc system (Fig 6.1). Due to several active hydrothermal vents in proximity of the comparatively shallow ocean in the EIO, retrieving a suitable sediment core for paleo-ventilation age studies remains challenging. Less fractured Ninety East ridge aligned in the north-south direction divides the EIO from the CIO basin (Tomczak and Godfrey, 2003).

Surface current in the eastern Equatorial Indian Ocean is mainly dominated by Equatorial Counter Current and South Equatorial Current. This region also contributes to the through-flow of waters from the Pacific Ocean to the Indian Ocean thermocline (Tomczak and Godfrey, 2003). The temperature of surface water is usually high in this region due to intrusion of water supplied through the Indo-Pacific warm pool (De Deckker, 2016). This highlights the importance of this region in the thermohaline circulation, by connecting the upwelling part of the thermohaline circulation from the N. Atlantic. The EIO basin is dominated by large Meridional Overturning Circulation compared to the WIO basin. Deep waters are mainly derived from the AABW originating in the Ross Sea and Adelie coast (Mantyla and Reid, 1995). The AABW derived water enters via the Australian-Antarctic basin to the South Australian basin through these regions of the southern Indian Ocean and then it replenishes the Perth basin and the West Australian basin (Sloyan, 2006). Just above this, northward moving water, southward moving nutrient-enriched and aged Indian Deep Water can be found (Kolla et al., 1976; Talley, 2013).

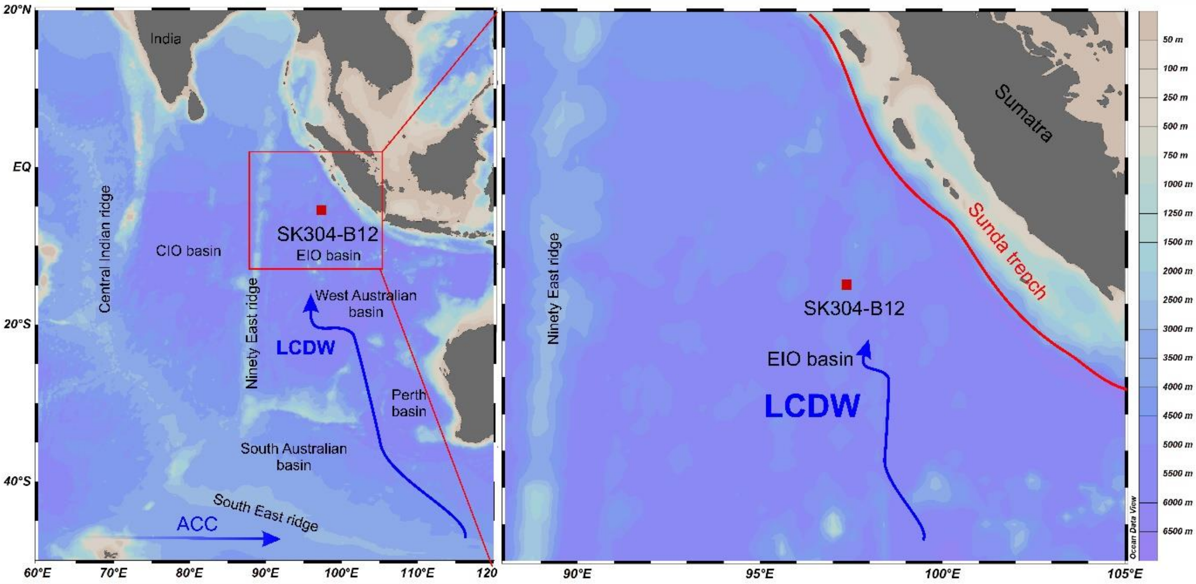

Figure 6.1: Study area: Bottom flow in the EIO basin. Core SK304/12 (5.46° S, 97.37° E, water depth-4206 m, core length-1.5 m) is located in the equatorial part of the EIO basin. Lower Circumpolar Deep Water (LCDW) ventilates the core location.

6.3 AMS Radiocarbon Chronology and Sedimentation Rate

The chronology of the core SK304/B12 was established using radiocarbon dating of *G. ruber* and *G. sacculifer* at 9 depths (Table 6.1). The obtained radiocarbon ages were calibrated using INTCAL20 curve in CALIB 8.2 software (Reimer et al., 2020). Since the top layer was dated to be 11.4 cal ka BP, inference for the Holocene couldn't be made using this core. This core located in the EIO basin witnessed large heterogeneity in the sedimentation rate (Figure 6.2), ranging between 0.3-12.3 cm.kyr$^{-1,}$ with an average value of 6.0 cm.kyr^{-1}. The wide variation in the sedimentation rate indicates the possibility of episodic terrestrial flux and/or volcanic material transport to the core location, or possibility of the mixed core at the top 20 cms. However, earlier study from a sediment core located ~ 500 km west of this study area doesn't report any signatures of volcanic input (Murgese and De Deckker, 2007). The sedimentation rate dropped remarkably during 32.5-13.5 ka BP (Figure 6.2), signifying decreased overhead productivity. An earlier study from this region has reported high productivity during the same period (e.g., Murgese and De Deckker, 2007).

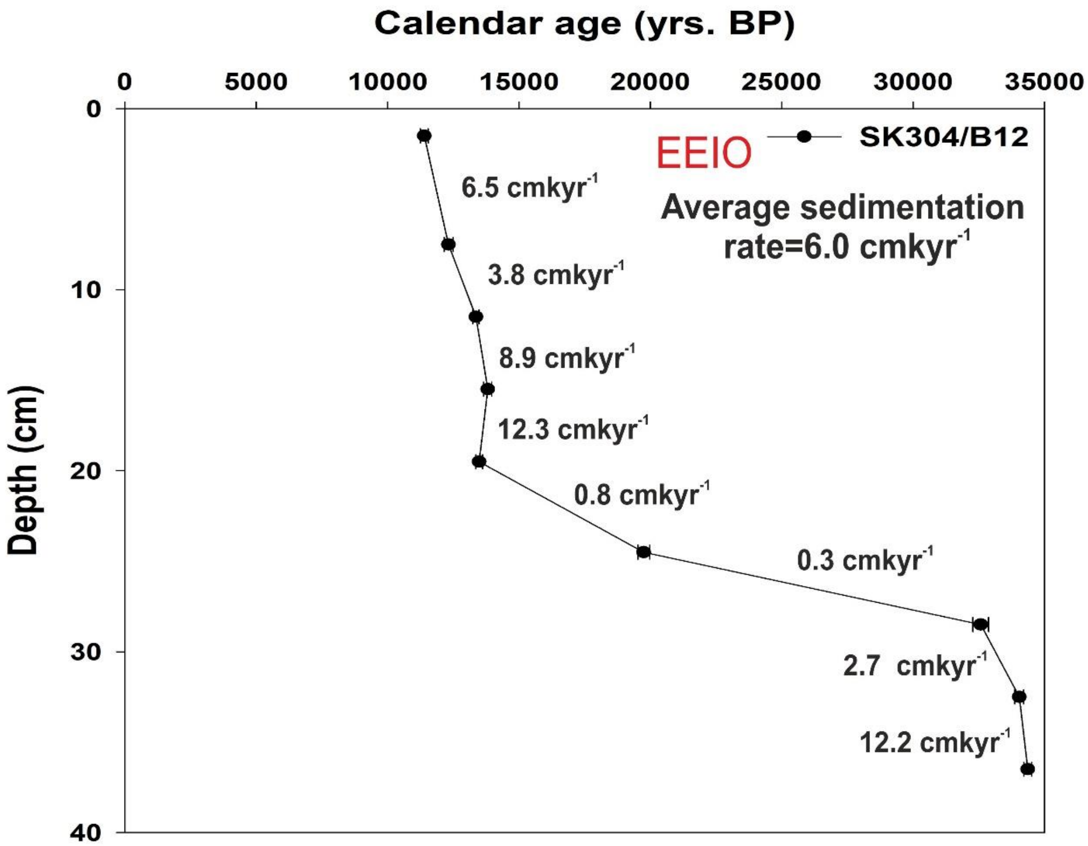

Figure 6.2: Age-depth model of the core SK304/B12 from the Eastern Equatorial Indian Ocean along with sedimentation rates in radiocarbon dated time intervals.

Table 6.1: Chronology of the core SK304/B12

LAB ID	Sample ID	Depth (cm)	Libby age (yrs)	Calendar age (yrs. BP)
AURIS-03350	SK304-B12/0-3/GS	0-3	10269±46	11397±150
AURIS-04168	SK304-B12/7-8/GR+GS	7-8	10862±69	12314±168
AURIS-03502	SK304-12/11-12/GS	11-12	11913±68	13358±123
AURIS-04169	SK304-B12/15-16/GR+GS	15-16	12288±81	13806±160
AURIS-03342	SK304-B12/19-20/GS	19-20	12035±61	13481±128
AURIS-04170	SK304-B12/24-25/GR+GS	24-25	16987±136	19750±220
AURIS-03501	SK304-12/28-29/GR+GS	28-29	29000±136	32572±301
AURIS-03500	SK304-12/32-33/GR+GS	32-33	30205±133	34037±167
AURIS-03499	SK304-12/36-37/GR+GS	36-37	30615±141	34364±153

6.4 Radiocarbon Measurements of Planktic and Benthic Foraminifera from the EIO Basin

Radiocarbon measurement was carried out on *Pulleniatina obliquiloculata*, along with *G. ruber* and mixed epifaunal benthic foraminifera (Figure 6.3). *P. obliquiloculata* is a subsurface to thermocline dwelling foraminifera species, which can switch depth regionally as well as vertically (Dang et al., 2018). For the top 20 cm, the radiocarbon age of both *P. obliquiloculata* and *G. ruber* were found to be nearly equal. However, for the 20-40 cm depth, radiocarbon age of *P. obliquiloculata* was much higher compared to *G. ruber*. This indicates that *P. obliquiloculata* was dwelling in the thermocline during this period. Interestingly during the same period, radiocarbon age of *P. obliquiloculata* was also higher compared to that of mixed epifaunal benthic foraminifera. This could result due to diffusive upwelling of the deep water in the Eq. Indian Ocean (Mantyla and Reid, 1995; Talley, 2013). However, in absence of any evidence or supporting data, along with no records of radiocarbon ventilation from the EIO, it needs to be attested using other proxies. The radiocarbon ages of the *P. obliquiloculata, G. ruber*, and epifaunal benthic foraminifera increased suddenly in consistance between 19-25 cm sediment core depth. The consistent radiocarbon dates of all these confirm that these changes resulted from the decreased sedimentation rate.

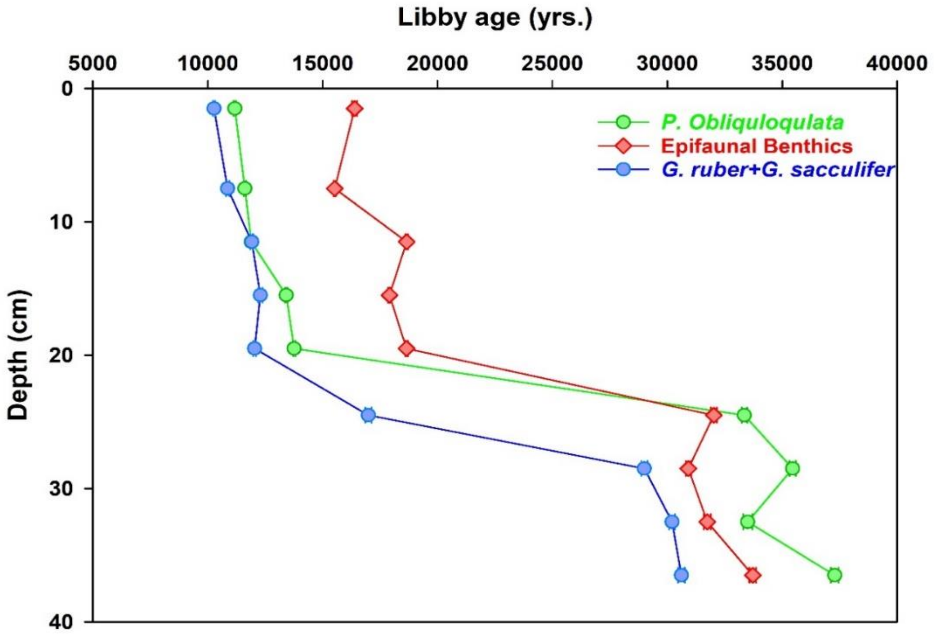

Figure 6.3: Radiocarbon ages (in terms of Libby age) of coexisting surface, thermocline, and deep foraminifera species.

6.5 Paleo Ventilation Age Estimates for the South West Indian Ocean Basin

(B-P) ^{14}C age offset and (B-Atm) age or (B-Atm) ^{14}C age offset in the EIO varied in consistance throughout the last 35 kyrs (Figure 6.4). Overall, large amplitude in the ventilation age estimates of the Eastern EIO compared to the compiled global deep ocean ventilation age record by Zhao et al., (2018) can be observed. Additionally, paleo ventilation estimates in the EIO were unexpectedly high (B-Atm age = 6286 yrs) during the deglaciation period. It was almost ~ 1500 yrs high compared to the deglaciation ventilation age record from the CIO basin. It was possibly due to the isolation of this basin from the deep water source regions during that time. The reduced formation of NADW resulted in the poor ventilation of the deep ocean during glaciation, which has been observed in various sediment cores from the Atlantic and Pacific Ocean (e.g., de la Fuente et al., 2015; Skinner et al., 2017; Zhao et al., 2018). The ventilation age during the deglacial period has shown large regional heterogeneity (Okazaki et al., 2010; Skinner et al., 2010; de la Fuente et al., 2015; Zhao et al., 2018; Gottschalk et al., 2020). One plausible reason for high ventilation age from the EIO region could be the contribution of dead CO_2 from the underwater volcanic sources or hydrothermal process in the Sunda-Banda arc. These hypotheses need to be substantiated using some other proxies (e.g., εND and/or trace element study), as required

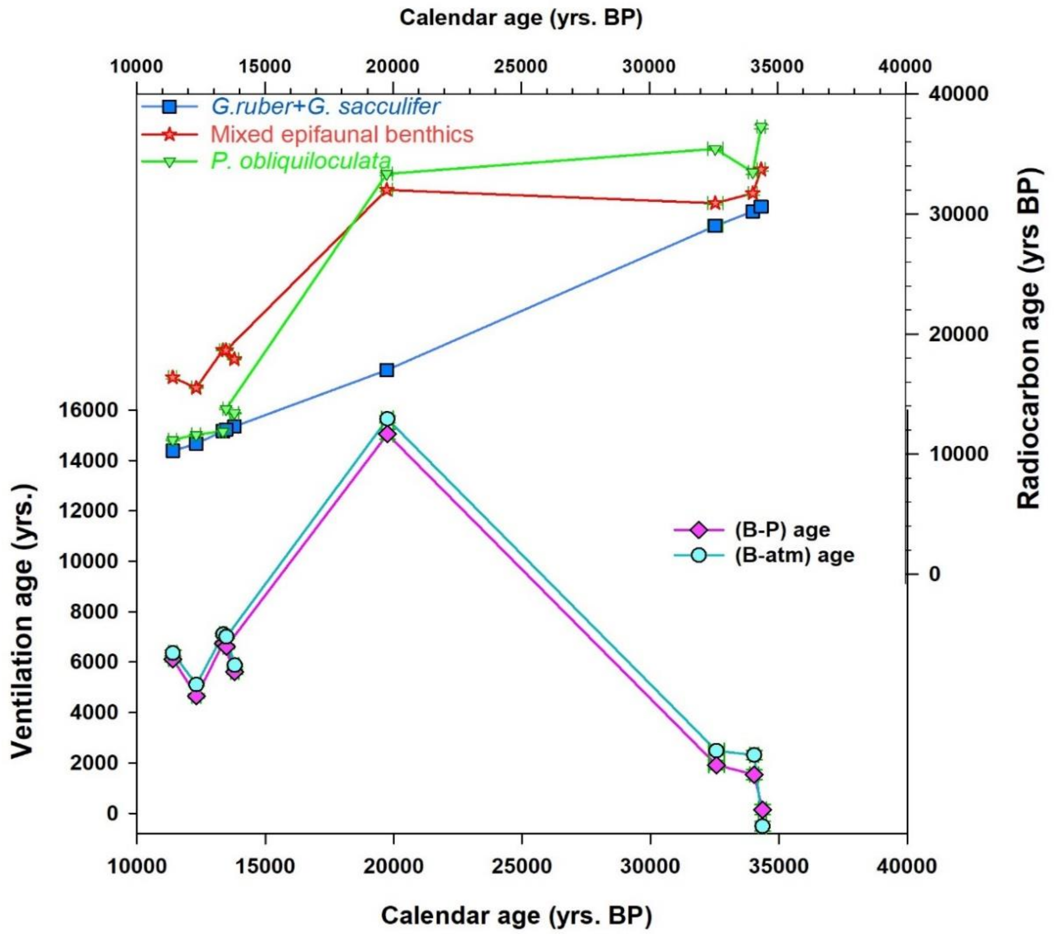

Figure 6.4: Paleo ventilation age and radiocarbon age vs. species in the EIO basin: Blue, red and green color marks the radiocarbon age of the surface species, mixed epifaunal benthic foraminifera and P. obliquiloculata respectively. Pink and cyan curve marks the B-P ^{14}C age offset and (B-Atm) ^{14}C age offset respectively.

to understand the role of volcanic/hydrothermal processes in the paleo-ventilation record. In addition, very high ventilation age peak (i.e. (B-Atm) age offset = 15642 yrs) was found at 19.7 ka BP. The occurrence of such large amplitude radiocarbon disequilibrium between surface and the deep ocean in the global ocean suggested that it was not related to any perturbation in the thermohaline circulation (de la Fuente et al., 2015; Skinner et al., 2017; Zhao et al., 2018). This happened possibly due to mantle-derived dead CO_2 at this location at 19.7 ka BP. This radiocarbon ventilation age anomaly is in proximity to a core ~ 1200 km away from the present study location SK304/B12 in the EIO, where positive $^{143}Nd/^{144}Nd$ and $^{87}Sr/^{86}Sr$ isotopic ratio anomaly was observed at 22.3 ka BP by Liu et al., (2015) They explained this anomaly as a distinct signature of volcanic eruption at 22.3 ka BP in Sunda-Banda arc. Thus, any sediment core located in the proximity of deep volcanic or hydrothermal sources should be carefully examined for its use for studies on ventilation age.

6.6 Conclusion

The high deglacial ventilation age record from the EIO was possibly due to isolation of this basin from the deep water formation region. The large heterogeneity in sedimentation rate suggests variation in the overhead productivity or remineralization of the export materials in the deep basin. Anomalously high ventilation age record from the EIO suggested contribution of dead CO_2 possibly from volcanic Sunda-Banda arc at 19.7 ka BP. It needs further conclusive evidence.

Chapter 7.

Summary and Scope for Future Work

The present work aims to reconstruct the first paleo-ventilation record for the northern part of the deep Indian Ocean and employ it to infer past deep-sea environment and paleo-deep circulation with the help of other supporting proxies. Towards this, isotopic and species abundance study was performed in planktic and benthic foraminifera along with geochemical study in the sediment. Due to the differences in deep-sea hydrography of the western, central, and eastern basins of the Indian Ocean, variation in the evolution of deep water ventilation was expected. The sediment cores were selected basin-wise; one sediment core from the South West Indian Ocean (SWIO) basin, two sediment cores from the Central Indian Ocean (CIO) basin, and one sediment core from the Eastern Indian Ocean (EIO) basin. The records of radiocarbon ventilation age was carried out in three major basins of the Indian Ocean. Stable carbon and oxygen isotope ratio of benthic and planktic foraminifera was measured in two sediment cores from the CIO basin. Benthic foraminifera assemblage and abundance study was done in one core from the central equatorial part of the CIO i.e. Central Equatorial Indian Ocean (CEIO).

This new paleo radiocarbon ventilation age reconstruction from the three different basins of the Indian Ocean showed large differences in the evolution of paleo-ventilation ages. Very high glacial ventilation age record from the CIO suggested an important role played by the Indian Ocean in glacial CO_2 sequestration in the global ocean, especially the CIO basin. Brief findings of the basin wise study using the above-discussed parameters is summarized below.

7.1 Paleo-productivity variation in the Central equatorial Indian Ocean (CEIO)

Benthic foraminifera assemblage and abundance study was done at 14 depth intervals covering the last 19 kyrs, along with OC, $CaCO_3$, $\delta^{13}C$, $\delta^{18}O$ value of planktic and benthic foraminifera in the CEIO (Figure 3.3). The abundances of productivity sensitive benthic foraminifera species (i.e. *Uvigerina* spp.; Figure 3.5) along with geochemical parameters (OC and $CaCO_3$) was used to decipher the paleo-productivity variation in the CEIO. The deep-sea oxygenation condition based on benthic foraminifera stable carbon isotope (Figure 3.4) and paleo radiocarbon ventilation age record was used to delineate between the export productivity and the overhead productivity based on the sediment preservation condition.

High export productivity was inferred during the LGM, based on increased abundances of *Uvigerina* spp. and high OC%. This can be attributed to the increased preservation led by poor bottom water ventilation. The high abundance of *Uvigerina* spp. during HS-1 despite low food supply and absence of *Uvigerina* spp. during Late Holocene, instead of moderate food supply, suggested its sensitivity to the inter-species competence. Food supply was moderate during the Holocene, instead of poor preservation environment led by high deep-sea ventilation/oxygenation. It suggested high overhead productivity in the CIO during Holocene, as purposed by earlier studies.

7.2 Paleo Deep Circulation and Deep-sea Environment in the Central Indian Ocean

Radiocarbon dating of surface dwelling planktic foraminifera and epifaunal benthic foraminifera was done in two sediment cores from the CEIO and the SBoB (Figure 4.2). These cores are ventilated by the N. Atlantic as well as the Southern Ocean sourced deep water at present. The present study provides new records of radiocarbon data, which demonstrates consistent ventilation changes across the last deglaciation in the CEIO and the SBoB, and appear to have been ventilated by the same water mass for the last 37 kyrs. Multi-proxy evidences (i.e., abundances of dissolved oxygen sensitive benthic foraminifera species, stable carbon and oxygen isotope ratio, Neodymium isotopes in sediment (Figure 4.5) suggest that the CIO basin contributed significantly to the low global average ventilation/oxygenation, and therefore atmospheric CO_2 sequestration during the last glacial period. Positive millennial-scale radiocarbon ventilation age anomalies that broadly coincide with HS-

1 and HS-2 suggest the influence of hydrographic/circulation changes originating in the N. Atlantic, in addition to the effects of gas-exchange and transport from the Southern Ocean. Of particular interest is the observation of a large radiocarbon ventilation change of >1000 ^{14}C yrs (~2561 yrs during 14.0-7.5 ka BP), which occurred subsequent to the B-A (Figure 4.6). This demonstrates that the deep ocean was not completely 'rejuvenated' half-way through the last deglaciation, as previously suggested by reports from outside the CIO basin. This underlines the potentially crucial, and previously under-appreciated role of the deep Indian Ocean in deglacial radiocarbon and carbon cycle change.

7.3 Paleo-ventilation of the Deep South-West Indian Ocean (SWIO)

Radiocarbon ventilation age estimates for the SWIO, which is ventilated by N. Atlantic as well as the Southern Ocean derived deep waters, was made using radiocarbon dating of *G. ruber* and mixed benthic foraminifera for the last 37 kyrs. Radiocarbon ventilation ages in the SWIO (Figure 5.3) were higher during the late HS-1, LGM as well as Holocene and lower during the HS-3, early HS-2, and HS-1. It was possibly the outcome of partial or total changes in the deep water source during that time. The other plausible explanation for this could be decreased air-sea gas exchange in the deep water source regions, during the occurrence of low (B-Atm) ^{14}C age offset. Overall, (B-Atm) ^{14}C age offset was always lower than 3000 yrs, which is less than half of the maximum ventilation age attained in the CIO basin. Contrasting ventilation-age evolution in the SWIO for the last 37 kyrs compared to the CIO indicate different circulation pattern and its evolution in the SWIO and the CIO basin. Also, much higher radiocarbon ventilation ages during the late Holocene in the SWIO, compared to the modern radiocarbon ventilation age estimates by Broecker et al., (2004) suggested the possibility of mantle-derived dead $^{14}CO_2$ input in the SWIO during the late Holocene. Further, the highly resolved radiocarbon ventilation age estimates in the SWIO, added with trace element study (e.g., Fe, Al, Nd etc.) etc would be able to delineate between the discussed possibilities.

7.4 Paleo ventilation of the deep Eastern Indian Ocean

The (B-Atm) ^{14}C age offset (Figure 6.4) in the EIO basin, which is ventilated by LCDW was calculated using radiocarbon dating of surface dwelling planktic foraminifera and mixed epifaunal benthic foraminifera. The large heterogeneity in sedimentation rate found in the EIO suggested large variation in the overhead productivity or preservation condition in the bottom water. Anomalously high (B-Atm) ^{14}C age offset in the EIO at 19.7 ka BP suggest contribution of dead CO_2, possibly from volcanic Sunda-Banda arc. However, the high deglacial radiocarbon ventilation age record in the EIO was possibly due to isolation of this basin from the deep water formation region.

7.5 Highlights of the Present Study

Abundance of the ecologically sensitive benthic foraminifera species suggested poor oxygenation during LGM and HS-1 and well oxygenated bottom water during the Holocene. Benthic foraminifera in the CIO were goverened by dissolved oxygen concentration as well as food supply. However *Uvigerina* spp. was found to be related to other factores too, probably to interspecies competence or higher limit of the bottom water dissolved oxygen. Surface productivity was found to be high during the Holocene. LGM also witnessed high food supply due to better preservation for the falling detrital environment in the deep CIO, but not due to high overhead producticity, as suggested by Punyu et asl., (2014) and Piotrowski et al., (2009).

CIO remained more isolated during the last glaciation compared to the global ocean, probably due to the role of Indian Ocean hydrographic changes . It was not fully rejuvenated up to the mid-Holocene, in contrast with most of the other basins, where rejuvenation started by the B-A warming. The highest radiocarbon ventilation age in the CIO basin attained during HS-2 and HS-1, suggests a clear response of the CIO to the hydrographic changes in the N. Atlantic.

Much higher radiocarbon ventilation age throughout the glaciation in the CIO, compared to the other oceanic basins suggests the role of the hydrographic changes in the Indian Ocean as well. Aging of the intermediate water in the CIO during glaciation was also found in the radiocarbon age of *G. menardii*. It was also very interesting to find much aged surface-subsurface water in the CIO during the early to mid-Holocene, compared to the intermediate water in the radiocarbon age of *G. menardii.*

Possibility of mantle derived dead $^{14}CO_2$ contribution was found in the SWIO, during the Holocene and during 19.7 ka BP in the EIO. Anomalous radicoarbon concentration in the well-preserved benthic foraminifera from the geologicaly active marine floor can be used to trace past volcanic events. The deep-circulation in the Western, Central, and the Eastern Indian Ocean basin, probably evolved differently during the last glaciation. The Central Indian Ocean basin contributed significantly to the changes in atmospheric CO_2 during the glacil events, which remained underappreciated so far in the global understanding.

7.6 Future Scope

- The present study underscores the underestimated role of the Indian ocean in modifying glacial-interglacial CO_2 due to its ~20% contribution to the global ocean water and isolation during the last glaciation, compared to the compiled paleo-ventilation age record. Further studies is required to cross check this inference using trace elemental study of the benthic foraminifera and other isotopic proxies like Nd isotopes, which can relate with the past deep ocean dissolved CO_2.
- The paleo-ventilation age reconstruction from the CIO basin suggested partial contribution of hydrographic changes in the Indian Ocean to the high radiocarbon ventilation age during HS-2 and HS-1. This need to be ascertained with the paleo-ventilation record for the intermediate water, which forms in the Indian Ocean.
- Deep water flow in the ocean is mainly constrained by the bottom topography. Hence, basin-wise difference is expected for the paleo-ventilation record of deep waters in the Indian Ocean. Other oceanic basins of the Indian Ocean e.g., the Arabian Sea, the Bay of Bengal, the Somali basin, the Mascarene basin, Madagascar basin, Perth basin, and the South-Australian basin remained unexplored regarding the deep water paleo-ventilation reconstruction. Hence, paleo-ventilation age reconstruction is needed from these basins of the Indian Ocean as well.
- The radiocarbon dates of *G. menardii* from the CIO suggested aged intermediate water during the entire duration of poor deep-sea ventilation in the CIO, compared to the Holocene. This could be linked with the thermocline upwelling of the deep water in the tropical Indian Ocean. Though, there are clues on present-day diffusive upwelling of deep water in the thermocline layer, various aspects e.g., area and depth coverage of the diffusive upwelling remains elusive. Further study could be done on these aspects.
- Past changes in the reservoir ages of the deep water source regions have been discussed in various recent studies, which is found to be a significant source

of error in estimating the transit time in terms of radiocarbon ventilation age record. Tephrochronology can be done to correct for past reservoir age changes. Chronostratigraphic alignment can also be done to constrain the local reservoir age changes.

- The anomalous (B-Atm) ^{14}C age offsets in the deep-sea hydrothermal areas can also be used to reconstruct the past hydrothermal events. Which can be used further in paleo-biogeochemical studies of the ocean.
- Further, neodymium isotope measurement in the benthic foraminifera and paleo deep water temperature reconstruction can be done to record the changes in the contribution of the N. Atlantic and the Southern Ocean derived water masses.

Appendix A (Paleo-Ventilation Age Calculation)

Past radiocarbon ventilation ages have been mainly estimated using three metrics. Each of these metrics has its advantages and limitations (Adkins & Boyle, 1997; DeVries & Primeau, 2010; Skinner & Shackleton, 2004). For example, there is need for accurate estimates of calendar age, source-region contributions, source-region 'preformed age' (i.e. reservoir age), or local surface reservoir age. Hence, ventilation age has been estimated using all three methods. Three methods are:

(1) Benthic versus Planktonic (B-P) Age Offsets (Broecker et al., 1984)

This method invokes the disequilibrium between overhead surface water and deep water and denoted as (B-P) age.

$$\text{(B-P) age} = {}^{14}\text{C age}_{\text{benthics}} - {}^{14}\text{C age}_{\text{planktics}}$$

Assumptions:

- Reservoir age of the overhead surface water and deep water formation region was equal and didn't change in the past.
- Deep water underwent closed system decay throughout its journey form the source to the core location.

(2) (B-Atm) Age Offsets (Soulet et al., 2016)

It is radiocarbon disequilibrium of deep waters relative to the atmosphere.

$$\text{(B-Atm) age} = {}^{14}\text{C age}_{\text{benthics}} - {}^{14}\text{C age}_{\text{atmosphere}}$$

${}^{14}\text{C age}_{\text{atmosphere}}$ = ^{14}C age of INTCAL20 atmosphere corresponding to the calendar age of planktic foraminifera.

Assumptions:

- Deep water formation region remained in equilibrium with the atmosphere.
- Deep water underwent closed system decay throughout its journey from the source to the core location.
- Contributing water masses remained same in the past.

(3) Projection Age (Adkins & Boyle, 1997)

Projection age method provides an independent way to choose an initial atmospheric $\Delta^{14}C$ value for the deep water mass. The intersection of the age projections and the atmospheric $\Delta^{14}C$ record indicate the time in the past the deep water left the surface. The difference between the benthic data point age and the intersection age is the ventilation age relative to the atmosphere. Calculation is done graphically, as mentioned in Chapter 4.3.

Projection age= Calendar age corresponding to the intersection of deep water $\Delta^{14}C$ decay trajectory and INTCAL20 $\Delta^{14}C$ curve - Calendar age (Calibrated using INTCAL20) corresponding to deep water $\Delta^{14}C$.

$$\text{Deep water } \Delta^{14}C = (F_{Ben} e^{\lambda * \text{calendar age}} - 1) * 1000$$

- F= fraction modern of Benthic foraminifera
- λ= 1/8257 ($t_{1/2}$ =5730 Yrs.)
- Calendar age=calibrated age of planktic foraminifera (Using INTCAL20 Calibration)
- Uncertainty in $\Delta^{14}C$ is compounded analytical uncertainty of F and calendar age and calculated using Monte Carlo Simulation.

Assumptions:

- Reservoir age in deep water formation region didn't change with time.
- Deep water underwent closed system decay throughout its journey form the source to the core location.
- Mixing ratio of contributing water masses remained same throughout the past.

Construction of Decay Trajectory of Deep Water $\Delta^{14}C$

Nearly 20-30 extrapolated $\Delta^{14}C$ data points (enough to intersect INTCAL20) were generated by increasing time by 100-300 years, taking calendar age of planktic foraminifera as initial value. Extrapolated $\Delta^{14}C$ was calculated at each depth, using F_{Ben} and extrapolated calendar age. $\Delta^{14}C_{deep\ water}$ data points at each depth were plotted with NH INTCAL20 $\Delta^{14}C$ in SigmaPlot 14.0 software, as multiple spline curve. Intersection points of INTCAL20 $\Delta^{14}C$ and $\Delta^{14}C_{deep\ water}$ decay trajectory was calculated graphically.

Appendix B (Benthic Foraminifera Microhabitat)

Table B.1: Preferred microhabitat of the benthic foraminifera species available in the core SS152/3828

S. N.	Species	Microhabitat Preference	References
1	*Ammodiscus planorbis*	Epifauna	(Kaminski et al., 1988; Reolid et al., 2008)
2	*Ammodiscus tenuis*	Epifauna	(Kaminski et al., 1988; Reolid et al., 2008)
3	*Astacolus brady*	Shallow Infuana	(Reolid et al., 2008)
4	*Astacolus* sp.1	Shallow Infuana	(Reolid et al., 2008)
5	*Astacolus* sp.2	Shallow Infuana	(Reolid et al., 2008)
6	*Bathysiphon* sp.	Sessile Epifauna	(Kuhnt et al., 2000)
7	*Cassidelina complanate*	Shallow Infauna	(Hayward et al., 2010)
8	*Cassidelina* sp.	Shallow Infauna	(Hayward et al., 2010)
9	*Chilostomella oolina*	Deep Infauna	(Corliss and Emerson, 1990; Mackensen et al., 1995; Hayward et al., 2010)
10	*Cibicidoides kullenbergi*	Epifauna	(Hayward et al., 2010)
11	*Cibicidoides brady*	Epifauna	(Hayward et al., 2010)
12	*Cibicidoides wuellerstorfi*	Epifauna	(Corliss, 1985; Corliss and Chen, 1988; Gooday, 1993)
13	*Cribrostomoides bradyi*	Deeper Infauna	(Corliss and Chen, 1988)
14	*Cyclammina* sp.	Shallow Infauna	(Phipps et al., 2012)
15	*Eggerella bradyi*	Shallow Infauna	(Kuhnt et al., 2000)
16	*Epistominella exigua*	Epifauna	(Corliss and Chen, 1988; Gooday, 1993; Smart et al., 1994)
17	*Favulina hexagona*	Shallow Infauna	(Hayward et al., 2010)
18	*Lagenosolenia* sp.1	Shallow Infauna	(Hayward et al., 2010)
19	*Lagenosolenia* sp.2	Shallow Infauna	(Hayward et al., 2010)
20	*Fursenkoina pauciloculata*	Shallow Infauna	(Hayward et al., 2010)
21	*Globocassidulina subglobosa*	Shallow Infauna	(Gooday, 1993; Mackensen et al., 1995; Hayward et al., 2010)
22	*Gyroidinoides soldanii*	Epifauna	(Corliss and Chen, 1988; Hayward et al., 2010)
23	*Gyroidinoides lamarkiana*	Epifauna	(Hayward et al., 2010)
24	*Haplophragmoides* sp.	Shallow Infauna	(Reolid et al., 2008)
25	*Hoeglundina elegans*	Epifauna	(Corliss, 1985)
26	*Laevidentalina* sp.	Shallow to Deep Infauna	(Reolid et al., 2008)

27	*Laevidentalina mucronate*	Shallow to Deep Infauna	(Reolid et al., 2008)
28	*Lagena hispidula*	Shallow infauna	(Hayward et al., 2010)
29	*Lagena cf. Lagena laevicoastata*	Shallow Infauna	(Hayward et al., 2010)
30	*Lagena* sp.1	Shallow Infauna	(Hayward et al., 2010)
31	*Lagena* sp.2	Shallow infauna	(Hayward et al., 2010)
32	*Lagena* sp.3	Shallow infauna	(Hayward et al., 2010)
33	*Lagena striata*	Shallow Infauna	(Hayward et al., 2010)
34	*Laticarinina pauperata*	Epifauna	(Hayward et al., 2010)
35	*Lenticulina* sp.	Epifauna	(Corliss and Chen, 1988)
36	*Melonis barleeanum*	Deep Infauna	(Mackensen et al., 1995)
37	*Melonis pompilioides*	Deep Infauna	(Mackensen et al., 1995)
38	*Melonis affinis*	Deep Infauna	(Mackensen et al., 1995)
39	*Oolina* sp.	Shallow Infauna	(Hayward et al., 2010)
40	*Oridorsalis umbonatus*	Epifauna	(Corliss and Chen, 1988; Gooday, 1993)
41	*Parafissurina marginata*	Shallow Infauna	(Corliss and Chen, 1988)
42	*Psammosphera* sp.	Shallow infauna	(Bernhard, 1989)
43	*Pullenia quinqueloba*	Shallow Infauna	(Mackensen et al., 1995)
44	*Pullenia bulloides*	Shallow Infauna	(Mackensen et al., 1995)
45	*Pyrgo murrhina*	Epifauna	(Corliss and Chen, 1988; Hayward et al., 2010)
46	*Pyrgo leavis*	Epifauna	(Hayward et al., 2010)
47	*Quinqueloculina* sp.	Epifauna	(Reolid et al., 2008)
48	*Quinqueloculina seminulum*	Epifauna	(Reolid et al., 2008)
49	*Recurvoides* sp.	Shallow to deep infauna	(Kuhnt et al., 2000; Reolid et al., 2008)
50	*Sigmoilopsis schlumbergeri*	Deeper Infauna	(Kuhnt et al., 2000)
51	*Sphaeroidina bulloides*	Shallow Infauna	(Hayward et al., 2010)
52	*Textularia earlandi*	Shallow to Deep infauna	(Reolid et al., 2008)
53	*Uvigerina peregrina*	Shallow Infauna	(Corliss and Emerson, 1990)
54	*Uvigerina proboscidea*	Shallow Infauna	(Corliss and Emerson, 1990)

Table B.2: Benthic foraminifera species identified in the core SS152/3828, based on morphological characters.

S. N.	Species	Morphological character	Microhabitat based on morphology
1	*Cerebrina sp*	Angular asymmetrical elongated	Shallow infaunal
2	*Cycloforina* sp.	Miliolid	Epifauna

3	*Favulina hexagona*	Angular asymmetrical elongated	Shallow infaunal
4	*Hyalinonetrion sp*	Angular asymmetrical elongated	Shallow infauna
5	*Marginulina obesa*	Angular asymmetrical elongated	Shallow infauna
6	*Polymorphina* sp.	Angular asymmetrical elongated	Shallow Infauna
7	*Pygmaeoseistron hispidula*	Angular asymmetrical elongated	Shallow Infauna
8	*Pygmaeoseistron* sp.1	Angular asymmetrical elongated	Shallow Infauna
9	*Uvigerina hispida*	Angular asymmetrical elongated	Shallow Infauna
10	*Uvigerina pygmaea*	Angular asymmetrical elongated	Shallow Infauna
11	*Euuvigerina auberiana*	Angular asymmetrical elongated	Shallow Infauna

Appendix C (Thesis Data)

Table C.1: Absolute abundances of benthic foraminifera species (>150µm) in core SS152/3828 at different climatic intervals (ka=kilo years before present). Note that that the absolute abundance is the abundance of benthic foraminifera normalized for 10 g of sediment.

Benthic foraminifera species	2.1 ka BP	4.1 ka BP	6.2 ka BP	7.5 ka BP	8.2 ka BP	11.9 ka BP	12.7 ka BP	14.0 ka BP	14.9 ka BP	15.4 ka BP	15.8 ka BP	16.6 ka BP	18.0 ka BP	18.9 ka BP
Ammodiscus planorbis	2	0	0	0	0	0	0	0	0	0	0	0	0	0
Ammodiscus tenuis	4	0	0	0	0	0	0	0	0	0	0	0	0	0
Astacolus brady	1	0	0	0	0	0	0	0	0	0	0	0	0	0
Astacolus sp.1	1	0	0	0	0	0	3	0	0	0	0	0	0	0
Astacolus sp.2	0	0	0	0	0	0	0	0	1	0	1	6	0	0
Bathysiphon sp.	0	0	0	0	0	0	0	0	0	0	1	0	0	0
Cassidelina complanate	0	0	0	0	0	2	0	0	0	0	0	2	0	0
Cassidelina sp.	2	2	0	0	0	0	0	6	7	4	0	0	0	2
Cerebrina sp.	2	0	0	6	0	4	0	0	0	0	12	0	0	4
Chilostomella oolina	0	0	0	0	0	5	0	0	3	0	1	0	16	16
Cibicidoides kullenbergi	4	5	0	5	0	2	0	22	0	0	27	0	0	15
Cibicidoides brady	8	15	8	0	8	20	19	4	13	10	4	4	0	0
Cibicidoides wuellerstorfi	36	23	27	10	27	29	43	34	28	54	31	79	66	114
Cribrostomoides bradyi	2	0	0	0	0	0	0	0	0	0	0	0	0	0
Cycloforina sp.	14	11	8	9	8	4	13	5	10	4	5	8	11	10
Cyclammina sp.	1	0	0	0	0	0	0	0	0	0	0	0	0	0
Eggerella bradyi	7	2	11	19	11	1	15	16	11	20	30	19	21	59

Epistominella exigua	37	17	8	12	8	14	23	24	30	46	67	79	61	153
Favulina hexagona	0	0	0	0	0	0	0	0	0	0	0	0	0	2
Lagenosolenia sp.1	2	2	2	6	2	10	0	10	8	1	19	15	4	31
Lagenosolenia sp.2	16	0	0	10	0	2	5	6	0	0	8	0	9	22
Fissurina sp.1	1	0	0	0	0	0	2	0	0	0	0	0	0	0
Fursenkoina pauciloculata	0	0	0	0	0	4	0	0	0	0	0	0	0	2
Globocassidulina subglobosa	70	31	35	25	35	17	27	0	28	13	18	19	14	30
Gyroidinoides soldanii	23	11	6	0	6	6	13	10	11	14	20	35	21	44
Gyroidinoides lamarkiana	0	0	10	0	10	0	5	0	10	0	12	25	13	0
Haplophragmoides sp.	2	0	0	0	0	0	0	0	0	0	0	0	0	0
Hoeglundina elegans	18	2	2	0	2	19	5	0	1	0	8	6	0	9
Hyalinonetrion elongate	0	0	0	0	0	0	0	0	0	0	0	0	0	2
Laevidentalina sp.	0	1	2	2	2	0	0	0	1	0	0	2	2	0
Laevidentalina mucronate	0	0	0	0	0	0	0	1	0	0	0	0	0	0
Lagena hispida	2	0	0	0	0	0	0	0	0	0	0	0	0	0
Lagena cf. Lagena laevicoastata	0	0	0	0	0	2	0	0	0	0	0	0	0	0
Lagena sp.1	0	6	2	4	2	0	0	0	0	3	0	0	4	2
Lagena sp.2	2	0	0	0	0	0	0	0	0	0	0	0	0	0
Lagena sp.3	2	0	0	0	0	0	0	0	0	0	0	0	0	0
Lagena striata	0	0	0	0	0	1	0	0	0	0	0	2	0	2
Laticarinina pauperata	17	28	10	6	10	20	10	8	8	1	1	0	0	0
Lenticulina sp.	4	0	0	0	0	0	0	0	0	0	0	0	0	6
Marginulina obesa	0	0	0	0	0	0	0	0	0	0	1	0	0	0
Melonis barleeanum	54	21	11	2	11	22	21	30	9	23	56	12	9	74
Melonis pompilloides	0	9	5	3	5	4	9	11	21	26	0	44	21	18
Melonis affinis	0	0	0	0	0	1	0	3	0	0	0	0	0	0
Oolina sp.	15	2	5	6	5	0	3	4	3	3	12	8	7	4

Oridorsalis umbonatus	48	27	19	61	19	32	37	28	24	33	41	44	32	72
Parafissurina marginate	0	11	8	1	8	1	11	5	10	10	2	27	11	4
Polymorphina sp.	12	9	6	8	6	14	0	6	0	1	14	0	4	0
Psammosphera sp.	0	0	0	0	0	0	0	0	0	0	0	0	0	0
Pullenia quinqueloba	10	15	13	12	13	0	20	6	14	23	12	15	14	18
Pullenia bulloides	29	20	5	9	5	21	21	18	16	22	21	29	30	41
Pygmaeoseistron hispidula	0	0	2	0	2	0	0	0	0	0	0	0	7	0
Pygmaeoseistron sp.1	0	0	0	0	0	0	4	0	0	0	0	0	0	0
Pyrgo murrhine	17	17	16	19	16	12	16	8	10	14	21	15	18	62
Pyrgo leavis	7	15	0	4	0	11	14	12	14	20	3	19	23	10
Quinqueloculina sp.	0	6	6	0	6	2	5	0	0	12	2	0	7	0
Quinqueloculina seminula	1	2	0	0	0	7	0	0	0	7	0	0	0	6
Recurvoides sp.	4	0	0	0	0	0	0	0	0	0	0	0	0	0
Sigmoilopsis schlumbergerella	1	4	0	1	0	0	4	0	1	3	1	10	4	0
Sphaeroidinella bulloides	8	6	3	12	3	8	14	14	14	9	0	6	0	24
Textularia earlandi	3	6	0	16	0	18	4	4	7	9	6	10	11	13
Uvigerina hispida	0	0	10	0	10	0	38	0	57	125	0	229	191	380
Uvigerina peregrina	0	0	5	4	5	8	0	15	0	10	37	42	34	27
Uvigerina proboscidea	0	2	6	2	6	10	0	0	10	7	70	19	20	0
Uvigerina pygmaea	0	4	6	8	6	10	20	10	18	6	11	0	0	122
Euuvigerina auberiana	0	0	0	0	0	0	0	0	0	0	45	0	0	48
Total	480	336	258	284	258	344	426	321	401	536	619	829	684	1449

Table C.2: Species composition of benthic foraminifera assemblage (>150µm) in core SS152/3828 and relative abundances with time intervals (ka BP=kilo years before present).

Benthic foraminifera species	2.1 ka BP	4.1 ka BP	6.2 ka BP	7.5 ka BP	8.2 ka BP	11.9 ka BP	12.7 ka BP	14.0 ka BP	14.9 ka BP	15.4 ka BP	15.8 ka BP	16.6 ka BP	18.0 ka BP	18.9 ka BP
Ammodiscus planorbis	0	0	0	0	0	0	0	0	0	0	0	0	0	0
Ammodiscus tenuis	1	0	0	0	0	0	0	0	0	0	0	0	0	0
Astacolus brady	0	0	0	0	0	0	0	0	0	0	0	0	0	0
Astacolus sp.1	0	0	0	0	0	0	2	0	0	0	0	0	0	0
Astacolus sp.2	0	0	0	0	0	0	0	0	0	0	0	2	0	0
Bathysiphon sp.	0	0	0	0	0	0	0	0	0	0	0	0	0	0
Cassidelina complanate	0	0	0	0	0	1	0	0	0	0	0	0	0	0
Cassidelina sp.	0	1	0	0	0	0	0	2	2	1	0	0	0	0
Cerebrina sp.	0	0	0	2	0	1	0	0	0	0	2	0	0	0
Chilostomella oolina	0	0	0	0	0	1	0	0	1	0	0	0	2	1
Cibicidoides kullenbergi	1	1	0	2	0	1	0	7	0	0	4	0	0	1
Cibicidoides brady	2	4	3	0	3	6	5	1	3	2	1	0	0	0
Cibicidoides wuellerstorfi	7	7	11	4	11	8	10	10	7	10	5	10	10	8
Cribrostomoides bradyi	0	0	0	0	0	0	0	0	0	0	0	0	0	0
Cycloforina sp.	3	3	3	3	3	1	3	1	3	1	1	1	2	1
Cyclammina sp.	0	0	0	0	0	0	0	0	0	0	0	0	0	0
Eggerella bradyi	1	1	4	7	4	0	4	5	3	4	5	2	3	4
Epistominella exigua	8	5	3	4	3	4	6	8	7	9	11	10	9	11
Favulina hexagona	0	0	0	0	0	0	0	0	0	0	0	0	0	0
Lagenosolenia sp.1	0	1	1	2	1	3	0	3	2	0	3	2	1	2
Lagenosolenia sp.2	3	0	0	4	0	1	1	2	0	0	1	0	1	2
Fissurina sp.1	0	0	0	0	0	0	1	0	0	0	0	0	0	0
Fursenkoina pauciloculata	0	0	0	0	0	1	0	0	0	0	0	0	0	0
Globocassidulina subglobosa	15	9	14	9	14	5	6	0	7	2	3	2	2	2

Gyroidinoides soldanii	5	3	3	0	3	2	3	3	3	3	3	4	3	3
Gyroidinoides lamarkiana	0	0	4	0	4	0	1	0	3	0	2	3	2	0
Haplophragmoides sp.	0	0	0	0	0	0	0	0	0	0	0	0	0	0
Hoeglundina elegans	4	1	1	0	1	6	1	0	0	0	1	1	0	1
Hyalinonetrion elongata	0	0	0	0	0	0	0	0	0	0	0	0	0	0
Laevidentalina sp.	0	0	1	1	1	0	0	0	0	0	0	0	0	0
Laevidentalina mucronate	0	0	0	0	0	0	0	0	0	0	0	0	0	0
Lagena hispida	0	0	0	0	0	0	0	0	0	0	0	0	0	0
Lagena cf. Lagena laevicoastata	0	0	0	0	0	1	0	0	0	0	0	0	0	0
Lagena sp.1	0	2	1	1	1	0	0	0	0	1	0	0	1	0
Lagena sp.2	0	0	0	0	0	0	0	0	0	0	0	0	0	0
Lagena sp.3	0	0	0	0	0	0	0	0	0	0	0	0	0	0
Lagena striata	0	0	0	0	0	0	0	0	0	0	0	0	0	0
Laticarinina pauperata	4	8	4	2	4	6	2	3	2	0	0	0	0	0
Lenticulina sp.	1	0	0	0	0	0	0	0	0	0	0	0	0	0
Marginulina obesa	0	0	0	0	0	0	0	0	0	0	0	0	0	0
Melonis barleeanum	11	6	4	1	4	6	5	9	2	4	9	1	1	5
Melonis pompilloides	0	3	2	1	2	1	2	3	5	5	0	5	3	1
Melonis affinis	0	0	0	0	0	0	0	1	0	0	0	0	0	0
Oolina sp.	3	1	2	2	2	0	1	1	1	1	2	1	1	0
Oridorsalis umbonatus	10	8	8	22	8	9	9	9	6	6	7	5	5	5
Parafissurina marginata	0	3	3	0	3	0	3	1	3	2	0	3	2	0
Polymorphina sp.	3	3	3	3	3	4	0	2	0	0	2	0	1	0
Psammosphera sp.	0	0	0	0	0	0	0	0	0	0	0	0	0	0
Pullenia quinqueloba	2	4	5	4	5	0	5	2	3	4	2	2	2	1
Pullenia bulloides	6	6	2	3	2	6	5	5	4	4	3	3	4	3
Pygmaeoseistron hispidula	0	0	1	0	1	0	0	0	0	0	0	0	1	0

Pygmaeoseistron sp.1	0	0	0	0	0	0	1	0	0	0	0	0	0	0
Pyrgo murrhina	3	5	6	7	6	4	4	3	3	3	3	2	3	4
Pyrgo leavis	1	4	0	1	0	3	3	4	3	4	0	2	3	1
Quinqueloculina sp.	0	2	3	0	3	1	1	0	0	2	0	0	1	0
Quinqueloculina seminula	0	1	0	0	0	2	0	0	0	1	0	0	0	0
Recurvoides sp.	1	0	0	0	0	0	0	0	0	0	0	0	0	0
Sigmoilopsis schlumbergerella	0	1	0	0	0	0	1	0	0	1	0	1	1	0
Sphaeroidinella bulloides	2	2	1	4	1	2	3	4	3	2	0	1	0	2
Textularia earlandi	1	2	0	5	0	5	1	1	2	2	1	1	2	1
Uvigerina hispida	0	0	4	0	4	0	9	0	14	23	0	28	28	26
Uvigerina peregrina	0	0	2	1	2	2	0	5	0	2	6	5	5	2
Uvigerina proboscidea	0	1	3	1	3	3	0	0	3	1	11	2	3	0
Uvigerina pygmaea	0	1	3	3	3	3	5	3	5	1	2	0	0	8
Euuvigerina auberiana	0	0	0	0	0	0	0	0	0	0	7	0	0	3
Total	100	100	100	100	100	100	100	100	100	100	100	100	100	100

Table C.3: Geochemical parameters of the core SS152/3828.

Depth	Cal age (ka BP)	OC %	N %	OC/ N	$CaCO_3$%	OC flux (g^{-2} yr^{-1})	$CaCO_3$ flux (g^{-2} yr^{-1})
3.5	2.2	1.92	0.21	9.15	67.82	0.20	6.97
4.5	2.9	1.61	0.18	8.70	63.35	0.15	6.01
6.5	4.1	1.46	0.18	8.13	64.72	0.14	6.17
7.5	4.7	1.67	0.20	8.36	64.16	0.16	6.10
8.5	5.3	1.75	0.19	9.07	63.13	0.17	5.98
9.5	5.9	1.68	0.19	8.89	62.50	0.42	15.58
11.5	6.3	1.64	0.18	9.24	62.75	0.41	15.66
12.5	6.6	1.65	0.19	8.81	65.31	0.37	14.64
13.5	6.8	1.80	0.19	9.55	65.20	0.40	14.61
14.5	7.1	1.57	0.17	9.44	65.19	0.35	14.60
16.5	7.6	1.64	0.18	9.29	59.93	0.14	4.99
17.5	8.3	1.25	0.13	9.61	65.54	0.11	5.57
18.5	8.9	1.35	0.13	10.23	63.81	0.19	8.86
19.5	9.4	1.16	0.12	9.33	65.06	0.09	4.86
21.5	10.9	1.16	0.12	9.95	64.22	0.09	4.78
23	12.0	1.01	0.11	9.63	64.73	0.16	9.93
24.5	12.6	1.09	0.11	10.25	63.91	0.18	10.36
26.5	13.3	0.91	0.10	9.17	64.54	0.15	10.49
27.5	13.6	0.95	0.10	9.73	65.47	0.16	10.68
28.5	14.0	0.87	0.09	9.33	61.10	0.04	3.11
29.5	15.1	0.87	0.09	9.59	61.69	0.28	19.47
31.5	15.5	0.98	0.10	10.27	60.97	0.31	19.19
34	15.9	0.97	0.10	9.75	62.16	0.08	5.38
35.5	16.9	1.37	0.13	10.36	63.12	0.12	5.47
36.5	17.5	1.27	0.13	9.84	62.05	0.09	4.51
37.5	18.3	2.45	0.22	10.91	62.67	0.14	3.53
38.5	19.3	2.57	0.23	11.18	61.04	0.29	6.85

Table C.4: Stable carbon and oxygen isotopic ratio in MMB, measured during planktic and benthic foraminiferal stable carbon and oxygen isotope measurement in the core SS152/3828 and core SS172/4040

S. N.	$\delta^{13}C_{VPDB}$ (‰)	σ $\delta^{13}C_{VPDB}$ (‰)	$\delta^{18}O_{VPDB}$ (‰)	σ $\delta^{18}O_{VPDB}$ (‰)
1	3.89	0.07	-10.73	0.04
2	4.03	0.11	-10.68	0.03
3	3.97	0.12	-10.79	0.06
4	3.96	0.13	-10.70	0.04
5	3.91	0.09	-10.75	0.05
6	4.05	0.09	-10.75	0.04
7	4.11	0.09	-10.71	0.06
8	4.07	0.10	-10.71	0.04

9	3.92	0.02	-10.71	0.05
10	4.10	0.15	-10.57	0.06
11	3.90	0.02	-10.81	0.04
12	4.04	0.11	-10.63	0.06
13	3.89	0.04	-10.70	0.04
14	4.00	0.06	-10.69	0.07
15	3.93	0.05	-10.73	0.05
16	3.95	0.07	-10.72	0.02
17	3.99	0.08	-10.76	0.04
18	4.02	0.07	-10.69	0.02
19	3.96	0.07	-10.71	0.04
20	3.96	0.07	-10.89	0.05
21	4.01	0.11	-10.74	0.05
22	3.97	0.10	-10.71	0.06
23	3.90	0.07	-10.74	0.02
24	4.03	0.12	-10.71	0.05
25	4.02	0.07	-10.66	0.05
26	4.03	0.05	-10.66	0.03
27	4.04	0.08	-10.89	0.06
28	3.84	0.05	-10.73	0.04
29	3.84	0.02	-10.87	0.06
30	3.96	0.06	-10.67	0.06
31	3.93	0.10	-10.71	0.03
32	4.05	0.08	-10.78	0.05
33	4.03	0.03	-10.61	0.06
34	4.05	0.04	-10.53	0.06
35	4.01	0.04	-10.60	0.06
36	4.00	0.08	-10.78	0.06
37	3.88	0.04	-10.84	0.06
38	3.89	0.03	-10.64	0.05
39	4.05	0.07	-10.65	0.05
40	4.02	0.07	-10.61	0.04
41	4.01	0.08	-10.78	0.05
42	3.95	0.05	-10.76	0.06
43	4.08	0.07	-10.61	0.04
44	4.05	0.08	-10.51	0.04
45	3.99	0.06	-10.68	0.06
46	4.07	0.05	-10.74	0.05
47	4.06	0.08	-10.62	0.02
48	4.11	0.08	-10.69	0.04
49	3.87	0.05	-10.71	0.05
50	4.03	0.08	-10.65	0.04
51	3.92	0.11	-10.74	0.04
52	4.04	0.08	-10.78	0.02
53	3.95	0.10	-10.69	0.04
54	4.00	0.03	-10.54	0.04
55	4.10	0.01	-10.69	0.07
56	4.02	0.03	-10.63	0.05

57	3.94	0.04	-10.85	0.08
58	4.04	0.02	-10.92	0.07
59	3.82	0.02	-10.67	0.08
60	3.91	0.04	-10.59	0.10
61	4.10	0.03	-10.78	0.06
62	4.04	0.01	-10.67	0.06
63	4.02	0.11	-10.53	0.07
64	4.05	0.11	-10.62	0.03
65	4.00	0.04	-10.89	0.03
66	4.00	0.06	-10.66	0.04
67	4.07	0.08	-10.55	0.03
68	4.00	0.09	-10.72	0.04
69	3.94	0.08	-10.79	0.04
70	3.96	0.04	-10.81	0.06
71	3.91	0.06	-10.58	0.04
72	4.00	0.07	-10.60	0.03
73	4.07	0.08	-10.55	0.03
74	4.00	0.09	-10.72	0.04
75	3.94	0.08	-10.79	0.04
76	3.96	0.04	-10.81	0.06
77	3.91	0.06	-10.58	0.04
78	4.00	0.07	-10.60	0.03
Average	3.99		-10.70	
Std Deviation	0.07		0.09	

Table C.5: Stable carbon and oxygen isotopic ratio in Coral Lab Standard (PRL-C) measured during planktic and benthic foraminiferal stable carbon and oxygen isotope measurement in the core SS152/3828 and core SS172/4040.

S. N.	$\delta^{13}C_{VPDB}$ (‰)	$\sigma\ \delta^{13}C_{VPDB}$ (‰)	$\delta^{18}O_{VPDB}$ (‰)	$\sigma\ \delta^{18}O_{VPDB}$ (‰)
1	-2.72	0.04	-5.55	0.05
2	-2.82	0.08	-5.62	0.03
3	-2.70	0.07	-5.52	0.03
4	-2.74	0.06	-5.52	0.02
5	-2.84	0.08	-5.59	0.03
6	-2.75	0.05	-5.56	0.04
7	-2.80	0.04	-5.63	0.02
8	-2.81	0.01	-5.64	0.06
9	-2.82	0.06	-5.44	0.04
10	-2.80	0.01	-5.63	0.08
11	-2.70	0.03	-5.47	0.05
12	-2.82	0.02	-5.74	0.05
13	-2.63	0.03	-5.45	0.08
14	-2.76	0.03	-5.54	0.03
15	-2.62	0.02	-5.55	0.04
16	-2.70	0.05	-5.53	0.03

17	-2.82	0.05	-5.71	0.04
18	-2.75	0.06	-5.73	0.03
19	-2.73	0.07	-5.49	0.05
20	-2.75	0.07	-5.68	0.05
21	-2.74	0.02	-5.78	0.03
22	-2.76	0.03	-5.69	0.02
23	-2.69	0.03	-5.70	0.04
24	-2.68	0.06	-5.49	0.03
25	-2.69	0.07	-5.41	0.05
26	-2.75	0.06	-5.54	0.02
27	-2.66	0.08	-5.49	0.05
28	-2.80	0.03	-5.60	0.03
29	-2.68	0.04	-5.47	0.02
30	-2.80	0.04	-5.56	0.04
31	-2.82	0.03	-5.55	0.03
32	-2.84	0.11	-5.82	0.06
33	-2.80	0.11	-5.74	0.06
34	-2.87	0.09	-5.63	0.03
35	-2.84	0.06	-5.66	0.03
Average	-2.76		-5.59	
Standard Deviation	0.07		0.10	

Table C.6: Stable carbon and oxygen isotopic ratio in NBS-18 measured during planktic and benthic foraminiferal stable carbon and oxygen isotope measurement in the core SS152/3828 and core SS172/4040.

S. N.	$\delta^{13}C_{VPDB}$ (‰)	$\sigma\ \delta^{13}C_{VPDB}$ (‰)	$\delta^{18}O_{VPDB}$ (‰)	$\sigma\ \delta^{18}O_{VPDB}$ (‰)
1	-5.05	0.09	-22.90	0.07
2	-4.79	0.06	-22.95	0.06
3	-4.92	0.03	-23.02	0.07
4	-4.89	0.05	-22.94	0.07
5	-4.90	0.07	-22.88	0.06
6	-4.86	0.07	-22.86	0.07
7	-4.92	0.04	-23.00	0.08
8	-4.98	0.08	-22.81	0.05
9	-4.76	0.01	-23.00	0.10
10	-4.75	0.05	-22.94	0.09
11	-4.80	0.03	-22.84	0.09
12	-4.95	0.03	-22.94	0.10
13	-4.86	0.08	-22.79	0.06
14	-4.81	0.03	-22.74	0.07
Average	-4.87		-22.90	
Std Deviation	0.09		0.08	

Table C.7: Stable carbon and oxygen isotopic ratio of Globigerinoides ruber in the core SS152/3828.

Depth (in cm)	Cal age (Bchron)	$\delta^{13}C$	$\sigma\ \delta^{13}C$	$\delta^{18}O$	$\sigma\delta^{18}O$
3.5	2.1	1.64	0.02	-2.38	0.06
4.5	2.9	1.33	0.02	-1.99	0.07
6.5	4.1	1.06	0.04	-2.42	0.07
7.5	4.6	1.53	0.03	-2.11	0.07
8.5	5.2	1.96	0.02	-1.86	0.06
9.5	5.8	1.32	0.06	-2.43	0.06
11.5	6.2	1.77	0.02	-2.19	0.05
12.5	6.5	1.29	0.02	-2.00	0.04
13.5	6.7	1.50	0.02	-2.30	0.05
14.5	7.0	1.98	0.04	-1.86	0.06
16.5	7.5	1.91	0.02	-2.76	0.05
17.5	8.2	2.07	0.02	-2.21	0.06
18.5	8.8	1.77	0.01	-2.22	0.04
19.5	9.3	1.63	0.02	-2.06	0.05
21.5	10.8	1.36	0.02	-2.44	0.06
23	11.9	1.34	0.02	-2.03	0.06
24.5	12.5	1.81	0.02	-1.64	0.04
26.5	12.7	1.09	0.03	-1.98	0.05
27.5	13.4	1.21	0.04	-1.46	0.08
28.5	14.0	1.23	0.12	-1.51	0.06
29.5	14.9	1.69	0.03	-1.16	0.05
32	15.4	1.30	0.02	-0.86	0.04
34	15.8	1.51	0.03	-1.23	0.05
35.5	16.6	1.83	0.01	-0.65	0.05
36.5	17.2	1.50	0.01	-0.77	0.04
37.5	18.0	1.64	0.02	-0.64	0.06
38.5	18.9	1.13	0.02	-0.79	0.04

Table C.8: Stable carbon and oxygen isotopic ratio of Globigerinoides ruber in the core SS172/4040.

Depth (cm)	Cal age (ka BP)	$\delta^{13}C$	$\sigma\ \delta^{13}C$	$\delta^{18}O$	$\sigma\delta^{18}O$
1	4.2	2.00	0.02	-2.24	0.09
3.5	6.1	1.42	0.03	-2.50	0.08
6.5	8.2	1.35	0.01	-2.11	0.07
8.5	9.3	1.25	0.04	-2.13	0.05
12.5	11.5	1.30	0.02	-1.99	0.07
15.5	12.7	1.43	0.05	-1.81	0.08
17.5	13.3	1.36	0.04	-1.82	0.08
20.5	14.2	1.55	0.04	-1.74	0.08
21.5	14.4	1.11	0.02	-1.55	0.06
24.5	15.9	1.72	0.02	-1.23	0.04
25.5	16.7	1.46	0.01	-1.32	0.05
26.5	17.7	1.56	0.03	-1.16	0.06
28.5	19.1	1.85	0.01	-0.79	0.04
29.5	19.7	1.65	0.02	-1.06	0.04
31	20.8	1.77	0.02	-0.95	0.04
33	21.7	1.82	0.01	-0.88	0.04
35	24.0	1.66	0.02	-1.13	0.05
37	24.5	1.71	0.01	-0.95	0.07
45	27.6	1.76	0.02	-1.14	0.06
51	32.96	1.58	0.03	-1.51	0.07
65	37.06	1.79	0.02	-1.45	0.04

Table C.9: Stable carbon and oxygen isotope ratio of cibicidoides species for the core SS152/3828. C. wuellerstorfi refers to Cibicidides wuellerstorfi and Cibicidoides sp. *refers to Cibicidoides species. Cal age is calendar age in kiloyears before present (ka BP).*

S.N.	Depth (cm)	Cal age (ka BP)	Species	$\delta^{13}C$ (‰)	±1 σ $\delta^{13}C$ (‰)	$\delta^{18}O$ (‰)	±1 σ $\delta^{18}O$ (‰)
1	3-4	2.1	*C. wuellerstorfi*	0.66	0.04	2.57	0.01
2	4-5	2.9	*C. wuellerstorfi*	0.34	0.11	2.21	0.03
3	7-8	4.7	*C. wuellerstorfi*	0.40	0.05	2.33	0.02
4	8-9	5.2	*C. wuellerstorfi*	0.80	0.04	2.58	0.02
5	11-12	6.3	*Cibicidoides* spp.	0.47	0.05	2.33	0.04
6	13-14	6.8	*C. wuellerstorfi*	0.33	0.06	2.67	0.03
7	14-15	7.1	*Cibicidoides* spp.	0.25	0.07	2.94	0.04
8	17-18	8.2	*Cibicidoides* spp.	-0.29	0.05	2.23	0.02
9	19-20	9.3	*Cibicidoides* spp.	0.11	0.03	2.86	0.03
10	21-22	10.9	*C. wuellerstorfi*	0.13	0.02	3.21	0.05
11	26-27	13.3	*C. wuellerstorfi*	0.03	0.03	3.42	0.04
12	28-29	14.1	*C. wuellerstorfi*	-0.46	0.07	3.67	0.03
13	29-30	15.1	*C. wuellerstorfi*	-0.41	0.06	2.98	0.03
14	31-33	15.5	*C. wuellerstorfi*	-0.04	0.03	3.44	0.04
15	33-35	15.8	*C. wuellerstorfi*	0.08	0.09	4.24	0.03
16	35-36	16.7	*C. wuellerstorfi*	-0.09	0.02	3.85	0.02
17	36-37	17.2	*C. wuellerstorfi*	-0.48	0.22	3.43	0.28
18	38-39	19.1	*C. wuellerstorfi*	-0.15	0.09	3.72	0.03

Table C.10: Carbon and oxygen isotope ratio of *cibicidoides species* for the core SS172/4040. *C. wuellerstorfi* refers to *Cibicidides wuellerstorfi* and *Cibicidoides* spp. refers to *Cibicidoides species.* Cal age is calendar age in kiloyears before present (ka BP).

S.N.	Depth (cm)	Cal age (ka)	Species	$\delta^{13}C$ (‰)	±1 σ $\delta^{13}C$ (‰)	$\delta^{18}O$ (‰)	±1 σ $\delta^{18}O$ (‰)
1	0-2	4.2	*C. wuellerstorfi*	0.44	0.07	2.64	0.04
2	13-14	11.8	*C. wuellerstorfi*	0.48	0.07	3.25	0.02
3	14-15	12.1	*C. wuellerstorfi*	0.17	0.09	2.95	0.05
4	16-17	13.0	*Cibicidoides* spp.	0.06	0.07	3.66	0.03
5	17-18	13.3	*C. wuellerstorfi*	0.30	0.14	3.50	0.04
6	19-20	13.9	*C. wuellerstorfi*	0.15	0.11	3.94	0.05
7	22-23	14.7	*C. wuellerstorfi*	-0.18	0.12	3.18	0.06
8	24-25	15.9	*C. wuellerstorfi*	0.51	0.06	3.40	0.02
9	27-28	18.3	*C. wuellerstorfi*	0.18	0.08	3.59	0.05
10	32-34	21.7	*Cibicidoides* spp.	-0.06	0.06	3.45	0.02
11	36-38	24.5	*Cibicidoides* spp.	0.12	0.11	3.09	0.04
12	38-40	25.5	*C. wuellerstorfi*	0.33	0.05	3.26	0.03
13	40-42	26.5	*Cibicidoides* spp.	0.19	0.07	3.16	0.03
14	42-44	27.1	*C. wuellerstorfi*	0.09	0.08	2.95	0.06
15	46-48	28.8	*Cibicidoides* spp.	0.31	0.06	3.27	0.05
16	48-50	30.91	*C. wuellerstorfi*	0.02	0.10	2.73	0.05
17	50-52	32.96	*C. wuellerstorfi*	0.11	0.05	2.99	0.02
18	56-58	35.87	*Cibicidoides* spp.	0.40	0.05	3.30	0.04
19	78-80	39.15	*Cibicidoides* spp.	0.04	0.10	3.24	0.03

Table C.11: Radiocarbon Results, calendar age calibrated using Calib8.2 and $\Delta^{14}C$ of the core SS152/3828 (planktic foraminifera).

S. N	Depth (cm)	Lab ID	Species	^{14}C age planktic (yrs BP)	±1 σ Error (yrs)	Cal age minima (yrs BP)	Cal age maxima (yrs BP)	Median Cal age (yrs BP)	±1 σ Error Cal age (yrs)	Fraction modern	±1 σ Fraction modern	$\Delta^{14}C$ (‰)
1	3-4	AURIS-02258	*G. ruber, G. sac*	2523	108	1990	2294	2142	152	0.73	0.01	-54
2	4-5	AURIS-01621	*G. ruber*	3164	45	2808	3000	2904	96	0.67	0.00	-42
3	9-10	AURIS-02301	*G. ruber*	5547	35	5747	5915	5831	84	0.50	0.00	16
4	12-13	AURIS-01623	*G. ruber*	6190	75	6415	6641	6528	113	0.46	0.00	19
5	16-17	AURIS-02299	*G. ruber*	7158	42	7467	7613	7540	73	0.41	0.00	23
6	18-19	AURIS-01619	*G. ruber*	8405	45	8800	9011	8906	106	0.35	0.00	31
7	19-20	AURIS-02296	*G. ruber*	8715	47	9236	9418	9327	91	0.34	0.00	46
8	22-24	AURIS-01605	*G. ruber*	10708	87	11873	12236	12055	182	0.26	0.00	133
9	24-25	AURIS-02294	*G. ruber*	11081	34	12478	12627	12553	75	0.25	0.00	161
10	26-27	AURIS-02292	*G. ruber*	11176	94	12524	12729	12627	103	0.25	0.00	146
11	28-29	AURIS-01603	*G. ruber*	12551	60	13986	14255	14121	135	0.21	0.00	157
12	29-30	AURIS-01599	*G. ruber*	13119	49	14946	15177	15062	116	0.20	0.00	208
13	33-35	AURIS-02290	*G. ruber*	13678	37	15671	15916	15794	123	0.18	0.00	231
14	35-36	AURIS-01597	*G. ruber*	14369	76	16539	16845	16692	153	0.17	0.00	259
15	36-37	AURIS-01595	*G. ruber*	14812	42	17084	17321	17203	119	0.16	0.00	267
16	37-38	AURIS-00880	*G. ruber*	15495	38	17956	18170	18063	107	0.15	0.00	292
17	38-39	AURIS-02258	*G. ruber, G. sac*	16453	199	18835	19326	19081	246	0.13	0.00	297

Table C.12: Radiocarbon Results, calendar age calibrated using Calib8.2 and $\Delta^{14}C$ of the core SS172/4040 (planktic foraminifera).

S. N	Depth (cm)	Lab ID	Species	^{14}C age $_{planktic}$ (yrs BP)	±1 σ Error (yrs)	Cal age maxima (yrs BP)	Cal age minima (yrs BP)	Median Cal age (yrs BP)	±1 σ Error Cal age (yrs)	Fraction modern	±1 σ Fraction modern	$\Delta^{14}C$ (‰)
1	3-4	AURIS-01652	*G. ruber*	5823	40	6058	6282	6170	112	0.48439	0.00239	22
2	5-6	AURIS-02256	*G. ruber*	7317	59	7611	7830	7721	110	0.40219	0.00296	23
3	8-9	AURIS-02254	*G. ruber*	8797	33	9328	9524	9426	98	0.33451	0.00138	46
4	12-13	AURIS-02252	*G. ruber*	10438	52	11485	11827	11656	171	0.27269	0.00177	117
5	14-15	AURIS-02250	*G. ruber*	10789	46	12066	12400	12233	167	0.26105	0.00149	146
6	15-16	AURIS-01650	*G. ruber*	11296	74	12656	12877	12767	111	0.24506	0.00225	148
7	18-19	AURIS-01647	*G. ruber*	12271	61	13617	13913	13765	148	0.21707	0.00164	147
8	20-21	AURIS-02247	*G. ruber*	12804	65	14399	14827	14613	214	0.20313	0.00164	190
9	21-22	AURIS-02245	*G. ruber*	12672	48	14146	14554	14350	204	0.20648	0.00122	171
10	23-24	AURIS-01646	*G. ruber*	13110	51	14939	15232	15086	147	0.19553	0.00123	213
11	24-25	AURIS-02228	*G. ruber*	14283	57	16447	16781	16614	167	0.16897	0.00120	261
12	25-26	AURIS-02226	*G. ruber*	13628	59	15607	15928	15768	161	0.18333	0.00134	235
13	26-27	AURIS-01644	*G. ruber*	15469	66	17921	18194	18058	137	0.14577	0.00119	295
14	27-28	AURIS-02224	*G. ruber*	15093	57	17431	17774	17603	172	0.15276	0.00109	284
15	28-29	AURIS-02221	*G. ruber*	17263	75	19932	20266	20099	167	0.11661	0.00108	326
16	29-30	AURIS-01631	*G. ruber*	16890	67	19482	19806	19644	162	0.12235	0.00103	317
17	30-32	AURIS-01629	*G. ruber*	19050	78	22112	22389	22251	139	0.09350	0.00091	380
18	32-34	AURIS-02199	*G. ruber*	18587	80	21575	21951	21763	188	0.09888	0.00099	375
19	34-36	AURIS-00875	*G. ruber*	21020	135	24179	24632	24406	227	0.07304	0.00123	399
20	36-38	AURIS-01627	*G. ruber*	21088	76	24291	24668	24480	189	0.07255	0.00069	402
21	40-42	AURIS-02197	*G. ruber*	23147	87	26473	26848	26661	188	0.05605	0.00061	410
22	44-46	AURIS-01625	*G. ruber*	24289	87	27568	27832	27700	132	0.04871	0.00053	389

23	46-48	AURIS-02194	*G. ruber*	23883	120	27214	27515	27365	151	0.05115	0.00076	401
24	50-52	AURIS-02192	*G. ruber*	29376	79	32957	33306	33132	175	0.02581	0.00025	420
25	56-58	AURIS-02190	*G. ruber*	32247	91	35871	36157	36014	143	0.01805	0.00021	408
26	64-66	AURIS-02188	*G. ruber*	33215	166	36805	37318	37062	257	0.01601	0.00033	417

Table C.13: Ventilation age reconstruction for the core SS152/3828: (B-P) age, (B-Atm) age, Projection age.

S. N	Depth (cm)	Bchron age (yrs BP)	±1 σ Error (yrs)	^{14}C age$_{planktic}$ (yrs BP)	±1 σ Error (yrs)	^{14}C age$_{Benthics}$ (yrs BP)	±1 σ Error (yrs)	B-P age (yrs)	±1 σ Error (yrs)	B-Atm (yrs)	±1 σ Error (yrs)	Projection age (yrs)
1	3-4	2103	322	2523	108	3232	45	708	117	1093	252	1310
2	4-5	2860	336	3164	45	3639	54	474	71	859	251	1044
3	9-10	5761	275	5547	35	5625	28	78	45	591	214	568
4	12-13	6468	170	6190	75	6360	65	169	99	667	178	741
5	16-17	7523	250	7158	42	8332	25	1174	49	1692	267	1782
6	18-19	8813	213	8405	45	8998	78	593	90	1037	178	1290
7	19-20	9278	323	8715	47	10519	52	1804	70	2234	176	3219
8	22-24	11897	326	10708	87	13122	79	2415	118	2896	177	3681
9	24-25	12462	112	11081	34	13489	50	2492	59	3052	94	3715
10	26-27	12697	194	11176	94	13496	49	2320	106	2819	202	3655
11	28-29	14026	345	12551	60	16335	101	3784	117	4198	267	5496
12	29-30	14917	228	13119	49	16251	53	3132	72	3714	146	4507
13	33-35	15758	191	13678	37	18825	57	5147	68	5681	147	7079
14	35-36	16610	209	14369	76	19904	86	5535	115	6175	160	7170
15	36-37	17165	209	14812	42	19831	110	5019	118	5707	206	6623
16	37-38	18000	297	15495	38	19921	85	4426	94	5238	261	5810
17	38-39	18928	385	16453	199	20483	107	4030	226	4793	384	5548

Table C.14: Ventilation age reconstruction for the core SS172/4040: (B-P) age, (B-Atm) age, Projection age.

S. N	Depth (cm)	Bchron age (yrs BP)	±1 σ Error (yrs)	^{14}C age$_{planktic}$ (yrs BP)	±1 σ Error (yrs)	^{14}C age$_{Benthics}$ (yrs BP)	±1 σ Error (yrs)	B-P age (yrs)	±1 σ Error (yrs)	B-Atm (yrs)	±1 σ Error (yrs)	Projection age (yrs)
1	3-4	6091	372	5823	40	6823	48	1000	62	1503	341	1501
2	5-6	7633	382	7317	59	8023	60	706	84	1204	388	1273
3	8-9	9347	369	8797	33	10699	67	1902	75	2363	279	3299
4	12-13	11474	269	10438	52	12440	63	2002	82	2428	195	3030
5	14-15	12094	167	10789	46	13639	36	2850	58	3301	87	4236
6	15-16	12667	200	11296	74	13553	42	2257	85	2925	117	3570
7	18-19	13643	177	12271	61	15028	52	2757	80	3227	177	4499
8	20-21	14174	127	12804	65	15722	54	2918	84	3447	121	4338
9	21-22	14370	139	12672	48	15672	61	3000	77	3293	91	4560
10	23-24	14986	252	13110	51	17048	85	3938	99	4462	176	5462
11	24-25	15946	437	14283	57	18610	71	4327	91	5323	303	5850
12	25-26	16680	548	13628	59	18719	101	5091	117	4939	390	6780
13	26-27	17724	542	15469	66	19189	63	3719	91	4669	432	4984
14	27-28	18290	541	15093	57	19991	73	4898	93	4913	473	6329
15	28-29	19139	497	17263	75	20179	90	2917	117	4286	449	4115
16	29-30	19658	401	16890	67	20220	66	3331	95	3890	330	4600
17	30-32	20849	426	19050	78	21909	62	2859	100	4624	327	3777
18	32-34	21745	412	18587	80	21820	96	3233	125	3940	345	4222
19	34-36	24039	359	21020	135	24698	132	3678	189	4649	340	4549
20	36-38	24466	230	21088	76	24797	114	3709	137	4418	202	4614
21	40-42	26518	286	23147	87	27732	77	4585	117	5412	243	5013
22	44-46	27600	290	24289	87	29832	85	5543	122	6468	384	6054
23	46-48	28849	909	23883	120	29158	134	5275	180	4458	897	6988
24	50-52	32962	592	29376	79	32069	112	2693	137	3451	416	3202

25	56-58	35868	295	32247	91	35841	180	3593	202	4363	380	4981
26	64-66	37062	299	33215	166	38074	208	4859	266	5338	340	5235

Table C.15: Radiocarbon results and $\Delta^{14}C$ of the core SS152/3828 (Benthic foraminifera).

S. N	Depth (cm)	Bchron age (yrs BP)	Lab ID	Species	^{14}C age Benthics (yrs BP)	±1 σ Error (yrs)	Fraction modern	±1 σ Fraction modern	$\Delta^{14}C$ (‰)
1	3-4	2103	AURIS-02259	*Epifaunal Benthics*	3232	45	0.66878	0.00376	-137.5
2	4-5	2860	AURIS-02257	*Epifaunal Benthics*	3639	54	0.63575	0.00431	-101.5
3	9-10	5761	AURIS-01620	*Epifaunal Benthics*	5625	28	0.49649	0.00171	-3.3
4	12-13	6468	AURIS-02300	*Epifaunal Benthics*	6360	65	0.45308	0.00369	-9.2
5	16-17	7523	AURIS-01622	*Epifaunal Benthics*	8332	25	0.35447	0.00112	-119.4
6	18-19	8813	AURIS-02298	*Epifaunal Benthics*	8998	78	0.32625	0.00317	-52.6
7	19-20	9278	AURIS-01618	*Epifaunal Benthics*	10519	52	0.26981	0.00173	-171.2
8	22-24	11897	AURIS-02295	*Epifaunal Benthics*	13122	79	0.19524	0.00192	-176.7
9	24-25	12462	AURIS-01608	*Epifaunal Benthics*	13489	50	0.18653	0.00115	-157.8
10	26-27	12697	AURIS-02293	*Epifaunal Benthics*	13496	49	0.18636	0.00114	-134.3
11	28-29	14026	AURIS-02291	*Epifaunal Benthics*	16335	101	0.13088	0.00164	-286.0
12	29-30	14917	AURIS-01602	*Epifaunal Benthics*	16251	53	0.13226	0.00088	-196.4
13	33-35	15758	AURIS-01598	*Epifaunal Benthics*	18825	57	0.09600	0.00068	-354.3
14	35-36	16610	AURIS-02289	*Epifaunal Benthics*	19904	86	0.08393	0.00090	-374.1
15	36-37	17165	AURIS-01596	*Epifaunal Benthics*	19831	110	0.08470	0.00116	-324.5
16	37-38	18000	AURIS-01594	*Epifaunal Benthics*	19921	85	0.08375	0.00089	-261.1

17	38-39	18928	AURIS-00879	*Mixed Benthics*	20483	107	0.07809	0.00104	-229.2

Table C.16: Radiocarbon Results and deep water Δ^{14}C of the core SS172/4040 (Benthic foraminifera)

S. N	Depth (cm)	Bchron age (yrs BP)	LAB ID	Species	^{14}C age $_{Benthics}$ (yrs BP)	±1 σ Error (yrs)	Fraction modern	±1 σ Fraction modern	Δ^{14}C (‰)
1	3-4	6091	AURIS-01651	*Epifaunal Benthics*	6823	48	0.42767	0.00255	-107
2	5-6	7633	AURIS-02255	*Mixed Benthics*	8023	60	0.36835	0.00276	-73
3	8-9	9347	AURIS-02253	*Mixed Benthics*	10699	67	0.26397	0.00222	-182
4	12-13	11474	AURIS-02251	*Epifaunal Benthics*	12440	63	0.21254	0.00166	-148
5	14-15	12094	AURIS-02249	*Epifaunal Benthics*	13639	36	0.18307	0.00082	-209
6	15-16	12667	AURIS-01649	*Epifaunal Benthics*	13553	42	0.18504	0.00096	-144
7	18-19	13643	AURIS-01648	*Epifaunal Benthics*	15028	52	0.15400	0.00099	-198
8	20-21	14174	AURIS-02246	*Epifaunal Benthics*	15722	54	0.14126	0.00095	-215
9	21-22	14370	AURIS-02244	*Epifaunal Benthics*	15672	61	0.14213	0.00107	-192
10	23-24	14986	AURIS-02229	*Infaunal Benthics*	17048	85	0.11976	0.00127	-266
11	24-25	15946	AURIS-01645	*Epifaunal Benthics*	18610	71	0.09860	0.00087	-321
12	25-26	16680	AURIS-02225	*Epifaunal Benthics*	18719	101	0.09727	0.00122	-268
13	26-27	17724	AURIS-01643	*Epifaunal Benthics*	19189	63	0.09175	0.00072	-217
14	27-28	18290	AURIS-02223	*Epifaunal Benthics*	19991	73	0.08303	0.00076	-241
15	28-29	19139	AURIS-02220	*Epifaunal Benthics*	20179	90	0.08110	0.00091	-179
16	29-30	19658	AURIS-01630	*Epifaunal Benthics*	20220	66	0.08065	0.00067	-130
17	30-32	20849	AURIS-01628	*Epifaunal Benthics*	21909	62	0.06540	0.00051	-186
18	32-34	21745	AURIS-02198	*Epifaunal Benthics*	21820	96	0.06612	0.00079	-82
19	34-36	24039	AURIS-00873	*Mixed Benthics*	24698	132	0.04621	0.00076	-154
20	36-38	24466	AURIS-01626	*Epifaunal Benthics*	24797	114	0.04564	0.00065	-120
21	40-42	26518	AURIS-02196	*Epifaunal Benthics*	27732	77	0.03167	0.00031	-217
22	44-46	27600	AURIS-02195	*Infaunal Benthics*	29832	85	0.02439	0.00026	-313
23	46-48	28849	AURIS-02193	*Epifaunal Benthics*	29158	134	0.02652	0.00044	-131
24	50-52	32962	AURIS-02191	*Epifaunal Benthics*	32069	112	0.01846	0.00026	-5

25	56-58	35868	AURIS-02189	*Epifaunal Benthics*	35841	180	0.01154	0.00026	-116
26	64-66	37062	AURIS-02187	*Epifaunal Benthics*	38074	208	0.00874	0.00023	-226

Table C.17: Radiocarbon Results and $\Delta^{14}C$ of the core SK312/09 (Benthic foraminifera)

S. N	Depth (cm)	Calendar ege (yrs BP)	LAB ID	Species	^{14}C age $_{Benthics}$ (yrs BP)	±1 σ Error (yrs)	Fraction modern	±1 σ Fraction modern	$\Delta^{14}C$ (‰)
1	1.5	4853	AURIS-03382	Mixed benthics	6390	54	0.45132	0.00306	-188.3
2	11	8183	AURIS-03379	Mixed benthics	10184	68	0.28144	0.00239	-242.7
3	20.5	12553	AURIS-03378	Mixed benthics	13399	90	0.18861	0.00211	-139.0
4	26.5	15767	AURIS-03375	Mixed benthics	14355	44	0.16746	0.000934	127.7
5	30.5	17687	AURIS-03373	Mixed benthics	17042	48	0.11984	0.000719	18.0
6	36.5	21875	AURIS-03372	Mixed benthics	20061	51	0.08230	0.000529	160.2
7	44.5	25183	AURIS-03370	Mixed benthics	23580	66	0.05311	0.00044	117.2
8	50.5	27501	AURIS-03369	Mixed benthics	24775	69	0.04577	0.000394	274.3
9	56.5	29464	AURIS-03367	Mixed benthics	26698	79	0.03602	0.000353	271.6
10	68.5	34351	AURIS-03365	Mixed benthics	30670	106	0.02197	0.00029	400.9

Table C.18: Ventilation age reconstruction for the core SK312/09: (B-P) age, Deep Reservoir age, Projection age.

S. N	Depth (cm)	Calendar age (yrs BP)	±1 σ Error (yrs)	^{14}C age planktic (yrs BP)	±1 σ Error (yrs)	^{14}C age Benthics (yrs BP)	±1 σ Error (yrs)	B-P age (yrs)	±1 σ Error yrs)	B-Atm (yrs)	±1 σ Error (yrs)	Projection age (yrs)
1	1.5	4853	4853	120	4796	35	6390	54	1594	64	2055	61
2	11	8183	8183	105	7899	36	10184	68	2285	77	2758	76
3	20.5	12553	12553	141	11183	107	13399	90	2216	140	2883	91
4	26.5	15767	15767	143	13764	40	14355	44	591	59	1167	63
5	30.5	17687	17687	164	15293	43	17042	48	1749	64	2545	67
6	36.5	21875	21875	190	18812	109	20061	51	1249	121	2090	70
7	44.5	25183	25183	166	21810	82	23580	66	1770	105	2666	86
8	50.5	27501	27501	160	24195	147	24775	69	580	162	1450	100
9	56.5	29464	29464	179	26104	74	26698	79	594	108	1410	95
10	68.5	34351	34351	125	30734	98	30670	106	-64	144	788	177
24	1.5	4853	4853	120	4796	35	6390	54	1594	64	2055	61
25	11	8183	8183	105	7899	36	10184	68	2285	77	2758	76
26	20.5	12553	12553	141	11183	107	13399	90	2216	140	2883	91

Table C.19: Ventilation age reconstruction for the core SK304/B12: (B-P) age, (B-Atm) age

Depth	Cal age (yrs BP)	Error (yrs)	LAB ID	Ben Libby age (yrs)	Error (yrs)	(B-P) age (yrs)	Error (yrs)	B-Atm age (yrs)	Error (yrs)
1.5	11397	150	AURIS-03503	16389	114	6120	122.931	6352	115
7.5	12314	168.5	AURIS-03347	15521	53	4659	87.0057	5106	55
11.5	13358	123	AURIS-03345	18653	57	6740	88.7299	7102	67
15.5	13806	160	AURIS-03343	17903	56	5615	98.4733	5870	64
19.5	13481	128	AURIS-03340	18649	60	6614	85.5628	7002	68
24.5	19750	220	AURIS-03338	32025	134	15038	190.924	15642	142
28.5	32572	301.5	AURIS-03336	30916	116	1916	178.751	2476	165
32.5	34037	167	AURIS-03334	31738	146	1533	197.497	2312	181
36.5	34364	153	AURIS-03332	33719	146	141	202.97	-515	186

Bibliography

Adkins, J.F., Boyle, E.A., 1997. Changing atmospheric $\Delta^{14}C$ and the record of deep water paleo ventilation ages. Paleoceanography 12, 337–344. doi:10.1029/97PA00379

Adkins, J.F., Cheng, H., Boyle, E.A., Druffel, E.R.M., Edwards, R.L., 1998. Deep-Sea Coral Evidence for Rapid Change in Ventilation of the Deep North Atlantic 15,400 Years Ago. Science 280, 725–728. doi:10.1126/science.280.5364.725

Adkins, J.F., McIntyre, K., Schrag, D.P., 2002. The Salinity, Temperature, and $\delta^{18}O$ of the Glacial Deep Ocean. Science 298, 1769–1773. doi:10.1126/science.1076252

Ahmad, S.M., Babu, G.A., Padmakumari, V.M., Raza, W., 2008. Surface and deep water changes in the northeast Indian Ocean during the last 60 ka inferred from carbon and oxygen isotopes of planktonic and benthic foraminifera. Palaeogeography, Palaeoclimatology, Palaeoecology 262, 182–188.

Ahmad, S.M., Zheng, H., Raza, W., Zhou, B., Lone, M.A., Raza, T., Suseela, G., 2012. Glacial to Holocene changes in the surface and deep waters of the northeast Indian Ocean. Marine Geology 329–331, 16–23. doi:10.1016/j.margeo.2012.10.002

Aken, H.M. van, Ridderinkhof, H., Ruijter, W.P.M. de, 2004. North Atlantic deep water in the south-western Indian Ocean. Deep Sea Research Part I: Oceanographic Research Papers 51, 755–776. doi:10.1016/j.dsr.2004.01.008

Almeida, F.K. de, Mello, R.M. de, Costa, K.B., Toledo, F.A.L., 2015. The response of deep-water benthic foraminiferal assemblages to changes in paleoproductivity during the Pleistocene (last 769.2 kyr), western South Atlantic Ocean. Palaeogeography, Palaeoclimatology, Palaeoecology 440, 201–212. doi:10.1016/j.palaeo.2015.09.005

Amakawa, H., Yu, T.-L., Tazoe, H., Obata, H., Gamo, T., Sano, Y., Shen, C.-C., Suzuki, K., 2019. Neodymium concentration and isotopic composition distributions in the southwestern Indian Ocean and the Indian sector of the Southern Ocean. Chemical Geology 511, 190–203. doi:10.1016/j.chemgeo.2019.01.007

Anderson, R.F., Ali, S., Bradtmiller, L.I., Nielsen, S.H.H., Fleisher, M.Q., Anderson, B.E., Burckle, L.H., 2009. Wind-driven upwelling in the Southern Ocean and the deglacial rise in atmospheric CO_2. Science 323, 1443–1448.

Banerjee, B., Ahmad, S.M., Babu, E.V.S.S.K., Padmakumari, V.M., Bejaa, S.K., Satyanarayanana, M., Krishna, A.K., 2019. Geochemistry and isotopic study of southern Bay of Bengal sediments: Implications for provenance and paleoenvironment during the middle Miocene. Palaeogeography, Palaeoclimatology, Palaeoecology 514, 156–167. doi:10.1016/j.palaeo.2018.10.022

Bard, E., 1998. Geochemical and geophysical implications of the radiocarbon calibration. Geochimica et Cosmochimica Acta 62, 2025–2038. doi:10.1016/S0016-7037(98)00130-6

Barker, S., Greaves, M., Elderfield, H., 2003. A study of cleaning procedures used for foraminiferal Mg/Ca paleothermometry. Geochemistry, Geophysics, Geosystems 4. doi:10.1029/2003GC000559

Barker, S., Knorr, G., Vautravers, M.J., Diz, P., Skinner, L.C., 2010. Extreme deepening of the Atlantic overturning circulation during deglaciation. Nat. Geosci. 3. doi:10.1038/ngeo921

Beaufort, L., 1997. Insolation Cycles as a Major Control of Equatorial Indian Ocean Primary Production. Science 278, 1451–1454. doi:10.1126/science.278.5342.1451

Bemis, B.E., Spero, H.J., Bijma, J., Lea, D.W., 1998. Reevaluation of the oxygen isotopic composition of planktonic foraminifera: Experimental results and revised

paleotemperature equations. Paleoceanography 13, 150–160. doi:10.1029/98PA00070
Benn, D., Evans, D.J.A., 2014. Glaciers and Glaciation, 2nd edition. Routledge.
Berben, S.M.P., Husum, K., Cabedo-Sanz, P., Belt, S.T., 2014. Holocene sub-centennial evolution of Atlantic water inflow and sea ice distribution in the western Barents Sea. Climate of the Past 10, 181–198. doi:10.5194/cp-10-181-2014
Berben, S.M.P., Husum, K., Navarro-Rodriguez, A., Belt, S.T., Aagaard-Sørensen, S., 2017. Semi-quantitative reconstruction of early to late Holocene spring and summer sea ice conditions in the northern Barents Sea. J. Quat. Sci. 32, 587–603. doi:https://doi.org/10.1002/jqs.2953
Berger, A., 1988. Milankovitch Theory and climate. Reviews of Geophysics 26, 624–657. doi:https://doi.org/10.1029/RG026i004p00624
Berggren, W.A., Miller, K.G., 1988. Paleogene tropical planktonic foraminiferal biostratigraphy and magnetobiochronology. Micropaleontology 34, 362–380.
Bernhard, J.M., 1989. The distribution of benthic Foraminifera with respect to oxygen concentration and organic carbon levels in shallow-water Antarctic sediments. Limnology and Oceanography 34, 1131–1141. doi:https://doi.org/10.4319/lo.1989.34.6.1131
Bernhard, J.M., 2000. Distinguishing Live from Dead Foraminifera: Methods Review and Proper Applications. Micropaleontology 46, 38–46.
Bernhard, J.M., Gupta, B.K.S., Borne, P.F., 1997. Benthic foraminiferal proxy to estimate dysoxic bottom-water oxygen concentrations; Santa Barbara Basin, U.S. Pacific continental margin. Journal of Foraminiferal Research 27, 301–310. doi:10.2113/gsjfr.27.4.301
Bernhard, J.M., Sen Gupta, B.K., Baguley, J.G., 2008. Benthic foraminifera living in Gulf of Mexico bathyal and abyssal sediments: Community analysis and comparison to metazoan meiofaunal biomass and density. Deep Sea Research Part II: Topical Studies in Oceanography, The Deep Gulf of Mexico Benthos Program 55, 2617–2626. doi:10.1016/j.dsr2.2008.07.011
Bertram, C.J., Elderfield, H., 1993. The geochemical balance of the rare earth elements and neodymium isotopes in the oceans. Geochimica et Cosmochimica Acta 57, 1957–1986. doi:10.1016/0016-7037(93)90087-D
Bharti, S.R., Verma, K., Singh, A.D., 2017. Potential Applicability of Benthic Foraminiferal Microhabitats in Deciphering Ocean-Bottom Oxygenation History of the Eastern Arabian Sea. In: Micropaleontology and Its Applications. Scientific Publishers (India).
Bhushan, R., Dutta, K., Somayajulu, B.L.K., 2001. Concentrations and burial fluxes of organic and inorganic carbon on the eastern margins of the Arabian Sea. Marine Geology 178, 95–113. doi:10.1016/S0025-3227(01)00179-7
Bhushan, R., Yadava, M.G., Shah, M.S., Banerji, U.S., Raj, H., Shah, C., Dabhi, A.K., 2019a. First results from the PRL accelerator mass spectrometer. Current Science (Bangalore) 116, 361–363.
Bhushan, R., Yadava, M.G., Shah, M.S., Raj, H., 2019b. Performance of a new 1MV AMS facility (AURiS) at PRL, Ahmedabad, India. Nuclear Instruments and Methods in Physics Research Section B: Beam Interactions with Materials and Atoms 439, 76–79. doi:10.1016/j.nimb.2018.12.003
Boersma, A., 1986. Eocene/Oligocene Atlantic Paleo-Oceanography Using Benthic Foraminifera. Developments in Palaeontology and Stratigraphy, termbal eocene events 9, 225–236. doi:10.1016/S0920-5446(08)70125-0
Böhm, E., Lippold, J., Gutjahr, M., Frank, M., Blaser, P., Antz, B., Fohlmeister, J., Frank, N., Andersen, M.B., Deininger, M., 2015. Strong and deep Atlantic meridional

overturning circulation during the last glacial cycle. Nature 517, 73–76. doi:10.1038/nature14059

Bolli, H.M., Bolli (Géologue), H.M., Beckmann, J.P., Saunders, J.B., Saunders, J.B., 1994. Benthic Foraminiferal Biostratigraphy of the South Caribbean Region. Cambridge University Press.

Bond, G., Heinrich, H., Broecker, W., Labeyrie, L., McManus, J., Andrews, J., Huon, S., Jantschik, R., Clasen, S., Simet, C., 1992. Evidence for massive discharges of icebergs into the North Atlantic ocean during the last glacial period. Nature 360, 245–249.

Broecker, W.S., Thurber, D.L., Goddard, J., Ku, T., Matthews, R.K., Mesolella, K.J., 1968. Milankovitch Hypothesis Supported by Precise Dating of Coral Reefs and Deep-Sea Sediments. Science 159, 297–300. doi:10.1126/science.159.3812.297

Broecker, W.S., Mix, A., Andree, M., Oeschger, H., 1984. Radiocarbon measurements on coexisting benthic and planktic foraminifera shells: potential for reconstructing ocean ventilation times over the past 20 000 years. Nuclear Instruments and Methods in Physics Research Section B: Beam Interactions with Materials and Atoms 5, 331–339. doi:10.1016/0168-583X(84)90538-X

Broecker, W.S., Matsumoto, K., Clark, E., Hajdas, I., Bonani, G., 1999. Radiocarbon age differences between coexisting foraminiferal species. Paleoceanography 14, 431–436. doi:https://doi.org/10.1029/1999PA900019

Broecker, W.S., Clark, E., Hajdas, I., Bonani, G., 2004a. Glacial ventilation rates for the deep Pacific Ocean. Paleoceanography 19. doi:https://doi.org/10.1029/2003PA000974

Broecker, W.S., Barker, S., Clark, E., Hajdas, I., Bonani, G., Stott, L., 2004b. Ventilation of the glacial deep Pacific Ocean. Science 306, 1169–1172.

Broecker, W.S., Clark, E., Barker, S., 2008. Near constancy of the Pacific Ocean surface to mid-depth radiocarbon-age difference over the last 20 kyr. Earth and Planetary Science Letters 274, 322–326.

Brovkin, V., Ganopolski, A., Archer, D., Rahmstorf, S., 2007. Lowering of glacial atmospheric CO_2 in response to changes in oceanic circulation and marine biogeochemistry. Paleoceanography 22. doi:https://doi.org/10.1029/2006PA001380

Bryan, S.P., Marchitto, T.M., Lehman, S.J., 2010. The release of ^{14}C-depleted carbon from the deep ocean during the last deglaciation: Evidence from the Arabian Sea. Earth and Planetary Science Letters 298, 244–254.

Burke, A., Robinson, L.F., 2012. The Southern Ocean’s Role in Carbon Exchange During the Last Deglaciation. Science 335, 557–561. doi:10.1126/science.1208163

Carson, B.E., Francis, J.M., Leckie, R.M., Droxler, A.W., Dickens, G.R., Jorry, S.J., Bentley, S.J., Peterson, L.C., Opdyke, B.N., 2008. Benthic Foraminiferal response to sea level change in the mixed siliciclastic-carbonate system of southern Ashmore Trough (Gulf of Papua). Journal of Geophysical Research 113, F01S20. doi:10.1029/2006JF000629

Chandana, K.R., Bhushan, R., Jull, A.J.T., 2017. Evidence of Poor Bottom Water Ventilation during LGM in the Equatorial Indian Ocean. Frontiers in Earth Science 5, 84. doi:10.3389/feart.2017.00084

Chandana, K.R., Banerji, U.S., Bhushan, R., 2018. Review on Indian summer monsoon (ISM) reconstruction since LGM from Northern Indian Ocean. Earth Science India 11.

Chen, T., Robinson, L.F., Burke, A., Southon, J., Spooner, P., Morris, P.J., Ng, H.C., 2015. Synchronous centennial abrupt events in the ocean and atmosphere during the last deglaciation. Science 349, 1537–1541.

Clark, P.U., Dyke, A.S., Shakun, J.D., Carlson, A.E., Clark, J., Wohlfarth, B., Mitrovica, J.X., Hostetler, S.W., McCabe, A.M., 2009. The Last Glacial Maximum. Science 325, 710–714. doi:10.1126/science.1172873

Clemens, S.C., Prell, W.L., Howard, W.R., 1987. Retrospective dry bulk density estimates from southeast Indian Ocean sediments — Comparison of water loss and chloride-ion methods. Marine Geology 76, 57–69. doi:10.1016/0025-3227(87)90017-X

Corliss, B.H., 1978. Studies of deep-sea benthonic foraminifera in the southeast indian-ocean. Antarctic Journal of the United States 13, 116–118.

Corliss, B.H., 1979. Recent deep-sea benthonic foraminiferal distributions in the southeast Indian Ocean: Inferred bottom-water routes and ecological implications. Marine Geology 31, 115–138.

Corliss, B.H., 1985. Microhabitats of benthic foraminifera within deep-sea sediments. Nature 314, 435–438. doi:10.1038/314435a0

Corliss, B.H., Chen, C., 1988. Morphotype patterns of Norwegian Sea deep-sea benthic foraminifera and ecological implications. Geology 16, 716–719.

Corliss, B.H., Emerson, S., 1990. Distribution of Rose Bengal stained deep-sea benthic foraminifera from the Nova Scotian continental margin and Gulf of Maine. Deep Sea Research Part A. Oceanographic Research Papers 37, 381–400.

Culver, S.J., 1991. Early Cambrian Foraminifera from West Africa. Science 254, 689–691. doi:10.1126/science.254.5032.689

Curry, W.B., Oppo, D.W., 2005. Glacial water mass geometry and the distribution of $\delta^{13}C$ of ΣCO_2 in the western Atlantic Ocean. Paleoceanography 20. doi:https://doi.org/10.1029/2004PA001021

Curry, W.B., Duplessy, J.C., Labeyrie, L.D., Shackleton, N.J., 1988. Changes in the distribution of $\delta^{13}C$ of deep water ΣCO_2 between the last glaciation and the Holocene. Paleoceanography 3, 317–341.

Dang, H., Jian, Z., Wu, J., Bassinot, F., Wang, T., Kissel, C., 2018. The calcification depth and Mg/Ca thermometry of Pulleniatina obliquiloculata in the tropical Indo-Pacific: A core-top study. Marine Micropaleontology 145, 28–40.

De Deckker, P., 2016. The Indo-Pacific Warm Pool: critical to world oceanography and world climate. Geoscience Letters 3, 20. doi:10.1186/s40562-016-0054-3

De, S., Gupta, A.K., 2010. Deep-sea faunal provinces and their inferred environments in the Indian Ocean based on distribution of Recent benthic foraminifera. Palaeogeography, Palaeoclimatology, Palaeoecology 291, 429–442. doi:10.1016/j.palaeo.2010.03.012

Devendra, D., Xiang, R., Zhong, F., Yang, Y., Tang, L., 2019. Palaeoproductivity and associated changes in the north-eastern Indian Ocean since the last glacial: Evidence from benthic foraminifera and stable isotopes. Journal of Asian Earth Sciences 181, 103913.

DeVries, T., Primeau, F., 2010. An improved method for estimating water-mass ventilation age from radiocarbon data. Earth and Planetary Science Letters 295, 367–378. doi:10.1016/j.epsl.2010.04.011

Dinauer, A., Adolphi, F., Joos, F., 2020. Mysteriously high $\Delta^{14}C$ of the glacial atmosphere: influence of ^{14}C production and carbon cycle changes. Climate of the Past 16, 1159–1185. doi:10.5194/cp-16-1159-2020

Donohue, K.A., Toole, J.M., 2003. A near-synoptic survey of the Southwest Indian Ocean. Deep Sea Research Part II: Topical Studies in Oceanography, Physical Oceanography of the Indian Ocean: from WOCE to CLIVAR 50, 1893–1931. doi:10.1016/S0967-0645(03)00039-0

Dowsett, H.J., 2007. Paleooceanography, Biological Proxies | Planktic Foraminifera. In: Elias, S.A. (Ed.), Encyclopedia of Quaternary Science. Elsevier, Oxford, pp. 1678–1682. doi:10.1016/B0-44-452747-8/00295-7

Drinia, H., Anastasakis, G., 2012. Benthic foraminifer palaeoecology of the Late Quaternary continental outer shelf of a landlocked marine basin in central Aegean Sea, Greece.

Quaternary International, IGCP 521: Caspian-Black Sea –Mediterranean Corridors during the last 30 ka: sea level change and human adaptive strategies Selected Papers 261, 43–52. doi:10.1016/j.quaint.2011.07.003

Duplessy, J.C., 1988. Deepwater source variations during the last climatic cycle and their impact on the global deepwater circulation. Paleoceanography 3.

Duplessy, J.C., Moyes, J., Pujol, C., 1980. Deep water formation in the North Atlantic Ocean during the last ice age. Nature 286, 479–482.

Dutta, K., Bhushan, R., Somayajulu, B.L.K., 2001. ΔR correction values for the northern Indian Ocean. Radiocarbon 43, 483–488.

Elliot, M., Labeyrie, L., Duplessy, J.C., 2002. Changes in North Atlantic deep-water formation associated with the Dansgaard–Oeschger temperature oscillations (60–10 ka). Quaternary Science Reviews 21, 1153–1165.

Emiliani, C., 1955. Pleistocene Temperatures. The Journal of Geology 63, 538–578. doi:10.1086/626295

Ernst, S., Zwaan, G.J.V.D., 2004. Effects of experimentally induced raised levels of organic flux and oxygen depletion on a continental slope benthic foraminiferal community. Deep Sea Research Part I: Oceanographic Research Papers 51, 1709–1739. doi:10.1016/j.dsr.2004.06.003

Fariduddin, M., Loubere, P., 1997. The surface ocean productivity response of deeper water benthic foraminifera in the Atlantic Ocean. Marine Micropaleontology 32, 289–310. doi:10.1016/S0377-8398(97)00026-1

Faure, G., 1986. Isotope systematics in two-component mixtures. Principles of isotope geology 141–153.

Fisher, R.L., Johnson, G.L., Heezen, B.C., 1967. Mascarene Plateau, Western Indian Ocean. GSA Bulletin 78, 1247–1266. doi:10.1130/0016-7606(1967)78[1247:MPWIO]2.0.CO;2

Fontanier, C., Jorissen, F.J., Licari, L., Alexandre, A., Anschutz, P., Carbonel, P., 2002. Live benthic foraminiferal faunas from the Bay of Biscay: faunal density, composition, and microhabitats. Deep Sea Research Part I: Oceanographic Research Papers 49, 751–785. doi:10.1016/S0967-0637(01)00078-4

Franois, R., Altabet, M.A., Yu, E.-F., Sigman, D.M., Bacon, M.P., Frank, M., Bohrmann, G., Bareille, G., Labeyrie, L.D., 1997. Contribution of Southern Ocean surface-water stratification to low atmospheric CO_2 concentrations during the last glacial period. Nature 389, 929–935.

Freeman, E., Skinner, L.C., Waelbroeck, C., Hodell, D., 2016. Radiocarbon evidence for enhanced respired carbon storage in the Atlantic at the Last Glacial Maximum. Nature Communications 7, 11998. doi:10.1038/ncomms11998

Frontalini, F., Coccioni, R., 2008. Benthic foraminifera for heavy metal pollution monitoring: A case study from the central Adriatic Sea coast of Italy. Estuarine, Coastal and Shelf Science 76, 404–417. doi:10.1016/j.ecss.2007.07.024

Fuente, M. de la, Skinner, L.C., Calvo, E., Pelejero, C., Cacho, I., 2015. Increased reservoir ages and poorly ventilated deep waters inferred in the glacial Eastern Equatorial Pacific. Nature Communications 6, 7420. doi:10.1038/ncomms8420

Galbraith, E.D., Skinner, L.C., 2020. The biological pump during the Last Glacial Maximum. Annual review of marine science 12, 559–586.

Galbraith, E.D., Jaccard, S.L., Pedersen, T.F., Sigman, D.M., Haug, G.H., Cook, M., Southon, J.R., Francois, R., 2007. Carbon dioxide release from the North Pacific abyss during the last deglaciation. Nature 449, 890–893. doi:10.1038/nature06227

Galbraith, E.D., Kwon, E.Y., Bianchi, D., Hain, M.P., Sarmiento, J.L., 2015. The impact of atmospheric pCO_2 on carbon isotope ratios of the atmosphere and ocean. Global Biogeochemical Cycles 29, 307–324.

Gamo, T., Chiba, H., Yamanaka, T., Okudaira, T., Hashimoto, J., Tsuchida, S., Ishibashi, J., Kataoka, S., Tsunogai, U., Okamura, K., Sano, Y., Shinjo, R., 2001. Chemical characteristics of newly discovered black smoker fluids and associated hydrothermal plumes at the Rodriguez Triple Junction, Central Indian Ridge. Earth and Planetary Science Letters 193, 371–379. doi:10.1016/S0012-821X(01)00511-8

Gherardi, J.M., Labeyrie, L., McManus, J.F., Francois, R., Skinner, L.C., Cortijo, E., 2005. Evidence from the Northeastern Atlantic basin for variability in the rate of the meridional overturning circulation through the last deglaciation. Earth and Planetary Science Letters 240, 710–723. doi:10.1016/j.epsl.2005.09.061

Goldstein, S.J., Lea, D.W., Chakraborty, S., Kashgarian, M., Murrell, M.T., 2001. Uranium-series and radiocarbon geochronology of deep-sea corals: implications for Southern Ocean ventilation rates and the oceanic carbon cycle. Earth and Planetary Science Letters 193, 167–182. doi:10.1016/S0012-821X(01)00494-0

Goldstein, S.T., Corliss, B.H., 1994. Deposit feeding in selected deep-sea and shallow-water benthic foraminifera. Deep Sea Research Part I: Oceanographic Research Papers 41, 229–241. doi:10.1016/0967-0637(94)90001-9

Gooday, A.J., 1993. Deep-sea benthic foraminiferal species which exploit phytodetritus: Characteristic features and controls on distribution. Marine Micropaleontology 22, 187–205. doi:10.1016/0377-8398(93)90043-W

Gooday, A.J., 1994. The biology of deep-sea foraminifera: a review of some advances and their significance in paleoecology. Palaios 9, 14–31.

Gooday, A.J., 1996. Epifaunal and shallow infaunal foraminiferal communities at three abyssal NE Atlantic sites subject to differing phytodetritus input regimes. Deep Sea Research Part I: Oceanographic Research Papers 43, 1395–1421.

Gooday, A.J., Rathburn, A.E., 1999. Temporal variability in living deep-sea benthic foraminifera: a review. Earth-Science Reviews 46, 187–212. doi:10.1016/S0012-8252(99)00010-0

Gooday, A.J., Levin, L.A., Linke, P., Heeger, T., 1992. The Role of Benthic Foraminifera in Deep-Sea Food Webs and Carbon Cycling. In: Rowe, G.T., Pariente, V. (Eds.), Deep-Sea Food Chains and the Global Carbon Cycle. Springer Netherlands, Dordrecht, pp. 63–91. doi:10.1007/978-94-011-2452-2_5

Gooday, A.J., Aranda da Silva, A., Pawlowski, J., 2011. Xenophyophores (Rhizaria, Foraminifera) from the Nazaré Canyon (Portuguese margin, NE Atlantic). Deep Sea Research Part II: Topical Studies in Oceanography 58, 2401–2419. doi:10.1016/j.dsr2.2011.04.005

Gornitz, V. (Ed.), 2009. Encyclopedia of paleoclimatology and ancient environments, Encyclopedia of earth sciences series. Springer, Dordrecht.

Goswami, V., Singh, S.K., Bhushan, R., 2014. Impact of water mass mixing and dust deposition on Nd concentration and εNd of the Arabian Sea water column. Geochimica et Cosmochimica Acta 145, 30–49. doi:10.1016/j.gca.2014.09.006

Gottschalk, J., n.d. Glacial heterogeneity in Southern Ocean carbon storage abated by fast South Indian deglacial carbon release 14.

Gottschalk, J., Riveiros, N.V., Waelbroeck, C., Skinner, L.C., Michel, E., Duplessy, J.C., Hodell, D.A., Mackensen, A., 2016. Stable oxygen and carbon isotopes of *C. wuellerstorfi*, *C. kullenbergi* and *Uvigerina* spp. from TN057-6GC (sub-Antarctic Atlantic) over the last 29 kyrs. doi:10.1594/PANGAEA.858264

Gottschalk, J., Michel, E., Thöle, L.M., Studer, A.S., Hasenfratz, A.P., Schmid, N., Butzin, M., Mazaud, A., Martínez-García, A., Szidat, S., 2020. Glacial heterogeneity in Southern Ocean carbon storage abated by fast South Indian deglacial carbon release. Nature communications 11, 1–14.

Gray, W.R., Rae, J.W.B., Wills, R.C.J., Shevenell, A.E., Taylor, B., Burke, A., Foster, G.L., Lear, C.H., 2018. Deglacial upwelling, productivity and CO_2 outgassing in the North Pacific Ocean. Nature Geoscience 11, 340–344. doi:10.1038/s41561-018-0108-6

Groeneveld, J., Hathorne, E.C., Steinke, S., DeBey, H., Mackensen, A., Tiedemann, R., 2014. Glacial induced closure of the Panamanian gateway during Marine Isotope Stages (MIS) 95–100 (~ 2.5 Ma). Earth and Planetary Science Letters 404, 296–306.

Gupta, A.K., Srinivasan, M.S., 1992. *Uvigerina proboscidea* abundances and paleoceanography of the northern Indian Ocean DSDP Site 214 during the Late Neogene. Marine Micropaleontology 19, 355–367. doi:10.1016/0377-8398(92)90038-L

Gupta, A.K., Thomas, E., 1999. Latest Miocene-Pleistocene Productivity and Deep-Sea Ventilation in the Northwestern Indian Ocean (Deep Sea Drilling Project Site 219). Paleoceanography 14, 62–73. doi:https://doi.org/10.1029/1998PA900006

Gupta, A.K., Thomas, E., 2003. Initiation of Northern Hemisphere glaciation and strengthening of the northeast Indian monsoon: Ocean Drilling Program Site 758, eastern equatorial Indian Ocean. Geology 31, 47–50.

Gupta, A.K., Sarkar, S., Mukherjee, B., 2006. Paleoceanographic changes during the past 1.9 Myr at DSDP Site 238, Central Indian Ocean Basin: Benthic foraminiferal proxies. Marine Micropaleontology 60, 157–166. doi:10.1016/j.marmicro.2006.04.001

Gupta, B.K.S., 1999. Modern foraminifera. Springer.

Hain, M.P., Sigman, D.M., Haug, G.H., 2014. Distinct roles of the Southern Ocean and North Atlantic in the deglacial atmospheric radiocarbon decline. Earth and Planetary Science Letters 394, 198–208. doi:10.1016/j.epsl.2014.03.020

Haine, T.W.N., Watson, A.J., Liddicoat, M.I., Dickson, R.R., 1998. The flow of Antarctic bottom water to the southwest Indian Ocean estimated using CFCs. Journal of Geophysical Research: Oceans 103, 27637–27653. doi:10.1029/98JC02476

Handmann, P., Fischer, J., Visbeck, M., Karstensen, J., Biastoch, A., Böning, C., Patara, L., 2018. The deep western boundary current in the Labrador Sea from observations and a high-resolution model. Journal of Geophysical Research: Oceans 123, 2829–2850.

Hayward, B.W., Sabaa, A.T., Thomas, E., Kawagata, S., Nomura, R., Schröder-Adams, C., Gupta, A.K., Johnson, K., 2010. Cenozoic record of elongate, cylindrical, deep-sea benthic foraminifera in the Indian Ocean (ODP Sites 722, 738, 744, 758, and 763). Journal of Foraminiferal Research 40, 113–133. doi:10.2113/gsjfr.40.2.113

Hayward, B.W., Sabaa, A.T., Grenfell, H.R., Neil, H., Bostock, H., 2013. Ecological distribution of recent deep-water foraminifera around New Zealand. Journal of Foraminiferal Research 43, 415–442. doi:10.2113/gsjfr.43.4.415

Hayward, B.W., Coze, F.L., Vandepitte, L., Vanhoorne, B., 2020. Foraminifera in the World Register of Marine Species (Worms) Taxonomic Database. Journal of Foraminiferal Research 50, 291–300. doi:10.2113/gsjfr.50.3.291

Heaton, T.J., Köhler, P., Butzin, M., Bard, E., Reimer, R.W., Austin, W.E.N., Ramsey, C.B., Abbott, P.M., Hughen, K.A., Kromer, B., Heniriques, P.J., Adkins, J., Burke, A., Cook, M.S., Olsen, J., Skinner, L.C., 2020. Marine20—The Marine Radiocarbon Age Calibration Curve (0–55,000 cal BP). Radiocarbon 62, 779–820. doi:10.1017/RDC.2020.68

Heezen, B.C., Nafe, J.E., 1964. Vema trench: western Indian Ocean. Deep Sea Research and Oceanographic Abstracts 11, 79–84. doi:10.1016/0011-7471(64)91083-6

Heinrich, H., 1988. Origin and consequences of cyclic ice rafting in the Northeast Atlantic Ocean during the past 130,000 years. Quaternary Research 29, 142–152. doi:10.1016/0033-5894(88)90057-9

Henry, L.G., McManus, J.F., Curry, W.B., Roberts, N.L., Piotrowski, A.M., Keigwin, L.D., 2016. North Atlantic ocean circulation and abrupt climate change during the last glaciation. Science 353, 470–474. doi:10.1126/science.aaf5529

Herguera, J.C., Berger, W.H., 1991. Paleoproductivity from benthic foraminifera abundance: Glacial to postglacial change in the west-equatorial Pacific. Geology 19, 1173–1176.

Hines, S.K., Southon, J.R., Adkins, J.F., 2015. A high-resolution record of Southern Ocean intermediate water radiocarbon over the past 30,000 years. Earth and Planetary Science Letters 432. doi:10.1016/j.epsl.2015.09.038

Hodell, D.A., Nicholl, J.A., Bontognali, T.R.R., Danino, S., Dorador, J., Dowdeswell, J.A., Einsle, J., Kuhlmann, H., Martrat, B., Mleneck-Vautravers, M.J., Rodríguez-Tovar, F.J., Röhl, U., 2017. Anatomy of Heinrich Layer 1 and its role in the last deglaciation. Paleoceanography 32, 284–303. doi:10.1002/2016PA003028

Howe, J.N.W., Piotrowski, A.M., Noble, T.L., Mulitza, S., Chiessi, C.M., Bayon, G., 2016. North Atlantic deep water production during the Last Glacial Maximum. Nature communications 7, 1–8.

Hughen, K.A., 2007. Chapter Five Radiocarbon Dating of Deep-Sea Sediments. In: Hillaire–Marcel, C., De Vernal, A. (Eds.), Developments in Marine Geology, Proxies in Late Cenozoic Paleoceanography. Elsevier, pp. 185–210. doi:10.1016/S1572-5480(07)01010-X

Hughes, P.D., Gibbard, P.L., Ehlers, J., 2013. Timing of glaciation during the last glacial cycle: evaluating the concept of a global 'Last Glacial Maximum' (LGM). Earth-Science Reviews 125, 171–198. doi:10.1016/j.earscirev.2013.07.003

Imbrie, J., Boyle, E.A., Clemens, S.C., Duffy, A., Howard, W.R., Kukla, G., Kutzbach, J., Martinson, D.G., McIntyre, A., Mix, A.C., Molfino, B., Morley, J.J., Peterson, L.C., Pisias, N.G., Prell, W.L., Raymo, M.E., Shackleton, N.J., Toggweiler, J.R., 1992. On the Structure and Origin of Major Glaciation Cycles 1. Linear Responses to Milankovitch Forcing. Paleoceanography 7, 701–738. doi:https://doi.org/10.1029/92PA02253

Ishibashi, J., Okino, K., Sunamura, M., 2015. Subseafloor Biosphere Linked to Hydrothermal Systems: TAIGA Concept. Springer.

Jayasankar, T., Murtugudde, R., Eldho, T.I., 2019. The Indian Ocean Deep Meridional Overturning Circulation in Three Ocean Reanalysis Products. Geophysical Research Letters 46, 12146–12155. doi:10.1029/2019GL084244

Johnson, G.C., Musgrave, D.L., Warren, B.A., Ffield, A., Olson, D.B., 1998. Flow of bottom and deep water in the Amirante Passage and Mascarene Basin. Journal of Geophysical Research: Oceans 103, 30973–30984. doi:10.1029/1998JC900027

Jorissen, F.J., 2003. Benthic foraminiferal microhabitats below the sediment-water interface. In: Gupta, B.K.S. (Ed.), Modern Foraminifera. Springer Netherlands, Dordrecht, pp. 161–179. doi:10.1007/0-306-48104-9_10

Jorissen, F.J., Stigter, H.C. de, Widmark, J.G.V., 1995. A conceptual model explaining benthic foraminiferal microhabitats. Marine Micropaleontology 26, 3–15. doi:10.1016/0377-8398(95)00047-X

Jorissen, F.J., Fontanier, C., Thomas, E., 2007. Chapter Seven Paleoceanographical Proxies Based on Deep-Sea Benthic Foraminiferal Assemblage Characteristics. In: Developments in Marine Geology. Elsevier, pp. 263–325. doi:10.1016/S1572-5480(07)01012-3

Kaiho, K., 1991. Global changes of Paleogene aerobic/anaerobic benthic foraminifera and deep-sea circulation. Palaeogeography, Palaeoclimatology, Palaeoecology, The Oceans of the Paleogene 83, 65–85. doi:10.1016/0031-0182(91)90076-4

Kaiho, K., 1994. Benthic foraminiferal dissolved-oxygen index and dissolved-oxygen levels in the modern ocean. Geology 22, 719–722.

Kaminski, M.A., Gradstein, F.M., Berggren, W.A., Geroch, S., Beckmann, J.P., 1988. Flysch-type agglutinated foraminiferal assemblages from Trinidad: taxonomy, stratigraphy and paleobathymetry. Abhandlungen der geologischen Bundesanstalt 41, 155–227.

Keigwin, L.D., Schlegel, M.A., 2002. Ocean ventilation and sedimentation since the glacial maximum at 3 km in the western North Atlantic. Geochemistry, Geophysics, Geosystems 3, 1–14. doi:https://doi.org/10.1029/2001GC000283

Kemle-von Mücke, S., Oberhänsli, H., 1999. The Distribution of Living Planktic Foraminifera in Relation to Southeast Atlantic Oceanography. In: Fischer, G., Wefer, G. (Eds.), Use of Proxies in Paleoceanography: Examples from the South Atlantic. Springer, Berlin, Heidelberg, pp. 91–115. doi:10.1007/978-3-642-58646-0_3

Key, R.M., 2001. Radiocarbon. In: Steele, J.H. (Ed.), Encyclopedia of Ocean Sciences. Academic Press, Oxford, pp. 2338–2353. doi:10.1006/rwos.2001.0162

Key, R.M., 2004. A global ocean carbon climatology: results from global data analysis project (GLODAP). Global Biogeochem. Cycles 18. doi:10.1029/2004GB002247

Kim, J., Kim, Y., Kang, H.-W., Kim, S.H., Rho, T., Kang, D.-J., 2020. Tracing water mass fractions in the deep western Indian Ocean using fluorescent dissolved organic matter. Marine Chemistry 218, 103720. doi:10.1016/j.marchem.2019.103720

Köhler, P., Muscheler, R., Fischer, H., 2006. A model-based interpretation of low-frequency changes in the carbon cycle during the last 120,000 years and its implications for the reconstruction of atmospheric $\Delta^{14}C$. Geochemistry, Geophysics, Geosystems 7. doi:https://doi.org/10.1029/2005GC001228

Kolla, V., Bé, A.W.H., Biscaye, P.E., 1976a. Calcium carbonate distribution in the surface sediments of the Indian Ocean. Journal of Geophysical Research 81, 2605–2616. doi:10.1029/JC081i015p02605

Kolla, V., Bé, A.. W., Biscaye, P.E., 1976b. Calcium carbonate distribution in the surface sediments of the Indian Ocean. Journal of Geophysical Research 81, 2605–2616.

Kuhnt, W., Collins, E., Scott, D.B., 2000. Deep water agglutinated foraminiferal assemblages across the Gulf Stream: distribution patterns and taphonomy. In: Proceedings of the Fifth International Workshop on Agglutinated Foraminifera. Grzybowski Foundation Special Publication. pp. 261–298.

Kumar, G.S., Prakash, S., Ravichandran, M., Narayana, A.C., 2016. Trends and relationship between chlorophyll- *a* and sea surface temperature in the central equatorial Indian Ocean. Remote Sensing Letters 7, 1093–1101. doi:10.1080/2150704X.2016.1210835

Kumar, M.D., Li, Y.-H., 1996. Spreading of water masses and regeneration of silica and ^{226}Ra in the Indian Ocean. Deep Sea Research Part II: Topical Studies in Oceanography 43, 83–110.

Lathika, N., Rahaman, W., Tarique, M., Gandhi, N., Kumar, A., Thamban, M., 2021. Deep water circulation in the Arabian Sea during the last glacial cycle: Implications for paleo-redox condition, carbon sink and atmospheric CO_2 variability. Quaternary Science Reviews 257, 106853. doi:10.1016/j.quascirev.2021.106853

Lea, D., Boyle, E., 1989. Barium content of benthic foraminifera controlled by bottom-water composition. Nature 338, 751–753. doi:10.1038/338751a0

Lee, J.-M., Boyle, E.A., Gamo, T., Obata, H., Norisuye, K., Echegoyen, Y., 2015. Impact of anthropogenic Pb and ocean circulation on the recent distribution of Pb isotopes in the Indian Ocean. Geochimica et Cosmochimica Acta 170, 126–144. doi:10.1016/j.gca.2015.08.013

Lejzerowicz, F., Pawlowski, J., Fraissinet-Tachet, L., Marmeisse, R., 2010. Molecular evidence for widespread occurrence of Foraminifera in soils. Environmental Microbiology 12, 2518–2526. doi:https://doi.org/10.1111/j.1462-2920.2010.02225.x

Linke, P., Lutze, G.F., 1993. Microhabitat preferences of benthic foraminifera—a static concept or a dynamic adaptation to optimize food acquisition? Marine Micropaleontology 20, 215–234. doi:10.1016/0377-8398(93)90034-U

Liu, E., Wang, X.-C., Zhao, J., Wang, X., 2015. Geochemical and Sr–Nd isotopic variations in a deep-sea sediment core from Eastern Indian Ocean: Constraints on dust provenances, paleoclimate and volcanic eruption history in the last 300,000 years. Marine Geology 367, 38–49.

Loeblich, A.R., Tappan, H., 1987. Foraminiferal Genera and Their Classification. Springer.

Lohrenz, S.E., Knauer, G.A., Asper, V.L., Tuel, M., Michaels, A.F., Knap, A.H., 1992. Seasonal variability in primary production and particle flux in the northwestern Sargasso Sea: U.S. JGOFS Bermuda Atlantic time-series study. Deep Sea Research Part I: Oceanographic Research Papers 39, 1373–1391. doi:10.1016/0198-0149(92)90074-4

Loubere, P., 1991. Deep-Sea Benthic Foraminiferal Assemblage Response to a Surface Ocean Productivity Gradient: A Test. Paleoceanography 6, 193–204. doi:10.1029/90PA02612

Loubere, P., 1998. The impact of seasonality on the benthos as reflected in the assemblages of deep-sea foraminifera. Deep Sea Research Part I: Oceanographic Research Papers 45, 409–432. doi:10.1016/S0967-0637(97)00092-7

Loubere, P., 2003. Remote vs. local control of changes in eastern equatorial Pacific bioproductivity from the Last Glacial Maximum to the Present. Global and Planetary Change 35, 113–126. doi:10.1016/S0921-8181(02)00139-X

Loubere, P., Fariduddin, M., 2003. Benthic Foraminifera and the flux of organic carbon to the seabed. In: Sen Gupta, B.K. (Ed.), Modern Foraminifera. Springer Netherlands, Dordrecht, pp. 181–199. doi:10.1007/0-306-48104-9_11

Loubere, P., Gary, A., Lagoe, M., 1993. Generation of the benthic foraminiferal assemblage: Theory and preliminary data. Marine Micropaleontology 20, 165–181. doi:10.1016/0377-8398(93)90031-R

Lund, D.C., Adkins, J.F., Ferrari, R., 2011a. Abyssal Atlantic circulation during the Last Glacial Maximum: Constraining the ratio between transport and vertical mixing. Paleoceanography 26. doi:https://doi.org/10.1029/2010PA001938

Lund, D.C., Mix, A.C., Southon, J., 2011b. Increased ventilation age of the deep northeast Pacific Ocean during the last deglaciation. Nature Geoscience 4, 771–774. doi:10.1038/ngeo1272

Lutze, G.F., 1980. Depth distribution of benthic foraminifera on the continental margin off NW Africa. 'Meteor'Forschungserbegnisse. Reihe C 32, 31–80.

Lutze, G.F., Coulbourn, W.T., 1984. Recent benthic foraminifera from the continental margin of northwest Africa: Community structure and distribution. Marine Micropaleontology 8, 361–401. doi:10.1016/0377-8398(84)90002-1

Lutze, G.F., Thiel, H., 1989. Epibenthic foraminifera from elevated microhabitats; *Cibicidoides wuellerstorfi* and *Planulina ariminensis*. Journal of Foraminiferal Research 19, 153–158. doi:10.2113/gsjfr.19.2.153

Lynch-Stieglitz, J., Stocker, T.F., Broecker, W.S., Fairbanks, R.G., 1995. The influence of air-sea exchange on the isotopic composition of oceanic carbon: Observations and modeling. Global Biogeochemical Cycles 9, 653–665. doi:https://doi.org/10.1029/95GB02574

Mackensen, A., Bickert, T., 1999. Stable carbon isotopes in benthic foraminifera: proxies for deep and bottom water circulation and new production. In: Use of Proxies in Paleoceanography. Springer, pp. 229–254.

Mackensen, A., Schmiedl, G., Harloff, J., Giese, M., 1995. Deep-sea foraminifera in the South Atlantic Ocean; ecology and assemblage generation. Micropaleontology 41, 342–358.

Mackensen, A., Schumacher, S., Radke, J., Schmidt, D.N., 2000. Microhabitat preferences and stable carbon isotopes of endobenthic foraminifera: clue to quantitative reconstruction of oceanic new production? Marine Micropaleontology 40, 233–258. doi:10.1016/S0377-8398(00)00040-2

MacKinnon, J.A., Johnston, T.M.S., Pinkel, R., 2008. Strong transport and mixing of deep water through the Southwest Indian Ridge. Nature Geoscience 1, 755–758. doi:10.1038/ngeo340

Mahoney, J.J., Natland, J.H., White, W.M., Poreda, R., Bloomer, S.H., Fisher, R.L., Baxter, A.N., 1989. Isotopic and geochemical provinces of the western Indian Ocean Spreading Centers. Journal of Geophysical Research: Solid Earth 94, 4033–4052. doi:10.1029/JB094iB04p04033

Mantyla, A.W., Reid, J.L., 1995. On the origins of deep and bottom waters of the Indian Ocean. Journal of Geophysical Research 100, 2417. doi:10.1029/94JC02564

Marchitto, T.M., Lehman, S.J., Ortiz, J.D., Flückiger, J., Geen, A.V., 2007. Marine Radiocarbon Evidence for the Mechanism of Deglacial Atmospheric CO_2 Rise. Science 316, 1456–1459. doi:10.1126/science.1138679

Marshall, J., Schott, F., 1999. Open-ocean convection: Observations, theory, and models. Reviews of Geophysics 37, 1–64. doi:https://doi.org/10.1029/98RG02739

McCave, I.N., Kiefer, T., Thornalley, D.J.R., Elderfield, H., 2005. Deep flow in the Madagascar–Mascarene Basin over the last 150000 years. Philosophical Transactions of the Royal Society A: Mathematical, Physical and Engineering Sciences 363, 81–99. doi:10.1098/rsta.2004.1480

McManus, J.F., Francois, R., Gherardi, J.M., Keigwin, L.D., Brown-Leger, S., 2004. Collapse and rapid resumption of Atlantic meridional circulation linked to deglacial climate changes. Nature 428. doi:10.1038/nature02494

Menviel, L., England, M.H., Meissner, K.J., Mouchet, A., Yu, J., 2014. Atlantic-Pacific seesaw and its role in outgassing CO^2 during Heinrich events. Paleoceanography 29, 58–70. doi:10.1002/2013PA002542

Menviel, L., Yu, J., Joos, F., Mouchet, A., Meissner, K.J., England, M.H., 2017. Poorly ventilated deep ocean at the Last Glacial Maximum inferred from carbon isotopes: A data-model comparison study. Paleoceanography 32, 2–17. doi:10.1002/2016PA003024

Miao, Q., Thunell, R.C., 1993. Recent deep-sea benthic foraminiferal distributions in the South China and Sulu Seas. Marine Micropaleontology 22, 1–32. doi:10.1016/0377-8398(93)90002-F

Mix, A.C., Bard, E., Schneider, R., 2001. Environmental processes of the ice age: land, oceans, glaciers (EPILOG). Quaternary Science Reviews 20, 627–657. doi:10.1016/S0277-3791(00)00145-1

Monnin, E., Indermühle, A., Dällenbach, A., Flückiger, J., Stauffer, B., Stocker, T.F., Raynaud, D., Barnola, J.M., 2001. Atmospheric CO_2 concentrations over the last glacial termination. Science 291, 112–114.

Monnin, E., Steig, E.J., Siegenthaler, U., Kawamura, K., Schwander, J., Stauffer, B., Stocker, T.F., Morse, D.L., Barnola, J.M., Bellier, B., 2004. Evidence for substantial accumulation rate variability in Antarctica during the Holocene, through synchronization of CO_2 in the Taylor Dome, Dome C and DML ice cores. Earth and Planetary Science Letters 224, 45–54.

Moodley, L., Zwaan, G.J.V.D., Herman, P.M.J., Kempers, L., Breugel, V.P., 1997. Differential response of benthic meiofauna to anoxia with special reference to Foraminifera

(Protista:Sarcodina). Marine Ecology Progress Series 158, 151–163. doi:10.3354/meps158151
Moodley, L., Schaub, B.E.M., Zwaan, G.J.V.D., Herman, P.M.J., 1998. Tolerance of benthic foraminifera (Protista: Sarcodina) to hydrogen sulphide. Marine Ecology Progress Series 169, 77–86. doi:10.3354/meps169077
Morgan, W.J., 1978. Rodriguez, Darwin, Amsterdam, ..., A second type of Hotspot Island. Journal of Geophysical Research: Solid Earth 83, 5355–5360. doi:10.1029/JB083iB11p05355
Murgese, D.S., De Deckker, P., 2005. The distribution of deep-sea benthic foraminifera in core tops from the eastern Indian Ocean. Marine Micropaleontology 56, 25–49. doi:10.1016/j.marmicro.2005.03.005
Murgese, D.S., De Deckker, P., 2007. The Late Quaternary evolution of water masses in the eastern Indian Ocean between Australia and Indonesia, based on benthic foraminifera faunal and carbon isotopes analyses. Palaeogeography, Palaeoclimatology, Palaeoecology 247, 382–401.
Muscheler, R., Beer, J., Wagner, G., Laj, C., Kissel, C., Raisbeck, G.M., Yiou, F., Kubik, P.W., 2004. Changes in the carbon cycle during the last deglaciation as indicated by the comparison of ^{10}Be and ^{14}C records. Earth and Planetary Science Letters 219, 325–340. doi:10.1016/S0012-821X(03)00722-2
Naidu, P.D., Malmgren, B.A., 1996. A High-resolution record of Late Quaternary upwelling along the Oman Margin, Arabian Sea based on planktonic foraminifera. Paleoceanography 11, 129–140. doi:https://doi.org/10.1029/95PA03198
Naik, S.S., Nisha, K., 2020. Increased Ventilation of the Northern Indian Ocean during the Last Deglaciation. Journal of the Geological Society of India 96, 148–150. doi:10.1007/s12594-020-1522-0
Nishioka, J., Obata, H., Tsumune, D., 2013. Evidence of an extensive spread of hydrothermal dissolved iron in the Indian Ocean. Earth and Planetary Science Letters 361, 26–33. doi:10.1016/j.epsl.2012.11.040
Okazaki, Yu., Timmermann, A., Menviel, L., Harada, N., Abe-Ouchi, A., Chikamoto, M., Mouchet, A., Asahi, H., 2010. Deepwater formation in the North Pacific during the last glacial termination. Science 329, 200–204.
Orsi, A.H., 2010. Recycling bottom waters. Nature Geoscience 3, 307–309. doi:10.1038/ngeo854
Orsi, A.H., Johnson, G.C., Bullister, J.L., 1999. Circulation, mixing, and production of Antarctic Bottom Water. Progress in Oceanography 43, 55–109. doi:10.1016/S0079-6611(99)00004-X
Orsi, A.H., Smethie, W.M., Bullister, J.L., 2002. On the total input of Antarctic waters to the deep ocean: A preliminary estimate from chlorofluorocarbon measurements. Journal of Geophysical Research: Oceans 107, 31-1-31–14. doi:10.1029/2001JC000976
Pahnke, K., Goldstein, S.L., Hemming, S.R., 2008. Abrupt changes in Antarctic Intermediate Water circulation over the past 25,000 years. Nature Geoscience 1, 870–874. doi:10.1038/ngeo360
Parnell, A.C., Haslett, J., Allen, J.R.M., Buck, C.E., Huntley, B., 2008. A flexible approach to assessing synchroneity of past events using Bayesian reconstructions of sedimentation history. Quaternary Science Reviews 27, 1872–1885. doi:10.1016/j.quascirev.2008.07.009
Penaud, A., Eynaud, F., Turon, J.L., Blamart, D., Rossignol, L., Marret, F., Lopez-Martinez, C., Grimalt, J.O., Malaizé, B., Charlier, K., 2010. Contrasting paleoceanographic conditions off Morocco during Heinrich events (1 and 2) and the Last Glacial

Maximum. Quaternary Science Reviews, Special Theme: Arctic Palaeoclimate Synthesis (PP. 1674-1790) 29, 1923–1939. doi:10.1016/j.quascirev.2010.04.011
Peterson, C.D., Lisiecki, L.E., 2018. Deglacial carbon cycle changes observed in a compilation of 127 benthic $\delta^{13}C$ time series (20–6 ka). Climate of the Past 14, 1229–1252.
Peterson, C.D., Lisiecki, L.E., Stern, J.V., 2014. Deglacial whole-ocean $\delta^{13}C$ change estimated from 480 benthic foraminiferal records. Paleoceanography 29, 549–563. doi:https://doi.org/10.1002/2013PA002552
Phipps, M., Jorissen, F., Pusceddu, A., Bianchelli, S., Stigter, H., 2012. Live benthic foraminiferal faunas along a Bathymetrical transect (282-4987 M) on the portuguese margin (NE Atlantic). Journal of Foraminiferal Research 42, 66–81. doi:10.2113/gsjfr.42.1.66
Picheral, M., Searson, S., Taillandier, V., Bricaud, A., Boss, E., Ras, J., Claustre, H., Ouhssain, M., Morin, P., Coppola, L., 2014. Vertical profiles of environmental parameters measured on discrete water samples collected with Niskin bottles during the Tara Oceans expedition 2009-2013. Marine Micropaleontology 8, 479–519.
Pichon, X.L., 1960. The deep water circulation in the southwest Indian Ocean. Journal of Geophysical Research (1896-1977) 65, 4061–4074. doi:10.1029/JZ065i012p04061
Pickard, G.I., 1979. Descriptive Physical Oceanography, An Introduction. 3rd (Sl) edition. Pergamon Press, New.
Piotrowski, A.M., Goldstein, S.L., Hemming, S., R., Fairbanks, R.G., Zylberberg, D.R., 2008. Oscillating glacial northern and southern deep water formation from combined neodymium and carbon isotopes. Earth and Planetary Science Letters 272, 394–405. doi:10.1016/j.epsl.2008.05.011
Piotrowski, A.M., Banakar, V.K., Scrivner, A.E., Elderfield, H., Galy, A., Dennis, A., 2009. Indian Ocean circulation and productivity during the last glacial cycle. Earth and Planetary Science Letters 285, 179–189.
Primeau, F., 2005. Characterizing transport between the surface mixed layer and the ocean interior with a forward and adjoint global ocean transport model. Journal of Physical Oceanography 35, 545–564.
Punyu, V.R., Banakar, V.K., Garg, A., 2014. Equatorial Indian Ocean productivity during the last 33 kyr and possible linkage to Westerly Jet variability. Marine Geology 348, 44–51.
Rahmstorf, S., 2002. Ocean circulation and climate during the past 120,000 years. Nature 419, 207–214.
Rahmstorf, S., 2006. Thermohaline Ocean Circulation. Encyclopedia of quaternary sciences 5, 10.
Rahmstorf, S., Crucifix, M., Ganopolski, A., Goosse, H., Kamenkovich, I., Knutti, R., Lohmann, G., Marsh, R., Mysak, L.A., Wang, Z., Weaver, A.J., 2005. Thermohaline circulation hysteresis: A model intercomparison. Geophys. 32. doi:https://doi.org/10.1029/2005GL023655
Raitzsch, M., Bijma, J., Benthien, A., Richter, K., Steinhoefel, G., Kučera, M., 2018. Boron isotope-based seasonal paleo-pH reconstruction for the Southeast Atlantic – A multispecies approach using habitat preference of planktonic foraminifera. Earth and Planetary Science Letters 487, 138–150. doi:10.1016/j.epsl.2018.02.002
Raj, M.S., Soma De, K.M., Gupta, A.K., 2009. Benthic foraminifer *Uvigerina proboscidea* as a proxy for winter monsoon (late Pliocene to Recent): DSDP Site 219, northwestern Indian Ocean. Geoenvironment: Challenges Ahead 311.
Rasmussen, S.O., Bigler, M., Blockley, S.P., Blunier, T., Buchardt, S.L., Clausen, H.B., Cvijanovic, I., Dahl-Jensen, D., Johnsen, S.J., Fischer, H., Gkinis, V., Guillevic, M., Hoek, W.Z., Lowe, J.J., Pedro, J.B., Popp, T., Seierstad, I.K., Steffensen, J.P., Svensson, A.M., Vallelonga, P., Vinther, B.M., Walker, M.J.C., Wheatley, J.J., Winstrup, M., 2014. A

stratigraphic framework for abrupt climatic changes during the Last Glacial period based on three synchronized Greenland ice-core records: refining and extending the INTIMATE event stratigraphy. Quaternary Science Reviews 106, 14–28. doi:10.1016/j.quascirev.2014.09.007

Rathburn, A.E., Corliss, B.H., 1994. The ecology of living (stained) deep-sea benthic foraminifera from the Sulu Sea. Paleoceanography 9, 87–150. doi:10.1029/93PA02327

Ravelo, A.C., Hillaire-Marcel, C., 2007. Chapter eighteen the use of oxygen and carbon isotopes of foraminifera in paleoceanography. Developments in marine geology 1, 735–764.

Raven, J.A., Falkowski, P.G., 1999. Oceanic sinks for atmospheric CO2. Plant, Cell & Environment 22, 741–755. doi:10.1046/j.1365-3040.1999.00419.x

Raza, T., Ahmad, S.M., 2013. Surface and deep water variations in the northeast Indian Ocean during 34–6 ka BP: Evidence from carbon and oxygen isotopes of fossil foraminifera. Quaternary International, Zanzibar to the Yellow Sea: A transect of Quaternary Studies from 6°S, 39°E to 35°N, 127°E 298, 37–44. doi:10.1016/j.quaint.2012.05.005

Reimer, P.J., Bard, E., Bayliss, A., Beck, J.W., Blackwell, P.G., Ramsey, C.B., Buck, C.E., Cheng, H., Edwards, R.L., Friedrich, M., Grootes, B., Guilderson, T.P., Haflidason, H., Hajdas, I., Hatté, C., Heaton, T.J., Hoffmann, D.L., Hogg, A.G., Hughen, K., Kaiser, K.F., Kromer, B., Manning, S.W., Niu, M., Reimer, R.W., Richards, D.A., Scott, E.M., Southon, J.R., Staff, R.A., Turney, C.S.M., Plicht, J. van der, 2013. IntCal13 and Marine13 Radiocarbon Age Calibration Curves 0–50,000 Years cal BP. Radiocarbon 55, 1869–1887. doi:10.2458/azu_js_rc.55.16947

Reimer, P.J., Austin, W.E., Bard, E., Bayliss, A., Blackwell, P.G., Ramsey, C.B., Butzin, M., Cheng, H., Edwards, R.L., Friedrich, M., 2020. The IntCal20 Northern Hemisphere radiocarbon age calibration curve (0–55 cal kBP). Radiocarbon 62, 725–757.

Reolid, M., Nagy, J., Rodríguez-Tovar, F.J., Olóriz, F., 2008. Foraminiferal Assemblages as Palaeoenvironmental Bioindicators in Late Jurassic Epicontinental Platforms: Relation with Trophic Conditions. Acta Palaeontologica Polonica 53, 705–722. doi:10.4202/app.2008.0413

Roberts, J., Kaczmarek, K., Langer, G., Skinner, L.C., Bijma, J., Bradbury, H., Turchyn, A.V., Lamy, F., Misra, S., 2018. Lithium isotopic composition of benthic foraminifera: A new proxy for paleo-pH reconstruction. Geochimica et Cosmochimica Acta, Chemistry of oceans past and present: A Special Issue in tribute to Harry Elderfield 236, 336–350. doi:10.1016/j.gca.2018.02.038

Robinson, L.F., 2005. Radiocarbon variability in the western North Atlantic during the last deglaciation. Science 310. doi:10.1126/science.1114832

Ronge, T.A., Tiedemann, R., Lamy, F., Köhler, P., Alloway, B.V., De Pol-Holz, R., Pahnke, K., Southon, J., Wacker, L., 2016. Radiocarbon constraints on the extent and evolution of the South Pacific glacial carbon pool. Nature Communications 7, 11487. doi:10.1038/ncomms11487

Ronge, T.A., Prange, M., Mollenhauer, G., Ellinghausen, M., Kuhn, G., Tiedemann, R., 2020. Radiocarbon Evidence for the Contribution of the Southern Indian Ocean to the Evolution of Atmospheric CO_2 Over the Last 32,000 Years. Paleoceanography and Paleoclimatology 35, e2019PA003733. doi:https://doi.org/10.1029/2019PA003733

Rosenthal, Y., Boyle, E.A., Slowey, N., 1997. Temperature control on the incorporation of magnesium, strontium, fluorine, and cadmium into benthic foraminiferal shells from Little Bahama Bank: Prospects for thermocline paleoceanography. Geochimica et Cosmochimica Acta 61, 3633–3643. doi:10.1016/S0016-7037(97)00181-6

Rutberg, R.L., Hemming, S.R., Goldstein, S.L., 2000. Reduced North Atlantic Deep Water flux to the glacial Southern Ocean inferred from neodymium isotope ratios. Nature 405, 935–938. doi:10.1038/35016049

Saraswat, R., Nigam, R., 2013. Paleoceanography, Biological proxies | Benthic Foraminifera. In: Elias, S.A., Mock, C.J. (Eds.), Encyclopedia of Quaternary Science (Second Edition). Elsevier, Amsterdam, pp. 765–774. doi:10.1016/B978-0-444-53643-3.00279-X

Sarkar, S., Gupta, A.K., 2014. Late Quaternary productivity changes in the equatorial Indian Ocean (ODP Hole 716A). Palaeogeography, Palaeoclimatology, Palaeoecology 397, 7–19.

Sarnthein, M., Pflaumann, U., Weinelt, M., 2003. Past extent of sea ice in the northern North Atlantic inferred from foraminiferal paleotemperature estimates. Paleoceanography 18.

Schmiedl, G., Mackensen, A., Müller, P.J., 1997. Recent benthic foraminifera from the eastern South Atlantic Ocean: Dependence on food supply and water masses. Marine Micropaleontology 32, 249–287. doi:10.1016/S0377-8398(97)00023-6

Schönfeld, J., 1997. The impact of the Mediterranean Outflow Water (MOW) on benthic foraminiferal assemblages and surface sediments at the southern Portuguese continental margin. Marine Micropaleontology 29, 211–236. doi:10.1016/S0377-8398(96)00050-3

Schönfeld, J., Alve, E., Geslin, E., Jorissen, F., Korsun, S., Spezzaferri, S., 2012. The FOBIMO (FOraminiferal BIo-MOnitoring) initiative—Towards a standardised protocol for soft-bottom benthic foraminiferal monitoring studies. Marine Micropaleontology 94–95, 1–13. doi:10.1016/j.marmicro.2012.06.001

Schott, F.A., McCreary, J.P., 2001. The monsoon circulation of the Indian Ocean. Progress in Oceanography 51, 1–123. doi:10.1016/S0079-6611(01)00083-0

Seierstad, I.K., Abbott, P.M., Bigler, M., Blunier, T., Bourne, A.J., Brook, E., Buchardt, S.L., Buizert, C., Clausen, H.B., Cook, E., 2014. Consistently dated records from the Greenland GRIP, GISP2 and NGRIP ice cores for the past 104 ka reveal regional millennial-scale $\delta^{18}O$ gradients with possible Heinrich event imprint. Quaternary Science Reviews 106, 29–46.

Shackleton, N., 1967. Oxygen Isotope Analyses and Pleistocene Temperatures Re-assessed. Nature 215, 15–17. doi:10.1038/215015a0

Shi, X., Lohmann, G., 2016. Simulated response of the mid-Holocene Atlantic meridional overturning circulation in ECHAM6-FESOM/MPIOM. Journal of Geophysical Research: Oceans 121, 6444–6469. doi:https://doi.org/10.1002/2015JC011584

Sigman, D.M., Boyle, E.A., 2001. Antarctic stratification and glacial CO_2. Nature 412, 606–606. doi:10.1038/35088132

Sigman, D.M., Hain, M.P., Haug, G.H., 2010. The polar ocean and glacial cycles in atmospheric CO_2 concentration. Nature 466, 47–55.

Sikes, E.L., Samson, C.R., Guilderson, T.P., Howard, W.R., 2000. Old radiocarbon ages in the southwest Pacific Ocean during the last glacial period and deglaciation. Nature 405, 555–559.

Sikes, E.L., Cook, M.S., Guilderson, T.P., 2016. Reduced deep ocean ventilation in the Southern Pacific Ocean during the last glaciation persisted into the deglaciation. Earth and Planetary Science Letters 438, 130–138.

Silva, J.C.B. da, New, A.L., Magalhaes, J.M., 2011. On the structure and propagation of internal solitary waves generated at the Mascarene Plateau in the Indian Ocean. Deep Sea Research Part I: Oceanographic Research Papers 58, 229–240. doi:10.1016/j.dsr.2010.12.003

Singh, A.D., Rai, A.K., Verma, K., Das, S., Bharti, S.K., 2015. Benthic foraminiferal diversity response to the climate induced changes in the eastern Arabian Sea oxygen

minimum zone during the last 30 ka BP. Quaternary International 374, 118–125. doi:10.1016/j.quaint.2014.11.052
Singh, R.K., Gupta, A.K., 2010. Deep-sea benthic foraminiferal changes in the Eastern Indian Ocean (ODP Hole 757B): their links to deep Indonesian (Pacific) flow and high latitude glaciation during the Neogene. Episodes 33, 74–82.
Skinner, L., McCave, I.N., Carter, L., Fallon, S., Scrivner, A.E., Primeau, F., 2015. Reduced ventilation and enhanced magnitude of the deep Pacific carbon pool during the last glacial period. Earth and Planetary Science Letters 411, 45–52. doi:10.1016/j.epsl.2014.11.024
Skinner, L.C., 2017. Radiocarbon constraints on the glacial ocean circulation and its impact on atmospheric CO2. Nature Communications 8.
Skinner, L.C., Shackleton, N.J., 2004a. Rapid transient changes in northeast Atlantic deep water ventilation age across Termination I. Paleoceanography 19. doi:https://doi.org/10.1029/2003PA000983
Skinner, L.C., Shackleton, N.J., 2004b. Stable carbon isotopes of *Planulina wuellerstorfi* of sediment core MD99-2334. In supplement to: Skinner, LC; Shackleton, NJ (2004): Rapid transient changes in northeast Atlantic deep water ventilation age across Termination I. Paleoceanography, 19(2), PA2005, https://doi.org/10.1029/2003PA000983. doi:10.1594/PANGAEA.619069
Skinner, L.C., Shackleton, N.J., 2005. An Atlantic lead over Pacific deep-water change across Termination I: implications for the application of the marine isotope stage stratigraphy. Quaternary Science Reviews 24, 571–580. doi:10.1016/j.quascirev.2004.11.008
Skinner, L.C., Shackleton, N.J., Elderfield, H., 2003. Millennial-scale variability of deep-water temperature and $\delta^{18}O_{dw}$ indicating deep-water source variations in the Northeast Atlantic, 0–34 cal. ka BP. Geochemistry, Geophysics, Geosystems 4. doi:https://doi.org/10.1029/2003GC000585
Skinner, L.C., Fallon, S., Waelbroeck, C., Michel, E., Barker, S., 2010. Ventilation of the deep Southern Ocean and deglacial CO_2 rise. Science 328, 1147–1151.
Skinner, L.C., Scrivner, A.E., Vance, D., Barker, S., Fallon, S., Waelbroeck, C., 2013. North Atlantic versus Southern Ocean contributions to a deglacial surge in deep ocean ventilation. Geology 41, 667–670. doi:10.1130/G34133.1
Skinner, L.C., Waelbroeck, C., Scrivner, A.E., Fallon, S.J., 2014. Radiocarbon evidence for alternating northern and southern sources of ventilation of the deep Atlantic carbon pool during the last deglaciation. Proceedings of the National Academy of Sciences 111, 5480–5484. doi:10.1073/pnas.1400668111
Skinner, L.C., Primeau, F., Freeman, E., Fuente, M. de la, Goodwin, P.A., Gottschalk, J., Huang, E., McCave, I.N., Noble, T.L., Scrivner, A.E., 2017. Radiocarbon constraints on the glacial ocean circulation and its impact on atmospheric CO_2. Nature Communications 8, 16010. doi:10.1038/ncomms16010
Skinner, L.C., Muschitiello, F., Scrivner, A.E., 2019. Marine Reservoir Age Variability Over the Last Deglaciation: Implications for Marine Carbon Cycling and Prospects for Regional Radiocarbon Calibrations. Paleoceanography and Paleoclimatology 34, 1807–1815. doi:https://doi.org/10.1029/2019PA003667
Skinner, L.C., Freeman, E., Hodell, D., Waelbroeck, C., Riveiros, N.V., Scrivner, A.E., 2021. Atlantic Ocean Ventilation Changes Across the Last Deglaciation and Their Carbon Cycle Implications. Paleoceanography and Paleoclimatology 36, e2020PA004074. doi:https://doi.org/10.1029/2020PA004074
Sliter, W.V., Baker, R.A., 1972. Cretaceous bathymetric distribution of benthic foraminifers. Journal of Foraminiferal Research 2, 167–183. doi:10.2113/gsjfr.2.4.167

Sloyan, B.M., 2006. Antarctic bottom and lower circumpolar deep water circulation in the eastern Indian Ocean. Journal of Geophysical Research: Oceans 111. doi:https://doi.org/10.1029/2005JC003011
Smart, C.W., King, S.C., Gooday, A.J., Murray, J.W., Thomas, E., 1994. A benthic foraminiferal proxy of pulsed organic matter paleofluxes. Marine Micropaleontology 23, 89–99. doi:10.1016/0377-8398(94)90002-7
Smart, C.W., Thomas, E., Ramsay, A.T.S., 2007. Middle–late Miocene benthic foraminifera in a western equatorial Indian Ocean depth transect: Paleoceanographic implications. Palaeogeography, Palaeoclimatology, Palaeoecology 247, 402–420. doi:10.1016/j.palaeo.2006.11.003
Smart, C.W., Waelbroeck, C., Michel, E., Mazaud, A., 2010. Benthic foraminiferal abundance and stable isotope changes in the Indian Ocean sector of the Southern Ocean during the last 20 kyr: Paleoceanographic implications. Palaeogeography, Palaeoclimatology, Palaeoecology 297, 537–548.
Soulet, G., Skinner, L.C., Beaupré, S.R., Galy, V., 2016. A note on reporting of reservoir ^{14}C disequilibria and age offsets. Radiocarbon 58, 205–211. doi:10.1017/RDC.2015.22
Southon, J., Kashgarian, M., Fontugne, M., Metivier, B., Yim, W.W.S., 2002. Marine reservoir corrections for the Indian Ocean and Southeast Asia. Radiocarbon 44, 167–180.
Spivack, A.J., You, C., Smith, H.J., 1993. Foraminiferal boron isotope ratios as a proxy for surface ocean pH over the past 21 Myr. Nature 363, 149–151. doi:10.1038/363149a0
Steens, T.N.F., Ganssen, G., Kroon, D., 1992. Oxygen and carbon isotopes in planktonic foraminifera as indicators of upwelling intensity and upwelling-induced high productivity in sediments from the northwestern Arabian Sea. Geological Society, London, Special Publications 64, 107–119. doi:10.1144/GSL.SP.1992.064.01.07
Stichel, T., Frank, M., Rickli, J., Haley, B.A., 2012. The hafnium and neodymium isotope composition of seawater in the Atlantic sector of the Southern Ocean. Earth and Planetary Science Letters 317, 282–294.
Stuiver, M., Polach, H.A., 1977. Discussion reporting of ^{14}C data. Radiocarbon 19, 355–363.
Stuiver, M., Reimer, P.J., Braziunas, T.F., 1998a. High-precision radiocarbon age calibration for terrestrial and marine samples. Radiocarbon 40, 1127–1151.
Stuiver, M., Reimer, P.J., Bard, E., Beck, J.W., Burr, G.S., Hughen, K.A., Kromer, B., McCormac, G., Plicht, J.D.R., Spurk, M., 1998b. INTCAL98 Radiocarbon Age Calibration, 24,000–0 cal BP. Radiocarbon 40, 1041–1083. doi:10.1017/S0033822200019123
Sun, X., Corliss, B.H., Brown, C.W., Showers, W.J., 2006. The effect of primary productivity and seasonality on the distribution of deep-sea benthic foraminifera in the North Atlantic. Deep Sea Research Part I: Oceanographic Research Papers 53, 28–47. doi:10.1016/j.dsr.2005.07.003
Talley, L., 2013. Closure of the Global Overturning Circulation Through the Indian, Pacific, and Southern Oceans: Schematics and Transports. Oceanogr. 26, 80–97. doi:10.5670/oceanog.2013.07
Talley, L.D., 2011. Descriptive physical oceanography: an introduction. Academic press.
Tao, C., Lin, J., Guo, S., Chen, Y.J., Wu, G., Han, X., German, C.R., Yoerger, D.R., Zhou, N., Li, H., Su, X., Zhu, J., and the DY115-19 (Legs 1–2) and DY115-20 (Legs 4–7) Science Parties, 2012. First active hydrothermal vents on an ultraslow-spreading center: Southwest Indian Ridge. Geology 40, 47–50. doi:10.1130/G32389.1
Teh, S., Koh, H., Lim, Y., 2018. Tsunami run-up amplification factors for real-time prediction of run-up heights and inundation distances for Penang Island. Journal of Physics: Conference Series 1123, 012049. doi:10.1088/1742-6596/1123/1/012049
Thomas, A.L., Henderson, G.M., Robinson, L.F., 2006. Interpretation of the ^{231}Pa/^{230}Th paleocirculation proxy: New water-column measurements from the southwest

Indian Ocean. Earth and Planetary Science Letters 241, 493–504. doi:10.1016/j.epsl.2005.11.031
Thunell, R., Sautter, L.R., 1992. Planktonic foraminiferal faunal and stable isotopic indices of upwelling: a sediment trap study in the San Pedro Basin, Southern California Bight. Geological Society, London, Special Publications 64, 77–91. doi:10.1144/GSL.SP.1992.064.01.05
Tiwari, M., Ramesh, R., Somayajulu, B.L.K., Jull, A.J.T., Burr, G.S., 2006. Paleomonsoon precipitation deduced from a sediment core from the equatorial Indian Ocean. Geo-Marine Letters 26, 23–30. doi:10.1007/s00367-005-0012-0
Tomczak, M., Godfrey, J.S., 2003. Regional Oceanography: An Introduction. Daya Books.
Toole, J.M., Warren, B.A., 1993. A hydrographic section across the subtropical South Indian Ocean. Deep Sea Research Part I: Oceanographic Research Papers 40, 1973–2019. doi:10.1016/0967-0637(93)90042-2
Umling, N.E., Thunell, R.C., 2017. Synchronous deglacial thermocline and deep-water ventilation in the eastern equatorial Pacific. Nature Communications 8, 14203. doi:10.1038/ncomms14203
Volk, T., Hoffert, M.I., 1985. Ocean carbon pumps: Analysis of relative strengths and efficiencies in ocean-driven atmospheric CO_2 changes. The carbon cycle and atmospheric CO2: natural variations Archean to present 32, 99–110.
Wacker, L., Němec, M., Bourquin, J., 2010. A revolutionary graphitisation system: Fully automated, compact and simple. Nuclear Instruments and Methods in Physics Research Section B: Beam Interactions with Materials and Atoms, Proceedings of the Eleventh International Conference on Accelerator Mass Spectrometry 268, 931–934. doi:10.1016/j.nimb.2009.10.067
Waelbroeck, C., Levi, C., Duplessy, J.C., Labeyrie, L., Michel, E., Cortijo, E., Bassinot, F., Guichard, F., 2006. Distant origin of circulation changes in the Indian Ocean during the last deglaciation. Earth and Planetary Science Letters 243, 244–251. doi:10.1016/j.epsl.2005.12.031
Warren, B.A., 1971. Evidence for a Deep Western Boundary Current in the South Indian Ocean. Nature Physical Science 229, 18–19. doi:10.1038/physci229018b0
Warren, B.A., 1974. Deep flow in the Madagascar and Mascarene basins. Deep Sea Research and Oceanographic Abstracts 21, 1–21. doi:10.1016/0011-7471(74)90015-1
Weiss, R.F., 1983. GEOSECS Indian Ocean Expedition: Hydrographic data 1977-1978.
Wilson, D.J., Piotrowski, A.M., Galy, A., McCave, I.N., 2012. A boundary exchange influence on deglacial neodymium isotope records from the deep western Indian Ocean. Earth and Planetary Science Letters 341–344, 35–47. doi:10.1016/j.epsl.2012.06.009
Wyrtki, K., 1973. Physical Oceanography of the Indian Ocean. In: Zeitzschel, B., Gerlach, S.A. (Eds.), The Biology of the Indian Ocean, Ecological Studies. Springer, Berlin, Heidelberg, pp. 18–36. doi:10.1007/978-3-642-65468-8_3
Yadav, R., Naik, S.S., Narvekar, J., 2021. The equatorial Indian Ocean upper water-column structure influenced by cross-basinal water exchange over the last ~40000 years. Quaternary International. doi:10.1016/j.quaint.2021.04.002
Yanko, V., Kronfeld, J., Flexer, A., 1994. Response of benthic Foraminifera to various pollution sources; implications for pollution monitoring. Journal of Foraminiferal Research 24, 1–17. doi:10.2113/gsjfr.24.1.1
You, Y., 2000. Implications of the deep circulation and ventilation of the Indian Ocean on the renewal mechanism of North Atlantic Deep Water. Journal of Geophysical Research: Oceans 105, 23895–23926. doi:10.1029/2000JC900105
Zhao, N., Marchal, O., Keigwin, L., Amrhein, D., Gebbie, G., 2018. A synthesis of deglacial deep-sea radiocarbon records and their (in)consistency with modern ocean ventilation. Paleoceanography and Paleoclimatology 33.

List of Publications

- **Bharti, N**., Bhushan, R., Muruganantham M., (2020). *Estimates of High-Resolution Ventilation Age from the Equatorial Indian Ocean during Last 40 ka: Implications to Paleo Deep Water Circulation*. Conference: Goldschmidt2020. https://doi.org/10.46427/gold2020.182.

- **Bharti, N.**, Bhushan, R., Skinner, L., Muruganantham, M., Jena, P. S., Dabhi, A., & Shivam, A. (2022). *Evidence of poorly ventilated deep Central Indian Ocean during the last glaciation.* Earth and Planetary Science Letters, 582, 117438.

- Jena, P. S., Bhushan, R., Shivam, A., Nambiar, R., & **Bharti, N.** (2021). *Production rate variation and changes in sedimentation rate of marine core dated with meteoric 10Be and 14C.* Journal of Environmental Radioactivity, 237, 106678. https://doi.org/10.1016/j.scitotenv.2021.149808.

- Jena, P. S., Bhushan, R., Ajay, S., **Bharti, N.,** & Sudheer, A. K. (2021). *^{10}Be depositional flux variation in the central Indian Ocean during the last 43 ka*. Science of The Total Environment, 149808. https://doi.org/10.1016/j.scitotenv.2021.149808.

- Samanta, A., Tripathy, G. R., Nath, B. N., Bhushan, R., Panchang, R., **Bharti, N.**, & Shrivastava, A. (2022). *Holocene variability in chemical weathering and ocean redox state: A reconstruction using sediment geochemistry of the Arabian Sea*. Journal of Asian Earth Sciences, 224, 105029.

- Shaji, J., Banerji, U. S., Maya, K., Joshi, K. B., Dabhi, A. J., **Bharti, N.,** ... & Padmalal, D. (2022). Holocene monsoon and sea-level variability from coastal lowlands of Kerala, SW India. Quaternary International.

- **Bharti N**., Bhushan R., Muruganantham, M., Shivam, A., Jena, P. S. *Benthic Foraminifera Assemblage in the Central Equatorial Indian Ocean and its Response to Paleo-Deep Water Environment*. Journal of Foraminiferal Research. (**Under review**)

- Samanta, A., Tripathy, G., Panchang, R., Nath, B.N., Bhushan R., **Bharti, N**. *Late Holocene intensification of chemical weathering due to human-induced rise in C4 vegetation*. Geology. (**Under review**)

Manuscript under preparation

- **Bharti N**., Bhushan R., Jena, P. S. Shivam, A. *Paleo ventilation of the deep South West Indian Ocean.*

- **Bharti N**., Bhushan R., Dhabhi, A., Nambiar R. *Paleo- ventilation of the deep Eastern Indian Ocean basin, evidence of mantle derived dead CO_2*.

- **Bharti N**., Sanjit, K. J., Bhushan R., Dhabhi, A., Shivam, A. *Radiocarbon variation in surface, intermediate and deep dwelling foraminifera from three cores of the Equatorial Indian Ocean*.
-